

June 1970

NVR-6432

CC 134231

NASA-CE-134231) INVESTIGATION OF
PREDICTION METHODS FOR THE LOADS AND
STRESSES OF APOLLO TYPE SPACECRAFT
PARACHUTES. VOLUME 2: (Northrop Corp.)
276 p HC \$17.00

874-19674

Unclass

CSCL 01B G3/02 34748

NORTHROP

*Investigation of Prediction Methods for the
Loads and Stresses of
Apollo Type Spacecraft Parachutes
Volume II - Stresses*

By

W. M. Mullins, D. T. Reynolds,
K. G. Lindh and M. R. Bottorff

Prepared under Contract NAS 9-8131 for
National Aeronautics and Space Administration
Manned Spacecraft Center

Northrop Corporation Ventura Division
Newbury Park, California 91320

SECRET

June 1970


NVR-6432

INVESTIGATION OF PREDICTION METHODS FOR THE
LOADS AND STRESSES OF
APOLLO TYPE SPACECRAFT PARACHUTES
VOLUME II - STRESSES

Prepared for
NASA Manned Spacecraft Center
Houston, Texas
under Contract NAS 9-8131

Prepared by
W. M. Mullins, D. T. Reynolds
K. G. Lindh and M. R. Bottorff

Approved by:


D. D. Warner, Manager
Engineering Department

NORTHROP CORPORATION, VENTURA DIVISION
1515 Rancho Conejo Boulevard
Newbury Park, California 91320

NV Project No. 0111

NVR-6432

Northrop

FOREWORD

This report presents the second volume of a two-volume final report on a one-year study entitled "Analysis of Apollo Spacecraft Parachutes." (The companion volume is listed as Reference 1.) This study was performed by Northrop Ventura for NASA/MSC under Contract NAS-9-8131. Messrs. M. A. Silveira, K. Hinson and C. Eldred of NASA/MSC monitored and reviewed the study.

This study, designated as Project 0111 at Northrop Ventura, was carried out with direction from the Systems Engineering Group under Mr. R. G. Iemm. Program direction was provided by Mr. T. W. Knacke of the Advanced Design Group, and the Project Engineer was Mr. F. E. Mickey of the Aerospace Landing Systems Project Office.

Principle authors of the sections in the body of the report are as follows:

Mr. W. M. Mullins, Section 3;
Mr. D. T. Reynolds, Section 4;
Dr. K. G. Lindh, Section 5; and
Mr. M. R. Bottorff, Section 6.

The authors greatly acknowledge the contribution of Mr. R. L. Ranes in the development of the structural analysis methods presented in Section 3 and also the valuable assistance of Mr. A. J. McEwan, who prepared Section 5.5.

CONTINUED

ABSTRACT

The major factors in structural analysis of parachutes are reviewed, including ultimate strength, design factors, safety factors, external loading, and internal loading of the individual structural members. A method for computing the internal load distribution for a parachute with a given applied riser load and canopy differential pressure distribution is presented, and comparisons of the predicted canopy shapes and internal loadings with Apollo development test results are given. The analysis discussed above is modified to give better representation of ribbon parachutes with vertical ribbons, and a comparison of results of the two analyses is given. A study of data obtained in dynamic loading tests of pilot chute risers adds to the understanding of the effects of high load onset rates which occur at main parachute canopy stretch. A study of methods for measuring parachute aerodynamic and internal loading is performed, and a plan is developed for a three-phase test program to acquire needed data.

CONTENTS

<u>SECTION</u>		<u>PAGE</u>
	FOREWORD	11
	ABSTRACT	111
	SYMBOLS	x11
1.0	INTRODUCTION	1
2.0	DISCUSSION OF PARACHUTE STRUCTURAL ANALYSIS	9
3.0	PARACHUTE INTERNAL LOAD DISTRIBUTION	13
	3.1 Program CANO - An Internal Load Analysis for Parachutes	13
	3.2 Program CANO 1 - An Internal Load Analysis for Ribbon Parachutes	29
4.0	TEST DATA REVIEW AND APPLICATION OF INTERNAL LOADS ANALYSIS	42
	4.1 Drogue Chute	44
	4.1.1 Drogue Chute Structural Model	44
	4.1.2 Drogue Chute Pressure Distribution	50
	4.1.3 Drogue Chute Growth	60
	4.1.4 Drogue Chute Film Analysis	62
	4.1.5 Drogue Chute Failure Analysis	66
	4.1.6 Analysis of Drogue Chute Using CANO 1	67
	4.2 Pilot Parachute	74
	4.2.1 Pilot Parachute Structural Model	74
	4.2.2 Pilot Parachute Pressure Distribution	74
	4.2.3 Pilot Parachute Film Analysis	79
	4.3 Main Parachute	81
	4.3.1 Structural Model of the Main Parachute	81
	4.3.2 Main Parachute Failure Analysis	87

CONTENTS (Cont'd)

<u>SECTION</u>		<u>PAGE</u>
	4.3.3 Main Parachute Pressure Distribution and Film Analysis	91
	4.3.4 Stress-Time Study of the Main Parachute	100
	4.3.5 Optimum Weight Calculation for the Main Parachute	111
5.0	PILOT PARACHUTE RISER DYNAMICS	114
	5.1 Test Equipment and Procedure	115
	5.2 Description of Specimens and Material Properties	117
	5.3 Force Gage Data	124
	5.4 The Linear-Elastic Approximation	124
	5.5 The Finite Difference Method	146
	5.6 Analysis of Films	154
	5.7 Summary of Pilot Chute Riser Dynamics Study	181
6.0	MEASUREMENT OF PRESSURE, LOADS, AND STRESSES	183
	6.1 Structural Analysis Data Requirements	183
	6.2 Summary of Prior Work on Canopy Pressure Measurement	187
	6.3 Pressure Measurement	192
	6.4 Strain Transducers	197
	6.5 Load Transducers	199
	6.6 Photographic Instrumentation	202
	6.7 Program Plan for Measuring Parachute Pressure Distribution, Load, Strain, and Shape	204
7.0	SUMMARY	220
8.0	CONCLUSIONS	226
9.0	RECOMMENDATIONS	228
	APPENDIX A: Summary of Apollo Aerial Drop Tests	230
	APPENDIX B: Example Margin of Safety Calcu- lations for the Apollo Main Parachute	248
	REFERENCES	258

LIST OF TABLES

<u>TABLE</u>		<u>PAGE</u>
1	Drogue Chute Failure Analysis	66
2	Main Parachute Failure Analysis	90
3	Load-Time History Used for the Stress-Time Study	103
4	Load-Time History of the Main Parachute Radial Tape	110
5	Comparison of Apollo Main Parachute Weight with Theoretically Optimum Weights	113
6	Impact Velocities and Peak Deadman Force from Pilot Chute Riser Tests	118
7	Specimen Parameters for Approximate Linear-Elastic Analysis	138
8	Parameters for Fine Resolution of Discontinuities in Specimen Type D5	144
9	Gage Mark Velocity after Passage of First Wave, Test D5-1	157
10	Webbing Strain, Test D5-1	159
11	Comparison of Wave Velocities, Particle Velocities and Strains	174
12	Determination of Points on the Dynamic Load - Strain Curves Using the First Longitudinal Wave Across the Specimen Trunks	179
13	Determination of Points on the Dynamic Load-Strain Curves Using Transverse Wave Velocity	179
14	Wind Tunnel Test Schedule	210
15	Test Conditions for Simulation of a Full Scale Parachute by Use of a One-Third Scale Model	218
A1	Summary of Apollo Drop Tests	231
B1	Design Loads for Main Parachute	249
B2	Sail Load-Strength Ratios	252
B3	Sail Margins of Safety	254

LIST OF FIGURES

<u>FIGURE</u>		<u>PAGE</u>
1	Differential Pressure vs. Time	12
2	Flow Diagram for Program CANO	26
3	Flow Diagram Detail Showing Skirt Equilibrium for an Unreefed Parachute	27
4	Flow Diagram Detail Showing Skirt Equilibrium for a Reefed Parachute	28
5	Ribbon Parachute with Vertical Members	30
6	Canopy Geometry	32
7	Flow Diagram for Program CANO 1	41
8	Drogue Chute Assembly	45
9	Drogue Chute Structural Model	46
10	Drogue Chute Canopy Profiles for Various Structural Models	47
11	Horizontal Tape Loads for Various Models of the Drogue Chute	48
12	Radial Tape Load for Various Models of the Drogue Chute	49
13	Horizontal Ribbon Loading for the Reefed Drogue Chute	51
14	Radial Tape Loads for the Reefed Drogue Chute	52
15	Pressure Distributions at Various Times after Deployment	54
16	Canopy Pressure Distributions Used for Sensitivity Study	55
17	Drogue Canopy Profile for Various Pressure Distributions	56
18	Horizontal Tape Loads in Drogue Chute for Various Pressure Distributions	57
19	Radial Tape Loads in Drogue Chute for Various Pressure Distributions	59
20	Variation of Canopy Size and Internal Loads with Axial Load	61
21	Comparison of Predicted and Measured Reefed Canopy Shapes for the Drogue Chute	63
22	Comparison of Measured and Predicted Canopy Diameters for the Drogue Chute	65

<u>FIGURE</u>		<u>PAGE</u>
23	Reefed Drogue Chute Profile	69
24	Disreefed Drogue Chute Profiles	70
25	Horizontal Ribbon Loading for Reefed and Open Drogue Canopies	71
26	Radial Tape Loading for Reefed and Open Drogue Canopies	72
27	Vertical Ribbon Loading and Horizontal Ribbon Displacement for Reefed and Open Drogue Canopies	73
28	Pilot Chute Structural Model	75
29	Canopy Pressure Distribution for the Pilot Parachute	76
30	Sail Loading for the Pilot Chute	77
31	Radial Tape Loads for the Pilot Chute	78
32	Comparison of Predicted and Measured Canopy Shapes for the Pilot Chute	80
33	Main Parachute Assembly	83
34	Structural Details for the Main Parachute Canopy	84
35	Main Parachute Structural Model	85
36	Sail Load-Strength Ratio for Three Versions of the Main Parachute	86
37	Reefed Main Parachute Pressure Distributions	94
38	Comparison of Measured and Predicted Profiles for the First Stage Reefed Main Parachute	95
39	Comparison of Measured and Predicted Profiles for the Second Stage Reefed Main Parachute	96
40	Fully Inflated Main Parachute Pressure Distributions	97
41	Comparison of Predicted and Measured Main Parachute Diameters at the Time of Maximum Canopy Diameter	98
42	Comparison of Predicted and Measured Main Parachute Diameters at the Time of Maximum Riser Load	99
43	Canopy Pressure Distributions Used for the Stress-Time Study	104

<u>FIGURE</u>		<u>PAGE</u>
44	Load-Time Trace for the 83.5 ft D ₀ Ringsail Parachute	105
45	Critical Sail Load vs. Time for the 83.5 ft D ₀ Ringsail Parachute	106
46	Sail Loading vs. Time for Sails 1, 2, 3 and 4 of the 83.5 ft D ₀ Ringsail Parachute	107
47	Sail Load vs. Time for Sails 5, 6, 7 and 8 of the 83.5 ft D ₀ Ringsail Parachute	108
48	Sail Load vs. Time for Sails 9, 10, 11 and 12 of the 83.5 ft D ₀ Ringsail Parachute	109
49	Pilot Chute Riser Dynamic Test Apparatus	116
50	Pilot Chute Riser Test Specimens D3, D4 and D6	119
51	Pilot Chute Riser Material Test Specimen	120
52	Static Load-Strain Curve for a Sample of MIL-W-5625 3/4" Nylon Webbing	121
53	Average Static Load-Strain Curve for MIL-W-4088 1" Nylon Webbing	122
54	Deadman Force Gage Record for Pilot Chute Riser Test D3-1	125
55	Deadman Force Gage Record for Pilot Chute Riser Test D3-2	126
56	Deadman Force Gage Record for Pilot Chute Riser Test D3-3	127
57	Deadman Force Gage Record for Pilot Chute Riser Test D4-5	128
58	Deadman Force Gage Record for Pilot Chute Riser Test D4-6	129
59	Deadman Force Gage Record for Pilot Chute Riser Test D5-1	130
60	Deadman Force Gage Record for Pilot Chute Riser Test D6-1	131
61	Wave Diagram, Linear-Elastic Approximation, Test Type D5	135
62	Strain Distribution Along the Length of the Trunk of Specimen Type D5. Approximate Linear-Elastic Analysis, $\tau = 2.8$	139

<u>FIGURE</u>		<u>PAGE</u>
63	Strain as a Function of Time at Three Stations, Approximate Linear-Elastic Analysis	140
64	Deadman Force as a Function of Time, Specimen Type D5	142
65	Strain at Deadman End of Specimen for the Cases of Coarse and Fine Resolution of Discontinuities	145
66	Wave Profile Determined by the AFTON Program for the Case of a Uniform Specimen	149
67	Comparison of Experimental Results with Deadman Force Computed by AFTON Program, Test D3-2	151
68	Comparison of Experimental Results with Deadman Force Computed by AFTON, Test D5-1	152
69	Space-Time Diagram, Test D5-1	155
70	Theoretical and Experimental Loci of the Transverse Wave in the Bridle, Test Type D5	165
71	Space-Time Diagram, Test D3-1	167
72	Space-Time Diagram, Test D3-2	168
73	Space-Time Diagram, Test D3-3	169
74	Space-Time Diagram, Test D4-5	170
75	Space-Time Diagram, Test D4-6	171
76	Space-Time Diagram, Test D6-1	172
77	Observed Longitudinal Wave Velocity vs. Velocity Calculated on the Basis of a Linear Load-Strain Curve	176
78	Dynamic Load-Strain Curves for the Specimen Trunk Material as Determined from Wave Velocities	180
79	CANO Program Input/Output Relationships	185
80	Schjeldahl and RdF West Pressure Measurement Systems	194
81	Manning Instrument Pressure Transducer	196

NORTHROP

<u>FIGURE</u>		<u>PAGE</u>
82	Variable Inductance Strain Transducer	198
83	Nonelectrical Maximum Strain Sensor	200
84	Radial Tape Load Transducer	201
85	Canopy Growth vs. Reefing Percentage	209
86	Typical Parachute Installation in 40 x 80-ft Tunnel	212
87	Parachute Deployment Bag	213
B-1	Pressure Distribution Curves	251

SYMBOLS

A	Projected area of canopy	in. ²
A _B	Projected area of one bulge	in. ²
a	Angle between suspension line and centerline	deg
b	Angle between tangent to canopy surface and canopy centerline at beginning of inflated canopy for reefed parachute	deg
C, c	Distance from skirt to tangent line for reefed canopies	in.
c	Lagrangian longitudinal wave propagation velocity	ft/sec
c*	Dimensionless wave propagation velocity (= ct_p/L)	
c _l	Longitudinal wave propagation velocity with respect to the laboratory	ft/sec
c _{lT}	Transverse wave propagation velocity with respect to the laboratory	ft/sec
c _T	Lagrangian transverse wave propagation velocity	ft/sec
F	Riser force	lb
h	Distance between radials	in.
k	Slope of linear load-strain curve	lb
K _p	Differential pressure coefficient	
L _R	Reefing line length	in.
L _S	Suspension line length	in.
M	Number of gores	
N _P	Horizontal component of N _ψ	lb/in.
N _Q	Component of N _ψ perpendicular to radial	lb/in.
N _R	Component of N _ψ normal to radial	lb/in.
N _θ	Unit circumferential load in canopy	lb/in.
N _ψ	Unit hoop load in horizontal members	lb/in.

NOTES

P_A	Reefing line load	lb
P_L	Suspension line load	lb
P_R	Load on one radial tape	lb
p	Differential pressure on canopy surface	lb/in. ²
P_{AVG}	Average differential pressure across canopy projected area at skirt (= V/A)	lb/in. ²
R_j	Reflection coefficient between sections j and $j + 1$	
R_S	Radius of curvature of horizontal member	in.
R_θ	Radius of curvature normal to meridian	in.
R_ϕ	Meridional radius of curvature	in.
r	Local radius of canopy in horizontal plane	in.
r_A	Horizontal distance from centerline to reefing line at a radial	in.
r_o	Radius of skirt in horizontal plane	in.
S_L	Circular length of horizontal member under load N_ϕ	in.
S_M	Manufactured length of horizontal member	in.
T_j	Transmission coefficient, section j to section $j + 1$	
t_p	Time required for longitudinal wave to propagate over the length of specimen	sec
V	Axial load at confluence of suspension lines; Particle velocity	lb; ft/sec
V_o	Impact velocity	ft/sec
Z	Vertical canopy coordinate	in.
α	Projection of gore half angle in plane normal to radial tape	radian
β	Angular displacement of horizontal member	radian
ΔN_V	Change in vertical member load	lb/in. ²
ΔP_R	Change in radial tape load	lb/in.
ΔS	Length of model radial tape segment	in.

CONTENTS

$\Delta\theta$	Change in angle between line normal to radial tape and canopy centerline	radian
ϵ_A	Unit strain of reefing line under load P_A	in./in.
ϵ_L	Unit strain of suspension line under load P_L	in./in.
ϵ_R	Unit strain of radial tape under load P_R	in./in.
ϵ_S	Unit strain of horizontal member under load N_v	in./in.
ϵ^*	Amplitude of initial elastic strain wave ($= V_0/c_1$)	
ρ	Lineal mass density	slugs/ft
ρ_0	Unstrained lineal density	slugs/ft
θ	Angle between line perpendicular to radial tape and canopy centerline	radian
ψ	Bulge half angle	radian

SECTION 1.0 INTRODUCTION

The Apollo parachute landing system was designed, developed and qualified by Northrop Ventura during the period 1962-1968. In the normal course of this development, many flight tests were made, and extensive data on the performance of the Apollo spacecraft parachutes were collected. These data were used as the basis for developing the methods that have been used during the course of the flight test program for estimating loads and in making structural analyses for the three Apollo parachute assemblies: the drogue, pilot and main parachutes.

It was recognized that there would be substantial value in an analysis effort that would review all the flight test data at one time. In particular, it was seen that an analysis effort at this time would be free of the day-to-day pressures associated with a development program, and that consequently it could upgrade the loads and stress analysis methods used for the Apollo parachutes in ways that could not have been done previously. The present study was therefore authorized with the objective of upgrading and improving the loads, stress and performance prediction methods for the Apollo spacecraft parachutes. Also, included in this study are the three additional tasks: (1) developing ideas for a new theoretical approach to the parachute opening process, (2) developing ideas for new experimental-analytical techniques to improve the measurement of pressures, stresses and strains in inflight parachutes, and (3) conducting a computer study to explain the data obtained in certain riser dynamics tests performed at Northrop Ventura in 1967.

The results of the study are published in two volumes as follows:

INVESTIGATION OF PREDICTION METHODS FOR THE LOADS
AND STRESSES OF APOLLO TYPE SPACECRAFT PARACHUTES
VOLUME I - LOADS

and

INVESTIGATION OF PREDICTION METHODS FOR THE LOADS
AND STRESSES OF APOLLO TYPE SPACECRAFT PARACHUTES
VOLUME II - STRESSES

The present volume is VOLUME II - STRESSES. The companion volume is listed as Reference 1.

1.1 INTRODUCTION TO VOLUME II

Increases in the Apollo spacecraft weight without corresponding increases in recovery system weight and volume brought about a need for increased accuracy in the structural analysis of parachutes. Improvements in the prediction of material and joint strengths were made by laboratory testing and by use of probability theory. Improvements in the predictions of internal load distribution were accomplished by development of improved analytical methods.

The internal load analysis method that was evolved during the Apollo development programs was a significant advance in the state of the art. However, the full potential of the method was not utilized because of the press of schedule. A large number of hand calculations were required to obtain a solution so that only a limited number of conditions could be investigated, even with a simplified structural model. Correlation of the analytical results with test data was also limited.

The purpose of this study is to further improve the structural analysis methods. Use is made of the Apollo flight test data to

CONTINUED

corroborate and refine the structural analysis methods. A digital computer program developed during this study is used to investigate the internal load distribution during the deployment process to a degree not previously possible. This analysis is further extended to give more realistic modeling of ribbon parachutes. An investigation of pilot chute riser dynamics utilizing Apollo laboratory test data is also included. The need for additional information on the aerodynamic forces acting on parachutes during deployment is demonstrated, and a plan for acquiring this data is developed.

Section 1.2 is a review of the literature on parachute structural analysis, starting with the work of Jones and Taylor published in 1923. In Section 2 the major terms used in the structural analysis of parachutes are defined and discussed.

The methods for determining internal loads used in this study are derived in Section 3, and flow diagrams of two computer programs, CANO and CANO 1 which implement the analyses are given.

In Section 4 the analyses discussed above are applied to the Apollo drogue, pilot and main parachutes, and the results are compared with test data accumulated during the Apollo development and qualification test programs. Included in Section 4 are the following analyses: Drogue chute reefed -- internal load distribution and comparison of shape with test photographs; Drogue chute disreefed -- modeling sensitivity study, pressure distribution sensitivity study, canopy growth study, film analysis, failure analysis, and vertical ribbon load analysis; Pilot parachute -- internal loads analysis and film analysis; Main Parachute internal load analysis, failure analysis, pressure distribution and film analysis, stress-time history, and optimum weight calculations.

In Section 5, a study of the dynamic loading of pilot parachute risers is given. Section 6 is a study of the techniques for measuring the parachute canopy differential pressure and internal loads.

CONTINUED

1.2 LITERATURE SURVEY - STRESS ANALYSIS METHODS

The stresses in a parachute canopy are dependent on the inflated shape, which in turn depends on the stress distribution. This interaction requires that the solutions of canopy stresses and shape be obtained simultaneously. It is understandable, therefore, that much of the effort in parachute stress analysis is concerned with canopy shapes.

The earliest analytical studies of parachute canopy shapes were performed by the British investigators Taylor, Southwell, Griffiths, Jones, and Williams at the Royal Aircraft Establishment in 1919. This work was summarized by Jones in 1923². The theoretical canopy shape (known as the Taylor Shape) that was derived has served as the basis for most theoretical work until recent times.

The "Taylor Shape" is the shape that would be assumed by an axisymmetric parachute with an infinite number of suspension lines and zero hoop stress. Taylor reasoned that this shape, which is a surface of revolution in the limit, would be the flattest possible and therefore the optimum profile. He then concluded that the excess material in the pleats or bulges could be removed without affecting the profile, thereby giving a parachute of minimum weight. Although his reasoning at this point was erroneous, (the effect of the excess material in the bulges does not disappear as the number of suspension lines approaches infinity), the shape derived gives a good approximation of the radial tape profiles of conventional parachutes.

Taylor also formulated the equations for equilibrium and continuity in a gore bulge and showed that his equation in general form is equivalent to the general membrane equation.

NORTHROP

If the differential pressure is uniform over a canopy, the Taylor shape is defined by:

$$\frac{r^2}{a^2} = \sin \phi$$

where:

- r = the local half-diameter
- a = the maximum half-diameter
- ϕ = angle between the central axis
and a normal to the canopy
surface

Tables of rectangular coordinates for the profile curve are given in Reference 2 for the constant pressure case and two nonuniform distributions expressed in functional form.

Equations are also developed by the other authors for shapes in which the hoop stress is not zero, and tables of rectangular coordinates are given for cases in which the hoop tension is constant or varies as a function of r. Weight estimates are presented for parachutes constructed to these theoretical shapes and cloth stresses are given. Section 3 of Reference 2 gives results of wind tunnel tests of these parachute shapes, including pressure and force measurements.

In 1942 Stevens and Johns³ considered the case of a parachute with a finite number of suspension lines which extended over the canopy. The cords were made shorter than the gore panels so that the cloth carried only hoop stress. Through an oversimplification of the geometry the erroneous conclusion was drawn that the tension in the cords would be constant from skirt to vent. It is interesting to note that in the analyses of Taylor the cloth stresses were in the meridional direction only, while Stevens and Johns obtained the same shape by assuming cloth stresses to be in the hoop direction only.

Beck⁴ summarized the German work on parachutes in 1942. Expressions are given for membrane stresses in surfaces of revolution for constant and linearly varying pressures.

Investigations of conical ribbon parachutes were conducted by Jaeger, Culver and Della-Vedova of Lockheed Aircraft⁵⁻⁸ in 1952. A method was developed for estimating the maximum horizontal and radial tape loads in conical ribbon parachutes loaded by uniform pressure. The upper portion of the canopy was assumed to be a cone with zero meridional load and the lower portion was assumed to be an ellipsoid, with zero hoop tension.

A comprehensive report by Topping, Marketos, and Costakos⁹ in 1955 brought together all previous work in the field of parachute stress analysis. This work approaches the practical limit of refinement in the approach used, i.e., the fitting of functional curves to the parachute shapes. Analytical solutions are given for fully inflated shapes of solid flat, extended skirt, personnel guide surface and conical ringslot parachutes loaded by uniform pressure. Various modifications to the Taylor equation were made to better approximate shapes observed in photograph of parachutes in steady descent. Radial cord tensions and cloth stresses consistent with the analytically determined shapes were calculated. Several representative dimensions obtained from the analytical solution for each of the four types of parachutes studied agreed with corresponding dimensions obtained from photographs within 9 percent. For the flat canopy, dimensions agreed within about 4 percent. Since this degree of accuracy might appear to be acceptable, it should be pointed out that the variation in stress implied is much greater than the percentages given. For a typical nylon material (MIL-C-7020 Type I, cloth) 5 percent variation in strain corresponds to a 50 percent change in stress. The effects of varying such parameters as the suspension line length, number of gores and cone angles, as well as the effect of other details, were studied.

NORTHROP

A generalized equation for Taylor type curves was given by Lester¹⁰ in 1962.

$$\sin \varnothing = \frac{1}{\lambda} \left[\lambda - 1 + \frac{r^2}{a^2} \right]$$

By varying the parameter λ , a family of curves is generated which may be used to represent different parachute types.

Heinrich, together with Monson and Jamison¹¹⁻¹⁴ developed a method for computing canopy cloth stresses for a known profile and pressure distribution. Since the gore centerline is usually the profile observed in photographs, equations were developed using this profile. A set of five simultaneous equations are given which can be solved by an iterative process to obtain cloth stresses. This method is also presented in the "Parachute Handbook"¹⁵.

A dynamic analysis presented by Asfour¹⁶ in 1966 is based on the assumption that the major (circumferential) stress is a result of a dynamic force in a plane perpendicular to that of the opening shock. Circumferential stresses are computed by equating the energy absorbed by the cloth to the kinetic energy of the air mass expanding to fill the canopy during inflation. It is assumed that each horizontal member forms a circular ring around the canopy, i.e., the bulges disappear, at the time of maximum stress. This assumption, together with that of a linear stress-strain relationship, gives these rings linear spring rates and makes it possible to solve the energy equation in closed form.

In the Apollo Block I stress analysis⁹ and ¹⁰ Speakman and Topp treated the parachutes as surfaces of revolution. The pilot chute and the reefed drogue and main parachutes were assumed to be hemispheres loaded by uniform pressure. Analysis of the drogue

and main parachutes in the full open condition were improved by approximating the shape observed in drop test photographs by ellipsoids. In the analysis of the main canopy, further refinement was made by using a nonuniform pressure distribution based on steady state wind tunnel test results.

In the Apollo Block II stress analysis of the main parachute by Ranes, Topp and Utzman,¹⁸ a new method was used which accounted for the effect of the bulging of the sails between the radial tapes and for the relationship between meridional curvature and forces. Pressure distribution data from wind tunnel tests were incorporated and the curvature of the radial tapes was assumed to be elliptical. Sail strain compatibility was used to select a best-fit ellipse. While this method represented a major step in development of a rational analytical method, it was limited by its reliance on a functional curve to describe canopy curvature. In effect, the canopy was forced into a convenient shape without regard for local member stiffness. As pointed out in that analysis, a change of 4 percent in the diameter at a particular section could result in a 50 percent change in the calculated stress.

In the Block II (H) Program, a major step was taken in the development of a more realistic method for determining the load distribution in a parachute canopy. This method, which is given in Section 3, determines the unique shape and internal load distribution which satisfies equilibrium and boundary conditions for a given parachute and applied loading. The final stress analysis for the Apollo Block II (H)¹⁹ used this method. However, verification of the method by correlation with test results was limited. Verification and continued refinement of the method by correlation with the test data obtained in the Apollo ELS test program is one of the goals of this study.

SECTION 2.0

DISCUSSION OF PARACHUTE STRUCTURAL ANALYSIS

The major factors encompassed in the structural analysis of a parachute are those appearing in the margin of safety equation.

$$MS = \frac{\text{Ultimate strength} \times \text{design factors}}{\text{Limit load} \times \text{safety factor}} - 1$$

Each of these factors is discussed in the paragraphs below.

2.1 MARGIN OF SAFETY

The margin of safety of a component is the ratio of excess strength to the required strength of the component. An ideal design would have a zero or small positive margin of safety for every member.

2.2 SAFETY FACTOR

The safety factor is the ratio of the required ultimate strength to the limit load applied to a member under the worst case that can be expected to occur with reasonable probability within the envelope of normal operating conditions. This is the "ignorance" factor which covers the uncertainties in load and strength predictions. Since the weight and volume of the parachute will vary almost linearly with this factor, it is desirable to use the lowest factor consistent with the accuracy of the analyses.

2.3 DESIGN FACTORS

Design factors account for reduction in ultimate strength due to environmental degradation and for increases in some member loads due to nonsymmetrical loading of the parachute.

2.4 ULTIMATE STRENGTH

The ultimate strength of a parachute member is usually limited by the strength of splices within the member or at joints with other members. In the Apollo program, representative joints were tested to destruction in the laboratory to determine the expected strength of the joints relative to the base material strength.

$$\text{Joint efficiency} = \frac{\text{Joint strength}}{\text{Base material strength}}$$

and

$$\text{Ultimate Strength} = \text{Material Rated Strength} \times \text{Joint Efficiency}$$

Strengths based on static (low speed) joint and material tests are presently used for most members. For pilot parachute risers, however, there is evidence that the high load onset rate at time of canopy stretch gives important dynamic effects. Section 5 is a study of the behavior of the Apollo pilot chute riser under dynamic loading.

2.5 LIMIT LOAD

The limit load in a member is a function of the external loading on the parachute and of the internal distribution of this loading.

2.5.1 External Loading

Primary external loads on a parachute are the riser load and the reacting differential pressure on the canopy surface. Most of the effort in parachute loads analysis is directed toward prediction of riser loads, and methods have been developed which predicts this load with a high degree of accuracy. (See, for example, Volume 1).

There is very little quantitative information on the differential pressure distribution on parachute canopies. The most meaningful empirical data available comes from the work done by Melzig.

References 20 and 21 give the results of wind tunnel and free flight tests in which local pressures were measured at four points in parachute canopies during opening. Further discussion of the details of these tests is given in Section 6.

Figure 1 is a plot of the data for a typical wind tunnel run from Reference 20. The variation in differential pressure coefficient versus time at the four pressure transducers is shown. It is seen that a pressure peak starts at the vent and moves rapidly down the canopy to the skirt. Correlation with load-time traces show that maximum load occurs at approximately the time this peak reaches the skirt, although development of maximum canopy projected area occurs somewhat later.

The results of drop tests given in Reference 21 differ from the wind tunnel data in that the pressure peak never reaches the skirt because of the decay in the dynamic pressure during opening under finite mass conditions. Canopy loading was very low (1/3 psf) for the tests of Reference 21. It would be expected that behavior of the more highly loaded spacecraft parachutes would be somewhere between the limits explored in References 20 and 21.

For reefed parachutes there are no pressure measurement data available. In the stress-time study of Section 4.3.4, the feasibility of inferring the pressure distribution from the shape of a parachute is explored.

2.5.2 Internal Loading

Loads in the individual parachute members for a given riser load and pressure distribution are determined by the method given in the following section.

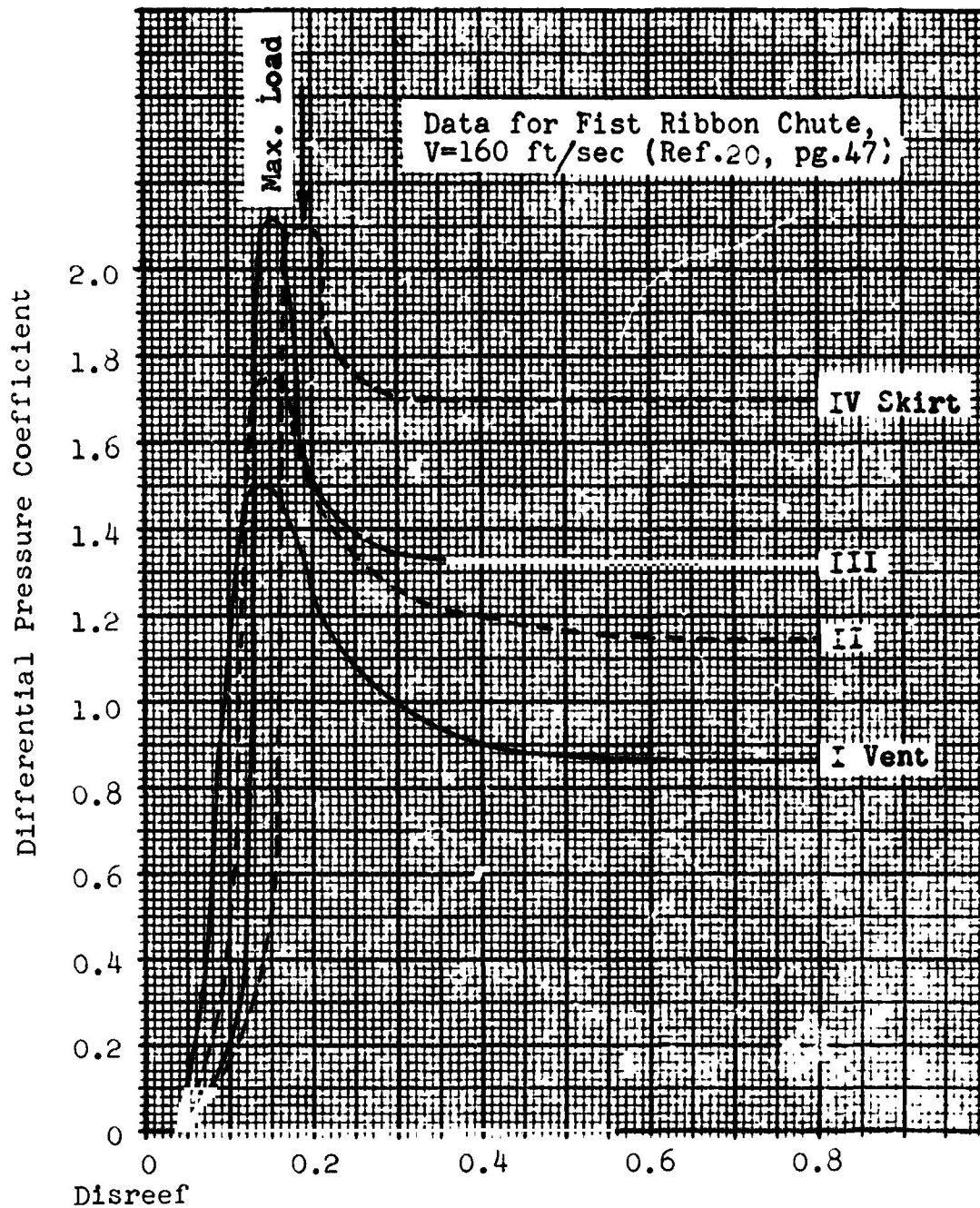


Fig. 1. Differential Pressure vs. Time

SECTION 3 PARACHUTE INTERNAL LOAD DISTRIBUTION

The determination of the internal load distribution for a given parachute and set of external loads is the subject of this section.

The basic analysis method, which has been implemented in a computer program called CANO, is derived in Section 3.1. This analysis is used for most of the test data correlation work in Section 4. A further refinement of the analysis, which is implemented in Program CANO 1, is presented in Section 3.2.

3.1 PROGRAM CANO - AN INTERNAL LOAD ANALYSIS FOR PARACHUTES

The analysis method which follows determines the unique shape and internal load distribution which satisfies equilibrium and boundary conditions for a given parachute under the influence of known riser and aerodynamic forces.

This analysis is applicable to either reefed or fully open symmetrical designs, such as the ribbon, ringslot, and ringsail parachutes, which have meridional members which may be assumed to carry all meridional forces.

A general description of the method and assumptions is given first, followed by derivation of the equations and a solution algorithm.

3.1.1 Description of the Method

The parachute is treated as a deformable membrane, and finite elements are used to represent the structure. The structural model of the canopy consists of horizontal slices (or segments) conveniently spaced along the meridional members from the skirt to the vent. Each segment is defined by its length along the meridian, the free length of the horizontal member connecting adjacent meridional members, and the load strain curves for these

members. Loads and geometry are computed at reference stations located at the midpoints of the segments.

The following assumptions are made:

- 1) Meridional curvature is constant over each segment, and the curvatures of adjacent segments are tangent at their junctions.
- 2) All meridional forces are in the meridional members (radial tapes).
- 3) Horizontal members have no meridional curvature, but each has a constant radius of curvature which is normal to the meridional member at the reference station.

The simplifying assumptions given above make it possible to compute the end reaction of a horizontal member as a free body. This end reaction is then resolved into three mutually perpendicular forces tangent and normal to the meridional member, from which the loading and radius of curvature of the meridional member can be computed.

The variation of differential pressure along the meridian is represented by a nondimensional distribution curve. Magnitude of the differential pressure is adjusted to give overall force balance by two factors; 1) the average pressure acting on the projected area of the skirt, and 2) an integration factor which accounts for the shape of the distribution curve and the geometric porosity of the model.

A solution is obtained for a trial skirt diameter and pressure integration factor by establishing equilibrium geometry, first at the skirt then at each successive station to the vent. This trial solution is then examined for compatibility with boundary conditions at the vent. (See discussion below) This process is repeated with corrected trial skirt diameters and pressure

MEMBER

factors until the boundary conditions at the vent are satisfied and an overall force balance is achieved.

Boundary conditions at the vent are checked as follows: The load in a meridional member at the vent band station is reacted by a vent line. The stretched length of the vent line under this loading is compared with the computed diameter. The other boundary condition is zero slope of the meridian at the vent, if an idealized case in which no pressure is acting on the vent lines is considered. This singularity is avoided in a practical manner by allowing a small positive slope. This slope is limited by a requirement that the total vertical component of the meridional member loads not exceed 75 percent of the force that would be produced by the local pressure acting on an area equal to that of the vent.

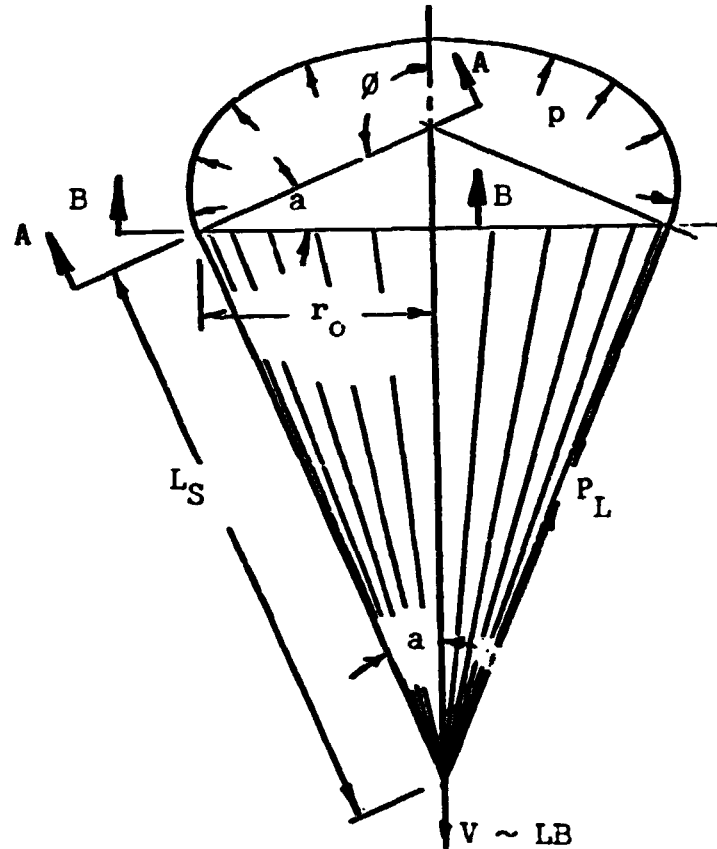
3.1.2 Derivation of Equations

Since the solution procedure is not straightforward, no attempt is made to follow the computing sequence in the derivations which follow. A solution algorithm is shown in the form of a flow diagram of computer program CANO in Figure 2, page 26.

10000000

Equilibrium below the skirt - unreefed

A profile view of a fully inflated, unreefed parachute is shown below.



For a given skirt diameter, equilibrium geometry is established as follows:

$$a = \sin^{-1} \left[\frac{r_0}{L'_S (1 + \epsilon_L)} \right] \quad (1)$$

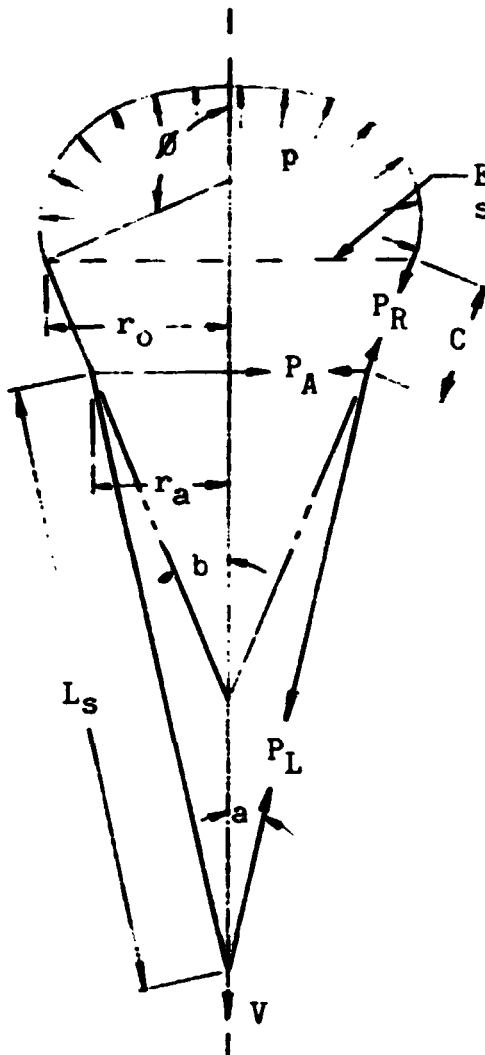
$$P_L = \frac{V}{M \cos a} \quad (2)$$

where: a = suspension line convergence angle
 L'_S = initial length of suspension lines
 ϵ_L = strain of the suspension lines under load, P_L
 V = applied riser load
 M = number of suspension lines (also number of gores)

Equations (1) and (2) are solved simultaneously by the method shown in Figure 3, page 27.

Equilibrium below the effective skirt, reefed

For reefed parachutes it is assumed that differential pressure acts on the inflated portion of the canopy only, so that the radial tapes are straight in the uninflated portion. For a given development angle, b , equilibrium geometry is established as follows:



$$a = \sin^{-1} r_a / L_S' (1 + \epsilon_L) \quad (3)$$

$$P_L = \frac{V}{M \cos a} \quad (4)$$

$$P_R = \frac{V}{M \cos b} \quad (5)$$

$$P_A = \frac{V}{2M \sin \pi/M} [\tan b - \tan a] \quad (6)$$

$$r_a = \frac{L_R' (1 + \epsilon_A)}{2M \sin \pi/M} \quad (7)$$

$$r_o = r_a + C' (1 + \epsilon_R) \sin b \quad (8)$$

Where:

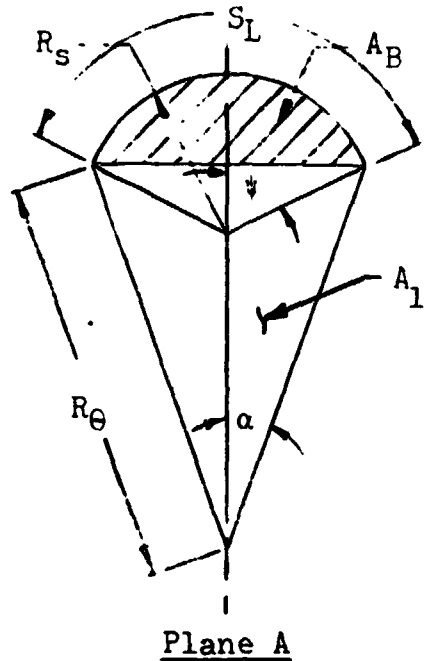
L_S' , L_R' , and C' are manufactured lengths

ϵ_L , ϵ_A , and ϵ_R are unit strains for loads

P_L , P_A , and P_R

Equations (3) through (8) are resolved simultaneously by the method shown in Figure 4, Page 28.

From View A-A



From the view of plane A

$$R_s = \frac{S_L}{2\psi} \quad (9)$$

$$A_B = \frac{R_s^2}{2} (2\psi - \sin 2\psi) \quad (10)$$

$$A_1 = \frac{R_\theta^2}{2} \sin \frac{2\alpha}{M} \quad (11)$$

Projected area in horizontal plane (view B-B)

$$A = M(A_B + A_1) \sin \phi \quad (12)$$

Local differential pressure

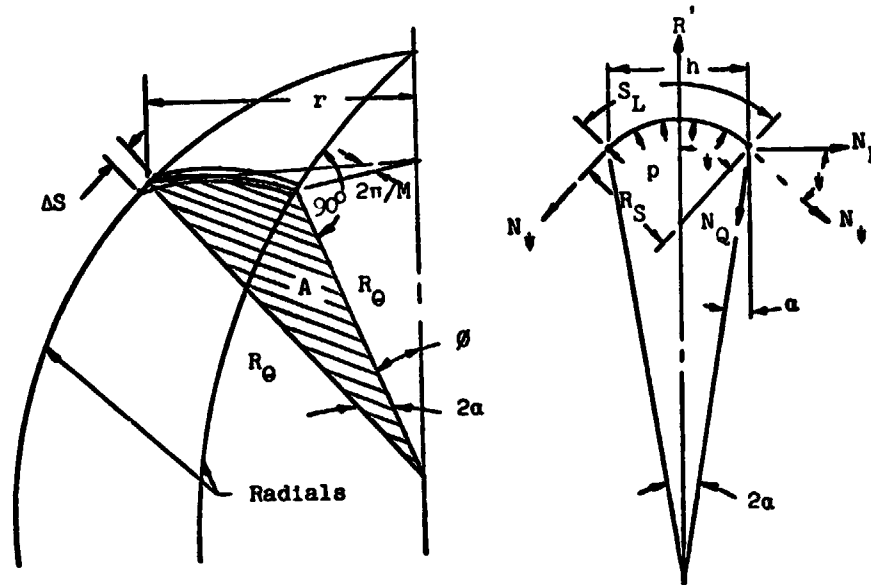
$$p = \frac{p' V/A}{k_p} \quad (13)$$

where: p = local differential pressure

p' = pressure coefficient from pressure distribution curve

k_p = integration factor-a function of the shape of the distribution curve and geometric porosity

The above equations are solved simultaneously by the method shown in Figure 3 or 4.

EQUILIBRIUM OF A TYPICAL HORIZONTAL ELEMENT

From summation of forces in direction R' View in Plane A

$$N_\psi = \frac{ph}{2 \sin \psi} \quad (14)$$

where: N_ψ = unit tension load in horizontal member

$$h = 2r \sin \pi/M \quad (15)$$

Therefore

$$N_\psi = \frac{pr \sin \pi/M}{\sin \psi} \quad (16)$$

The arc length S_L is given by

$$S_L' = 2 \psi R_S \quad (17)$$

Since:

$$R_S \sin \psi = r \sin \pi/M \quad (18)$$

$$S_L' = \frac{2\psi r \sin \pi/M}{\sin \psi} \quad (19)$$

The length of the horizontal element

$$S_L = S_M (1 + \epsilon_S) \quad (20)$$

where: S_M = manufactured length of the horizontal member

ϵ_S = unit strain of the horizontal member for load N_ψ

A value for ψ is found by iteration to give

$$S_L = S_L' \quad (21)$$

This procedure is shown schematically in Figure 2, page 26.

Resolution of N_ψ

The edge force in a horizontal member, N_ψ , is resolved into three mutually perpendicular components; (1) ΔP_R , tangent to the meridional member, (2) N_R , normal to the meridional member in a plane which includes the central axis, and (3) N_θ , a circumferential force.

From the view in Plane A:

$$N_Q = N_\psi \sin \psi / \cos \alpha \quad (22)$$

$$\text{and } N_P = N_\psi \left[\cos \psi + \frac{\sin \psi \sin \alpha}{\cos \alpha} \right] \quad (23)$$

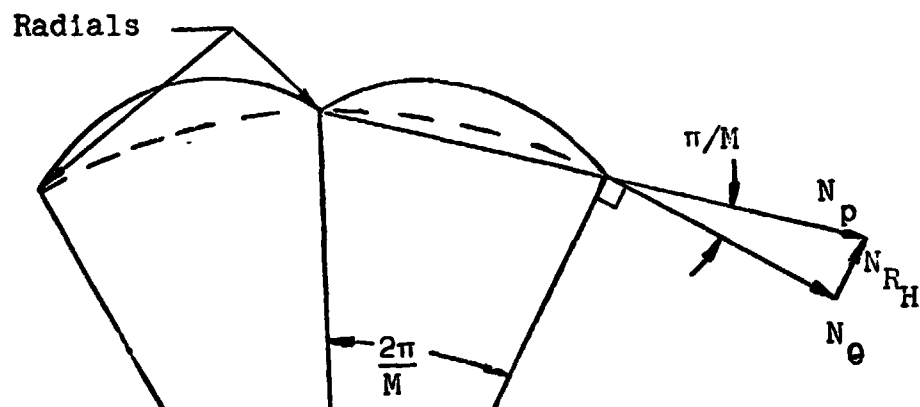
Angle α is defined as follows

From Equation (15)

$$h = 2r \sin \pi/M$$

$$\sin \alpha = \frac{h}{2R_\theta} = \frac{2r \sin \pi/M}{2r/\sin \phi} = (\sin \pi/M) \sin \phi \quad (24)$$

N_P is resolved into components in the desired directions by first resolving it into two components in the horizontal plane as shown below.

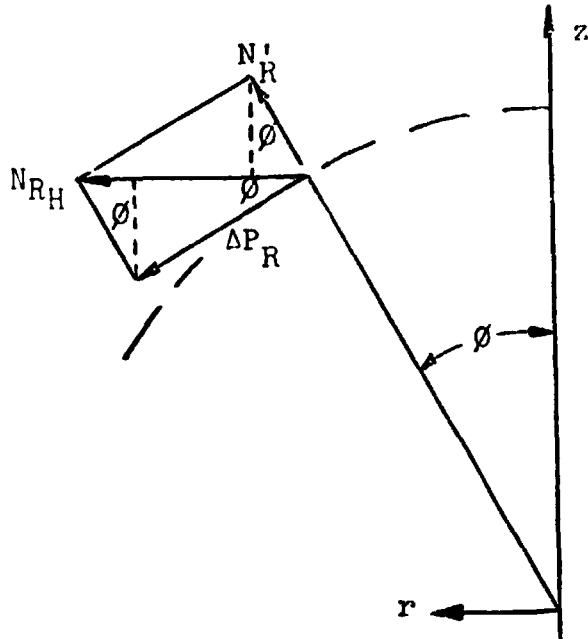


View In Horizontal Plane

$$N_\theta = N_P \cos \pi/M = N_\psi \cos \pi/M \left[\cos \psi + \frac{\sin \psi \sin \alpha}{\cos \alpha} \right] \quad (25)$$

$$N_{RH} = N_P \sin \pi/M \quad (26)$$

The resolution of N_{RH} into the directions of N_R and ΔP_R can be seen with a view in the plane of a meridional member.



View In Plane Of Radial Tape

From $\sum F_z = 0$

$$\Delta P_R = \frac{N'_R \cos \phi}{\sin \phi} \quad (27)$$

From $\sum F_R = 0$ and equation 23 and 24

$$\begin{aligned} N'_R &= N_{RH} \sin \phi = N_p \sin \alpha \\ &= N_\psi \sin \alpha [\cos \psi + \sin \psi \sin \alpha / \cos \alpha] \end{aligned} \quad (28)$$

Combining equations (22) and (28)

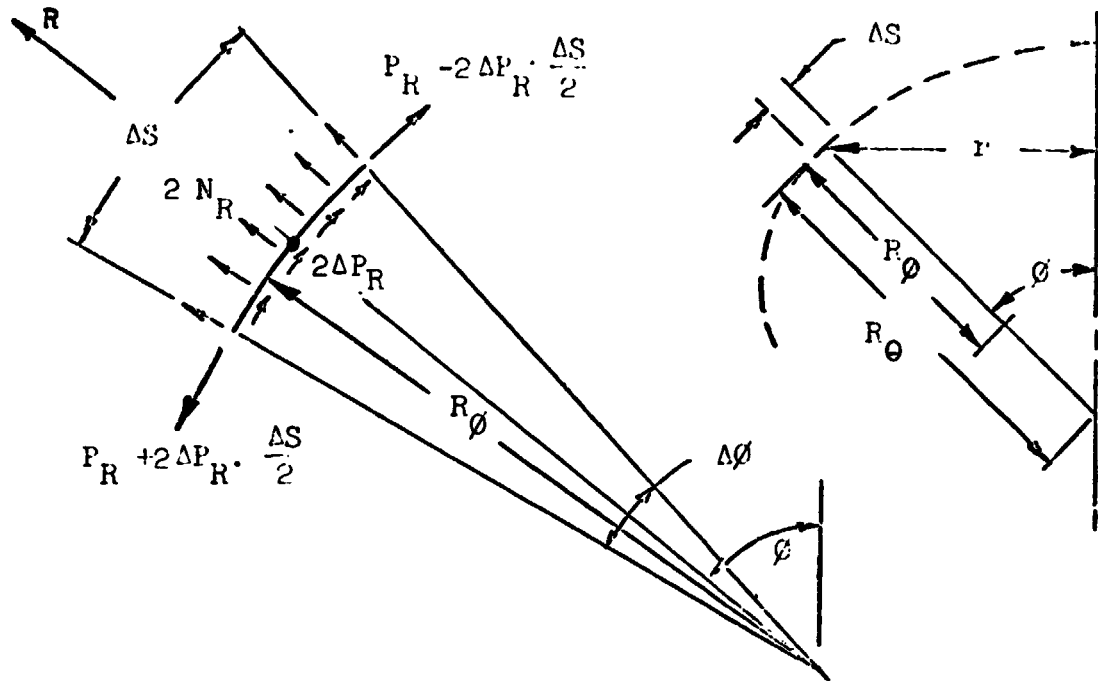
$$\begin{aligned} N_R &= N_Q - N'_R \\ N_R &= N_\psi [\sin \psi / \cos \alpha - \sin \alpha (\cos \psi + \sin \psi \sin \alpha / \cos \alpha)] \end{aligned} \quad (29)$$

Substituting equation (28) into (27)

$$\Delta P_R = N_\psi \sin \pi/M \cos \phi (\cos \psi + \sin \psi \sin \alpha / \cos \alpha) \quad (30)$$

EQUILIBRIUM OF A SEGMENT OF A MERIDIONAL MEMBER

(loaded by two adjacent horizontal member ends)



$\Delta\phi$ is sufficiently small to make $\Delta P_R \Delta S$ negligible compared to P_R . Summation of forces in direction R results in:

$$2(2 N_R R_\phi \sin \Delta\phi/2) = 2(P_R \sin \Delta\phi/2)$$

therefore

$$R_\phi = P_R / 2N_R \quad (31)$$

The above equations can be combined to give a form similar to the general membrane equation ($p = \frac{N_\phi}{R_\phi} + \frac{N_\theta}{R_\theta}$):

$$p = \left[\frac{P_R}{2r R_\phi \sin \frac{\pi}{M}} + \frac{N_\theta \sin \phi}{r \cos \frac{\pi}{M}} \right] \sqrt{1 - \sin^2 \frac{\pi}{M} \sin^2 \phi}$$

LOAD IN THE MERIDIONAL MEMBER, P_R

At the skirt the axial load in the meridional member is equal to the suspension line load.

$$P_R (\text{skirt}) = \frac{V}{M \sin \phi} \quad (32)$$

At subsequent stations P_R is computed by subtracting the accumulated ΔP_R from the initial value. Since there are two horizontal member ends acting on each meridional member, the load at station j is given by

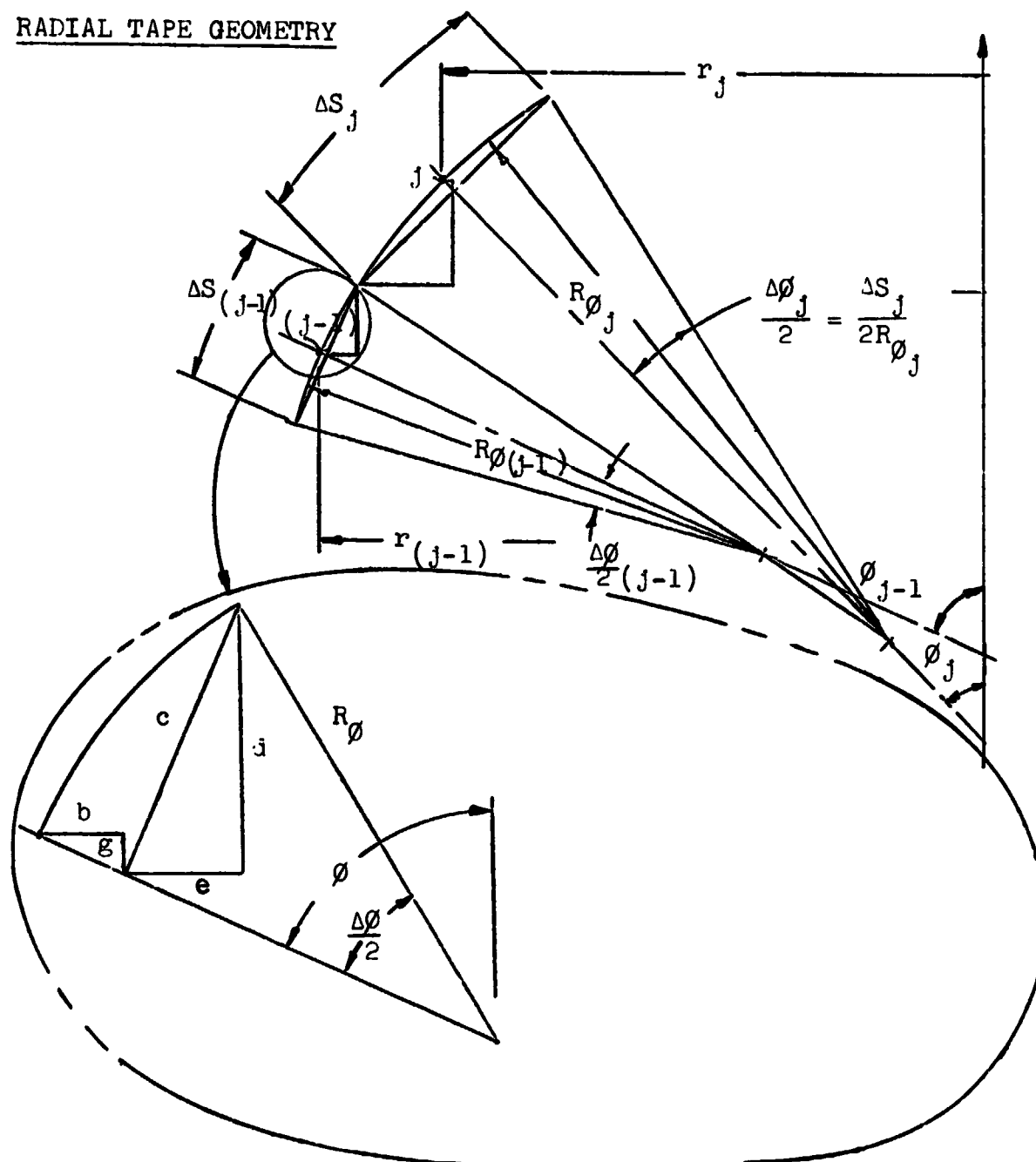
$$P_{Rj} = P_{R(j-1)} - (2 \Delta P_R \Delta S/2)_{(j-1)} - (2 \Delta P_R \Delta S/2)_j \quad (33)$$

Length of segment j is given

$$\Delta S_j = \Delta S'_j (1 + \epsilon_{Rj})$$

where:

$\Delta S'_j$ is the manufactured length of the segment
 ϵ_{Rj} is unit strain under load P_{Rj} .

RADIAL TAPE GEOMETRY

$$r_j = r_{(j-1)} - [b + e]_{(j-1)} + [b - e]_j \quad (34)$$

$$\begin{aligned} r_j &= r_{(j-1)} - [R_\phi (1 - \cos \frac{\Delta \phi}{2}) \sin \phi + R_\phi \sin \frac{\Delta \phi}{2} \cos \phi]_{(j-1)} \\ &\quad + [R_\phi (1 - \cos \frac{\Delta \phi}{2}) \sin \phi - R_\phi \sin \frac{\Delta \phi}{2} \cos \phi]_j \\ z_j &= z_{(j-1)} - [g - d]_{(j-1)} + [g + d]_j \\ z_j &= z_{(j-1)} - [R_\phi (1 - \cos \frac{\Delta \phi}{2}) \cos \phi - R_\phi \sin \frac{\Delta \phi}{2} \sin \phi]_{(j-1)} \\ &\quad + [R_\phi (1 - \cos \frac{\Delta \phi}{2}) \cos \phi + R_\phi \sin \frac{\Delta \phi}{2} \sin \phi]_j \end{aligned} \quad (35)$$

NORTHROP

3.1.3 Solution Algorithm

A flow diagram for Program CANO is presented in Figure 2.
A user's manual which includes a listing of this program is
given in Reference 22.

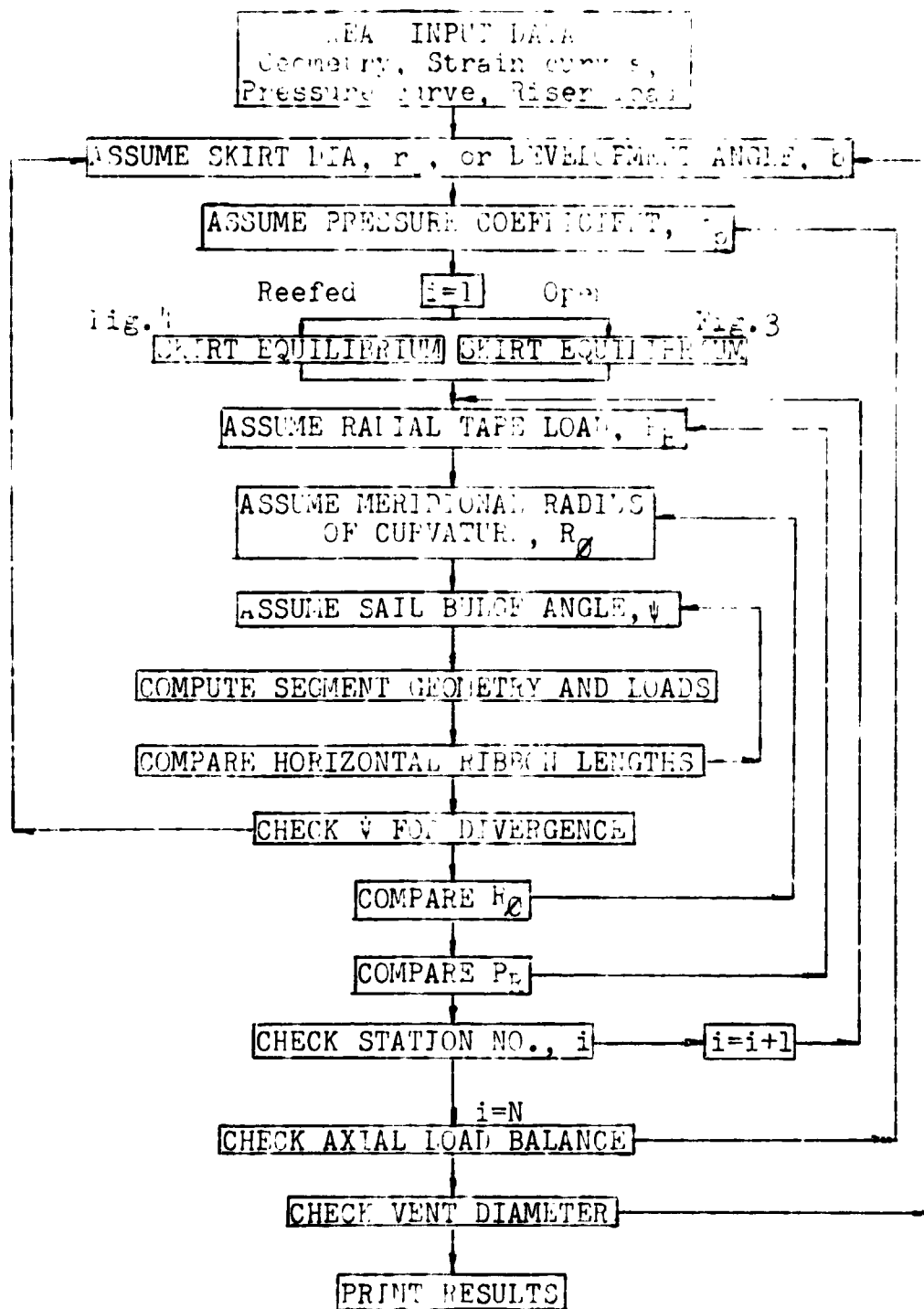


Fig. 2 . Flow Diagram for Program CANO

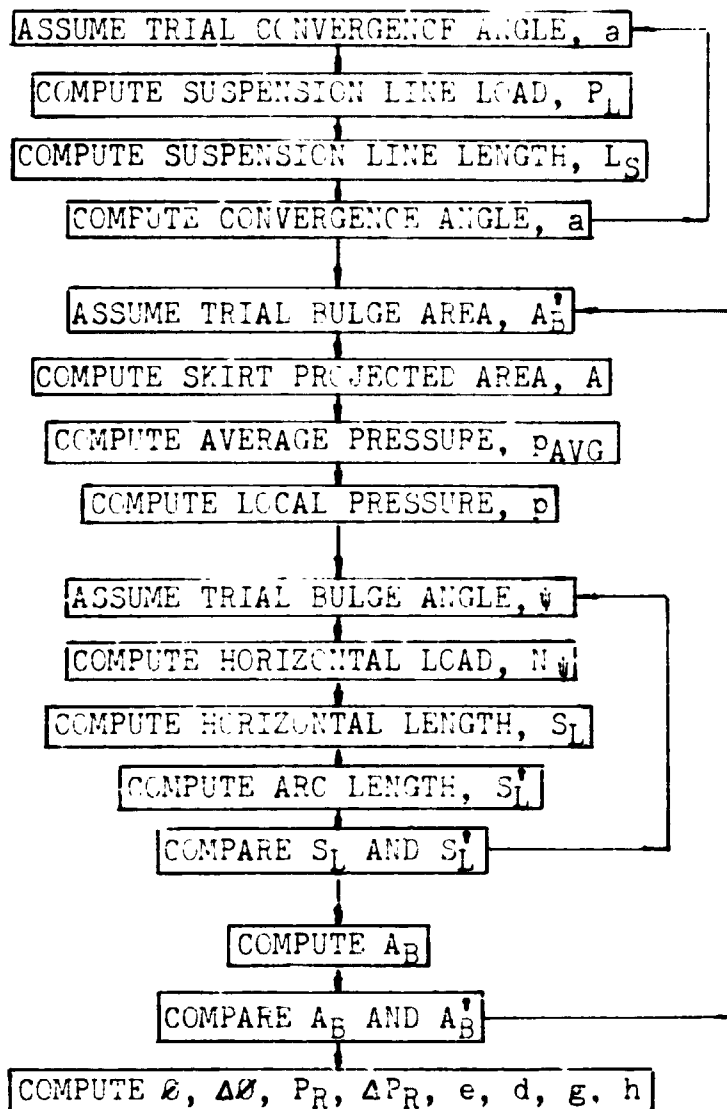


Fig. 3 . Flow Diagram Detail Showing Skirt Equilibrium for an Unreefed Parachute

CONTINUED

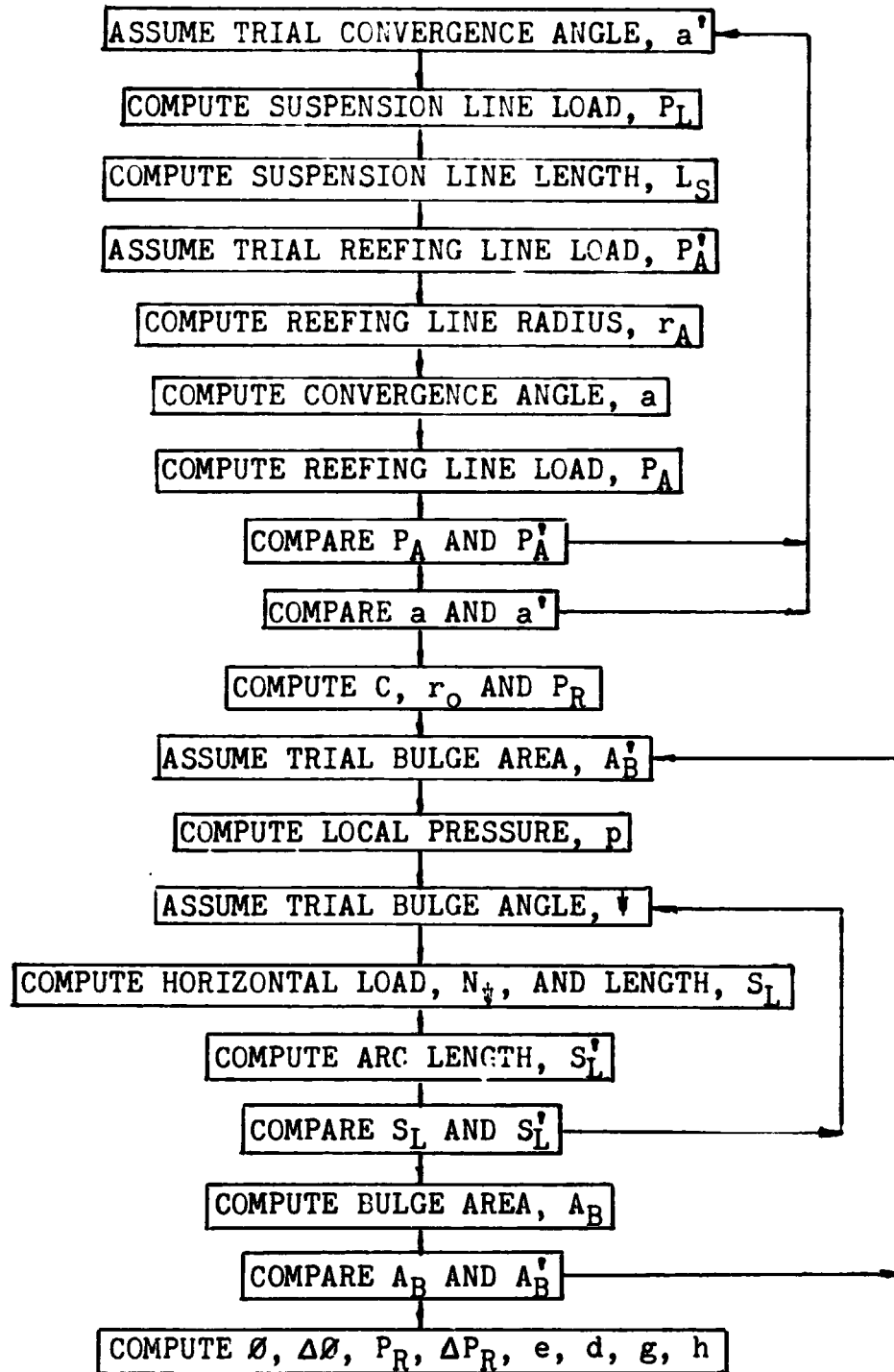


Fig. 4 . Flow Diagram Detail Showing Skirt Equilibrium for a Reefed Parachute

3.2 PROGRAM CANO 1 - AN INTERNAL LOADS ANALYSIS FOR RIBBON PARACHUTES

In deriving the equations for canopy internal load distribution, Section 3.1, it was assumed that the horizontal members bulge outward perpendicular to the meridional members, i.e., angle $\beta = 0$ in Figure 5. It is seen in the photograph in Figure 5 that this assumption is not realistic for ribbon parachutes. The vertical members between the meridional members, or radial tapes, pull the skirt band and adjacent horizontal members up so they are not perpendicular to the meridians. As a result, the vertical members pick up axial load which would otherwise be in the radial tapes. This analysis attempts to account for the effect of the vertical members on the internal load distribution in the canopy.

3.2.1 Description of the Analysis Method and Assumptions

This analysis is identical to the CANO analysis given in Section 3.1, except that the equations and solution procedure are modified to include the effect of the vertical members. The structural model consists of horizontal slices (or segments) of the canopy. Each segment is represented by a length of radial tape, a horizontal member, and a vertical member which is uniformly distributed across the width of the gore. Loads and geometry are computed at reference stations located at the midpoints of the segments.

The following assumptions are made:

- 1) Meridional curvature is constant over each segment, and the curvatures are tangent at the junction between adjacent segments.
- 2) The horizontal ribbons have no meridional curvature.
- 3) The edges of a horizontal ribbon lie in planes parallel to the Plane B (Figure 6.)

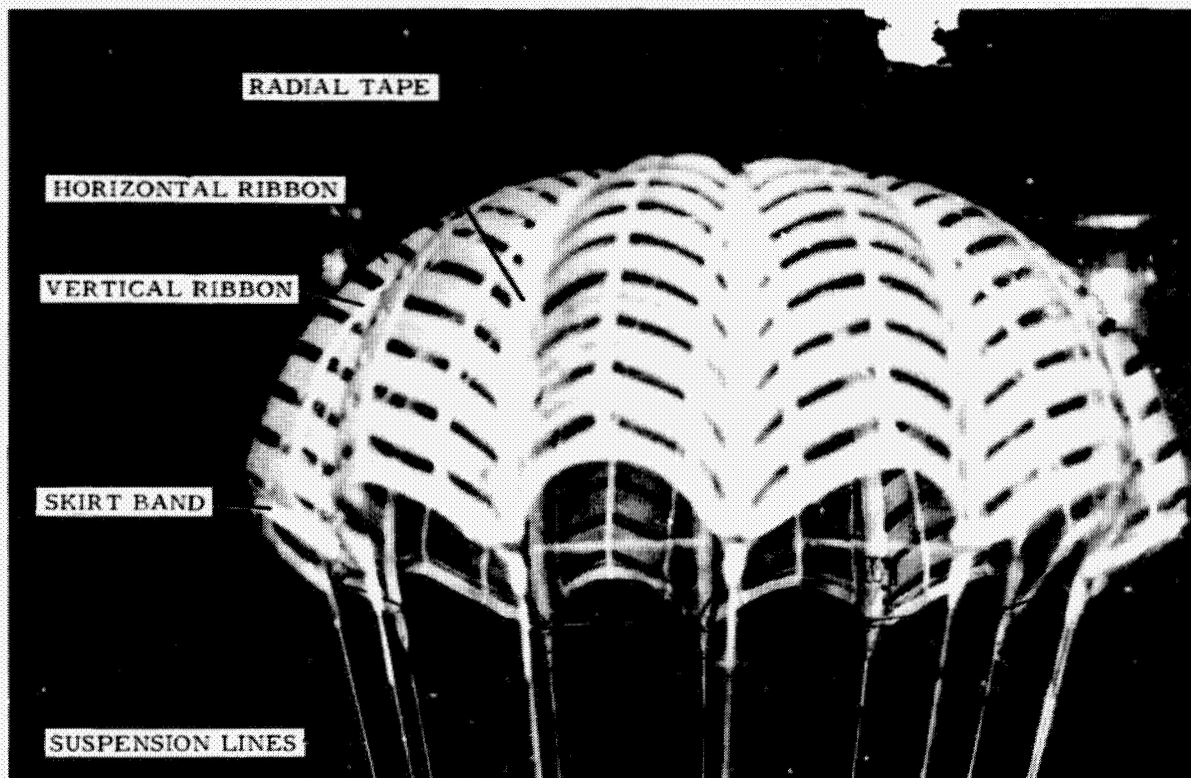
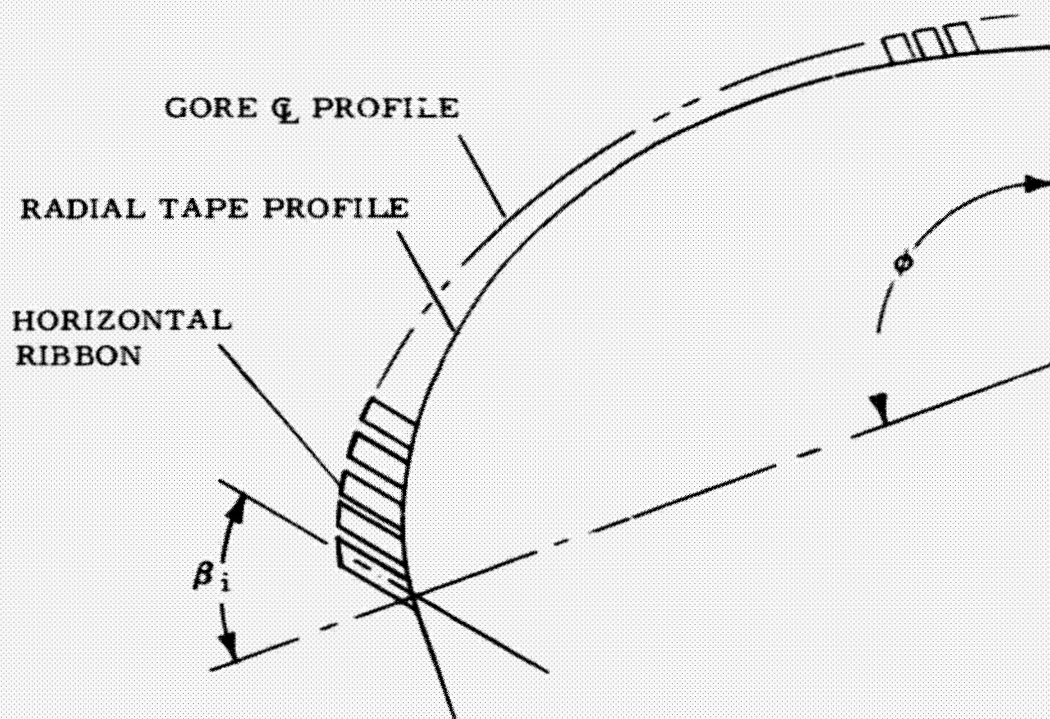


Figure 5 . Ribbon Parachute With Vertical Members

- 4) The projection of the horizontal ribbon on Plane A (Figure 6) is a circular arc.
- 5) The horizontal ribbon is held in equilibrium by a variable distributed force from the vertical ribbons. This force is parallel to the horizontal ribbon width, and is of a magnitude such that the resultant of the force system acting on the horizontal ribbon is in Plane B (Figure 6).
- 6) The axial loads in the vertical ribbons are transferred to the radial tapes over each segment from skirt to vent in proportion to the decrease in gore width.

3.2.2 Derivation of Equations

Since the solution procedure is not straightforward, no attempt is made to follow the computing sequence in the derivations which follow. A solution algorithm is shown in the form of a flow diagram for computer program CANO 1 in Figure 7 , page 41 .

CONTINUED

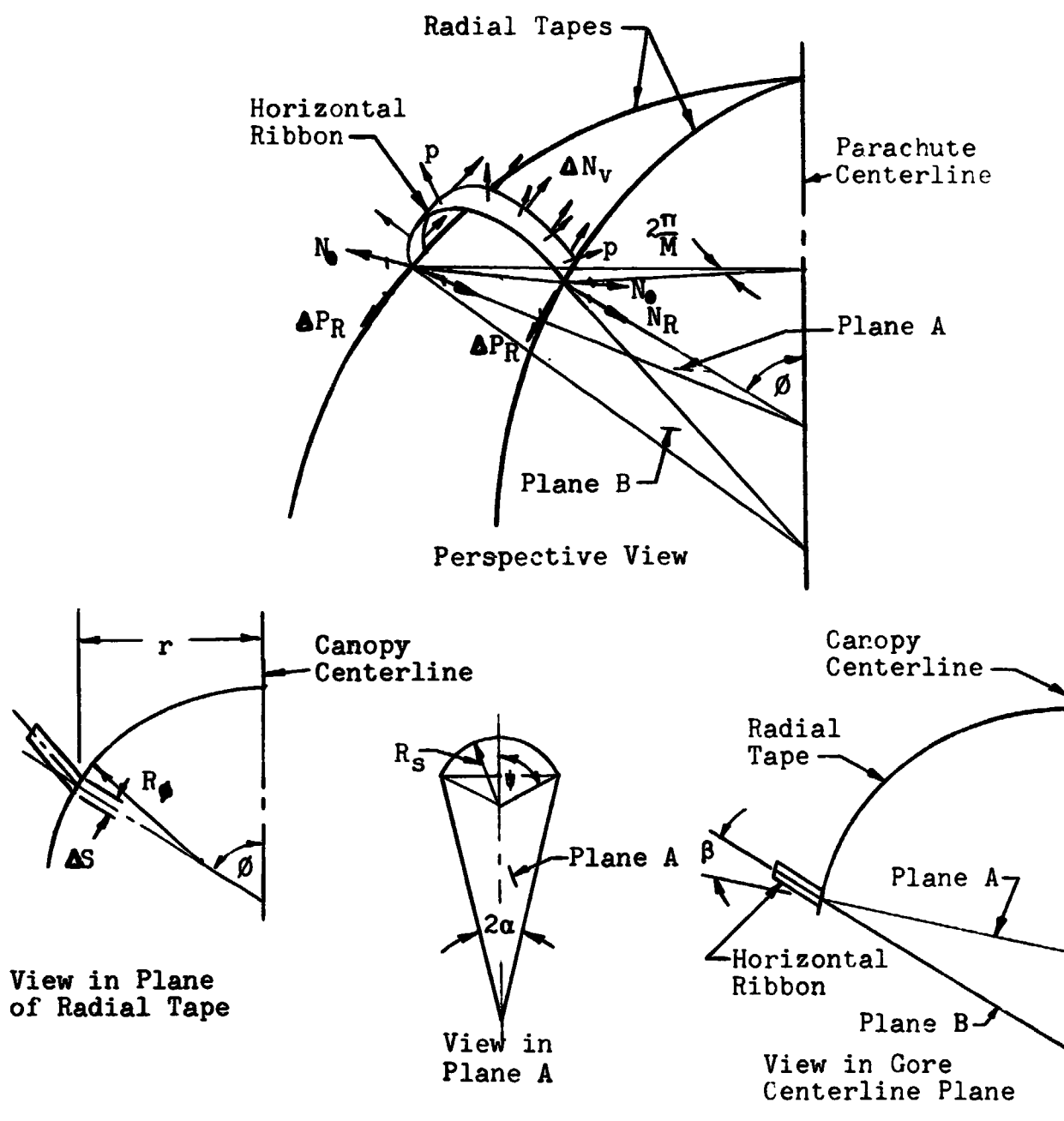


Fig. 6. Canopy Geometry

CONTINUED

EQUILIBRIUM OF A TYPICAL HORIZONTAL RIBBON

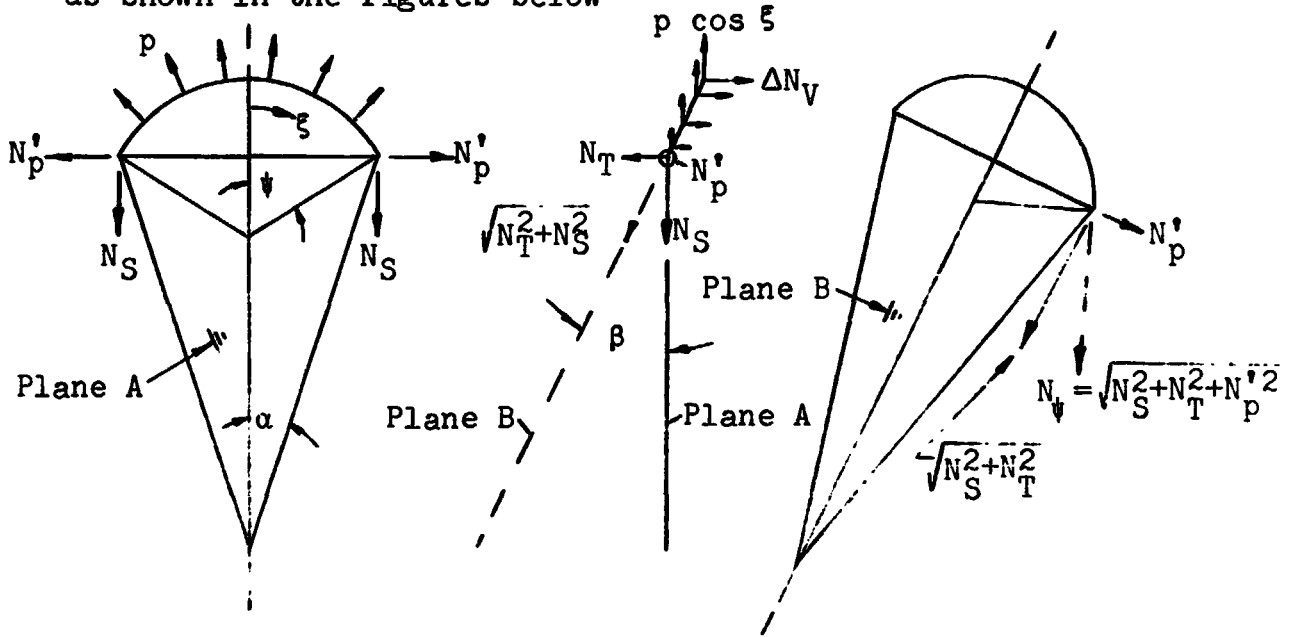
From the assumptions that:

- 1) The load increment ΔN_V (from the vertical ribbon) is perpendicular to Plane A.
- 2) The pressure load is in Plane A.
- 3) The resultant of the two loads is in Plane B.

It follows that

$$\Delta N_V = p \cos \xi \tan \beta \quad (36)$$

as shown in the figures below



The end reaction is found as follows:

$$N_S = \int_0^\psi p \cos \xi R_S d\xi = p R_S \sin \psi \quad (37)$$

$$N_T = \int_0^\psi p \cos \xi \tan \beta R_S d\xi = p R_S \sin \psi \tan \beta \quad (38)$$

$$N_P' = p R_S \left[1 - \int_0^\psi \sin \xi d\xi \right] = p R_S \cos \psi \quad (39)$$

$$N_\psi = \left[N_S^2 + N_T^2 + (N_P')^2 \right]^{1/2} = pr \sin \pi/M \left[\csc^2 \psi + \tan^2 \beta \right]^{1/2}$$

Length of the elliptical arc is given by

$$S_L' = \frac{2RS}{\cos \beta} \int_0^{\pi/2} \sqrt{(1 - \sin^2 \beta \sin^2 \xi)} d\xi$$

$$S_L' = \frac{2 r \sin \pi/M}{\sin \psi \cos \beta} \int_0^{\pi/2} \sqrt{(1 - \sin^2 \beta \sin^2 \xi)} d\xi \quad (40)$$

Stretched length of the horizontal ribbon is given by:

$$S_L = S_M (1 + \epsilon_S) \quad (41)$$

where:

S_M = manufactured length of horizontal ribbon

ϵ_S = unit strain for load N_ψ

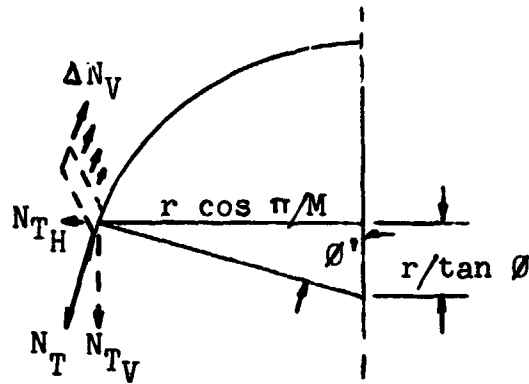
A value for ψ is found by iteration to give

$$S_L = S_L' \quad (42)$$

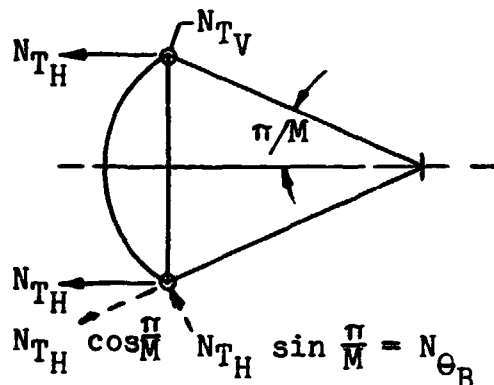
This procedure is shown schematically in Figure 7, page 41.

The three components of the horizontal ribbon end reaction, N_T , N_S , N_P' , will be resolved individually into three orthogonal components perpendicular and tangent to the radial tape.

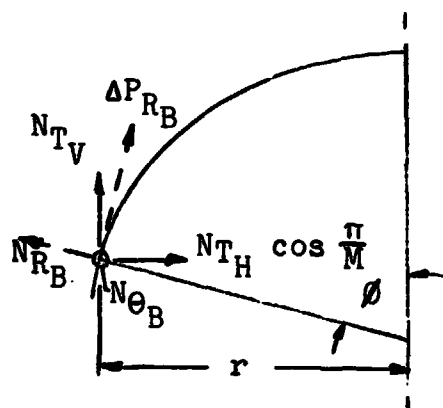
RESOLUTION OF REACTION N_T



View in gore
centerline plane



View in horizontal plane



forces on radial
from one horizontal

View in radial plane

$$\begin{aligned} \sin \phi' &= \frac{r \cos \pi/M}{\sqrt{(r \cos \pi/M)^2 + (r/\tan \phi)^2}} \\ &= \frac{\sin \phi \cos \pi/M}{\cos \alpha} \end{aligned} \quad (43)$$

$$\cos \phi' = \sqrt{1 - \sin^2 \phi'} = \frac{\cos \phi}{\cos \alpha} \quad (44)$$

$$\alpha = \sin^{-1} (\sin \phi \sin \pi/M)$$

$$N_{TH} = N_T \cos \phi' \quad (45)$$

$$N_{TV} = N_T \sin \phi' \quad (46)$$

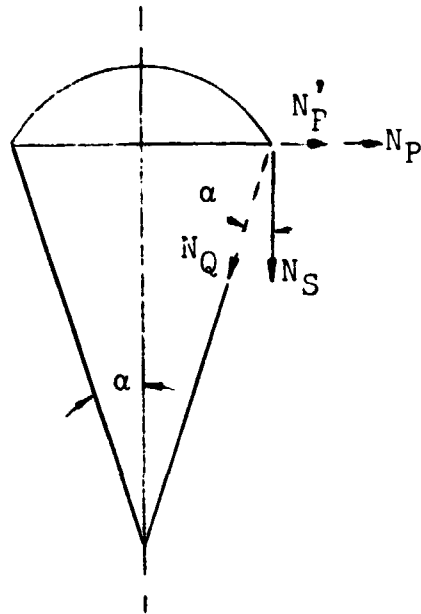
$$N_{\theta_B} = N_{TH} \sin \pi/M \quad (47)$$

$$N_{RB} = N_{TV} \cos \phi - N_{TH} \cos \pi/M \sin \phi$$

$$\therefore N_{RB} = 0 \quad (48)$$

$$\Delta P_{RB} = N_{TV} \sin \phi + N_{TH} \cos \pi/M \cos \phi \quad (49)$$

Resolution of N'_P and N_S

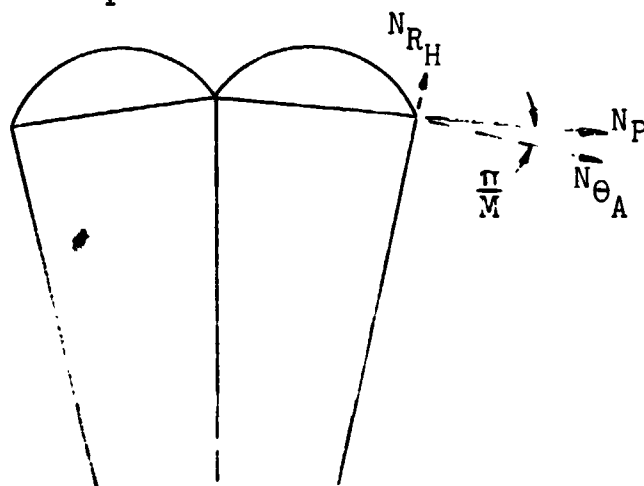


View in plane A

$$N_P = N'_P + \frac{N_S}{\cos \alpha} \sin \alpha \quad (50)$$

$$N_Q = \frac{N_S}{\cos \alpha} \quad (51)$$

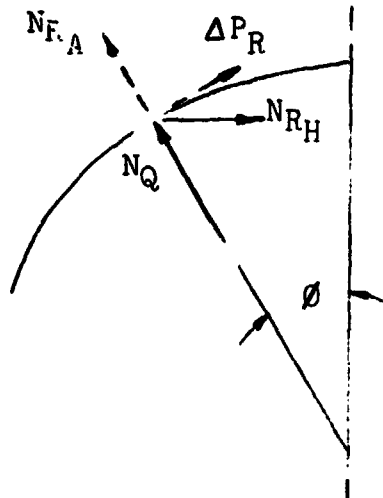
Resolution of Reaction N_P



View in horizontal plane

$$N_{\Theta A} = N_P \cos \pi/M \quad (52)$$

$$N_{RH} = N_P \sin \pi/M$$



$$N_{RA} = N_Q - N_{RH} \sin \phi \quad (53)$$

$$\Delta P_{RA} = N_{RH} \cos \phi \quad (54)$$

(Forces on radial tape
from one horizontal ribbon)

View in plane of radial tape

Combining components of N_T , N_S , and N_p

$$N_\theta = N_{\theta A} + N_{\theta B}$$

From Equations (37), (38), (39), (44), (45), (47), (50) and (52)

$$N_\theta = \frac{pr \sin \pi/M}{\sin \psi} \left[\cos \pi/M (\cos \psi + \sin \psi \tan \alpha) - \tan \beta \cos \phi \frac{\sin \pi/M \sin \psi}{\cos \alpha} \right] \quad (55)$$

$$N_R = N_{RA} + N_{RB}$$

From Equations (37), (39), (48), (50), (52), and (53)

$$N_R = pr \frac{\sin \pi/M}{\sin \psi} \left[\frac{\sin \psi}{\cos \alpha} - \sin \alpha (\cos \psi + \sin \psi \tan \alpha) \right] \quad (56)$$

$$\Delta P_R = \Delta P_{RA} + \Delta P_{RB}$$

From Equations (37), (38), (39), (43), (44), (45), (46), (49), (50), (52), and (54)

$$\Delta P_R = pr \frac{\sin \pi/M}{\sin \psi} \left[\sin \pi/M \cos \phi (\cos \psi + \sin \psi \tan \alpha) + \tan \beta \cos \pi/M \frac{\sin \psi}{\cos \alpha} \right] \quad (57)$$

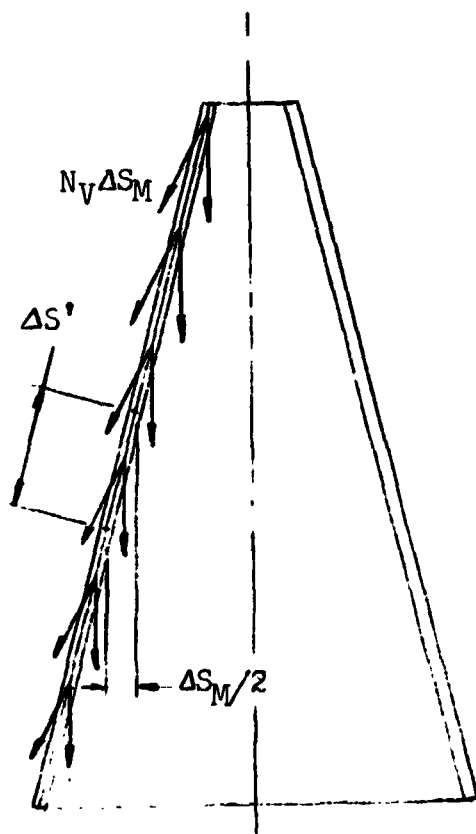
The load in the vertical ribbons is zero at the skirt since this is a free edge. Each horizontal ribbon adds an increment of load, $\Delta N_V \Delta S$, so that the loading at station j is given by

$$N_{Vj} = N_{V(j-1)} + (\Delta N_V \Delta S/2)_{(j-1)} + (\Delta N_V \Delta S/2)_j \quad (58)$$

Since the verticals intersect the radials as the gore width decreases from skirt to vent, the vertical ribbon load is transferred to the radial tape. It is assumed that this transfer is proportional to the decrease in gore width between reference stations. The force applied to a radial over a length $\Delta S'$ is given by:

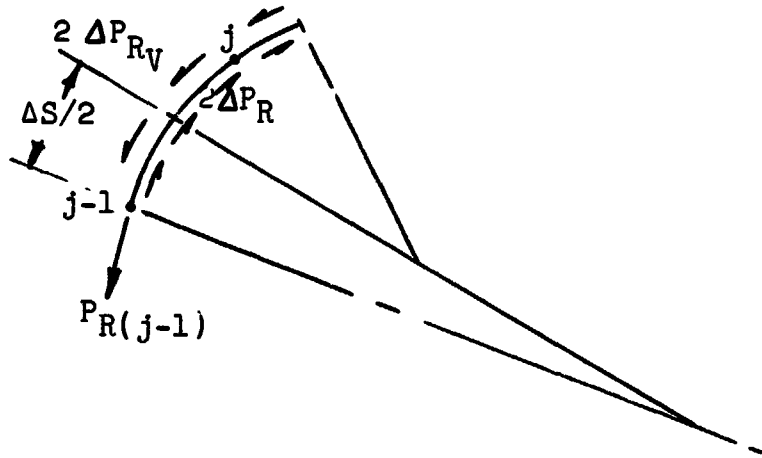
$$\Delta P_{R_V} \Delta S' = N_V \Delta S_M \cos \pi/M$$

$$\Delta P_{R_V} = N_V \frac{\Delta S_M}{\Delta S'} \cos \pi/M \quad (59)$$



$\frac{\pi}{M}$ (approx)
Flat Pattern of Gore

The load in a radial tape at station (j) is given by:



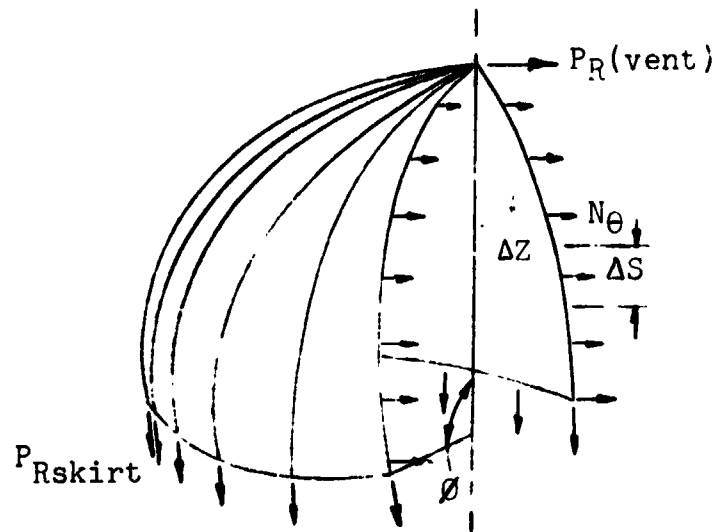
$$P_R(j) = P_R(j-1) - 2(\Delta P_R \Delta S/2)_{(j-1)} - 2(\Delta P_R \Delta S/2)_j + 2(\Delta P_{R_V} \Delta S/2)_{(j-1)} + 2(\Delta P_{R_V} \Delta S/2)_j \quad (60)$$

Curvature of Radial Tape

The following approximation is used for the radius of curvature of the radial tape:

$$R_\theta = \frac{P_R + N_V S_M}{2 N_R} \quad (61)$$

This equation is identical to that derived in Section 3.1 except that the term $N_V S_M$ is added to account for the load in the vertical members. In the solutions obtained for the drogue chute (Section 4.1.6), use of this equation results in equilibrium for a vertical section through the canopy when checked by the method shown below.



$$\sum F_H = 0 = 2 \sum_{\text{skirt}}^{\text{vent}} N_{\theta} \Delta S + \left[(2 M P_R / 2\pi r) r \cos \phi \right]_{\text{skirt}}^{\text{vent}} + \left[(2 M P_R / 2\pi r) r \cos \phi \right]_{\text{vent}} - 2 \sum_{\text{skirt}}^{\text{vent}} p r \Delta z \quad (62)$$

Solution Algorithm

The equations for skirt equilibrium, radial tape geometry and differential pressure are the same as those given in Section 3.1. A solution algorithm is given in the form of a flow diagram for computer program CANO 1 is given in Figure 7.

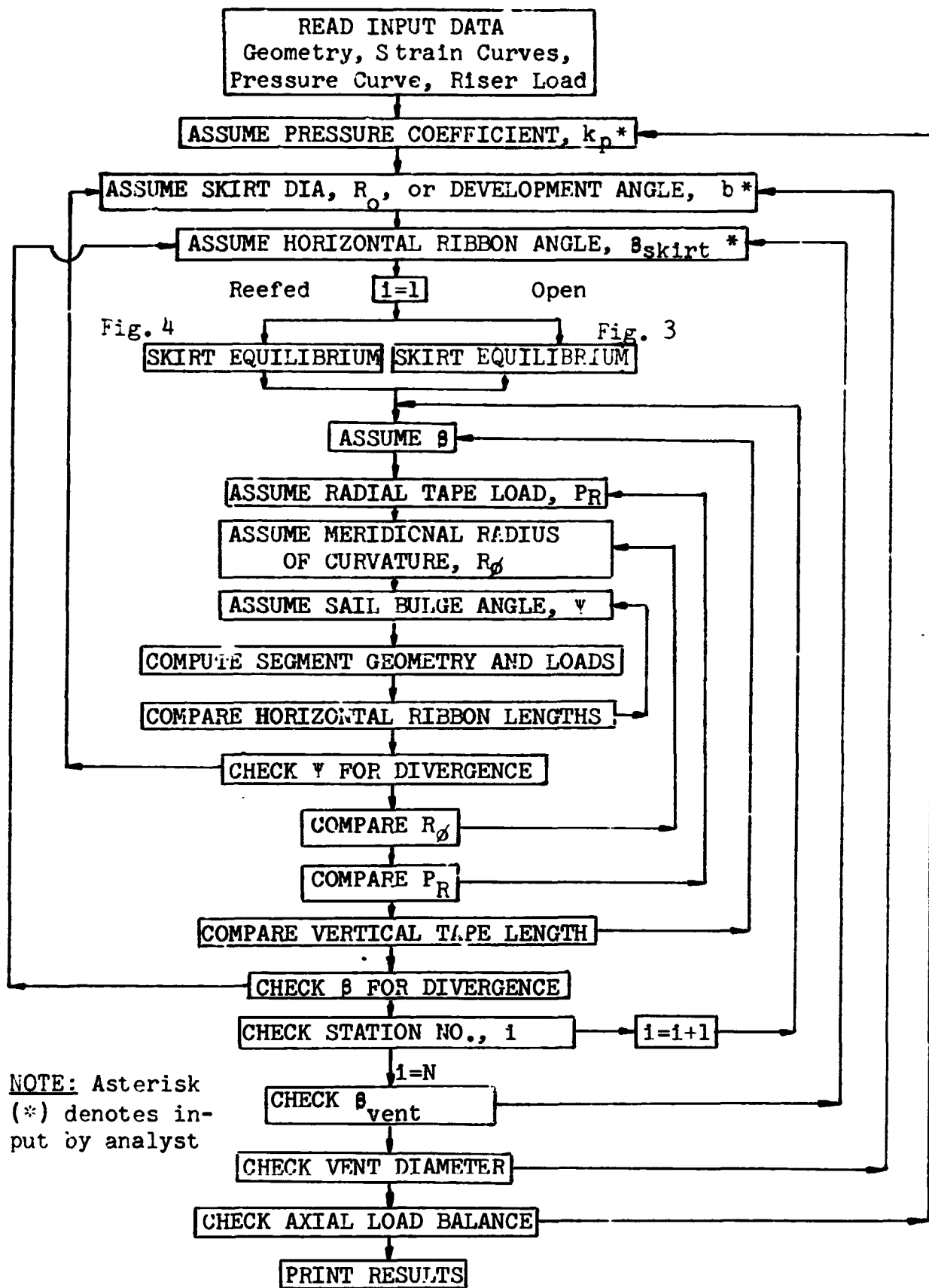


Fig. 7. Flow Diagram for Program CANO 1

SECTION 4.0

TEST DATA REVIEW AND APPLICATION OF INTERNAL LOADS ANALYSIS

The objective of this section is to upgrade the structural analysis methods by use of the test data acquired during the Apollo Test Programs. The forms of test data available are: 1) high-speed motion picture coverage from onboard, air-to-air, and ground cameras; 2) load-time traces at the parachute riser; 3) dynamic pressure history from ASKANIA tracking; and 4) failure analyses of drop tests in which parachutes were damaged or destroyed. Appendix A summarizes the drop tests of the Apollo ELS Block I, Block II and Block II (H) programs.

In this section, two methods are used to verify the analysis methods presented in Section 3. First, drop test photographs are compared with the shape predicted analytically for the test loading conditions. Since a unique shape is predicted for a given pressure distribution and axial loading for a given parachute construction, correlation of the predicted and actual shapes is evidence that the internal load prediction is correct (if the pressure distribution used is correct). This is further verified by comparison of predicted ultimate strength and failure modes with test results.

Additional analyses are presented to show the sensitivity of canopy size and internal loading to variations in canopy construction and pressure distribution.

Analysis of the main parachute is extended to include a stress-time study throughout the opening process and optimum weight calculation for the spacecraft design.

Three types of parachutes are used in the Apollo Earth Landing System, the drogue, pilot, and main parachutes. The first

NORTHROP

two parachutes to be deployed are drogue chutes, which are ribbon type parachutes that incorporate one stage of reefing. Three pilot parachutes are deployed just as the drogues are disconnected to extract the main parachutes from their packing bags. The pilot chute has a ringslot type canopy with an overinflation line attached to the skirt. Final deceleration of the spacecraft to descent velocity is accomplished by the three main parachutes. These are ringsail parachutes with two stages of reefing. The analyses that follow will consider the parachutes in the order of deployment.

CONTINUED

4.1 DROGUE CHUTE

4.1.1 Drogue Chute Structural Model

Structural details of the drogue chute are given in Figure 8 and the corresponding structural model is defined in Figure 9. In modeling the canopy, all horizontal members, including the skirt and vent bands, are represented as finite elements. Initial lengths and tape rated strengths are taken from the engineering drawings and appropriate load-strain curves are input to the computer in tabular form. The reefing and overinflation lines, which are attached at or near the skirt band, are included in the model by the method discussed in Section 3.

Modeling of the meridional members presents a problem because of vertical ribbons between the radial tapes. There is experimental evidence that the verticals carry significant meridional load, but the method used in program CANO assumes that all the meridional load is carried by the radial tapes. To approximate their effect in the structural model used by CANO, the stiffness contributed by the verticals is added to that of the radial tapes. Results of a study to determine the sensitivity of the solution of a fully inflated canopy to variations in meridional stiffness are given in Figures 10, 11 and 12. Canopy profile, horizontal member loading, and radial tape loading for three models differing only in the stiffness of the meridional members are compared. Model I has radial tapes only; Model II has the two verticals nearest the radial fully effective; and Model III has all of the verticals fully effective. In the latter two models, the vertical stiffness is diminished linearly from fully effective at the station with maximum diameter to zero at the skirt. It is concluded from these figures that modeling variations of the meridional members are not significant in determination of the canopy profile but can affect the maximum load in horizontal tapes. A difference of approximately eight percent in the maximum horizontal tape load is observed between Models I and III. Further study of the effect of vertical ribbons using the analysis of Section 3.2 is presented in Section 4.1.6.

VERTICAL

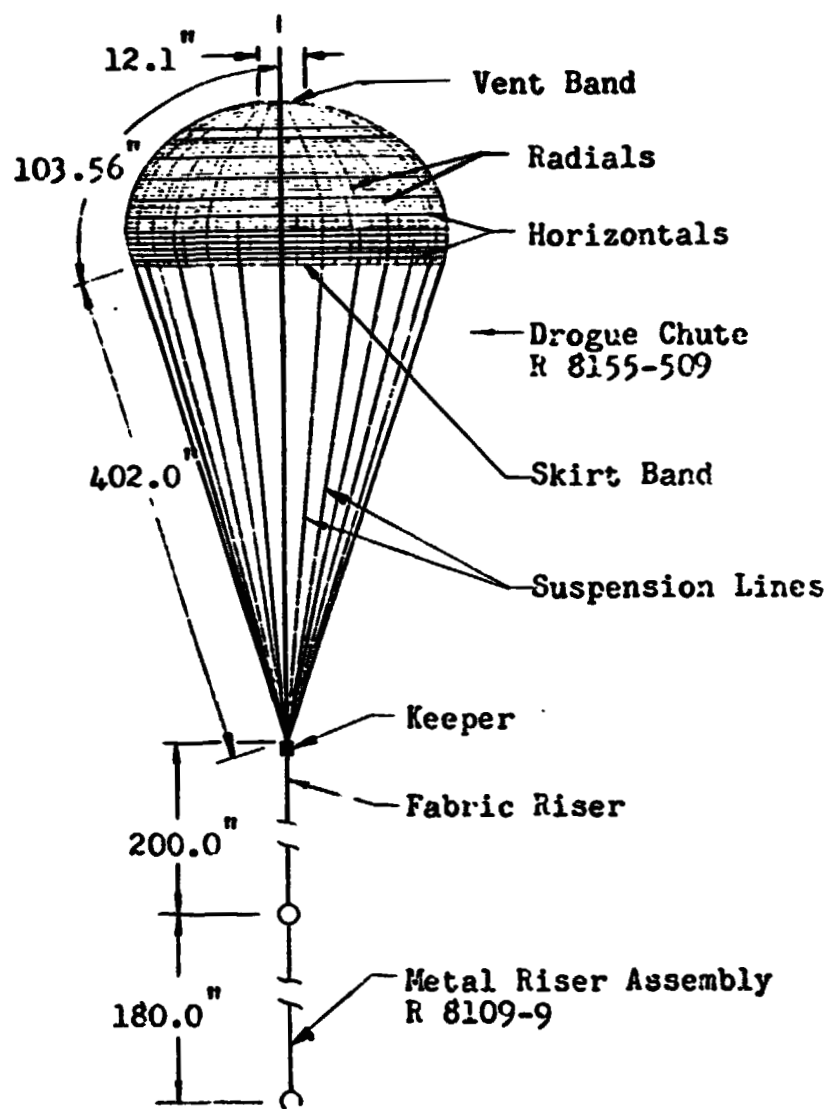
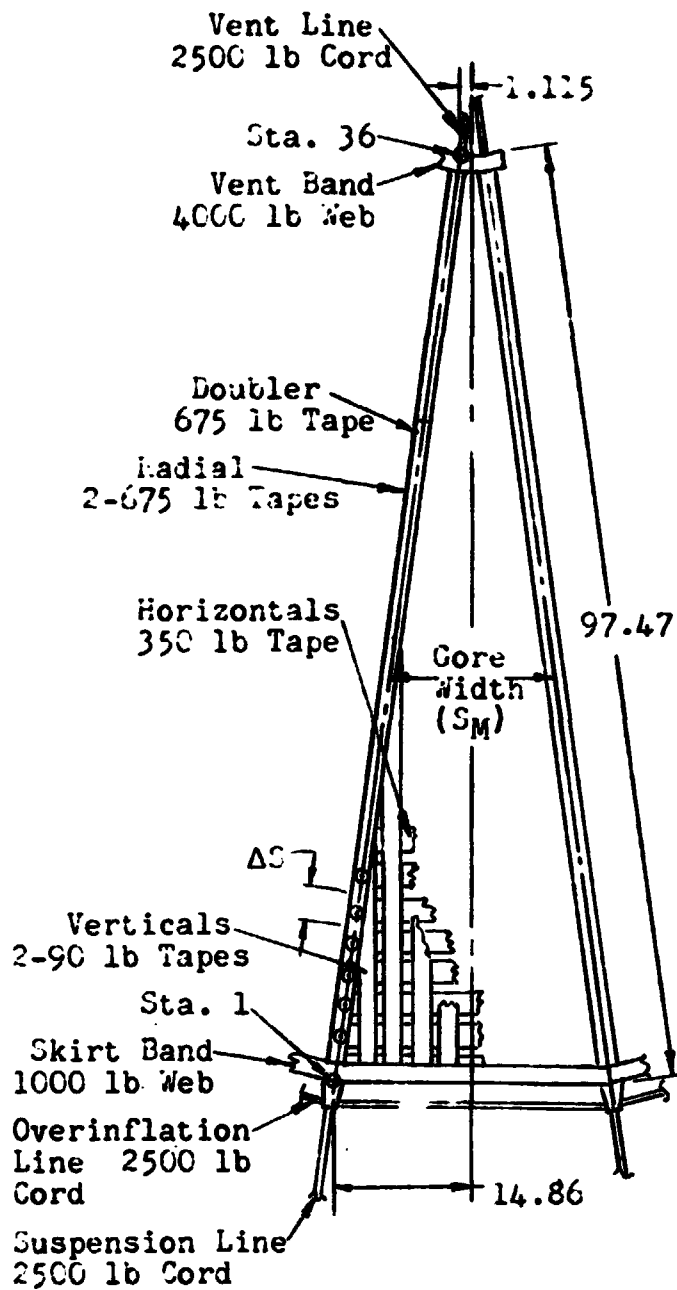


Fig. 8 . Drogue Chute Assembly

NORTHROP



STA*	AS in.	S _M in.
36	2.36	2.230
35	2.73	3.456
34		4.216
33		4.975
32		5.734
31		6.493
30		7.252
29		8.012
28		8.771
27		9.530
26		10.289
25		11.048
24		11.808
23		12.567
22		13.326
21		14.085
20		14.844
19		15.604
18		16.363
17		17.122
16		17.881
15		18.640
14		19.400
13		20.159
12		20.918
11		21.677
10		22.436
9		23.196
8		23.955
7		24.714
6		25.473
5		26.232
4		26.992
3		27.751
2	2.73	28.510
1	2.36	29.270

*Sta. 2 to 35 on
C of Horizontals

Fig. 9. Drogue Chute Structural Model

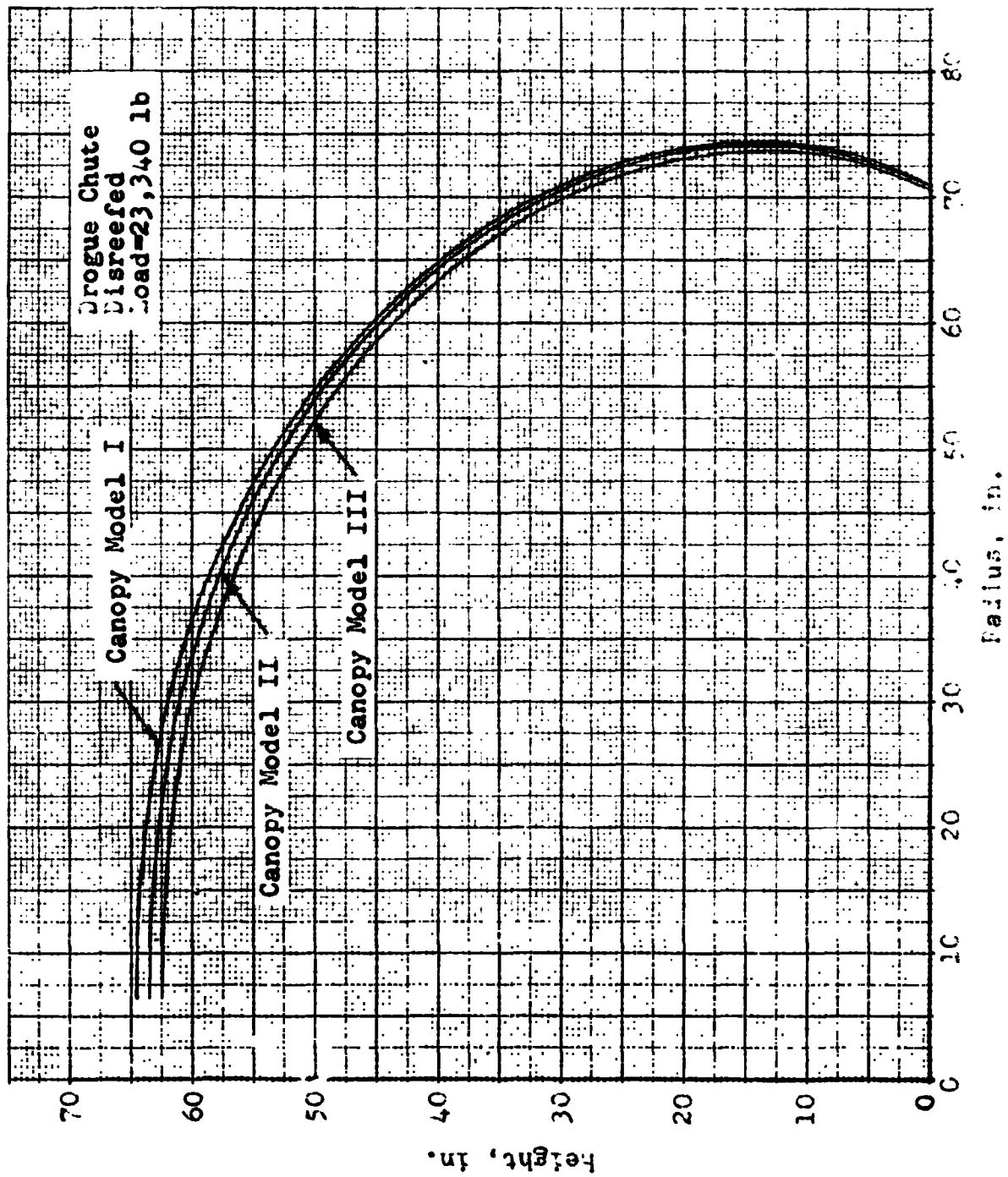


Fig. 10 Drogue Chute Canopy Profiles for Various Structural Models

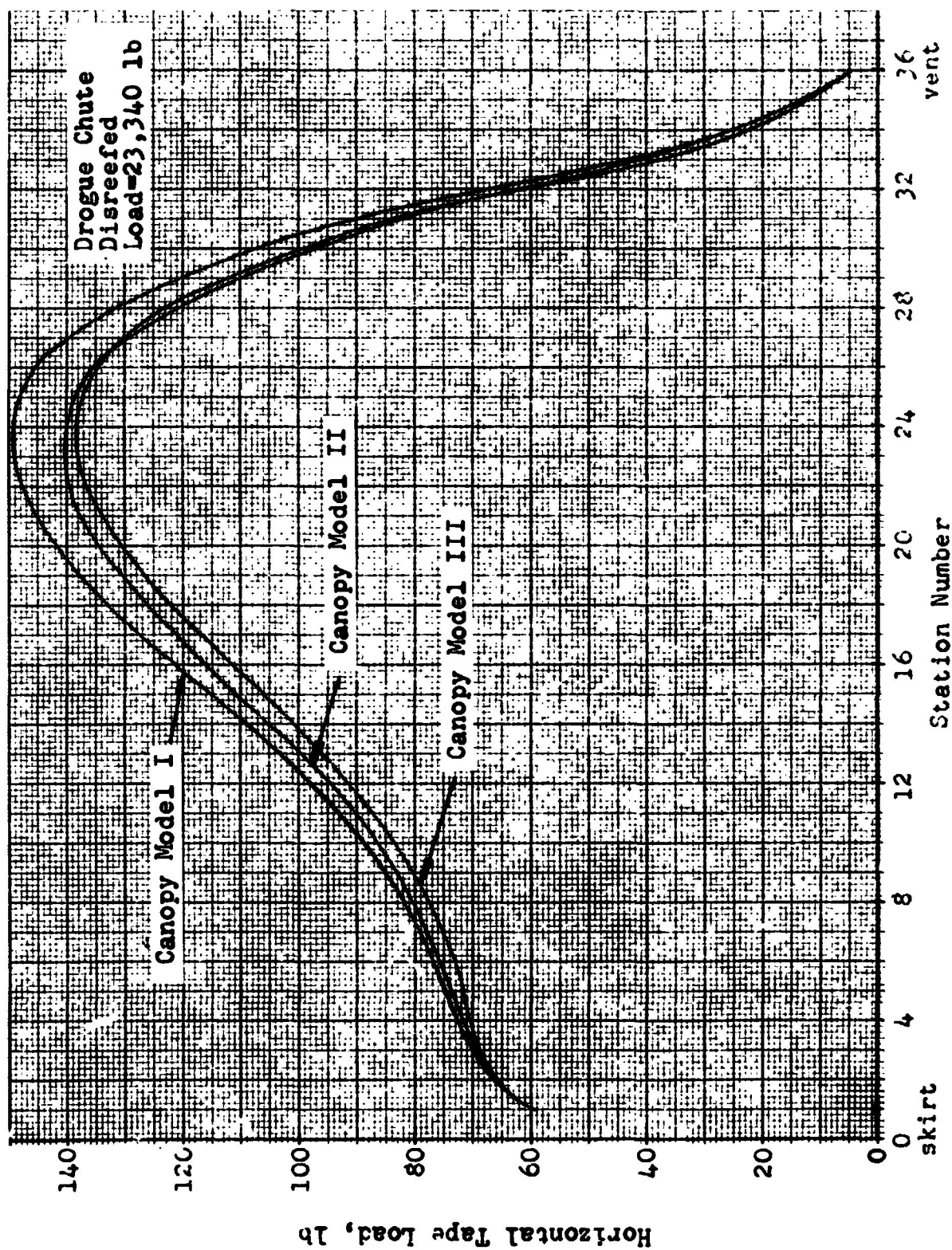


Fig. 11. Horizontal Tape Loads for Various models of the Drogue Chute

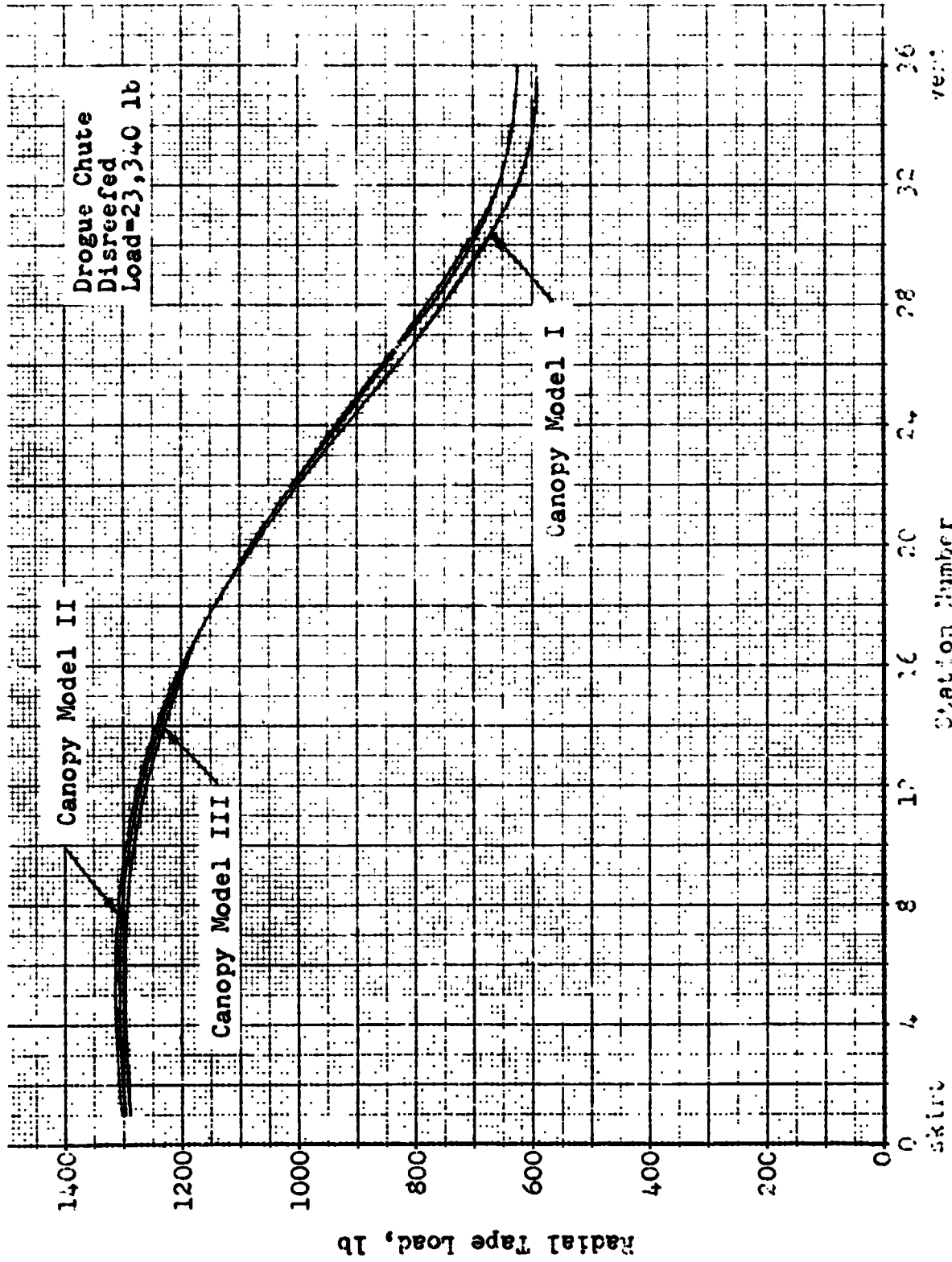


FIG. 10. Radial Tape Load for Various Models of the Drogue Chute

4.1.2 Drogue Chute Pressure Distributions

The drogue parachute is analyzed for both the reefed and open stages since not all canopy members are subjected to their critical loads in the same stage.

Since pressure distribution data for reefed parachutes is not available, the canopy is assumed to have a uniform pressure differential over the inflated portion of the canopy. The degree of canopy inflation depends on the length of the reefing line, which restricts the inflow of air, and on the porosity of the canopy. The degree of inflation of the reefed drogue was determined from photographs taken during an aerial drop test. (See Section 4.1.4) Figures 13 and 14 show the horizontal ribbon loading, and radial tape loading for the reefed drogue chute with a uniform pressure distribution. To determine whether this is the appropriate pressure distribution, the predicted canopy shape is compared to the measured canopy shape in Section 4.1.4. The reefed canopy is analyzed for a riser load of 21,000 pounds which is the peak canopy loading occurring in the flight test used for the shape comparison.

Some empirical data is available for pressure distributions in ribbon canopies for the full open condition. The wind tunnel pressure distribution data, Reference 20, is applicable for the drogue chute since the dynamic pressure decay is only about 2 percent from time of disreef to maximum load. Test data for a circular ribbon parachute with 18 percent geometrical porosity are given in Reference 20. The drogue chute is a conical ribbon parachute with a geometrical porosity of 22 percent. The drogue chute has an overinflation line, which might affect the pressure

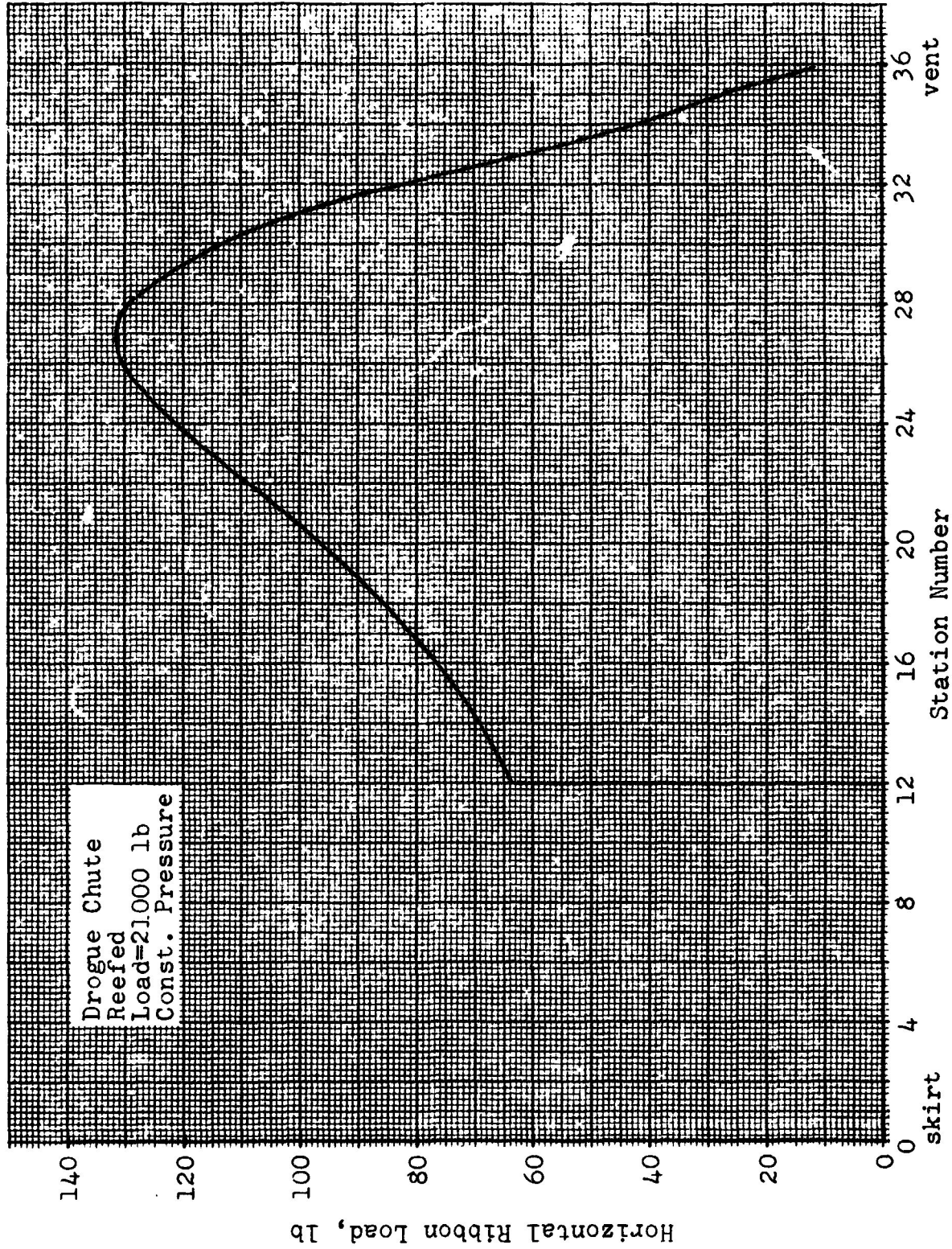


Fig. 13. Horizontal Ribbon Loading for the Reefed Drogue Chute

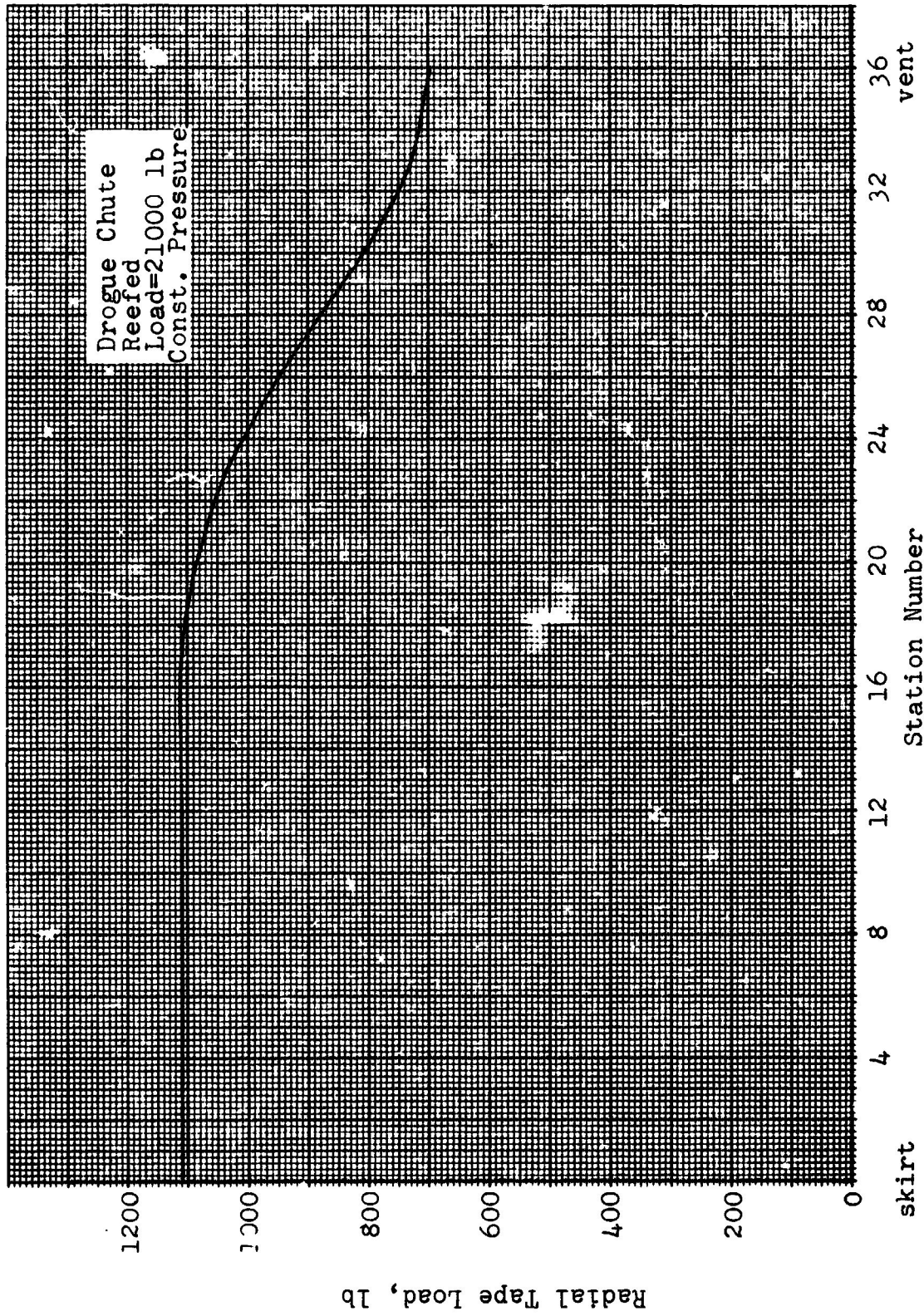


Fig. 14. Radial Tape Loads for the Reefed Drogue Chute

distribution at the skirt, and it inflates from a 43 percent reefed condition, whereas the wind tunnel model inflated from a zero percent reefed condition. No test data are available to indicate the effects of these differences.

In Figure 15, the data of Reference 20 is replotted to show the differential pressure across the canopy at different times for the four test velocities. Two significant observations can be made from Figure 15; 1) the general shapes of the curves are similar at the three event times shown--maximum diameter, maximum load, and steady state, and 2) no trend with varying velocity is indicated. On the basis of these observations it is concluded that the mean curve indicated in Figure 15 is a reasonable approximation for use in the analyses which follow.

In order to determine the effect of variations in pressure distribution on canopy shape and internal loading, a sensitivity study was performed using the four pressure distributions shown in Figure 16. Distribution A is the mean curve from Figure 15 and curves B, C, and D are arbitrary distributions. In distribution B, the pressure is constant throughout the canopy. In distribution C, the maximum pressure is at the vent while in distribution D the maximum is at the skirt. In distributions C and D the maximum pressure is twice the minimum value.

Figure 17 shows the variations in the canopy profile for the four pressure distributions. As expected, the peak pressure at the skirt gives the largest canopy diameter, while peak pressure at the vent gives the largest profile height.

The variation of horizontal ribbon load with these pressure distributions is given in Figure 18. It is seen that distribution D (peak pressure at the skirt) gives peak loading 11 percent higher than that of distribution C (peak pressure at skirt). The peak horizontal tape load occurs higher in the canopy as the peak pressure moves from skirt to vent.

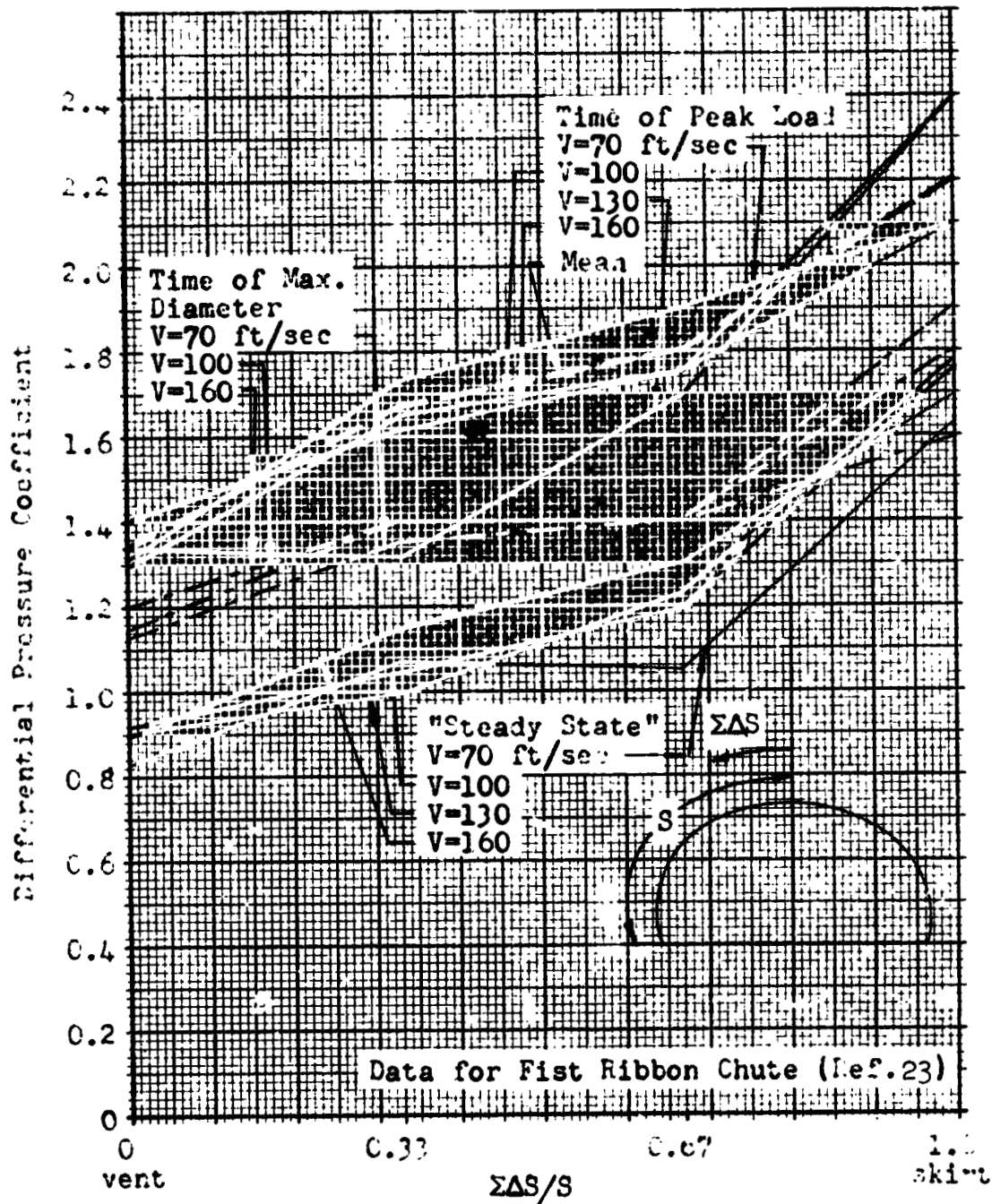


Fig. 15 . Pressure Distributions At Various Times After Deployment.

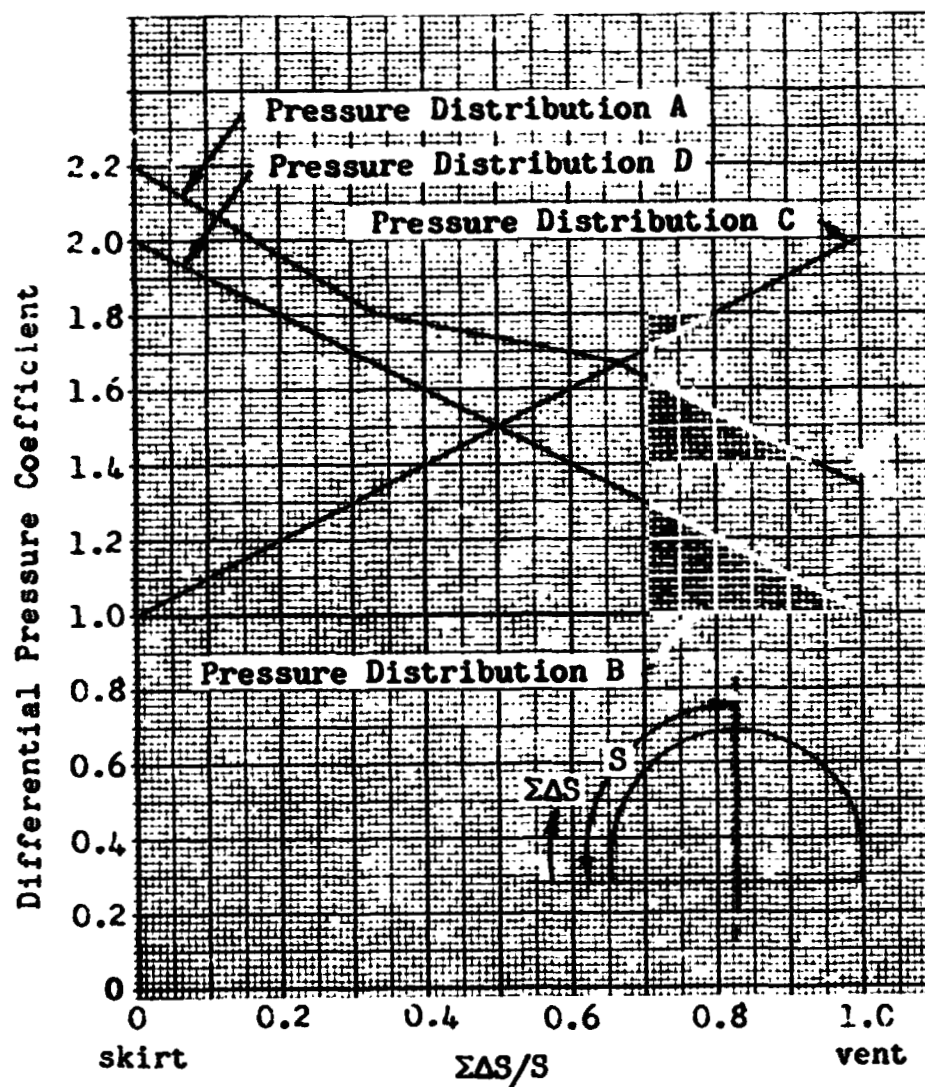


Fig. 16. Canopy Pressure Distributions Used for Sensitivity Study

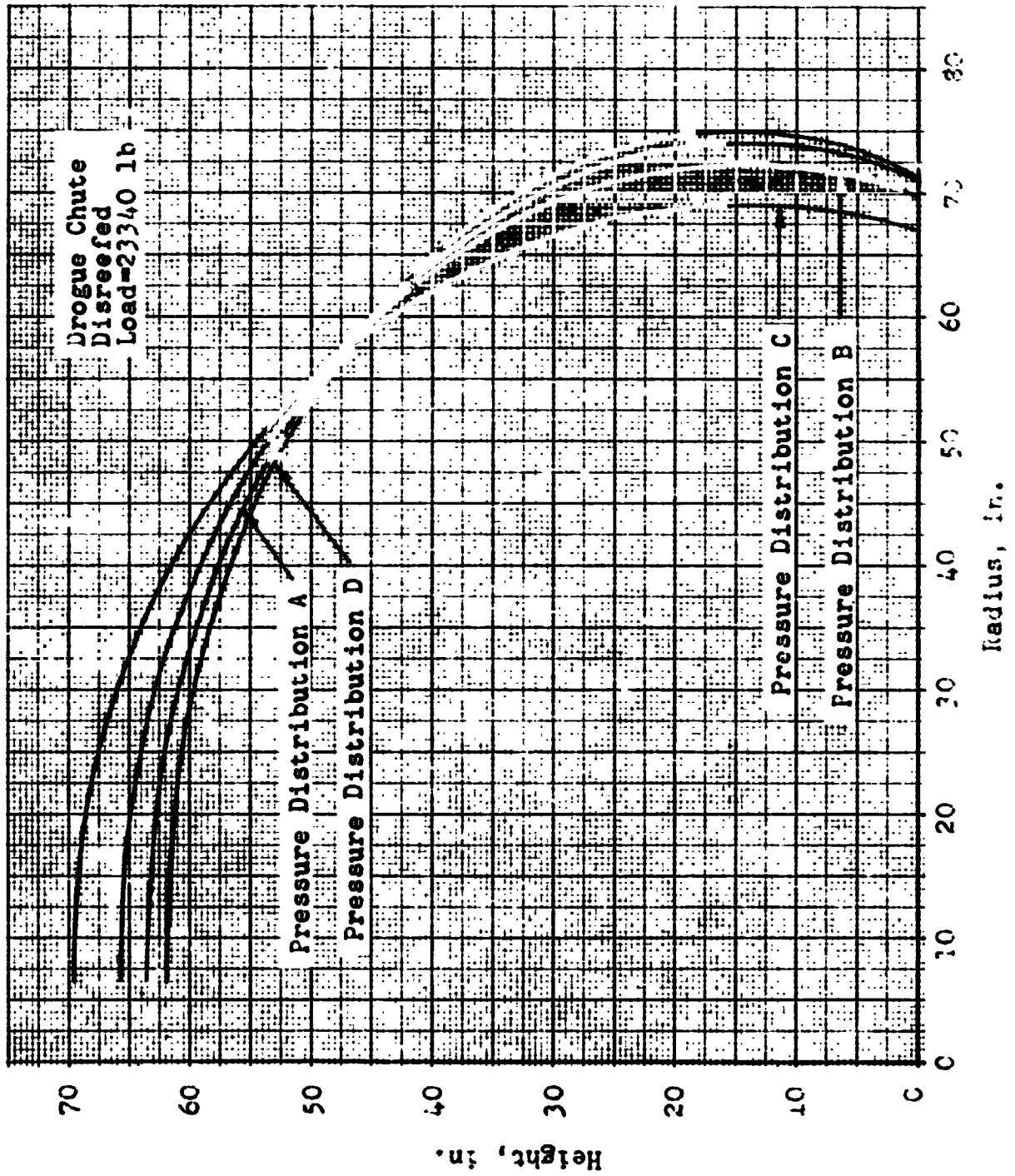


Fig. 17. Drogue Canopy Profile for Various Pressure Distributions

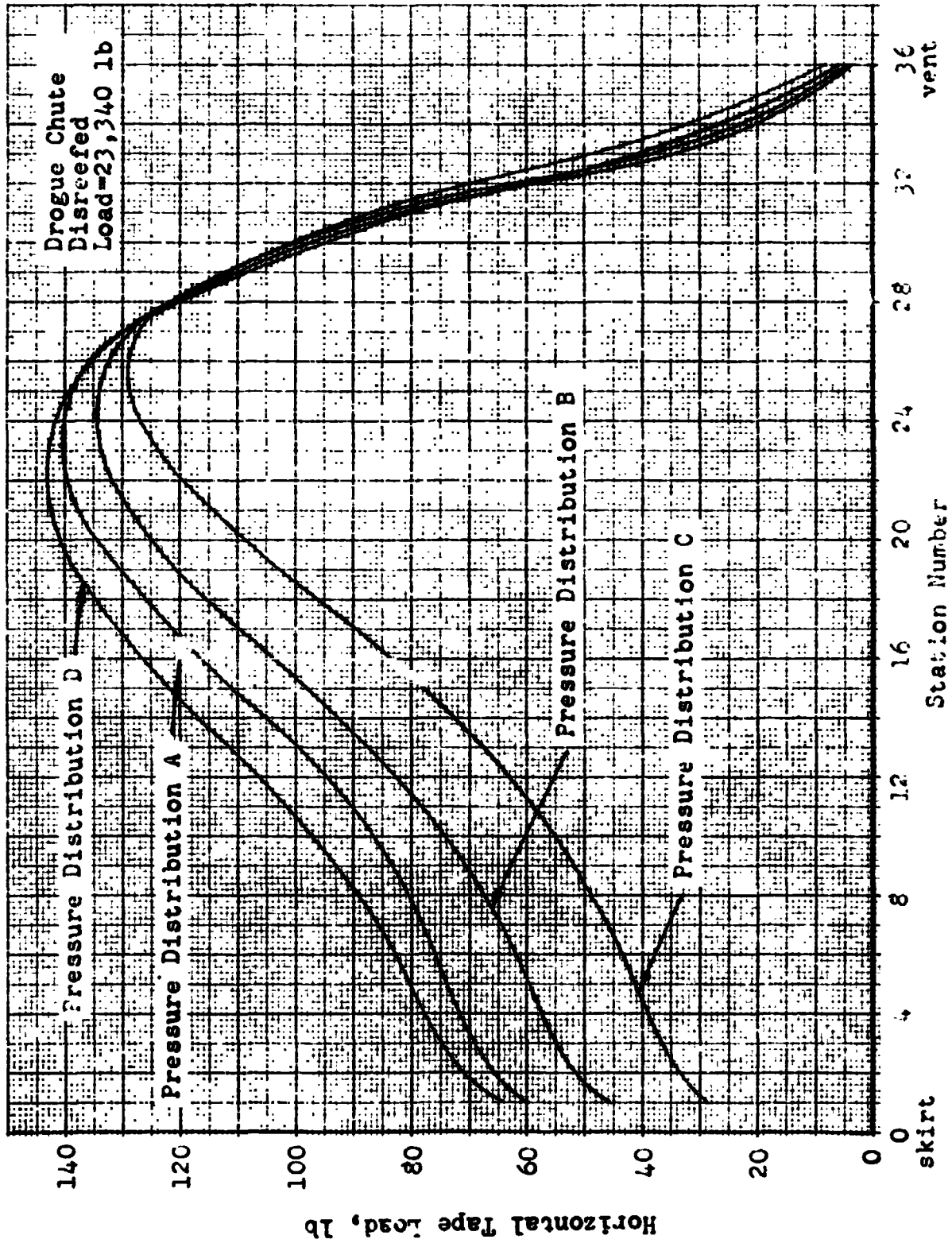


Fig. 13. Horizontal Tape Loads in Drogue Chute for Various Pressure Distributions

NORTHROP

In Figure 19 the radial tape loads for the four pressure distributions are shown. Distribution D produces the highest loading at the skirt, while distribution C gives higher loads in the crown.

It is concluded from these figures that the differential pressure distribution across a parachute canopy has a first order effect on internal loading. Further investigation of pressure distributions in inflating canopies is, therefore, essential for accurate internal load predictions.

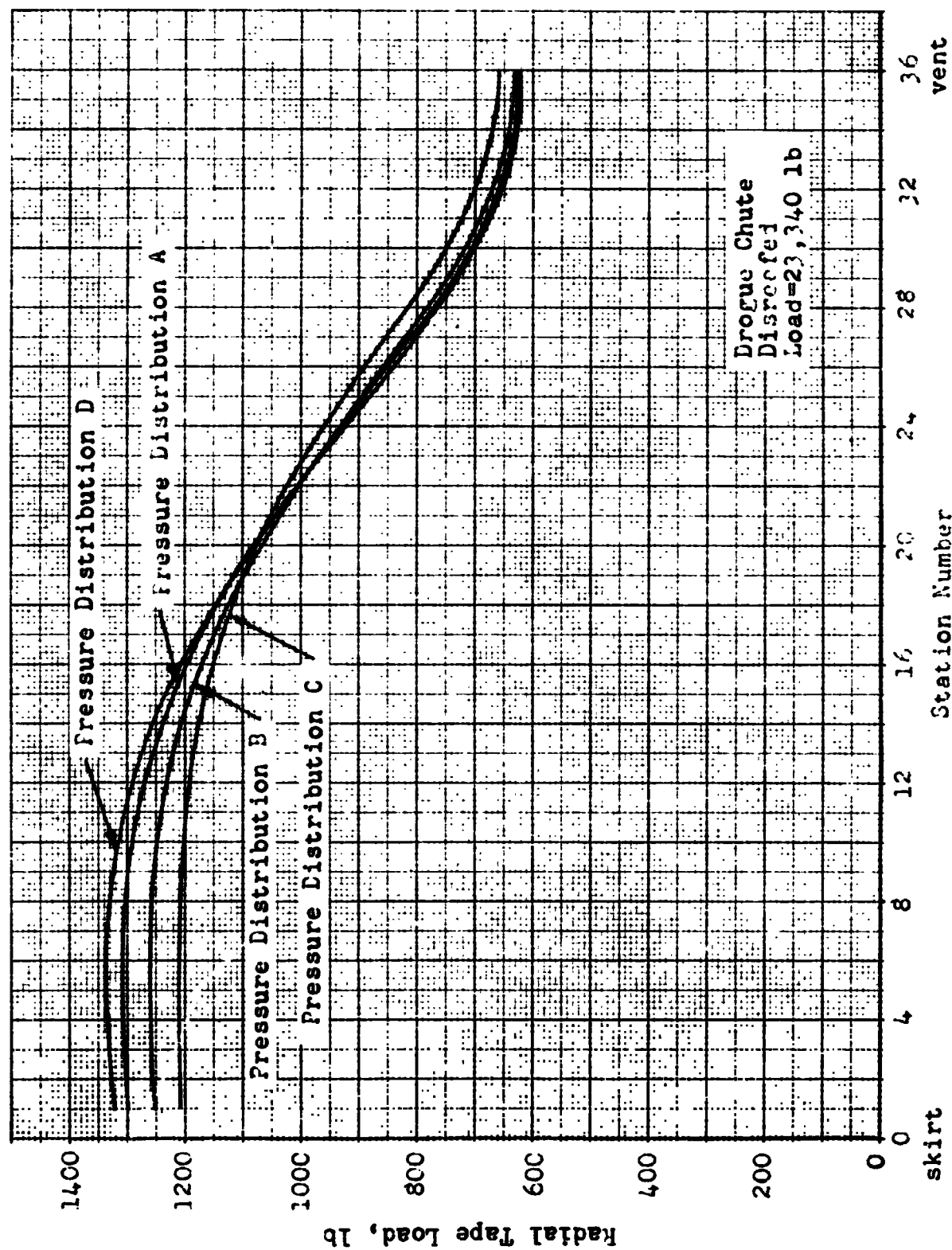


Fig. 19. Radial Tape Loads in Drogue Chute for Various Pressure Distributions

4.1.3 Drogue Canopy Growth

Results of a study of the variation in canopy shape and internal loading with applied axial load are shown in Figure 20 . Solutions were obtained for the disreefed drogue chute, structural Model II, for axial loads of 5,000, 10,000, 15,000 and 23,340 pounds, with all other parameters constant. In Figure 20 maximum diameter, projected area, radial tape load, and horizontal ribbon load are plotted versus applied axial load. The variation of these quantities is practically linear with load. The slight curvature observed can be attributed to the shapes of the load strain curves of the parachute materials. Since this effect is negligible for small changes in load, canopy loads can be proportioned directly with axial load.

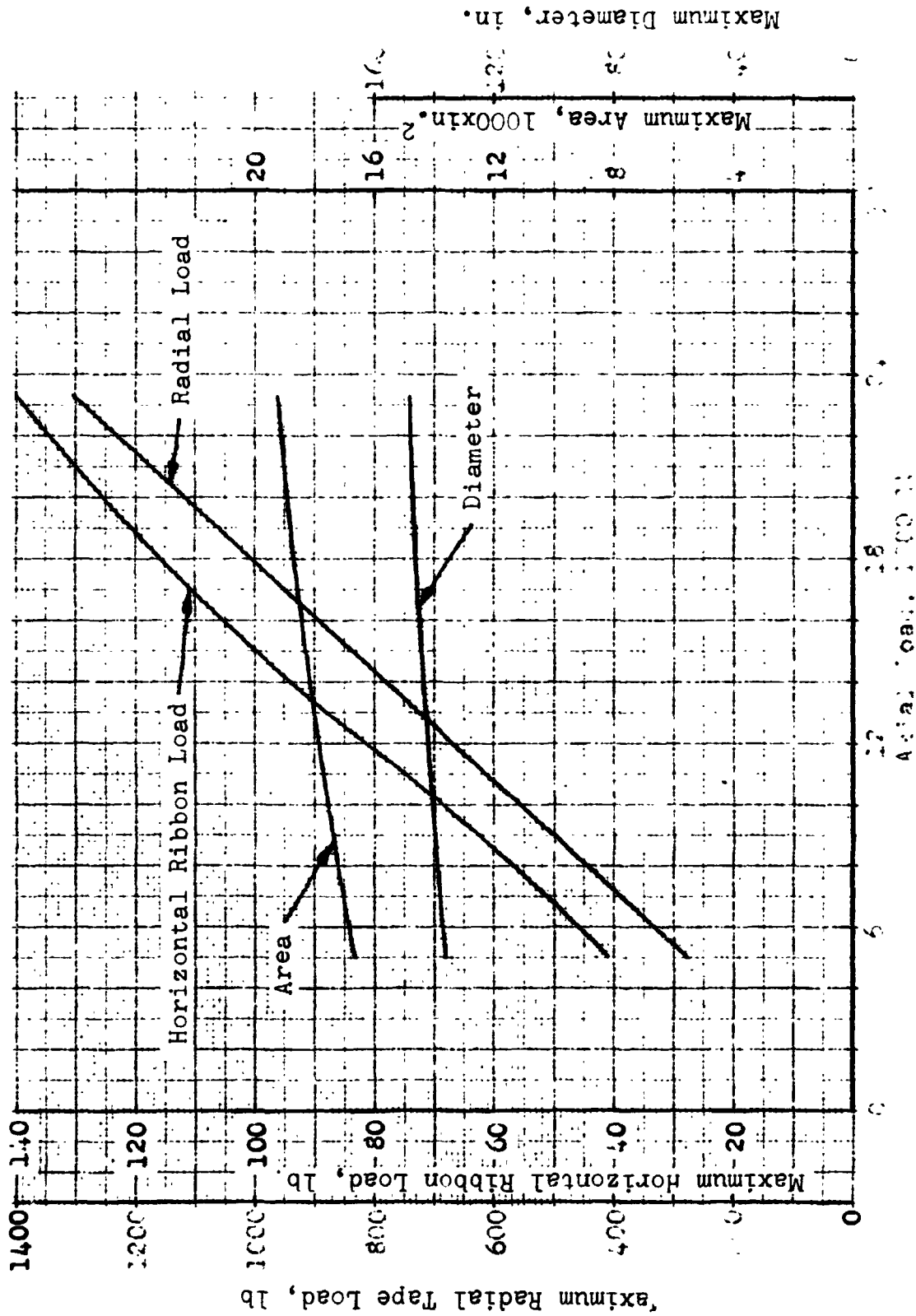


Fig. 20. Variation of Canopy Size and Internal Loads with Axial Load

4.1.4 Drogue Chute Film Analysis

Three types of photographic coverages are available from the Apollo Drop Test Programs: air-to-air, ground-to-air, and onboard. It is desirable to measure the profile view of the canopy in order to obtain the most accurate shape comparison. These measurements would have to come from the air-to-air or ground-to air coverages. Due to the size, velocity, and deployment altitude of the drogue chute, the air-to-air and ground-to-air coverages are inadequate to provide shape measurements. It is, therefore necessary to use onboard cameras coverage. The individual ribbons can be identified in these photographs so that canopy diameter as a function of station number (as defined in Section 4.1.1) can be measured. To obtain actual dimensions of the canopy from the photographic images, the measurements are converted as follows:

$$\text{Diameter} = \text{Image Diameter} \times \text{Lens Factor} \times \text{Distance from Camera}$$

where the lens factor is calculated by measuring the image of a known length at a known distance. The distance from the camera to the skirt is calculated from the free lengths of the risers and suspension lines and their elongations. Distances from the skirt to specific horizontal members are taken from the analytically predicted geometry.

Figure 21 shows the comparison of the reefed drogue shapes for constant pressure over the inflated portion of the canopy. From the onboard photographs, it was seen that the first eleven horizontal tapes above the skirt were not inflated. The pressure distribution used to predict the analytical shape was, therefore, adjusted so that the first eleven horizontals had zero differential pressure. Since the predicted canopy shape is close to the observed shape, the computed internal canopy loading may be assumed to be close to actual values. (See Figures 13 and 14 .)

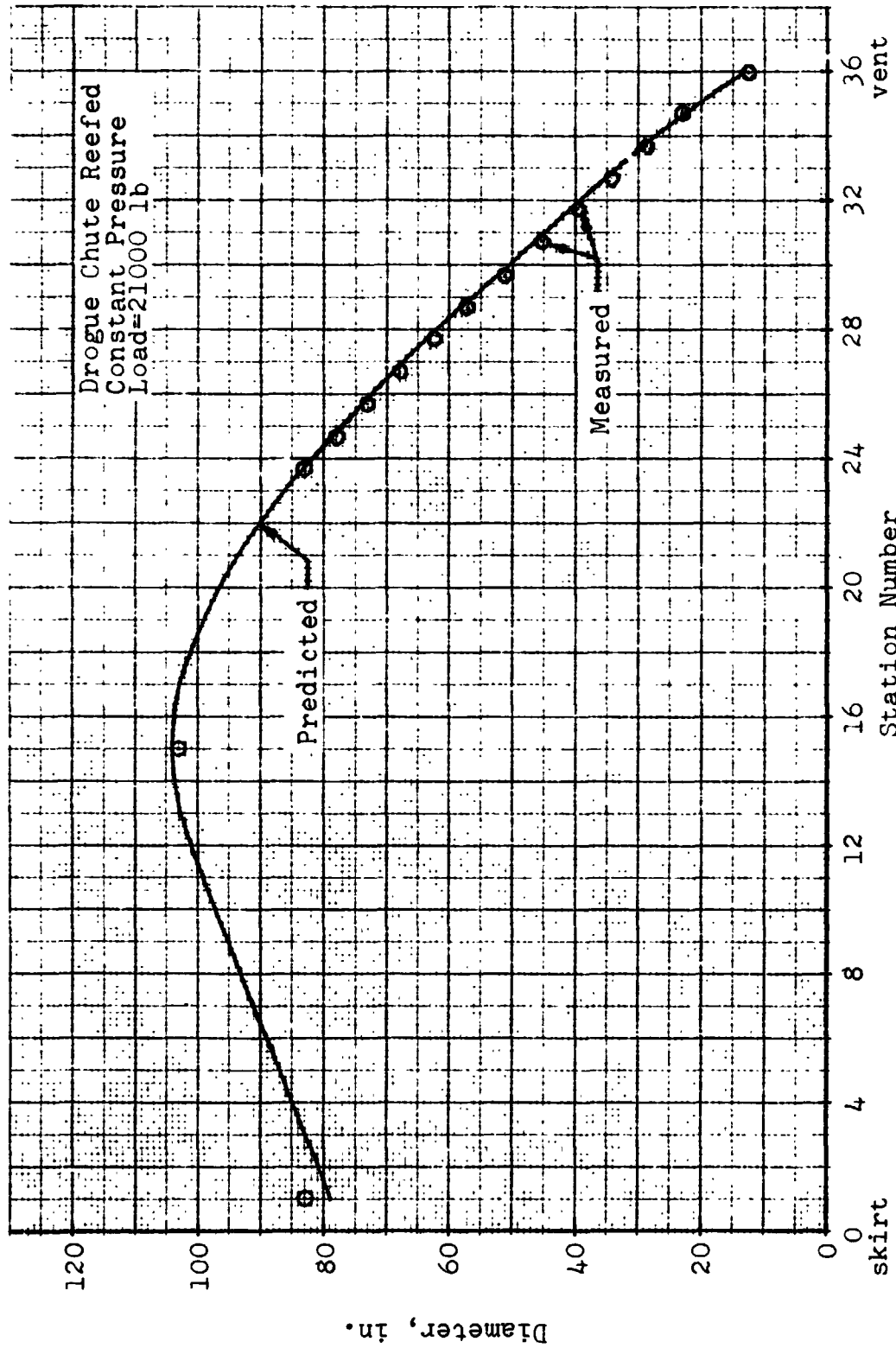


Fig. 21. Comparison of Predicted and Measured Reefed Canopy Shapes for the Drogue Chute

Figure 22 shows the comparison of the disreefed drogue shapes for pressure distribution A in Figure 16. The effect of the overinflation line on the disreefed canopy is to control the expansion of the skirt and not to restrict the inflation of the canopy. All of the horizontal tapes, therefore, become inflated. It is seen in Figure 22 that good agreement exists in the upper portion of the parachute, but in the lower portion the predicted diameter is too large. A significant difference in shape exists at the skirt which would result in larger than actual loads in the radials and overinflation line. This discrepancy is attributed to the presence of the overinflation line which causes a large development angle at the skirt (25°). This would tend to reduce the differential pressure in the skirt area, so that the test data used to obtain this distribution curve is not applicable.

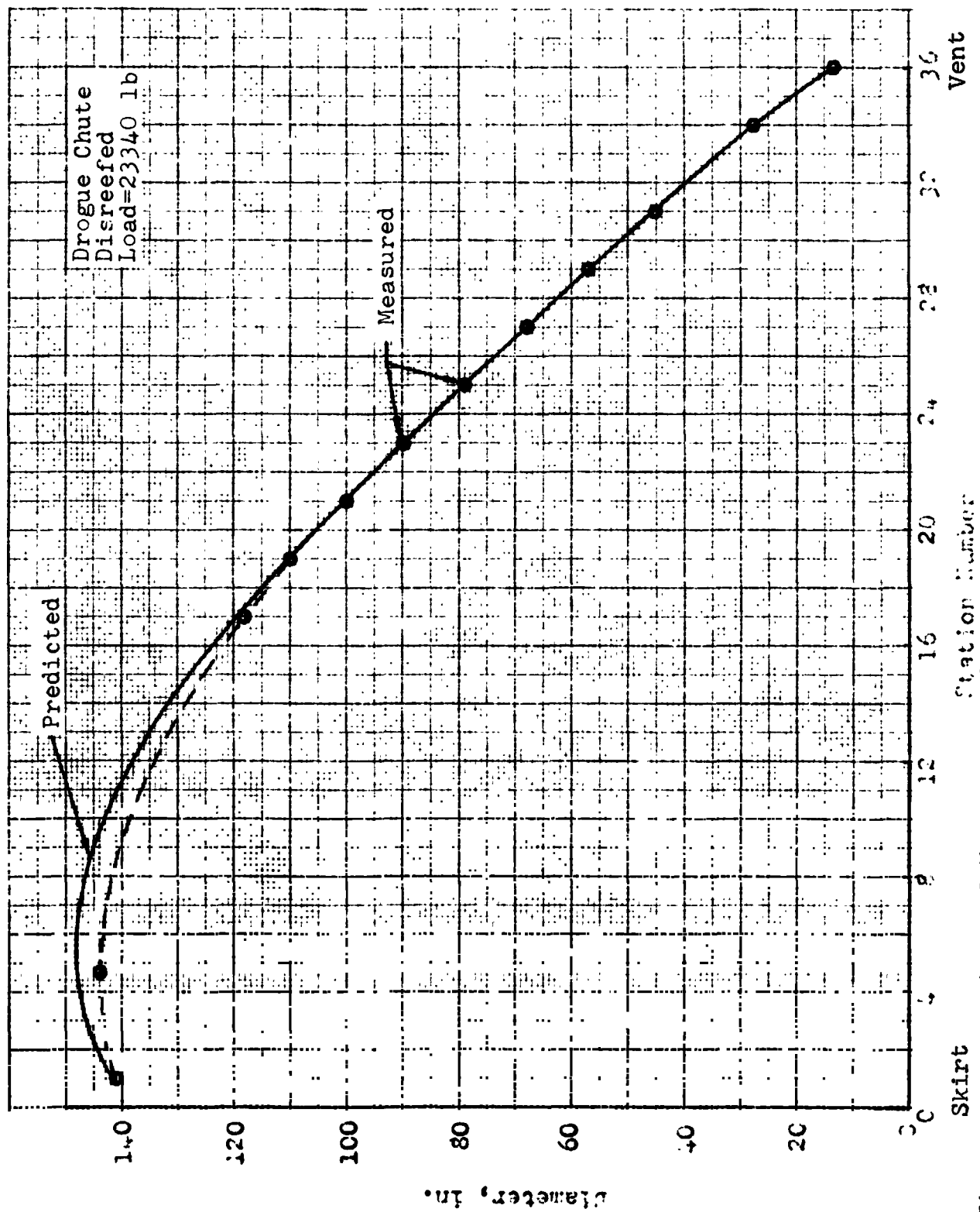


FIG. 22. Comparison of Measured and Predicted Canopy Diameters for the Drogue Chute

4.1.5 Failure Analysis

Table 1 gives a comparison of predicted strengths and failure modes with test results for the two tests in which ultimate load was applied to fully opened drogue canopies. This comparison, although limited in scope by the number of test points available, shows reasonable agreement between predicted and actual strengths and failure modes.

Table 1 Drogue Chute Failure Analysis

Test No.	Measured Riser Load	Test Damage or Failure Mode	Calculated Ultimate Strength	Predicted Failure Mode
84-4*	27,250 lb	No significant Damage	30,300 lb*	Gore Split
99-2**	35,930 lb	Gore split from Vent to Skirt	34,960 lb**	Gore Split

* R8155-507 had 9 rows of stitching to secure the horizontals at the radials (Joint Efficiency = .75)

** R8155-505 had 10 rows of stitching to secure the horizontals at the radials (Joint Efficiency = .83)

4.1.6 Analysis of the Drogue Chute Using CANO 1

As was pointed out in Section 4.1.1, there is experimental evidence that the vertical ribbons carry a significant portion of the meridional load in the canopy. To include the effect of the vertical members the CANO 1 Program was developed, as discussed in Section 3.2. Solutions have been obtained for the reefed and fully open drogue parachutes to quantitatively evaluate the effect of the vertical members. The pressure distributions used are identical to those used to analyze the parachute by the CANO Program as discussed in Section 4.1.2 and 4.1.4. The riser loads have been revised to the design ultimate loads of 23,530 pounds for the reefed condition and 24,560 pounds for the fully inflated condition.

Comparison of canopy profiles for the reefed and open parachutes are shown in Figures 23 and 24, respectively. The main effect that the verticals have on the canopy shape is to lift the first few inflated horizontal ribbons so that they are not perpendicular to the radial tape as was assumed in the previous analysis. Radial tape profiles calculated for the reefed drogue canopy with and without verticals are nearly identical, as shown in Figure 23. The gore centerline profiles differ only in the area of the first few inflated horizontal ribbons. Canopy profiles for the open drogue canopy also compare closely except in the area of the skirt. While the effect of the verticals on canopy shape does not appear too large, their effect on internal loading is substantial. Figures 25 and 26 show the variation of hoop load in the horizontal ribbons and meridional load in the radial tapes for the drogue canopy with and without vertical ribbons. Figure 25 shows that the hoop stresses rise sharply at the first inflated ribbon in the reefed condition and at the skirt in the open

NORTHROP

condition due to the "hiking" of the skirt by the vertical ribbons. The contribution of the vertical ribbons in carrying meridional load is clearly indicated in Figure 26 by the reduction in radial tape loading for both the reefed and open conditions. Figure 27 shows the variation over the canopy of the vertical ribbon membrane loading and the horizontal ribbon displacement angle for the reefed and open parachute.

It should be pointed out that arbitrary assumptions were made in this analysis, so that supporting test data is necessary before it can be considered a design tool.

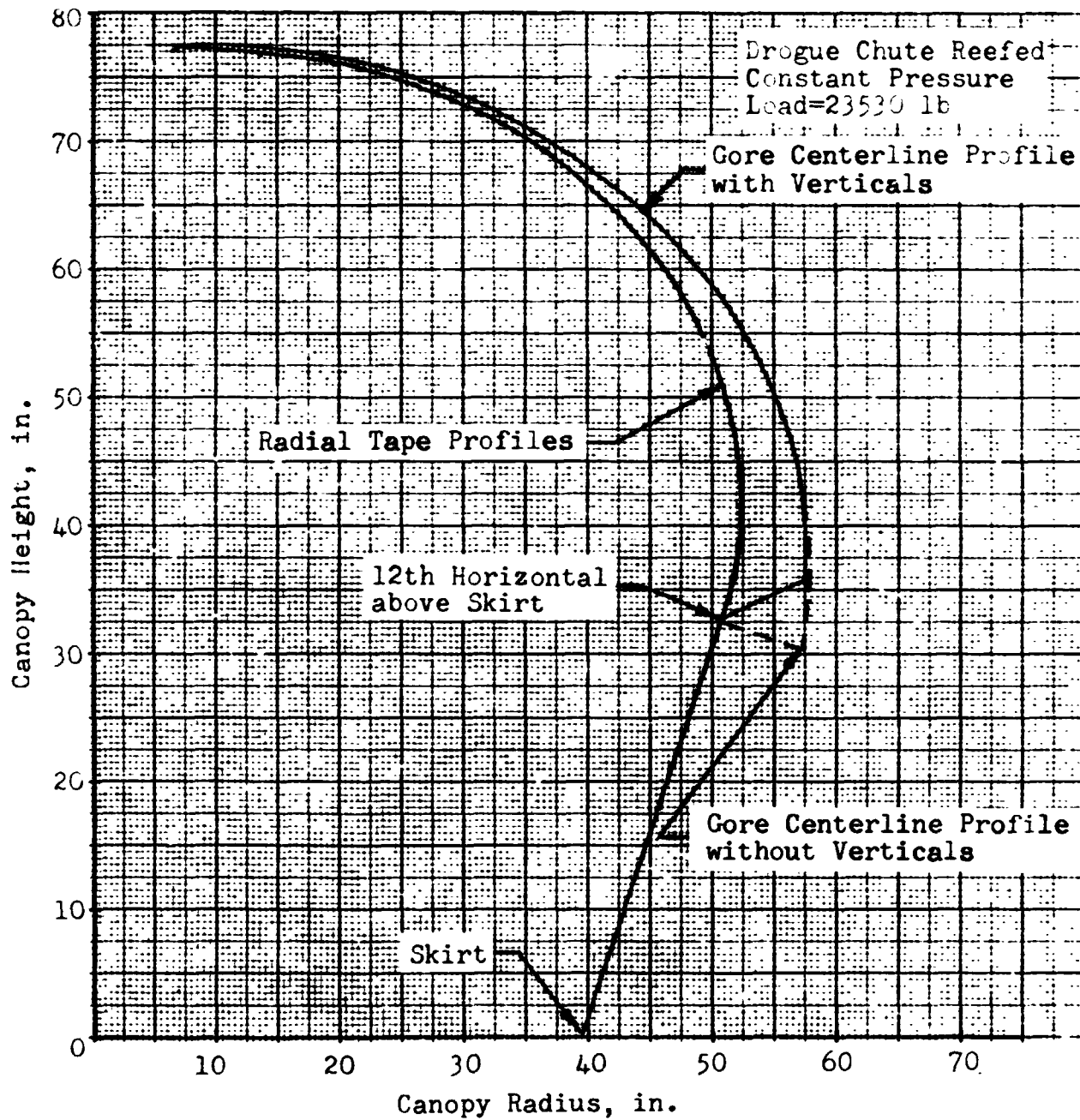
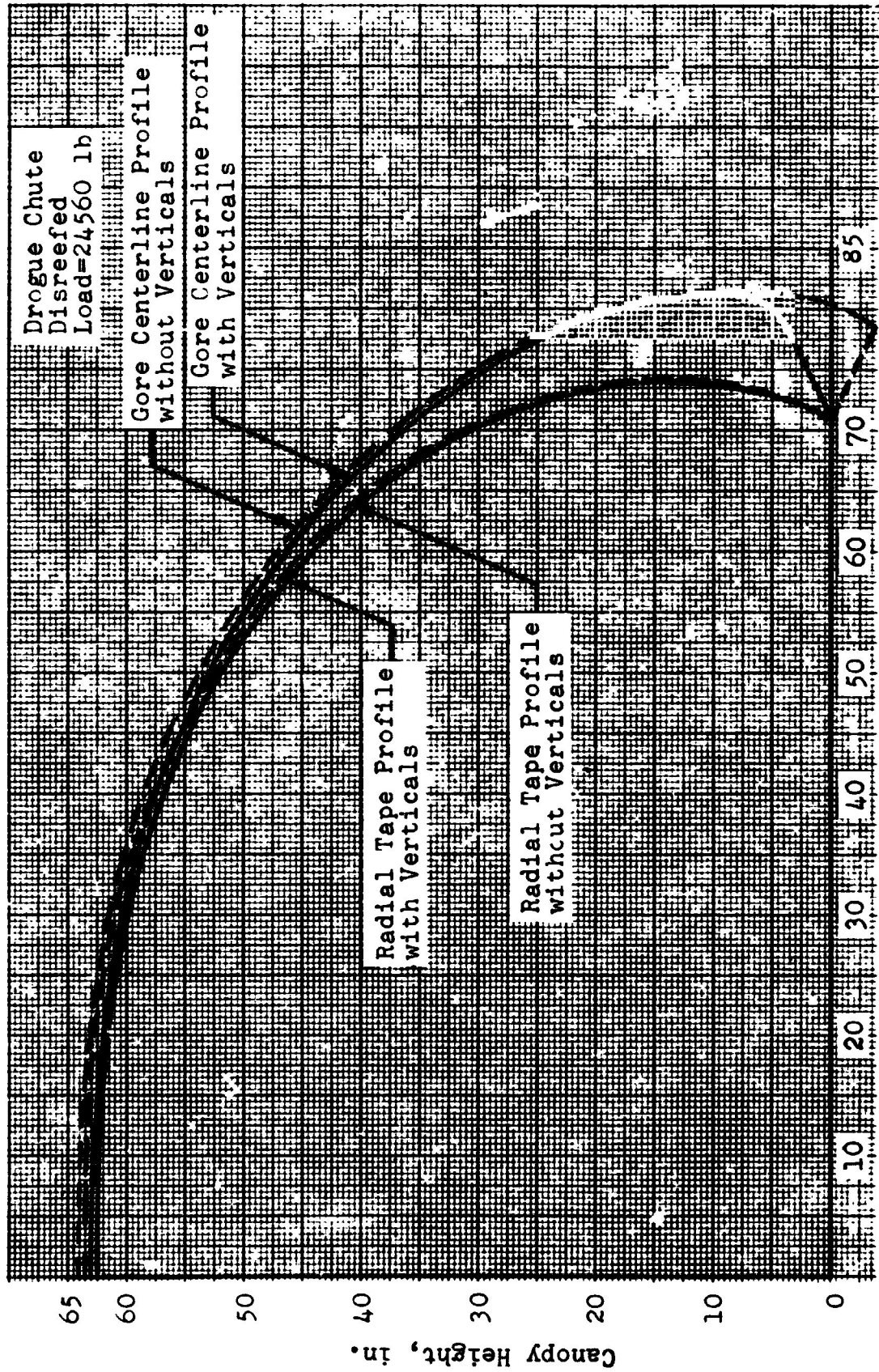


Fig. 23. Reeved Drogue Chute Profile



Canopy Radius, in.

Fig.24 . Disreefed Drogue Chute Profiles

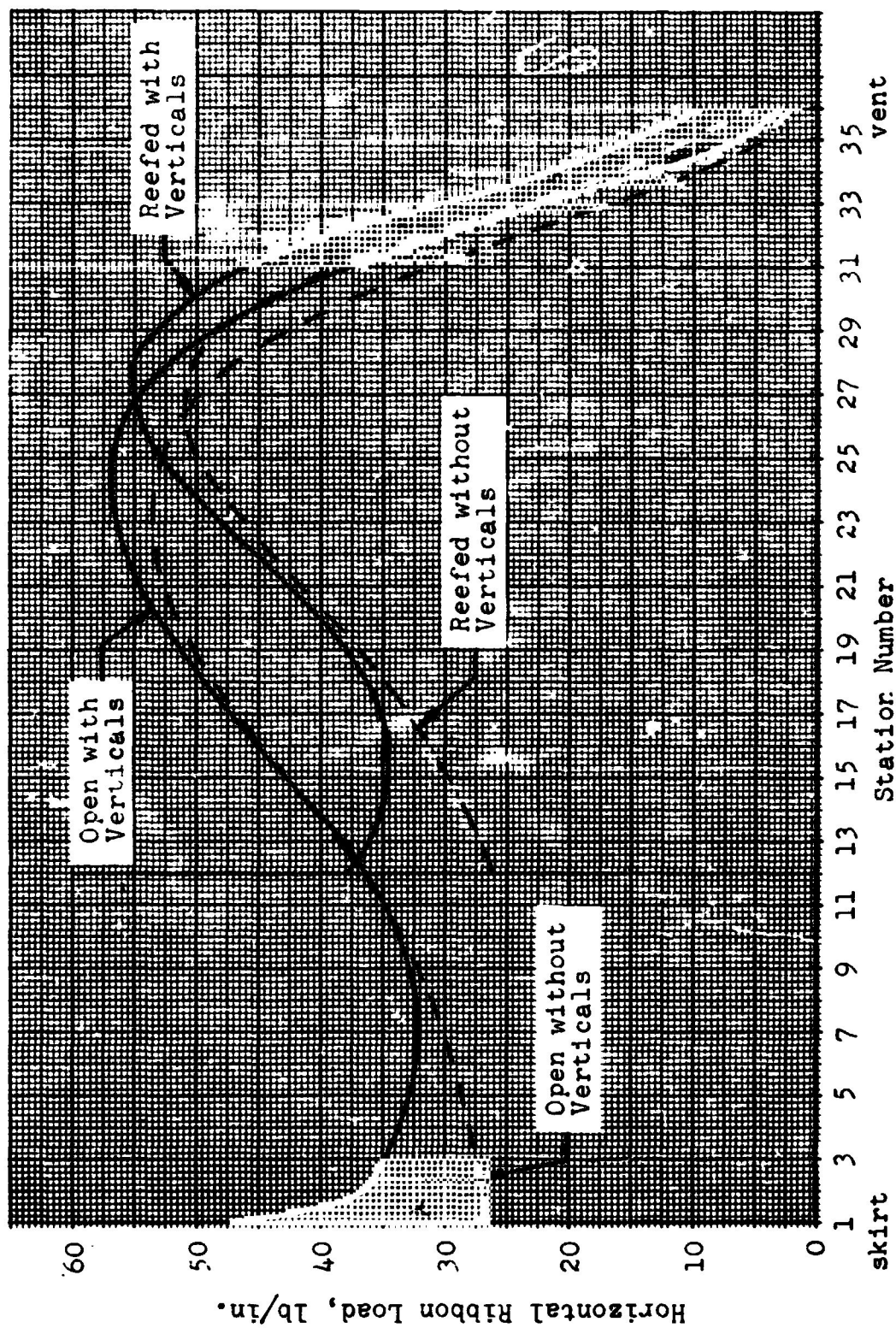


Fig. 25. Horizontal Ribbon Loading for Reefed and Open Drogue Canopies

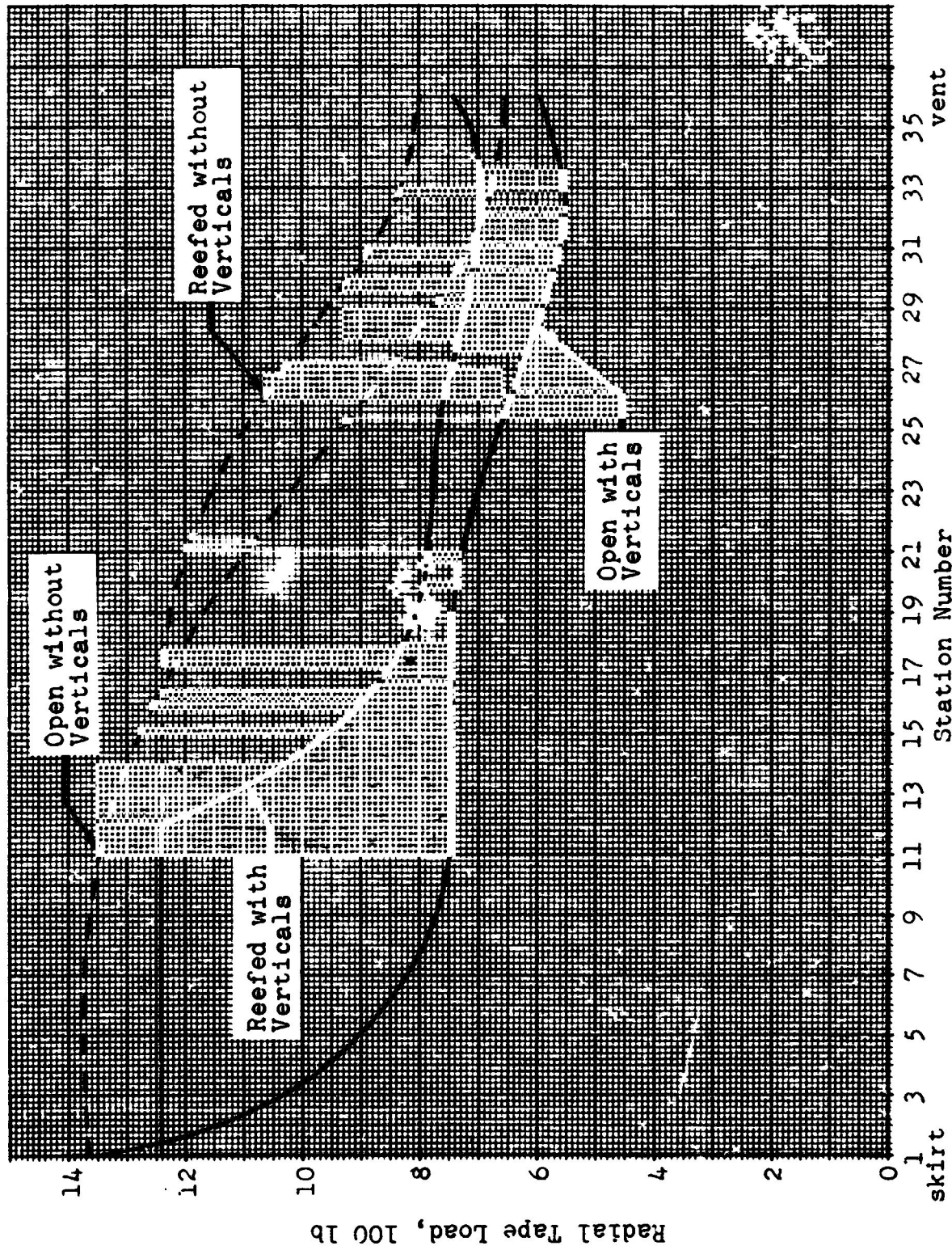


Fig. 26. Radial Tape Loading for Reefed and Open Drogue Canopies

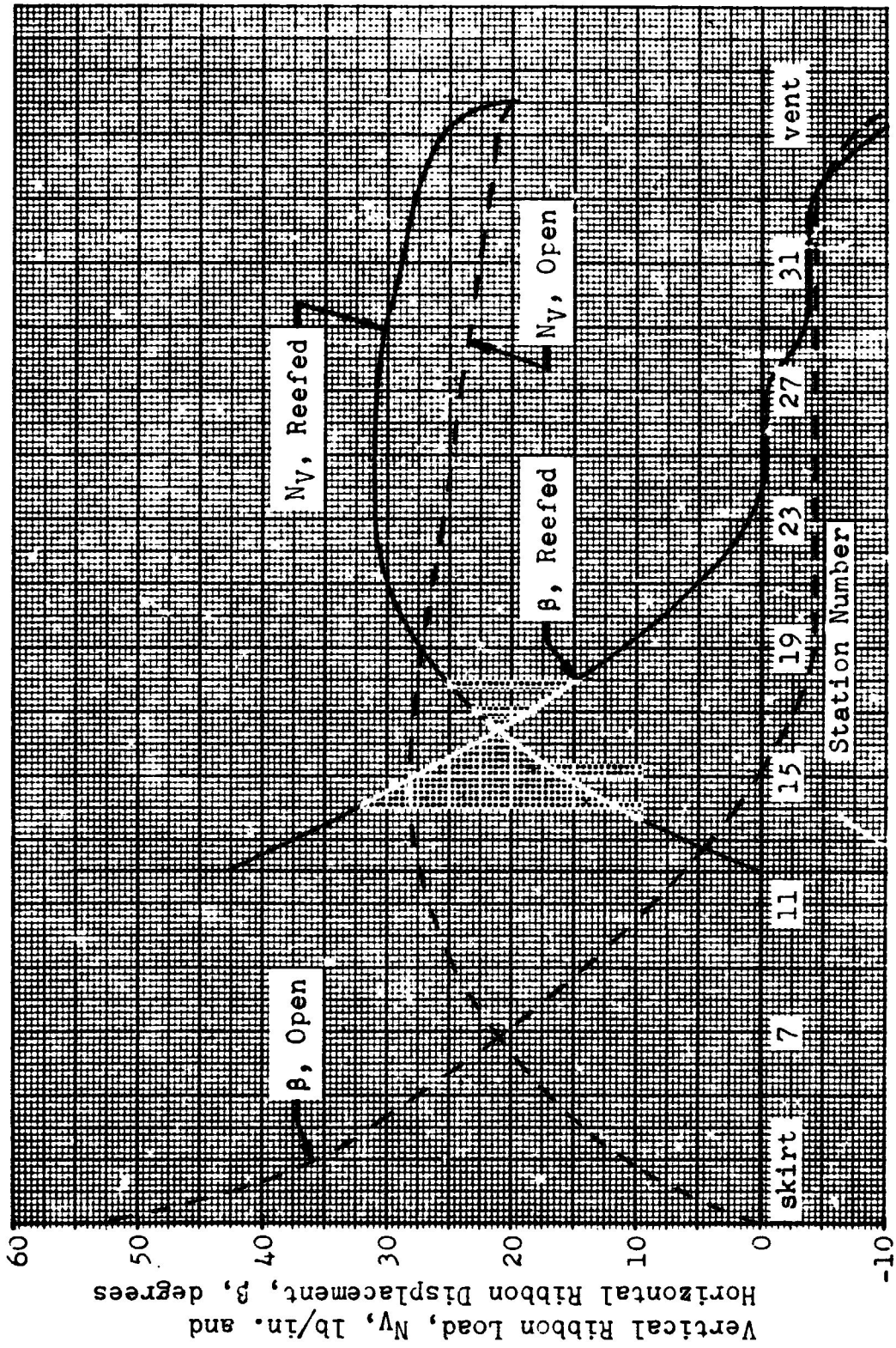


Fig. 27. Vertical Ribbon Loading and Horizontal Ribbon Displacement for Reefed and Open Drogue Canopies

4.2 PILOT PARACHUTE

4.2.1 Pilot Parachute Structural Model

The pilot parachute has a twelve gore, ringslot canopy that is constructed as shown in Figure 28 . A typical gore consists of five sails (42 lb/in cloth), three verticals (2-70 lb tapes), vent band and skirt band. The leading and trailing edges of the sails are reinforced by 0.6 inch wide seams. The radials are reinforced by a 250-lb tape extending from the skirt to the trailing edge of Sail 4. The drag area of the canopy is controlled by an overinflation line which is attached to radial tape loops below the skirt. All meridional load in the canopy is assumed to be taken by the radial tapes and the effect of the vertical members is neglected.

4.2.2 Pilot Parachute Pressure Distribution

Pressure distribution data has been obtained from wind tunnel tests of ringslot canopies by Melzig²⁰ . The pressure distribution shown in Figure 29 was derived from this data. The predicted shape and internal loads for this design ultimate riser load of 4185 lb and this pressure distribution were computed by means of program CANO. Figure 30 shows that the maximum load to strength ratio for the sails occurs in the middle of Sail 3 at a value of 0.664. Also shown in this figure is the variation in hoop load from skirt to vent. The hoop load is largest at the leading and trailing edges of the sails. Due to the increased strength in these areas (three plys of fabric in the leading and trailing edge seams) the ratio of hoop load to rated strength is lower than at the center of the sail panel. Figure 31 shows the variation of radial tape load from skirt to vent. Maximum radial tape loading of 433 pounds occurs eight inches above the skirt.

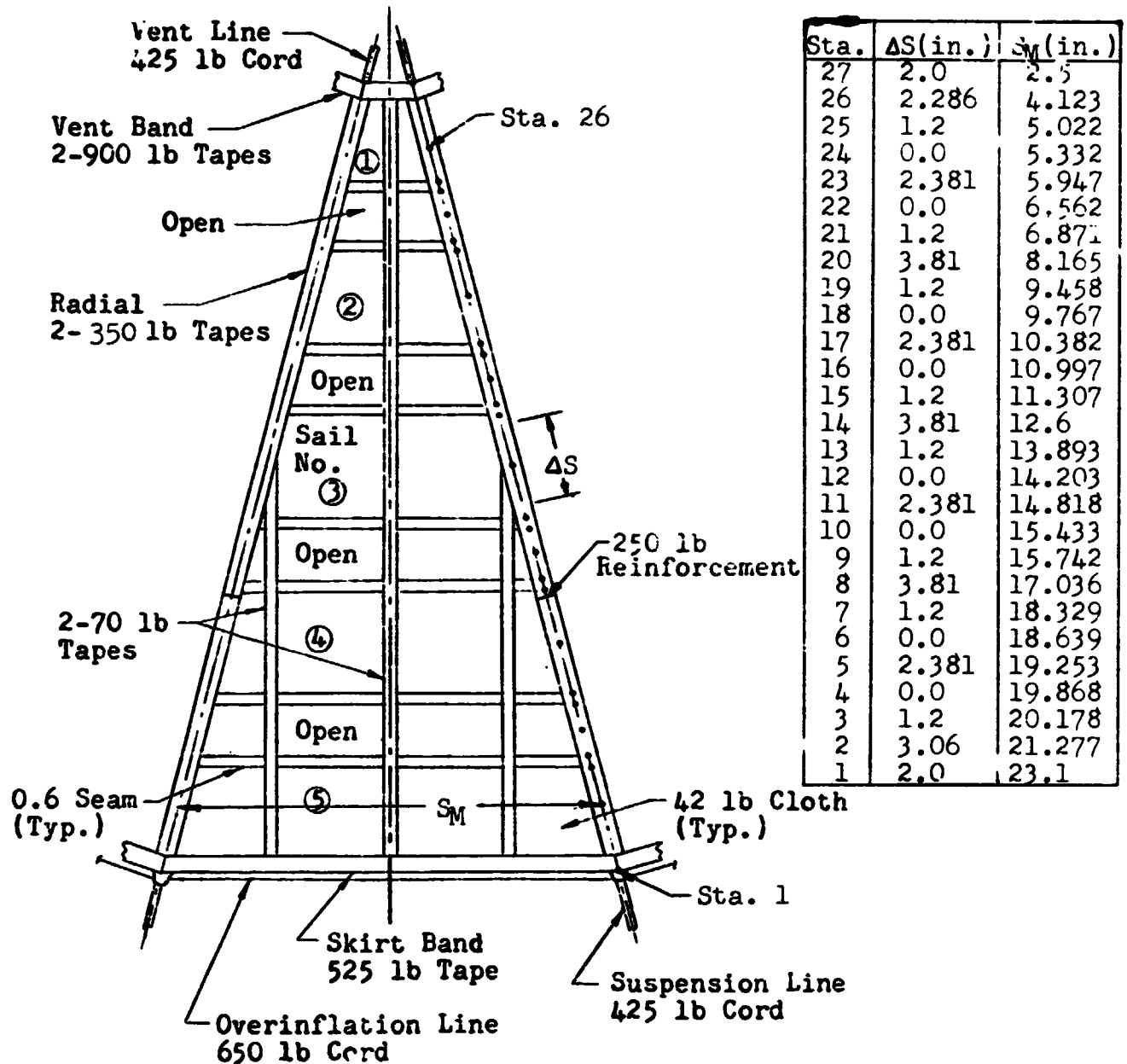


Fig.28 . Pilot Chute Structural Model

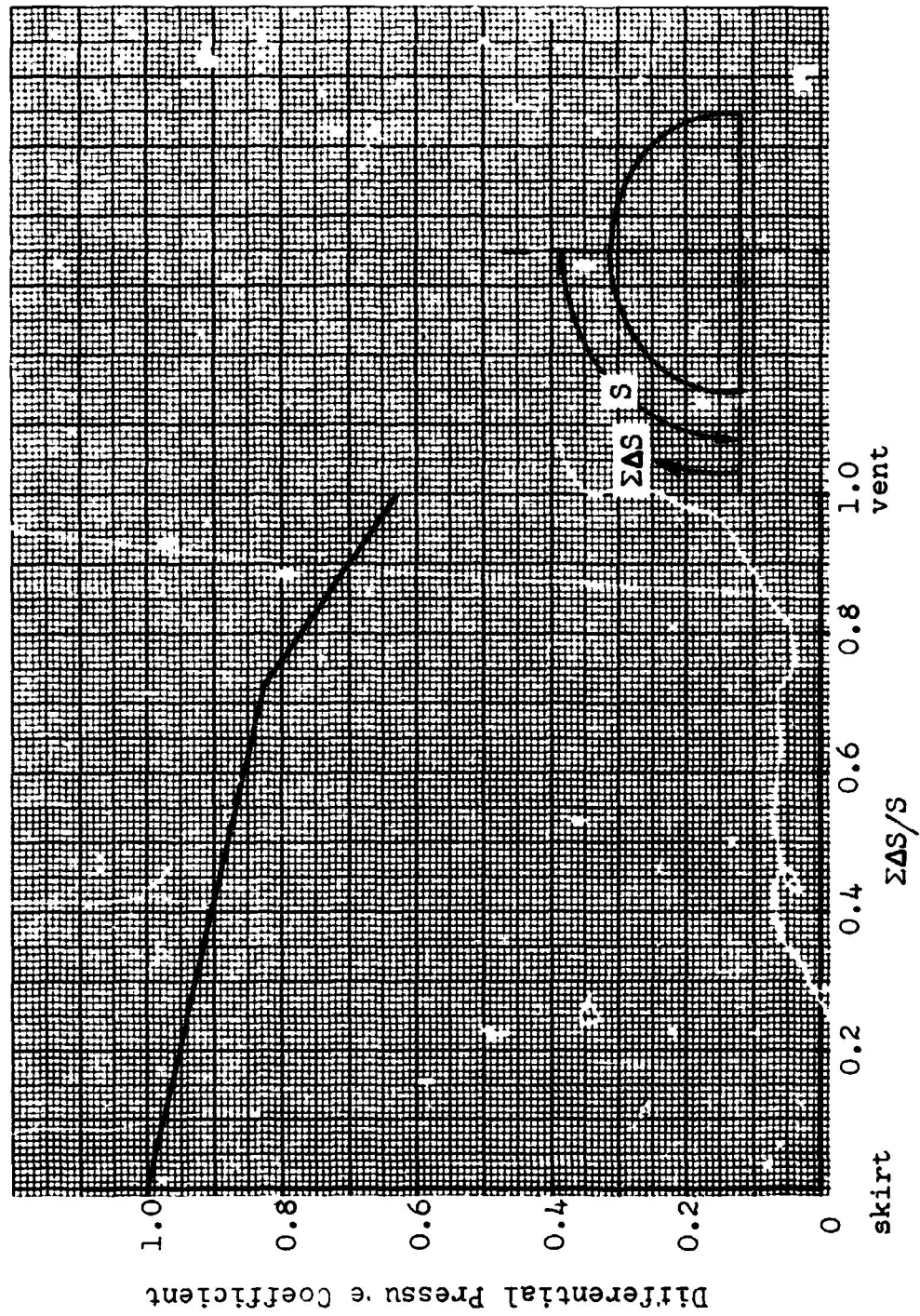


Fig. 29. Canopy Pressure Distribution for the Pilot Parachute

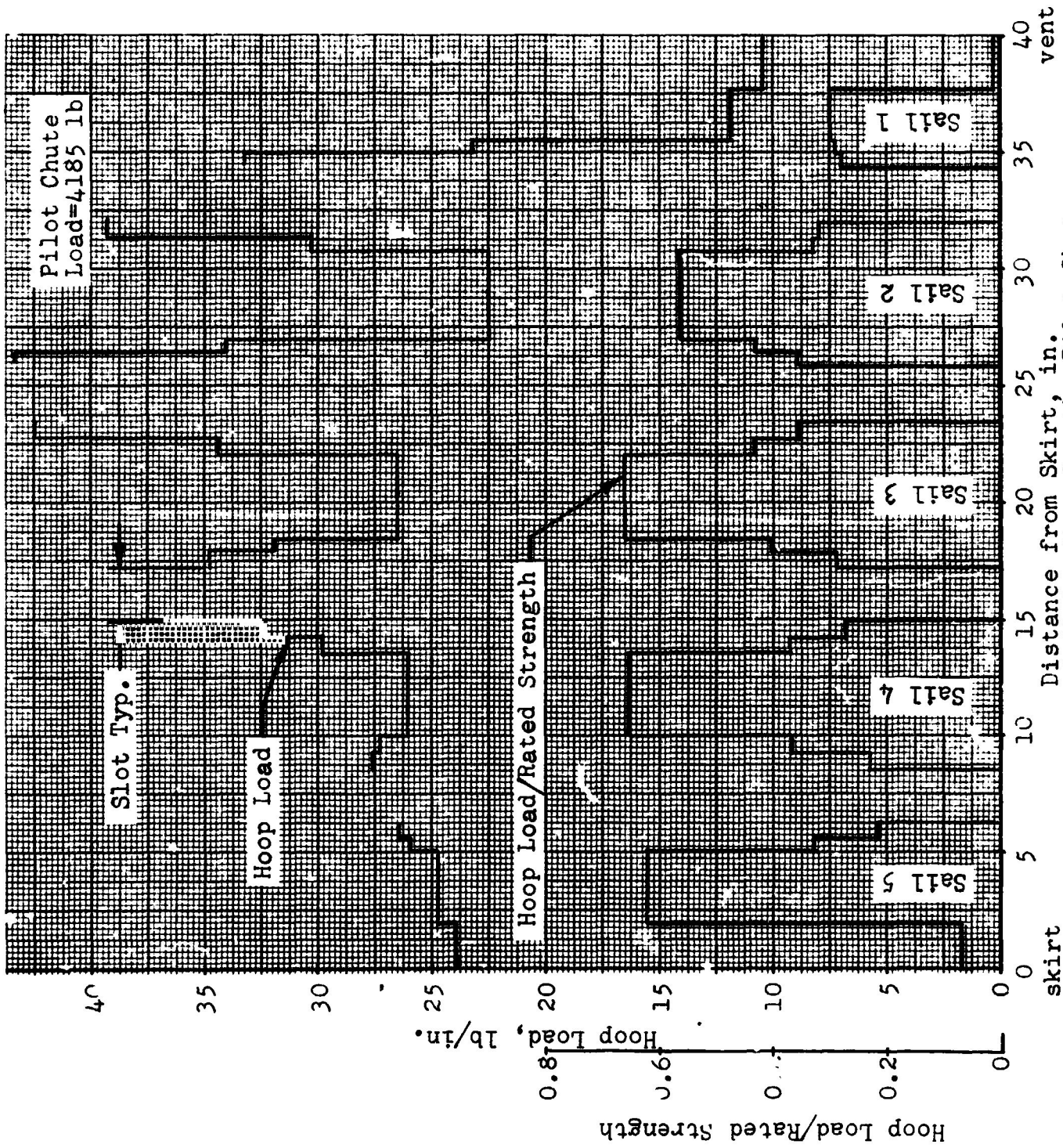


Fig. 30. Sail Loading for the Pilot Chute

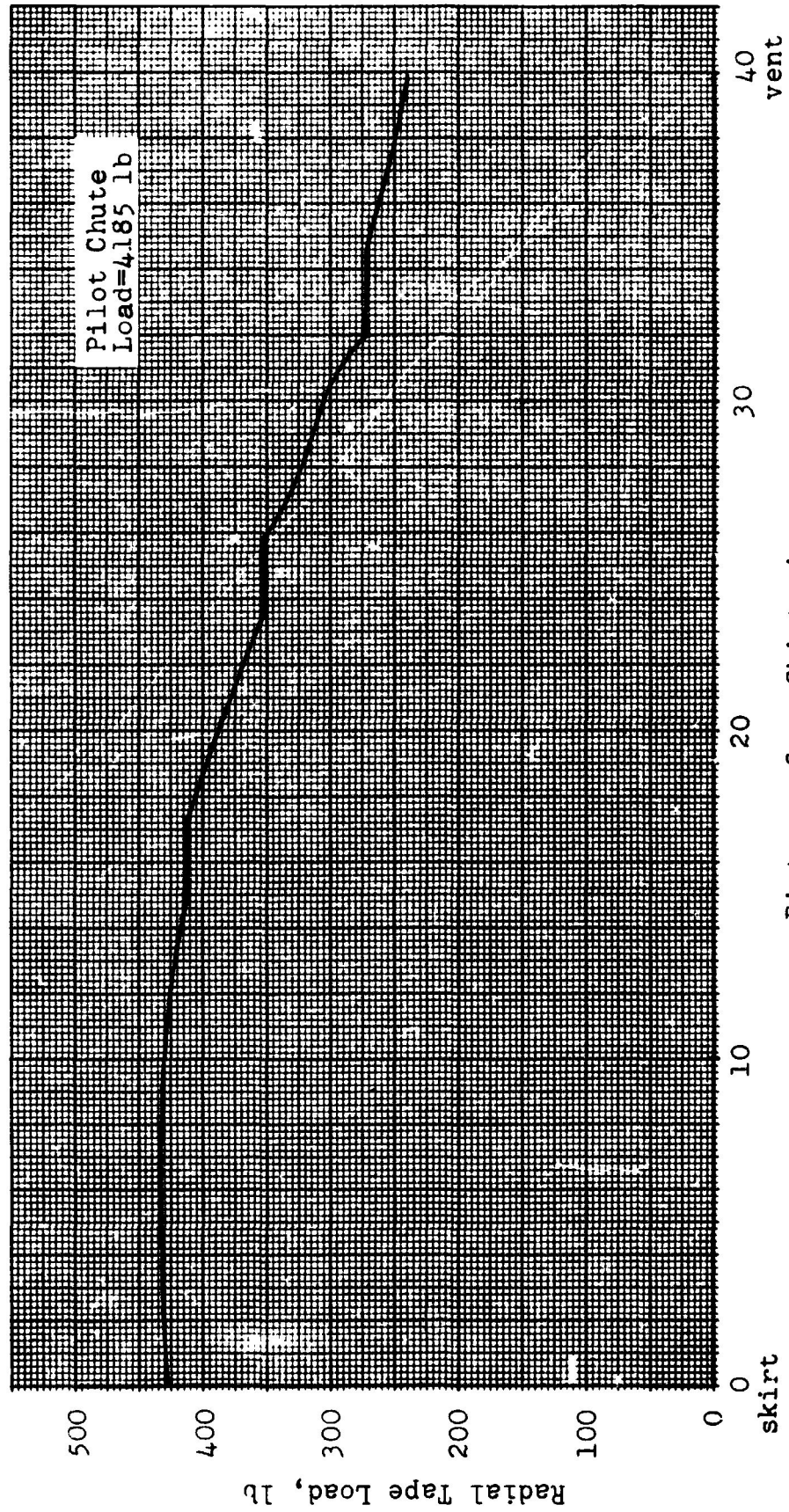
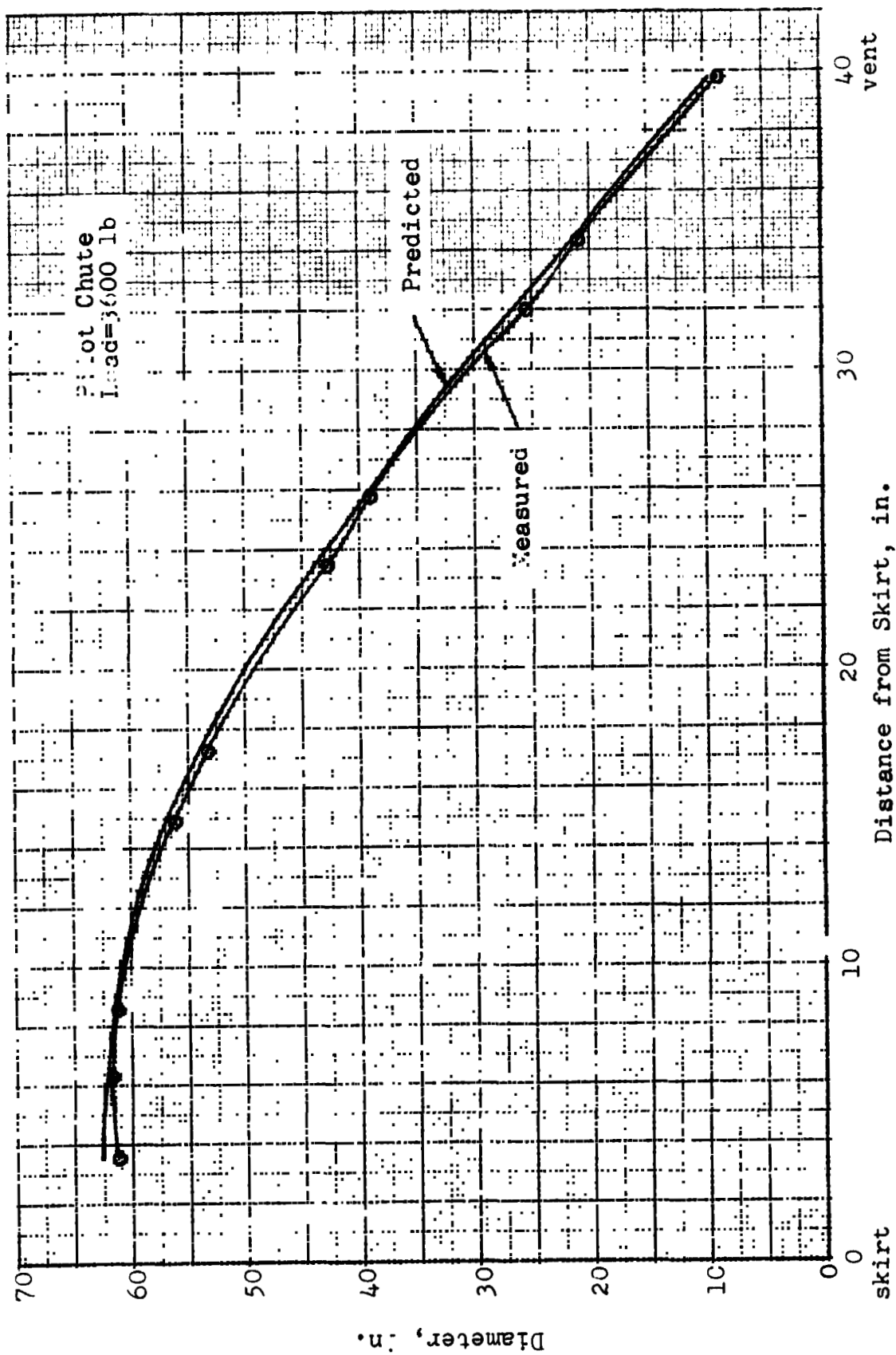


Fig.31 . Radial Tape Loads for the Pilot Chute

4.2.3 Pilot Parachute Film Analysis

In order to verify the analysis used to predict the internal loads in Figures 30 and 31, a comparison of predicted and measured canopy shapes is made. The air-to-air and ground-to-air photographic coverage is inadequate for canopy measurements. Onboard coverage is used to compare canopy diameters as a function of the distance from the skirt. Figure 32 shows a comparison of predicted and measured canopy diameters for the pilot chute at a load of 3,600 pounds. The photograph used was taken just as the main parachute pack was lifted from the vehicle. Load traces indicate that the pilot chute had an axial load of 3,600 pounds at this time. The close correlation of the predicted and measured canopy shapes supports the internal load analysis of Section 3.1.



-g. 32. Comparison of Predicted and Measured Canopy Shapes for the Pilot Chute

4.3 MAIN PARACHUTE

4.3.1 Structural Models of the Main Parachute

The construction of the main parachute requires an elaborate model to reasonably simulate the nonuniform geometry and stiffness. Such features as sail fullness and reinforcing bands are represented in the model by horizontal elements with appropriate geometry and stiffness. Estimation of the width over which a heavy reinforcing member acts is problematical, but the overall solution is not overly sensitive to this modeling. Use of allowable strains rather than allowable load for stress analysis of the adjacent area gives a second check on the margins of safety. Slots are accounted for in the solution by traversing the slot segment with no change in meridional member load or slope. The canopy is reefed in two stages by reefing lines attached to the skirt band at midgore points. Main parachute construction is shown in Figures 33 and 34 and the corresponding structural model is shown in Figure 35 .

Three different models corresponding to the three major steps in the evolution of the final design are analyzed for the fully inflated condition. They differ only in the number and strength of reinforcing bands on the sails.

Version 513 has additional tapes added to the trailing edges of sails, numbers 5 through 10. Version 519 has additional rip-stop bands at the trailing edges of Sails 5, 9 and 10.

Solutions obtained for the three versions under identical loading conditions give an insight into the effect of the reinforcing bands on the internal load distribution. In Figure 36 , a comparison of the ratio of applied load to rated strength of the sails for the three versions is given. It is seen that in addition to providing additional strength locally, the bands reduce the load in adjacent areas by reducing the overall diameter of the canopy. The critical areas which occur at the trailing edges of the sails with leading edge fullness give the highest

peaks. The trailing edges of Sails 7, 8, 9 and 10 are the critically loaded horizontal members.

Sail 8 trailing edge has a load-to-strength ratio of 0.55 for the 507 version. If this member had an efficiency of 55 percent, a failure would be predicted at an axial load of 32,800 pounds. The addition of reinforcing tapes to the parachute to form the 513 version reduced the load to strength ratio at the trailing edge of Sail 8 to 0.45. If this area remained critical in the parachute, the axial load capability of the 513 parachute would be increased by ten percent over the 507 version. However, the trailing edge of Sail 9 is seen to be critical for the 513 version with a load to strength ratio of 0.51.

The load to strength ratio for Sail 9 in the 519 version is reduced to 0.24 by the addition of two 1200-pound tapes to the trailing edge. The failure analysis in Section 4.3.3 verifies the failure predictions of Figure 36 .

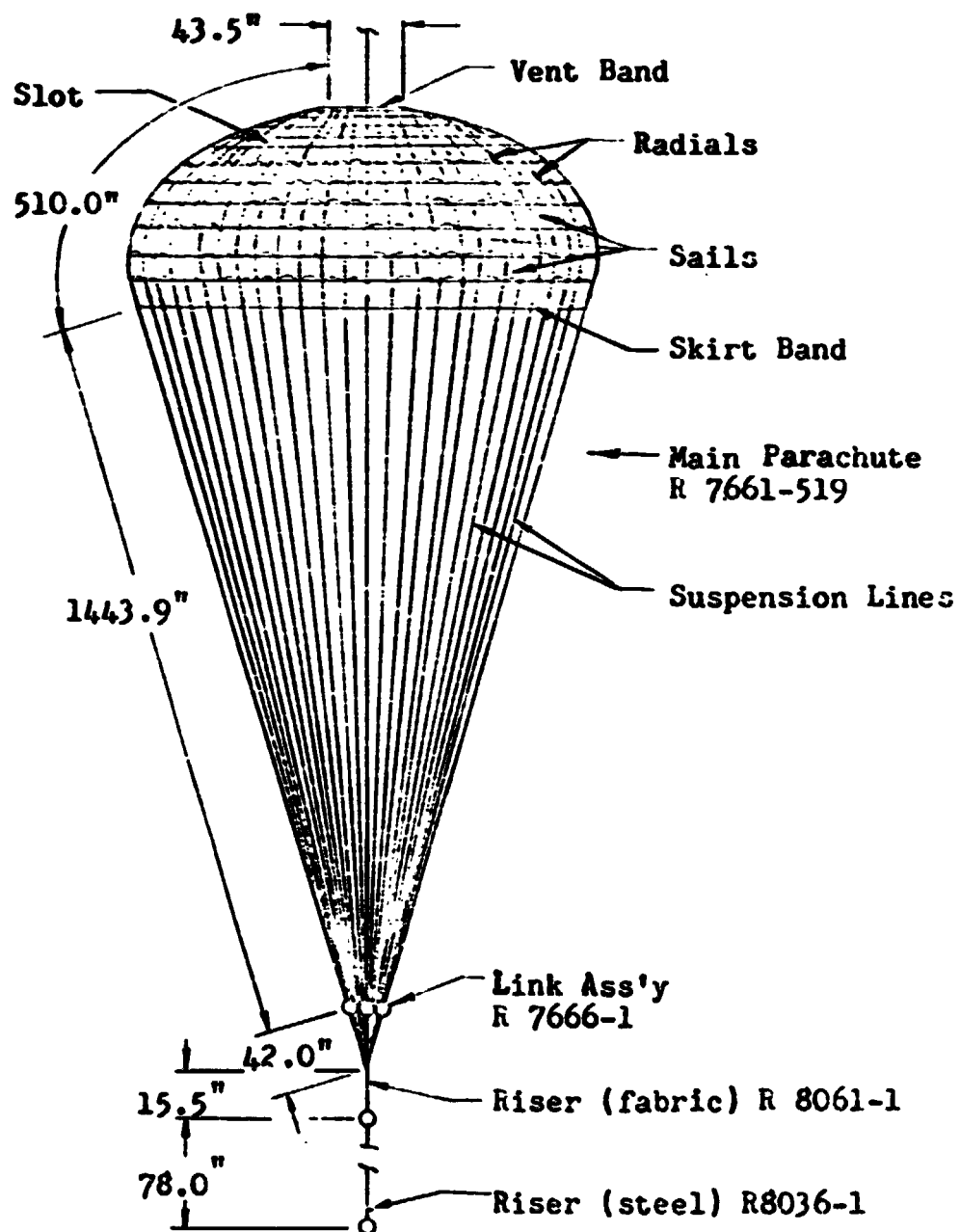


Fig. 33 Main Parachute Assembly

SECRET

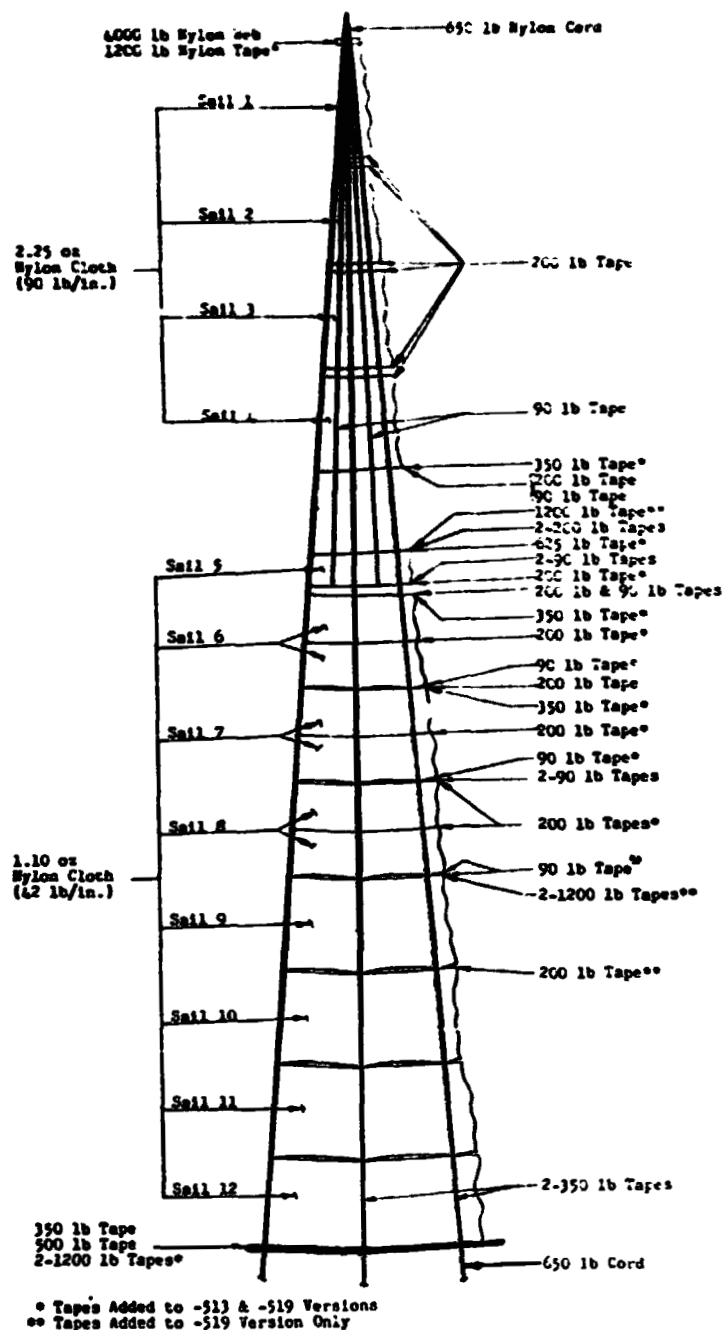


Fig. 34. Structural Details of the Main Parachute Canopy

NORTHROP

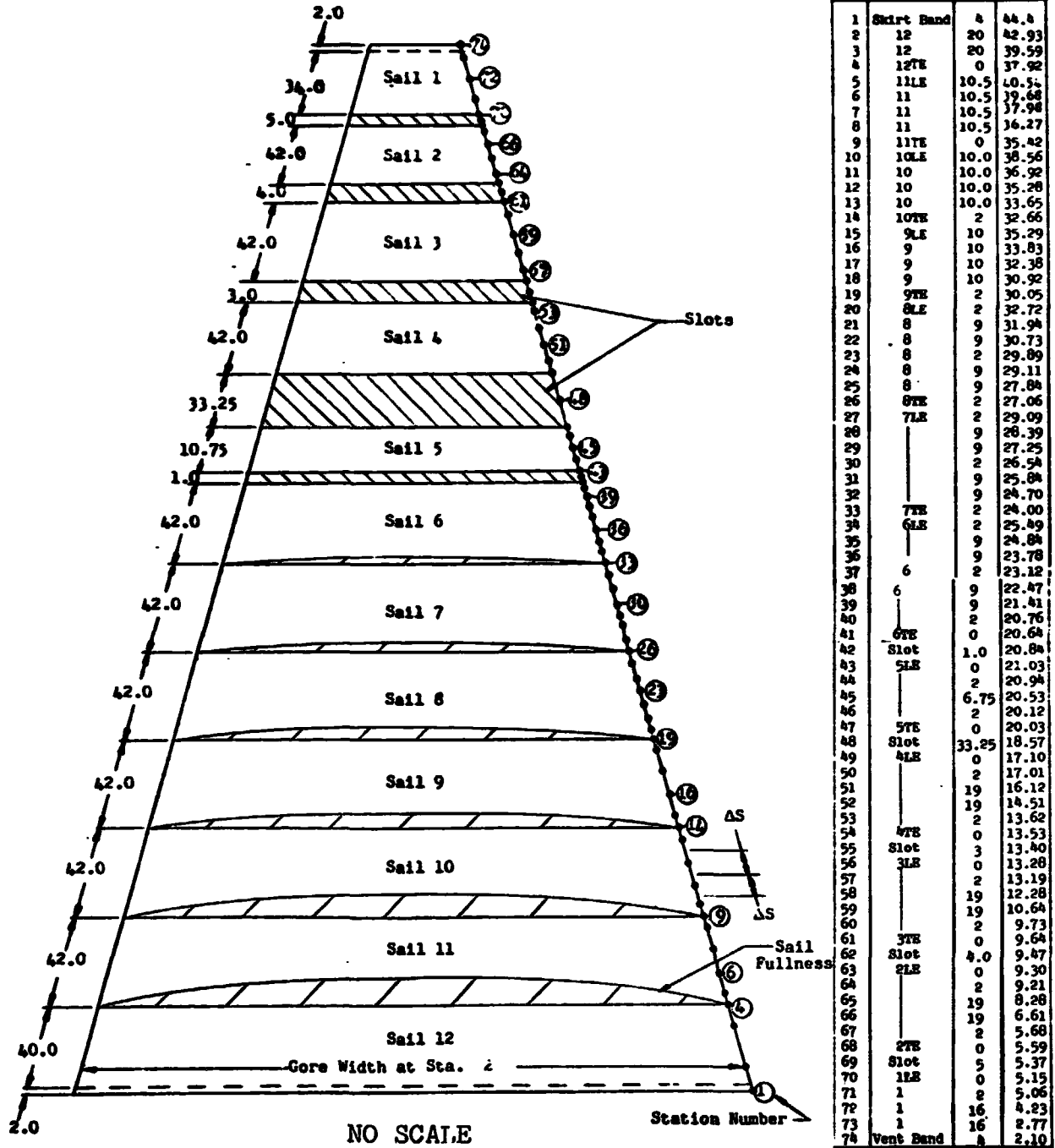


Fig. 35 . Main Parachute Structural Model

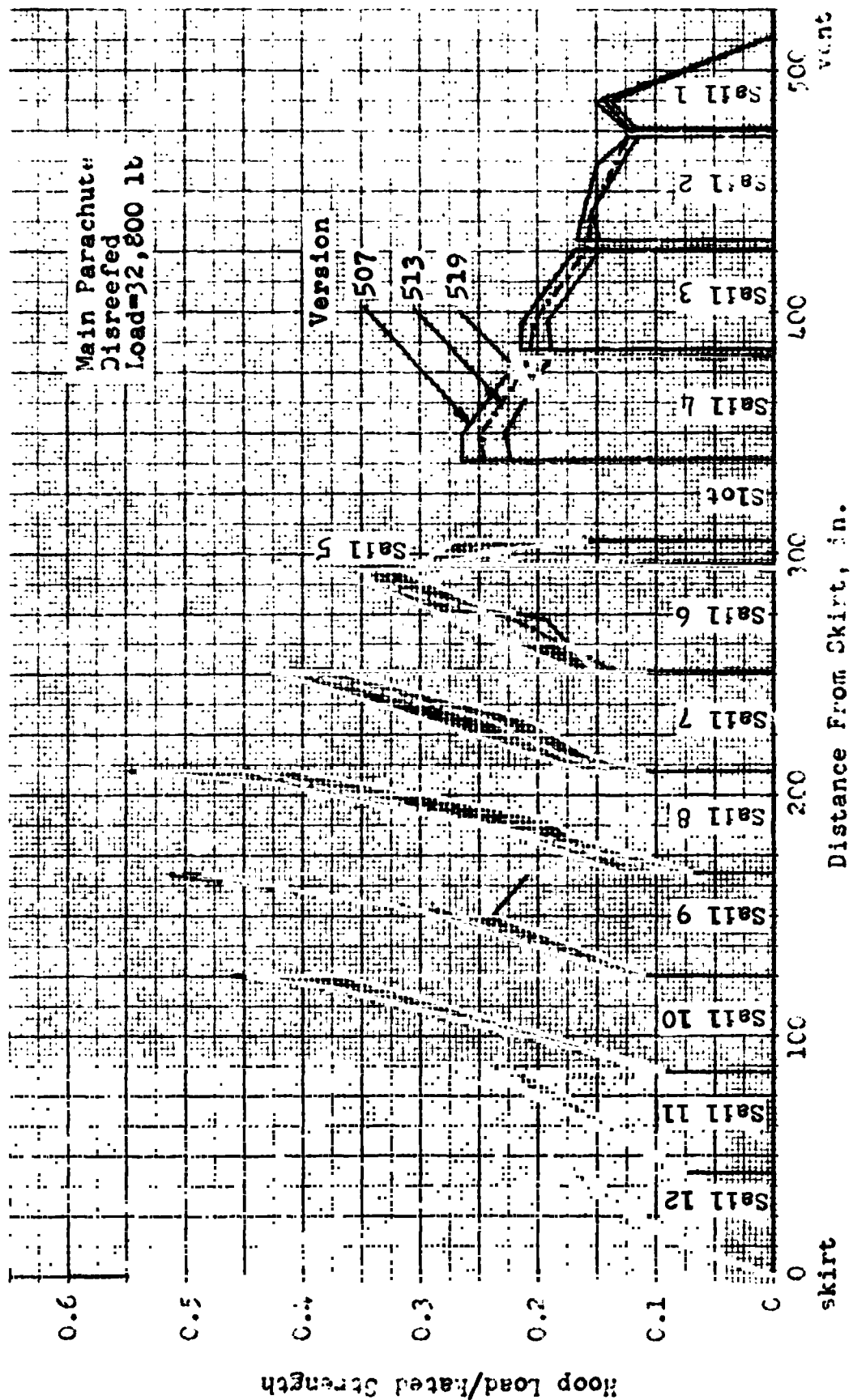


Fig . 36. Sail Load-Strength Ratio For Main Parachute

4.3.2 Main Parachute Failure Analysis

Several versions of the R7661 main parachute were tested during the evolution of the final design. For this analysis these versions are analyzed in three groups. The versions in each group are essentially the same structurally and the groups correspond to the three versions analyzed in Section 4.3.1. All of these versions have 75 percent of Sail 5 removed.

The first generation (Group 1), consisting of versions 501 through 507, had five ultimate strength tests: Drop Tests 29-3A, 46-2, 46-1A, 46-3 and 48-4. Group 2 consisting of versions 509 through 513, had three tests at or near design ultimate load: Drop Tests 46-4, 46-5 and 70-3.

Group 3, which includes the present spacecraft configuration, consists of versions 515 through 519. This group has had three ultimate load tests in the full open condition: Drop Tests 30-2, 30-3 and 82-4.

Group 1 canopies were an early version with a minimum of sail edge reinforcements (See Figure 34). Using the analysis of Section 4.3.1, together with appropriate joint efficiency and design factors (net efficiency = 0.52), gives a predicted ultimate strength 31,100 lb, with failure starting at Sail 8. Of the five tests, three are considered nonrepresentative because of the following reasons: In Test 46-1A, the parachute was overloaded to 33,900 lb in the reefed condition, which probably damaged critical joints. In Tests 46-3 and 48-4, Sail 8 failed by splitting along the gore centerline. Since the radial seam joint is normally weaker than the base material, this type of failure indicates that the sail cloth was damaged in this area.

Post test examination of the parachutes used in Tests 29-3A, 46-1A and 46-3 revealed creases and small splits along the gore centerlines of several sails. This damage was attributed to improper packing procedures. In the remaining two tests of Group 1, canopy failures occurred at loads of 27,600 lb in Test 29-3A and 35,050 in Test 46-2. These values vary about 13 percent from the predicted failure load of 31,100 lb.

The first two tests of Group 2 canopies show good agreement with predicted strengths. In Test 46-4 no major damage occurred at a load of 32,350 lb, and in Test 46-5 which reached a load of 35,060 lb, a gore split started at a Sail 7 radial seam. The predicted ultimate load is 33,400 lb with failure at the trailing edge of Sail 9. The failure that occurred in Test 70-3 at 22,390 lb cannot be explained by the stress analysis. Both Group 1 and Group 2 canopies had been subjected to higher loads than that which caused failure in Test 70-3. However, these higher loads were achieved by increasing test dynamic pressure, whereas in Test 70-3 a heavier test vehicle was used to achieve the high loading. The effect of the heavy test vehicle is that peak loading occurs later in the opening process, thereby increasing the loading in the lower sails. In the post test evaluation of this test, it was concluded that the canopy was structurally inadequate, and as a result, heavy reinforcing rings were added to the trailing edges of Sails 5 and 9. The separation of the pilot chute during Test 70-3 was not considered to have been an important factor at that time. In two later tests, 80-3 and 80-3R, pilot chute separation preceded failure by gore splitting at near limit load (reefed). Although the mechanics of the relationship cannot be determined with the information available, it is believed that these failures were related in Test 70-3.

NORTHROP

Group 3 canopies have heavy "rip stop" bands on Sails 5 and 9, which increase the load required to start gore splitting, and also prevent any splits which might result from deployment damage from propagating to canopy collapse. The predicted load for sail failure is approximately 40,000 lb for Group 3 canopies, but the ultimate strength is limited to 33,700 lb by the strength of the suspension lines. This prediction is supported by the three ultimate strength tests of Group 3 parachutes. In Test 30-2 no major damage occurred at 32,840 lbs. In Test 82-4 the three suspension line breaks which occurred at 32,200 lb were attributed to deployment damage in post test evaluation. In Test 30-3 catastrophic failures of suspension lines and radial tapes occurred at 34,300 lbs.

A summary of the main parachute failure analysis is presented in Table 2.

Table 2. Main Parachute Failure Analysis

Parachute Version	Test No.	P ₀ Measured Load	Test Damage or Failure Mode	Predicted Ultimate Load	Predicted Failure Mode
-501	29-3A	27,660 †	Gore split beginning at Sail 7 radial seam	31,100	Gore split starting at Sail 8
-501	46-2	35,050	Gore split beginning at Sail 8 centerline	31,100	Gore split starting at Sail 8
-501	46-1A	23,580*	Gore split beginning at Sail 7 radial seam	31,100	Gore split starting at Sail 8
-507	46-3	27,730*	Gore split beginning at Sail 8 centerline	31,100	Gore split starting at Sail 8
-507	48-4	27,300*†	Gore split beginning at Sail 8 centerline	31,100	Gore split starting at Sail 8
-509	46-4	32,350	No major damage	33,400	Gore split starting at Sail 9
-509	46-5	35,060	Gore split beginning at Sail 7 radial seam	33,400	Gore split starting at Sail 9
-513	70-3	22,390 *	Gore split beginning at Sail 9	33,400	Gore split starting at Sail 9
-515	30-2	32,840	No major damage	33,700	Suspension line failure
-515	30-3	34,350	Suspension line failure	33,700	Suspension line failure
-519	82-4	32,200	Suspension line failure	33,700	Suspension line failure

* These tests are believed to be nonrepresentative because of unusual conditions as follows:

46-3 and 48-4: Failure started at gore centerline rather than at the radial seam, which should have lower strength. Post test examination revealed slits along the center of several intact sails, believed to be caused by improper packing.

46-1A: Parachute was overloaded to 33,900 lb in the reefed stage. This probably damaged critical joints.

70-3: Failure of the main parachute bridle caused separation of the pilot chute. In Tests 80-3 and 80-3R, pilot chute separation preceded failure by gore splitting at near limit load. It is believed that the canopy failure in Test 70-3 was also caused by the separation of the pilot chute, although the mechanics of the causality cannot be determined with the information available.

† 29-3A and 48-4 were two chute cluster tests. The unsymmetrical shapes developed due to aerodynamic interference may increase local loading by more than the 1.05 factor used in the analysis to account for unsymmetrical loading. Lack of data from cluster tests at ultimate load precludes making a quantitative evaluation of this factor.

4.3.3 Main Parachute Pressure Distributions and Film Analysis

Pressure distribution data for reefed parachutes are not available. In the stress analysis of the Apollo Earth Landing System, it was assumed that the pressure distribution at peak riser load was uniform. This study shows that pressure distributions can be approximated by comparing predicted and measured canopy profiles.

A review of the Apollo Drop Test film coverage failed to produce adequate profile views of the reefed main parachutes at the time of peak loading. Two usable profiles were found, however for the parachute in steady state descent.

A profile of the first stage reefed canopy was found in air-to-air coverage of Drop Test 46-1A. By using the widths of the slot and a sail panel as reference lengths, dimensions of the canopy were calculated from the photographic image. In the first stage the canopy was observed to inflate from the vent to the Sail 5 slot only. Using the leading edge of Sail 4 as a starting point, the analysis method given in Section 3.1 was used to solve for the equilibrium canopy shape. A range of pressure distributions as shown in Figure 37 is used to determine the sensitivity of the canopy profile to variations in pressure. The first stage pressure distributions have zero pressure from skirt to the leading edge of Sail 4 (66 percent of the distance from skirt to vent), linearly increasing pressure to three locations above this point, and then constant pressure to the vent. Figure 38 shows the observed first stage profile compared to predicted profiles for the three first stage pressure distributions in Figure 37. The constant pressure shape (distribution A) is seen to have a flatter profile than that observed in photographs. Pressure distribution C produces a profile that is in close agreement with the observed steady state profile.

A peak can be seen in the first stage profile at the vent. This appears to be due to the pull of the attached pilot chute. No provision has yet been made to the theoretical model to account for this affect.

Since the canopy is not critical during steady state descent, the internal load predictions are not included here. For the internal load predictions of the main parachute during the opening process, see the stress-time study in Section 4.3.4.

A profile of the second stage reefed main parachute was found on ground-to-air coverage of Drop Test 82-1R. The canopy was observed to inflate from the vent to the leading edge of Sail 8. Using this starting point, the analysis method given in Section 3.1 was used to solve for equilibrium canopy shape. The second stage pressure distributions shown in Figure 37 are used to show the sensitivity of the canopy profile to variations in the pressure distribution. The differential pressures are zero below Sail 8 (33 percent of the distance from skirt to vent), increasing linearly to three locations above the first inflated sail, and then remain constant to the vent. Figure 39 shows the observed profile compared to predicted profiles for the three second stage pressure distributions in Figure 37. Pressure distribution C produced best agreement with the measured profile but further refinement of the pressure distribution would improve this comparison. Since the steady state descent phase of the second stage is not critical, the internal load predictions are not presented here. The internal loads at the critical times in the opening process are discussed in Section 4.3.4.

Pressure distribution for the fully inflated main parachute is approximated by interpolating the wind tunnel test data taken from Reference 20 for a solid circular and a ringslot

parachute. Figure 40 shows the resulting distribution with peak pressure at the skirt. While the infinite mass condition of wind tunnel testing is considerably different from the drop test conditions being analyzed, this is the best data available, and the analysis which follows shows reasonable correlation.

It has been observed in drop test films that the parachute is not inflated to its maximum diameter at the time of peak riser load. (See stress-time analysis, Section 4.3.4). For this reason the disreefed canopy is analyzed at both the time of maximum diameter and time of peak riser load.

Figure 41 shows that the pressure distribution described above produces a good comparison of predicted and measured canopy shapes for the time of maximum diameter. The measured canopy shapes are from the onboard coverage of Drop Tests 30-2 and 32-4. The method of obtaining canopy dimensions from the photographic image is described in Section 4.1.4. Measurements of the canopy at the time of peak riser load, however, indicate a smaller canopy. By extending the pressure distributions used in the analysis of reefed canopies, the second distribution in Figure 40 was found to produce a shape that agreed with drop test measurements as shown in Figure 42. The pressure distribution indicates low pressure at the skirt, increasing linearly to a location above the skirt equal to 12 percent of the radial tape length, and then remaining constant to the vent. Internal load predictions for the canopy at the times of maximum diameter and peak riser load are presented in Section 4.3.4.

Results of this study show that the differential pressure distributions on reefed and open canopies can be approximated from photographic records of canopy shape.

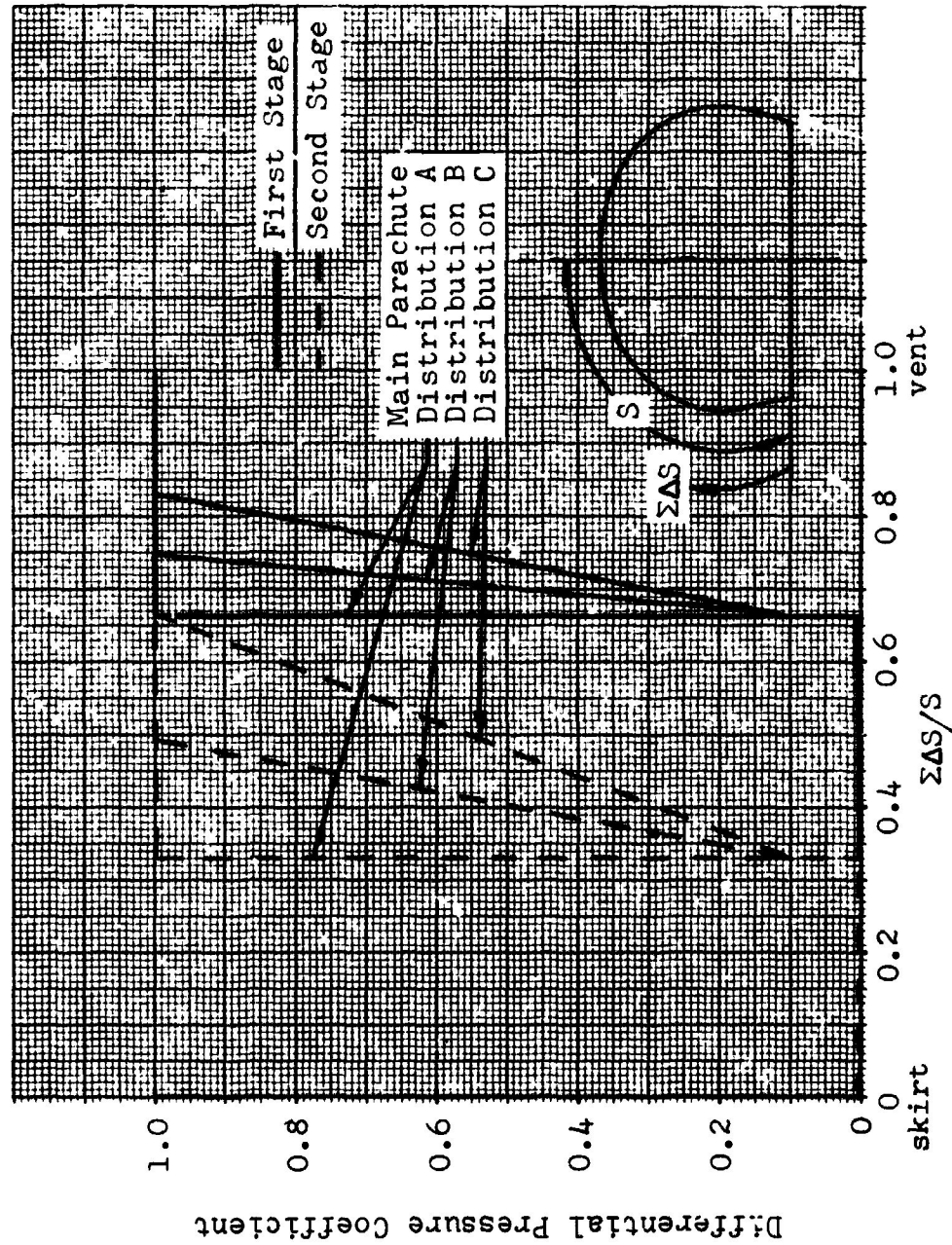


Fig. 37. Reefed Main Parachute Pressure Distributions

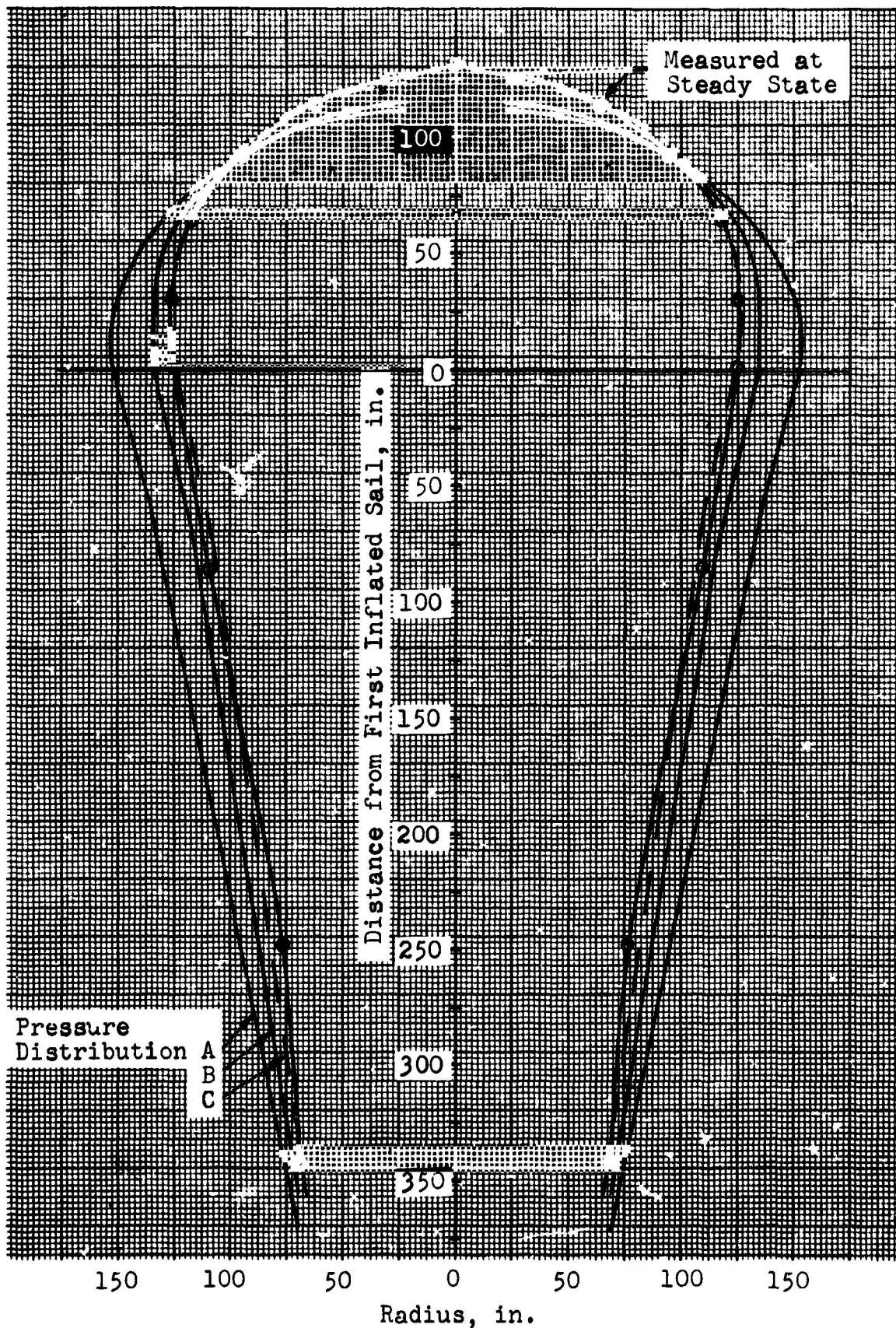


Fig. 38. Comparison of Measured and Predicted Profiles for the First Stage Reefed Main Parachute

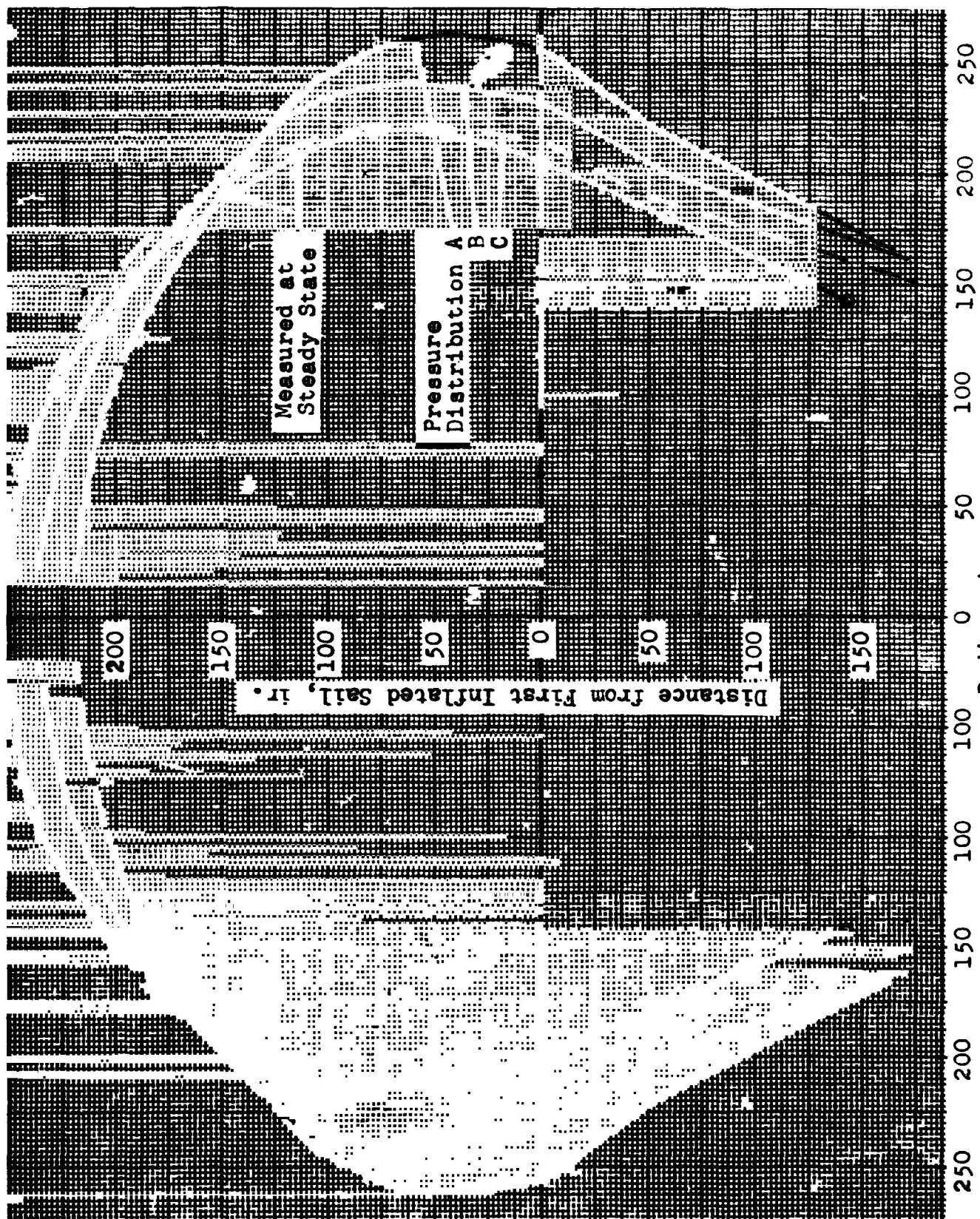


Fig. 39. Comparison of Measured and Predicted Profiles for the Second Stage Reefed Main Parachute

CONTINUED

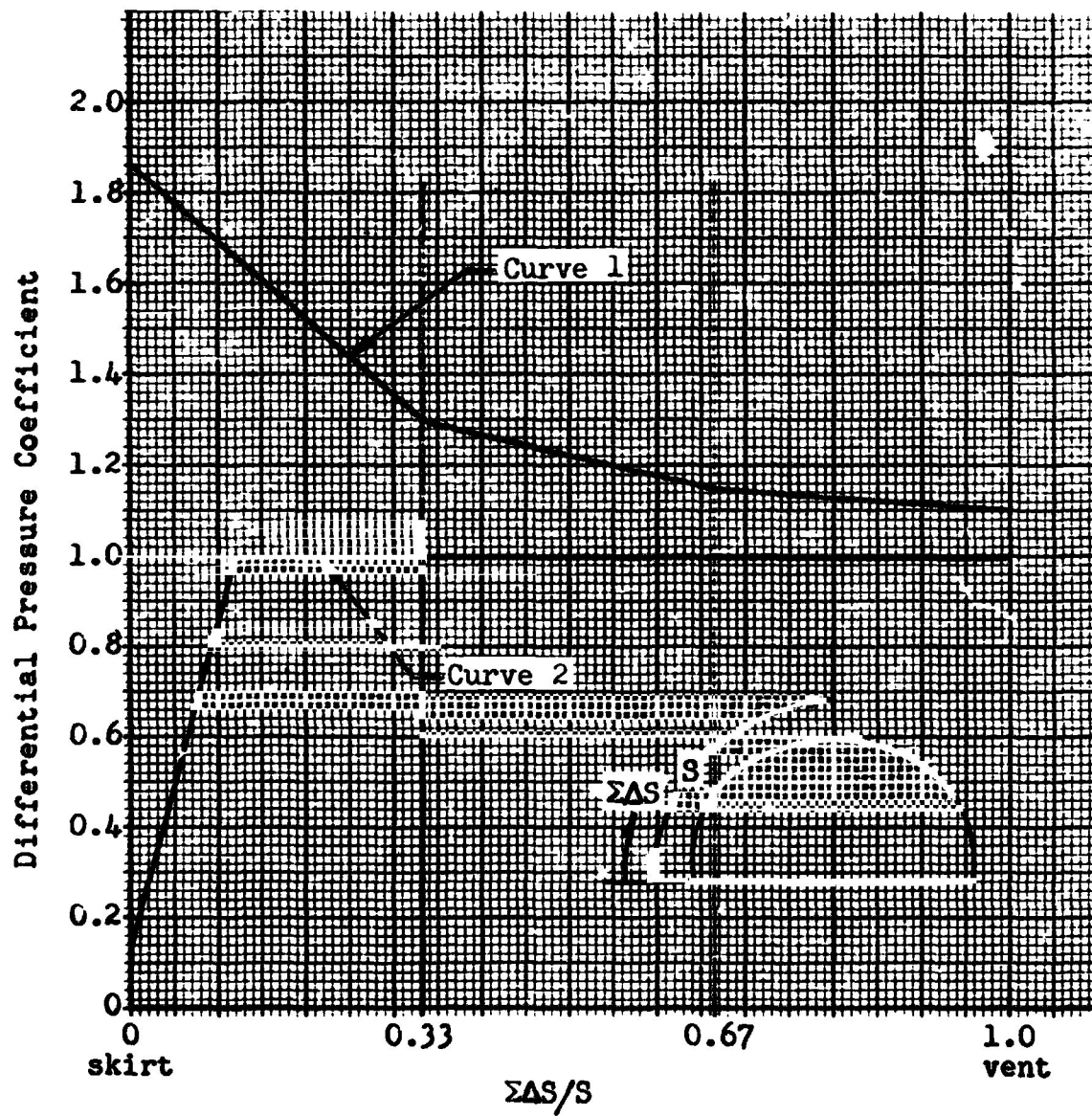


Fig. 40. Fully Inflated Main Parachute Pressure Distributions

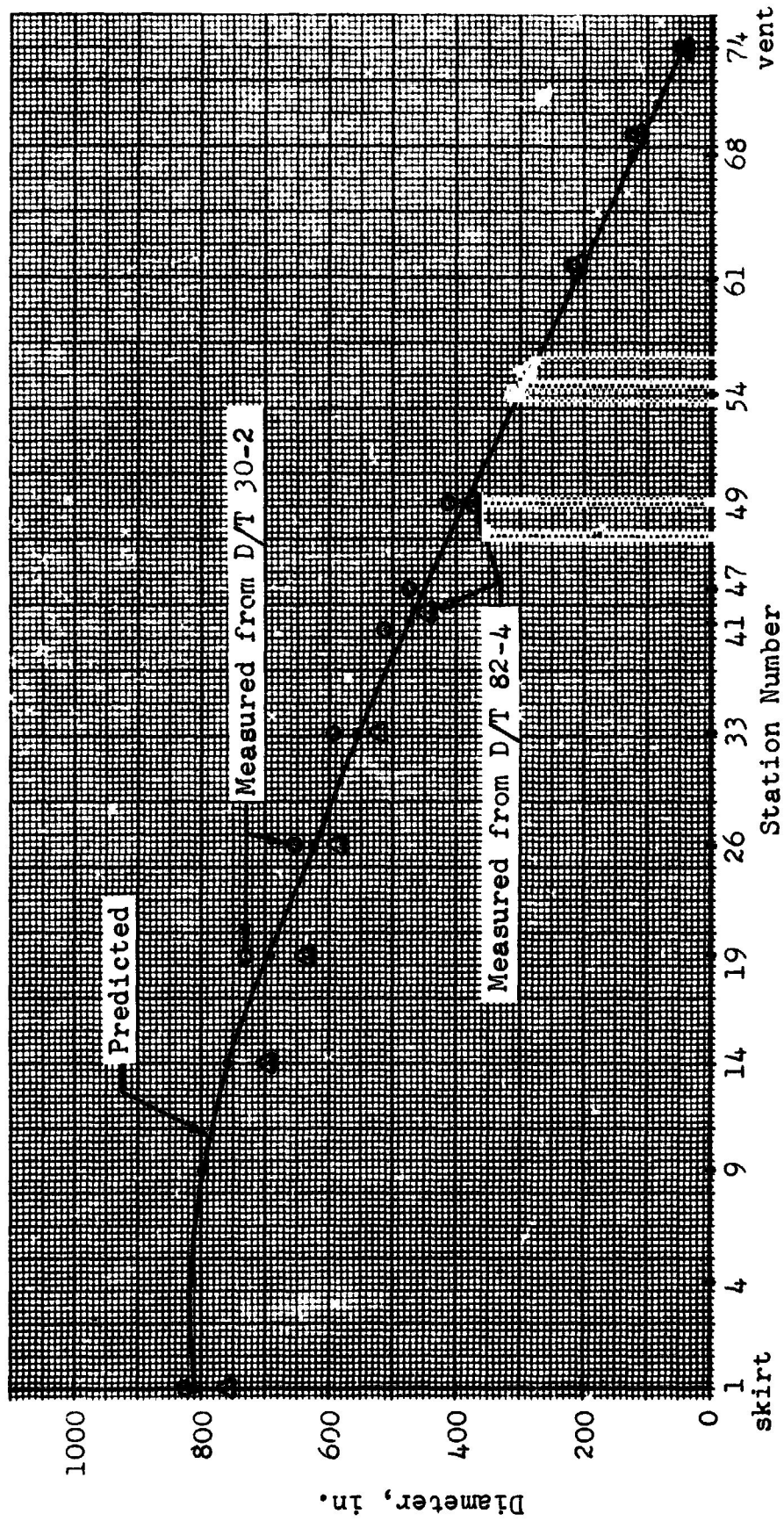


Fig. 41. Comparison of Predicted and Measured Main Parachute Diameters at the Time of Maximum Canopy Diameter

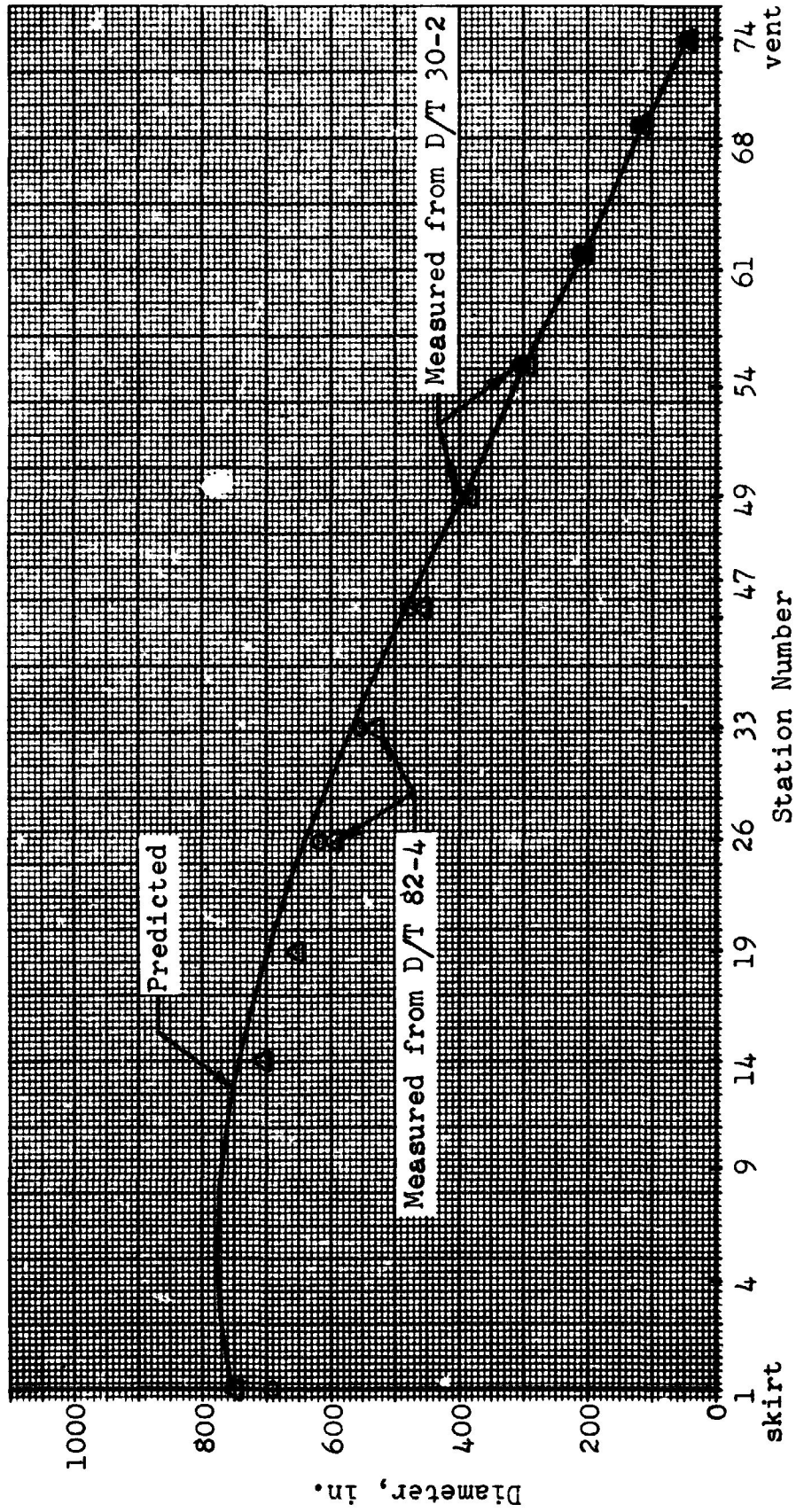


Fig.42 . Comparison of Predicted and Measured Main Parachute Diameters at the Time of Maximum Riser Load

4.3.4 Stress-Time Study of the Apollo Main Parachute

Previous analyses of the main parachute considered only three instants of the inflation process. First stage reefed, second stage reefed, and full open. It was assumed that maximum internal loading occurred at the instant of maximum riser loading for each of the three stages and that all the sails in the stage were inflated at this time. The present analysis improves the margin of safety calculations by eliminating the above assumptions.

In order to correlate analytical results with empirical evidence, the canopy is analyzed at times corresponding to the instant each sail becomes inflated. The term "inflated" is defined as the time at which a sail ceases to flutter randomly. The empirical data needed includes the riser load and pressure distribution over the canopy as each sail inflates. Photographic coverage provides the time at which each sail becomes inflated and the load-time trace gives the riser loading at each of these times. Since the parachutes were not instrumented to record pressure distribution, the canopy shapes are used to infer the pressure distribution.

Drop Test 82-2 was found to be the most acceptable test to provide the needed empirical data. The test resulted in high canopy loadings for all three stages of inflation and had good correlation between film coverage and the load trace. A comparison of test loads with design ultimate loads is given below:

<u>Stage</u>	<u>Design Ultimate</u>	<u>Max. Test Load</u>
Stage 1 Reefed	29,700 lbs	20,375 lbs
Stage 2 Reefed	32,000 lbs	32,710 lbs
Stage 3 Disreefed	30,900 lbs	28,135 lbs

The test loads at the selected times are multiplied by the ratio of the design ultimate to the maximum test load for that stage. This calculation is valid because the internal loads vary linearly over short ranges of loading as was shown in Section 4.1.3. Table 3 gives the design loads used in this study.

By using assumed pressure distributions and the design loads listed above, the internal loading at each state of inflation was calculated by computer program CANO. The computer program also calculated canopy shapes for each state of inflation. The analytical shapes were compared to measured shapes from photographic coverage of Test 82-2. If the shapes did not agree for a particular state, the pressure distribution was revised and a new computation was made. This procedure was continued until the analytical canopy shapes at each state of inflation matched the measured shapes. Figure 43 shows the pressure distributions that produced good agreement of canopy shapes.

The pressure distributions indicate that as the inflation process continues, the inflated portion of the canopy has low pressure at its leading edge, increasing to a uniform pressure over the upper portions of the canopy. The uninflated portion of the canopy is assumed to have zero differential pressure. For example, at the instant Sail 6 inflates, 49 percent of the canopy is uninflated and the leading edge of Sail 6 has a differential pressure of 0.1, increasing linearly to a point 62.5 percent of the distance from the skirt to the vent. The pressure then remains uniform to the vent. At the time of maximum canopy diameter, the pressure is maximum at the skirt. Accurate profile views of the inflating canopy would improve the assumed pressure distributions shown in Figure 43. The best photographic coverage of Test 82-2 was provided by the ground-to-air cameras. Profile views of the canopy were limited to the early states of inflation.

The shape of the canopy after first stage disreef was based on measurements of maximum diameter, skirt diameter and suspension line angle. Some error can be expected in the pressure distributions obtained by matching the analytical shape to only these three measured quantities. The actual canopy dimensions for each state of inflation were calculated by using the length of various canopy elements, such as slot width, sail width and reefing line diameter as reference lengths.

Figure 44 shows the riser load-time trace for the design loads in Table 3. Figure 45 shows the critical sail loadings as a function of time. The critical sail loading for the entire inflation process occurs at Sail 1 just as Sail 4 inflates. The riser load at this time is 29,700 pounds as compared to a maximum riser load of 32,200 pounds occurring just as Sail 6 inflates. Figures 46, 47 and 48 show the loading on each sail throughout the inflation process.

The dashed lines in Figures 45, 46, 47 and 48 indicate assumed sail loadings for the portions of the inflation process that were not analyzed. These portions of the process are at times of decreasing riser load when the canopy is approaching a steady state condition.

Results of this study show that the assumption that the maximum sail load-strength ratio for each stage occurs at the time of maximum riser load for that stage is valid. The assumption that maximum riser load for a stage occurs when all sails of that stage become inflated is valid for the first reefed stage and full open, but is not true for the second reefed stage. Peak riser load for the second reefed stage occurs just as Sail 6 becomes inflated, 1.08 seconds before complete inflation of this stage.

NORTHROP

Table 3 . Load-Time History Used for the Stress-Time Study

Time From Launch (sec)	Inflation State	Test Load (lbs)	Load Ratio	Design Load (lbs)
23.94	Sail 2 Inflated	16,430	$\frac{29,700}{20,375}$	24,026
24.09	Sail 3 Inflated	17,970	$\frac{29,700}{20,375}$	26,195
24.30	Sail 4 Inflated	20,375	$\frac{29,700}{20,375}$	29,700 (Stage 1 Peak Load)
27.40	M.C.D.R. 1			
27.90	Sail 6 Inflated	32,710	$\frac{32,200}{32,710}$	32,200 (Stage 2 Peak Load)
28.31	Sail 7 Inflated	26,780	$\frac{32,200}{32,710}$	26,350
28.98	Sail 8 Inflated	19,330	$\frac{32,200}{32,710}$	19,060
34.30	M.C.D.R. 2			
34.74	Sail 9 Inflated	18,140	$\frac{30,900}{28,135}$	19,920
34.92	Sail 10 Inflated	22,380	$\frac{30,900}{28,135}$	24,580
35.11	Sail 11 Inflated	26,840	$\frac{30,900}{28,135}$	29,476
35.27	Peak Load	28,135	$\frac{30,900}{28,135}$	30,900 (Stage 3 Peak Load)
35.36	Sail 12 Inflated	26,782	$\frac{30,900}{28,135}$	29,414
35.63	Sail 12 Expanded*	15,370	$\frac{30,900}{28,135}$	16,900
* At time of maximum skirt diameter.				

NOTE: M.C.D.R. denotes "Main Canopy Disreef"

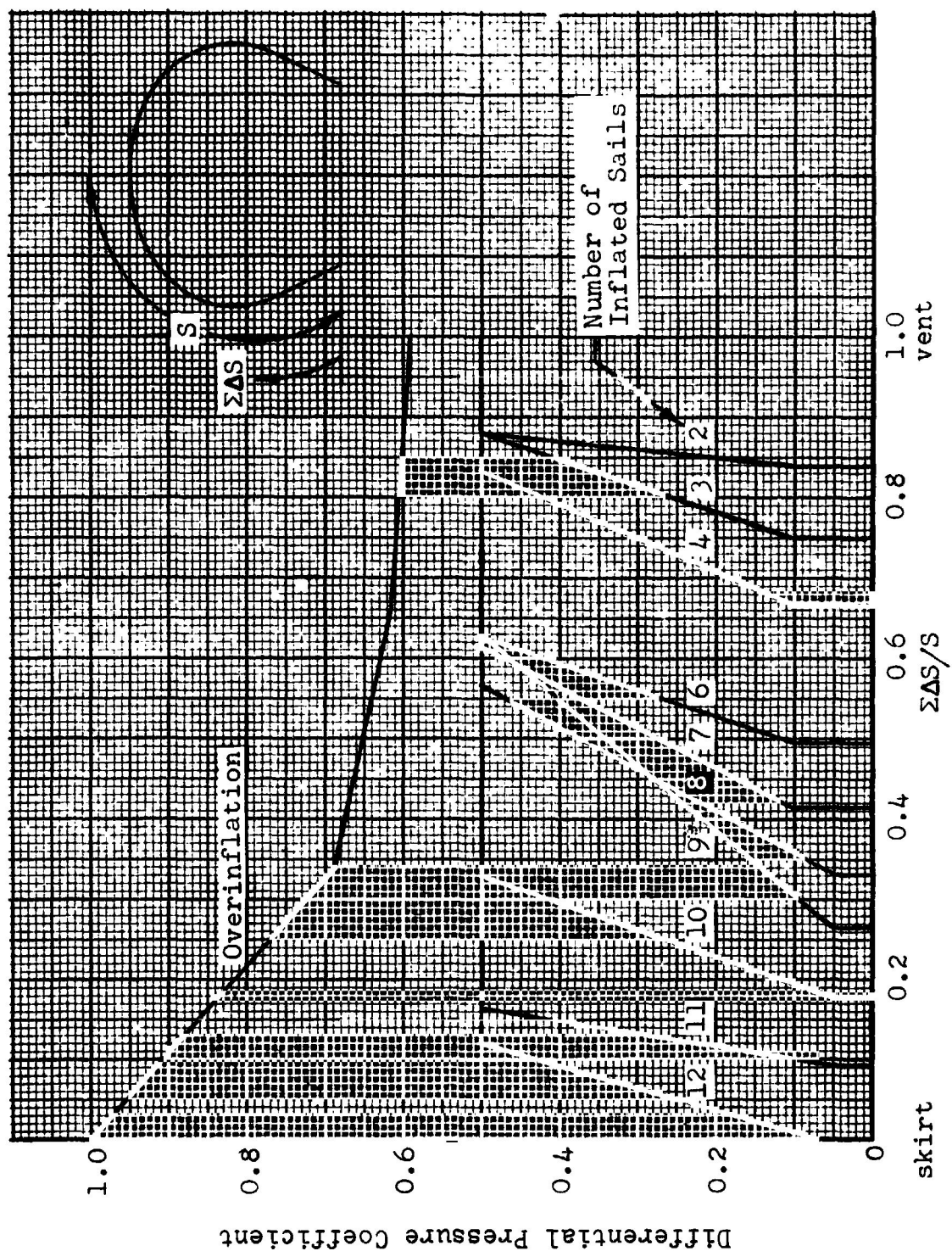


Fig.43. Canopy Pressure Distributions Used for Stress-Time Study

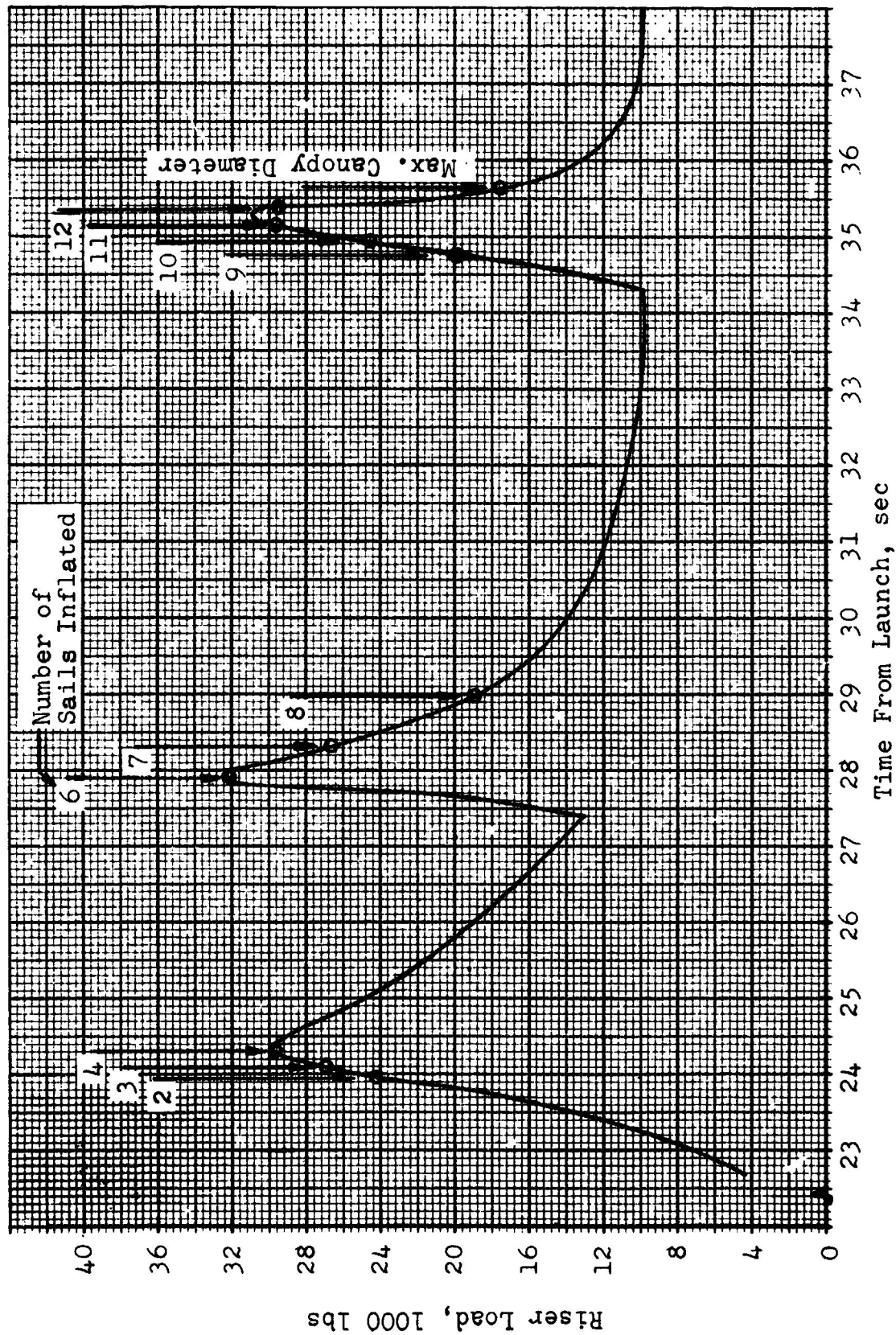


Fig. 44. Load-Time Trace for the 83.5 ft. D₀ Ringsail Parachute

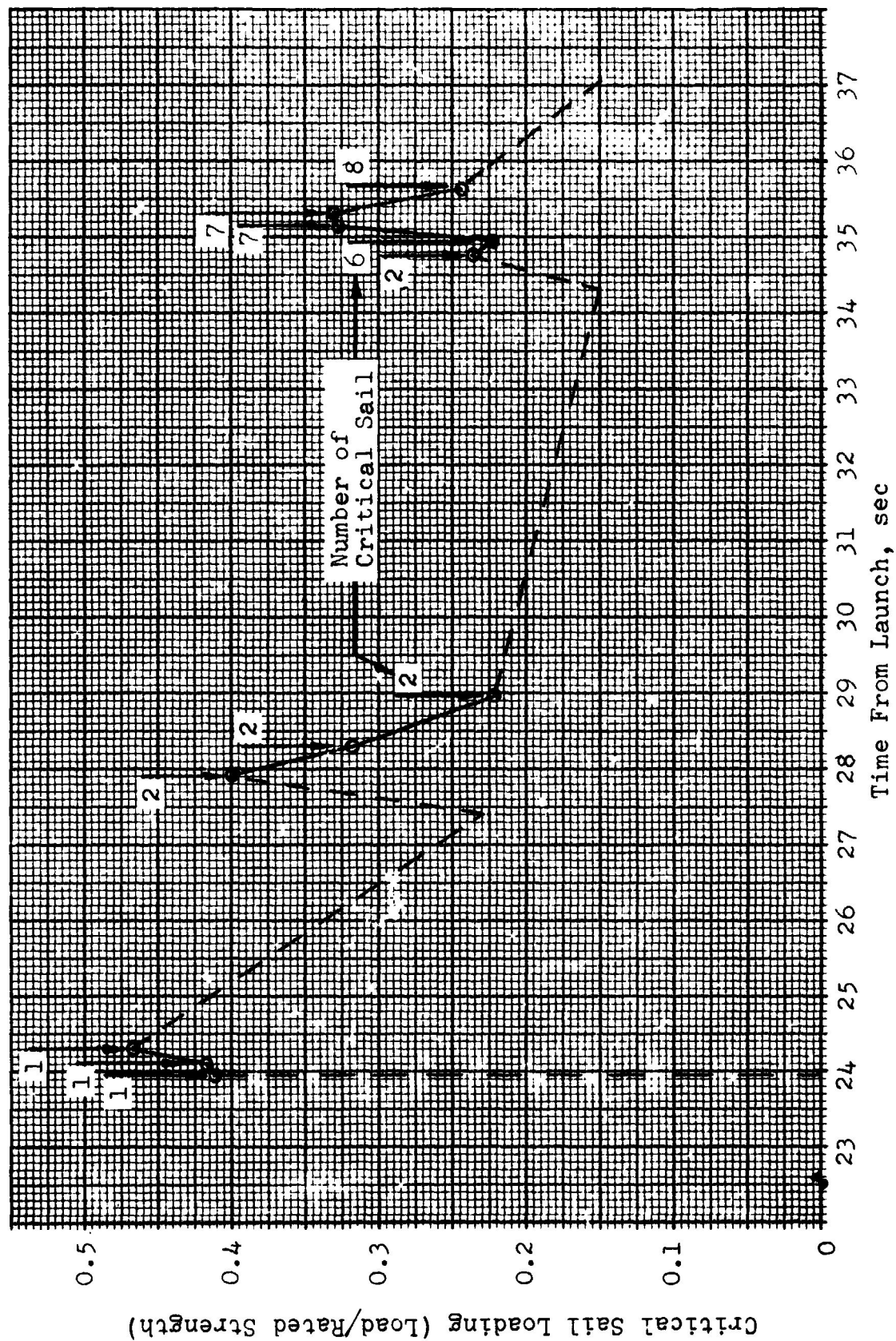


Fig. 45. Critical Sail Load vs. Time for the 83.5 ft D_0 Ringsail Parachute

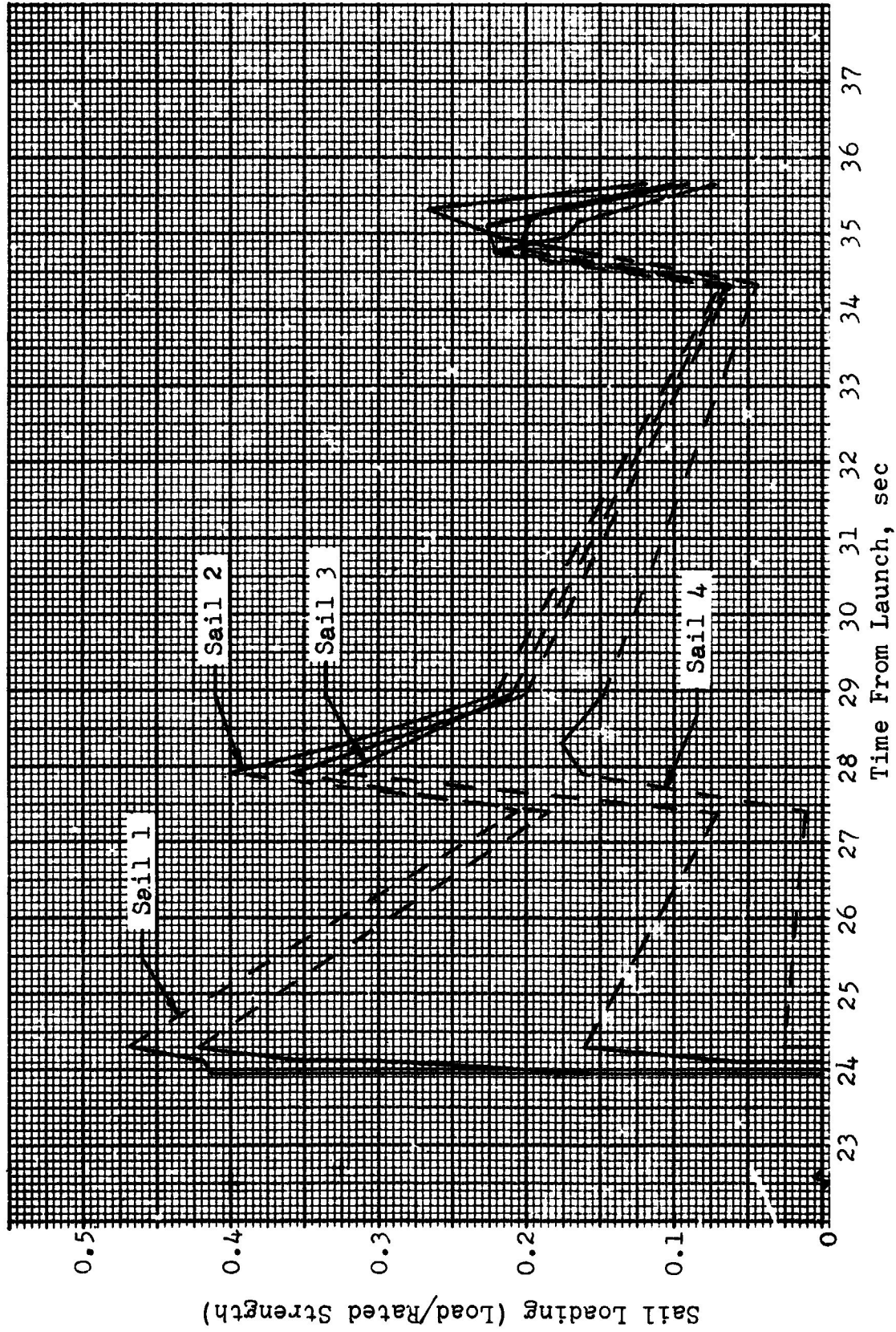


Fig. 46. Sail loading vs. Time for Sails 1, 2, 3, and 4 of the 83.5 ft D_0 Ringsail Parachute

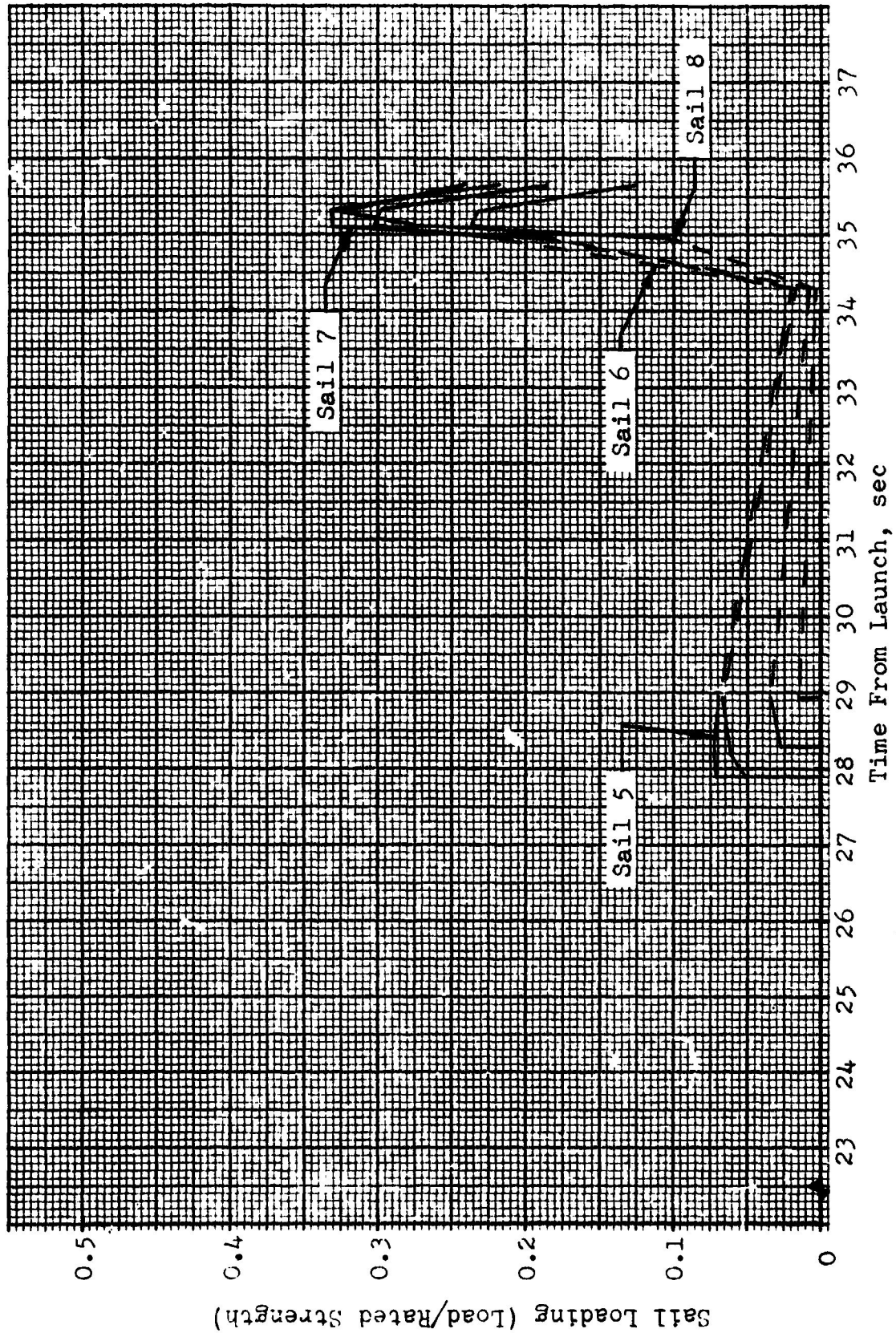


Fig. 47. Sail Load vs. Time for Sails 5, 6, 7, and 8 of the 83.5 ft D₀ Ringsail Parachute

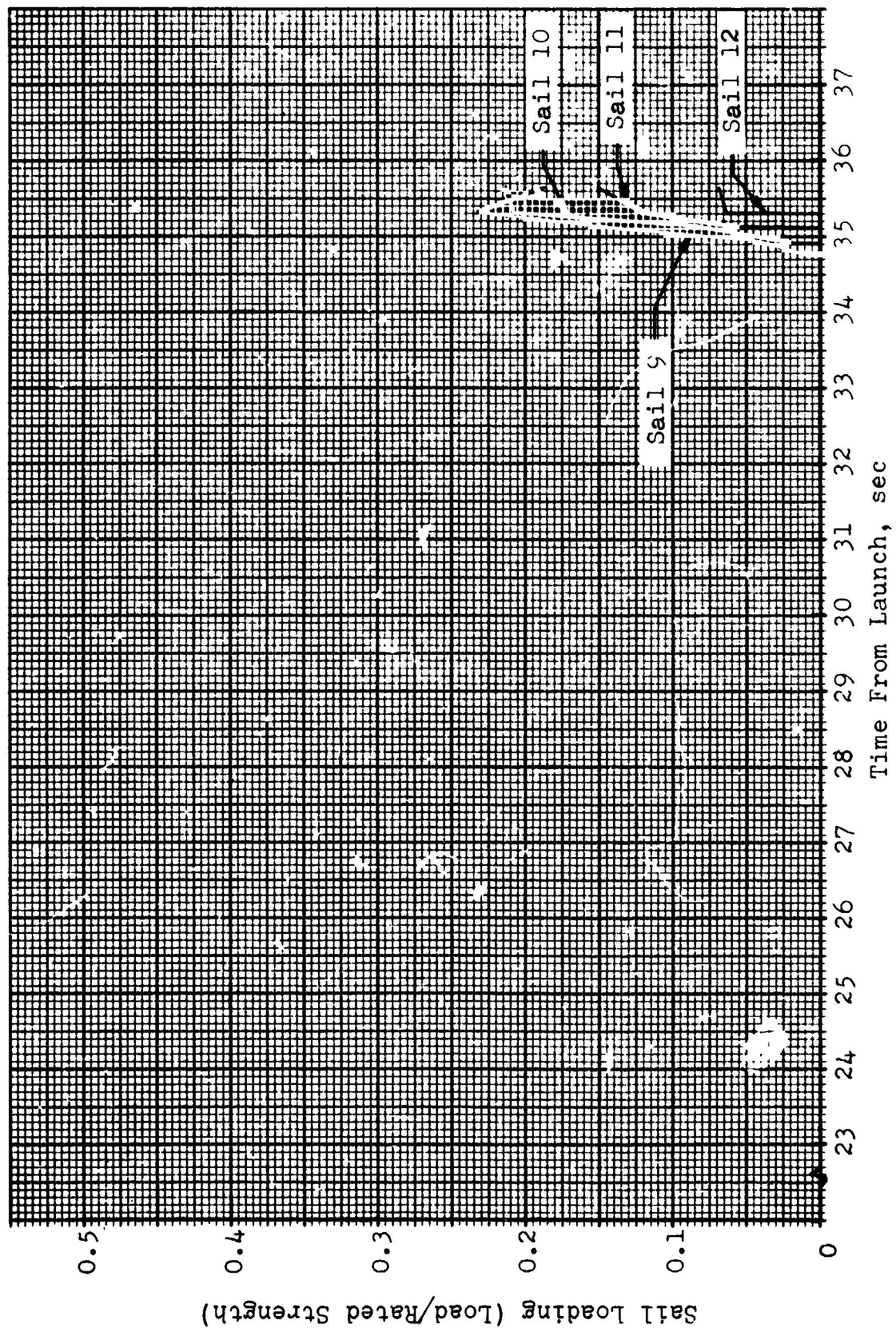


Fig. 48. Sail Load vs. Time for Sails 9, 10, 11, and 12 of the 83.5 ft D_0 Ringsail Parahute

REMARKS

Table 4 shows the maximum radial tape load-strength ratio for each of the states of inflation. Peak radial load of 68.1 percent of the rated strength occurs just as Sail No. 6 inflates. Thus, the radial tape load-strength ratio is maximum at the time of maximum riser load.

Table 4. Load-Time History of Main Parachute Radial Tape

Time from Launch sec	Number of Sails Inflated	Maximum Radial Tape Loading <div>Load Rated Strength</div>	Location of Maximum Load
23.94	2	0.505	L.E., Sail 2
24.09	3	0.553	Middle, Sail 3
24.30	4	0.631	Middle, Sail 4
27.90	6	0.681	Middle, Sail 6
28.31	7	0.564	L.E., Sail 6
28.98	8	0.416	Middle, Sail 7
34.74	9	0.444	Middle, Sail 8
34.92	10	0.525	Middle, Sail 9
35.11	11	0.634	L.E., Sail 10
35.36	12	0.635	L.E., Sail 11
35.63	12 (Max. Diameter)	0.367	T.E., Sail 12

Margin of safety calculations for the critical entry condition are presented in Appendix B.

CONTINUED

4.3.5 Optimum Weight Calculation for the Main Parachute

Since weight is one of the most critical parameters in designing spacecraft recovery systems, an insight to the theoretical weight optimum of a parachute would be useful. A theoretically optimum parachute would have continuous members (100 percent joint efficiency) and materials that would be just strong enough at every point to withstand the design loads.

Although this optimum weight is a value that can never be achieved in practice, it serves as a yardstick for judging the efficiency of a parachute design. Optimum weight could also serve as a sound basis for predicting the weight of a new design. Optimum weight factors for existing parachutes of given type and class could be computed and averaged to obtain a typical value. The product of this factor and the calculated optimum weight for a new design of the same type and class would give a predicted weight.

In this study, two optimum weight factors are calculated. The first factor is the ratio of spacecraft main parachute weight to optimum parachute weight including typical joint efficiencies. The second factor is the ratio of present main parachute weight to optimum parachute weight assuming 100 percent joint efficiencies. This factor gives an absolute optimum weight by assuming all the members to be continuous as well as being of minimum strength. Redundant members (the two rip-stop bands and one of the first stage reefing lines) are omitted from the calculation, as are nonstructural items such as reefing line cutters and pockets.

The strength-to-weight ratio for a fabric material is found by dividing its rated strength by its density in consistent units. The strength-to-weight ratio has units of length and can be visualized as the length that could just support its own weight. The values used in this analysis are 1.11×10^6 in. for tapes, 1.56×10^6 in. for cord, and 0.81×10^6 in. for cloth. These values are average minimums for fabric materials in the "Parachute Handbook".¹⁵

Using the results of the parachute opening stress-time study (Section 4.3.4), an evaluation of optimum canopy weight was made by reducing the rated strength of each canopy member to give a zero margin of safety. Efficiency factors such as joint efficiency, abrasion, and unsymmetrical loading were included to give a realistic weight comparison with the present spacecraft parachute (thermal factors were neglected to simplify the analysis). After the rated strengths had been reduced, additional computer runs were made at each of the critical loading conditions using averaged load-strain curves. The equilibrium shape and internal loading was found for the pressure distributions shown in Figure 43. Based on the results of these computer runs, the rated strengths were again revised to give zero margins of safety for all elements and further computer runs were made. This procedure was continued until the computed internal loads resulted in zero margins of safety for all canopy elements. Average strength-to-weight ratios for tape, cloth and cord were then used to compute the optimum canopy weight of the parachute. By using the same average strength-to-weight ratios, the weight of the spacecraft parachute was also found. The ratio of the spacecraft main parachute weight to the optimum parachute weight with typical joint efficiencies is 1.53. To obtain the second of the optimum weight factors, the rated strength of each element in the parachute was reduced to give a zero margin of safety for 100 percent joint efficiency. The weight of the parachute was then found by using the same average strength-to-weight ratios as were used above. Table 5 contains the weight of each parachute component for the spacecraft design, for the optimum design with typical joint efficiencies and for the optimum design with 100 percent joint efficiencies. The ratio of spacecraft main parachute weight to optimum parachute weight with 100 percent joint efficiencies is 2.17.

Table 5 . Comparison of Apollo Main Parachute Weight
with Theoretically Optimum Weights.

Item	Spacecraft Design	Optimum 1*	Optimum 2**
Suspension Lines	42.10 lbs	41.19 lbs	30.89 lbs
Sail 1	1.15	1.08	0.54
Sail 2	2.53	2.22	1.11
Sail 3	3.89	2.43	1.21
Sail 4	5.38	2.49	1.25
Sail 5	3.29	0.65	0.34
Sail 6	4.14	1.92	0.97
Sail 7	4.77	2.24	1.11
Sail 8	5.13	2.59	1.30
Sail 9	9.72	2.89	1.44
Sail 10	5.30	1.50	0.75
Sail 11	5.75	1.38	0.69
Sail 12	6.12	0.73	0.36
Skirt Band	6.51	3.00	2.73
Vent Band	0.67	0.56	0.51
Vent Lines	0.62	0.26	0.16
First Stage Reefing Line	0.52	0.15	0.14
Second Stage Reefing Line	0.89	0.49	0.33
Radial Tapes	<u>22.00</u>	<u>17.66</u>	<u>14.30</u>
Total	130.48 lbs	85.43 lbs	60.13 lbs

* Optimum 1 includes typical joint efficiencies.

** Optimum 2 includes 100% joint efficiencies.

SECTION 5.0

PILOT CHUTE RISER DYNAMICS

A series of riser dynamics tests were performed as part of an effort to determine the cause of two failures that had occurred in Apollo drop tests conducted in August of 1967 (Tests 80-3 and 80-3R). In both drop test cases, the pilot chute riser failed at time of main parachute canopy stretch. Both failures were, therefore, due to impact loadings rather than parachute opening loads. The predicted loads, using analysis methods employed at that time, were well below the strength of the riser assembly. In addition, the failures occurred in free lengths, rather than in the joints which are weaker than the parent material. In order to study the mode of failure, the fabric riser dynamics tests were conducted in the Northrop Ventura laboratories. The resulting data are the subject of this analysis.

Longitudinal impact loading was applied at a velocity of 300 ft/sec to samples of pilot chute riser material (nylon webbing) and structure elements. Test data consisted of high speed film sequences and strip chart force gage records. It is the purpose of this study to explain these data and to prepare recommendations for additional riser dynamics test and analysis.

The approach employed in the endeavor to understand the phenomena occurring during the impact loading of the specimens is to first perform a simplified analysis of the observed wave motion. The method of characteristics is applied to an approximate mathematical model obtained by the application of eleven assumptions regarding the system boundary conditions, material properties and general behavior. The most significant of these approximations are the assumptions that the nylon webbing used in the specimens behaves

in a linear-elastic manner and that the elastic modulus is independent of loading rate. The application of this method of analysis contributes significantly to the understanding of the performance of the test specimens but is unsuitable for the prediction of webbing stresses; i.e., the assumptions used are excessively restrictive. This work is described in Section 5.4.

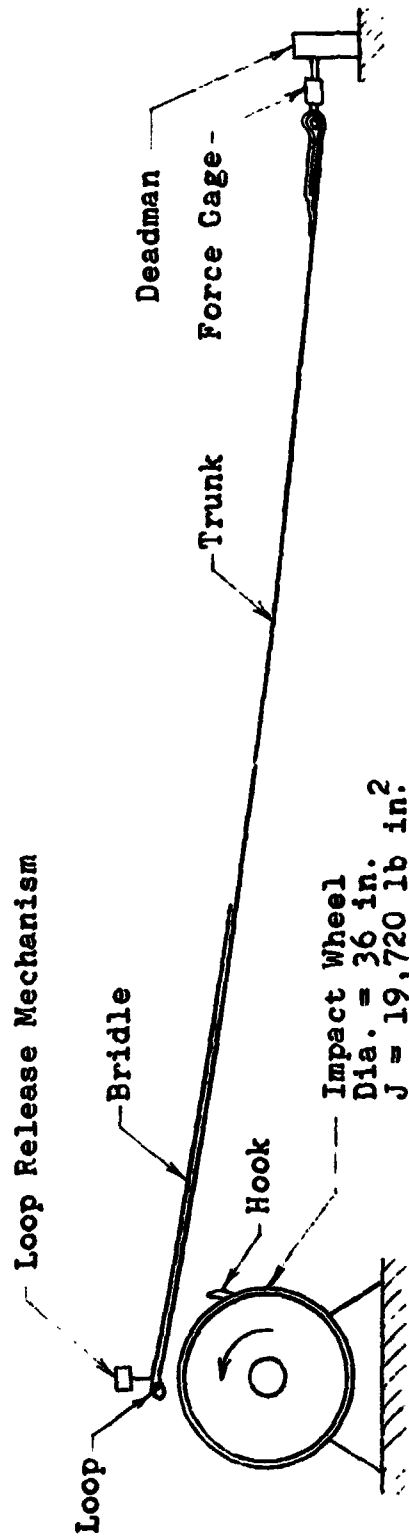
When the complexity of the problem is increased by the necessary annulment of several of the assumptions listed in Section 5.4, the use of a high speed computer becomes desirable. Section 5.5 is a description of a computerized application of the finite difference method of solution to the system of partial differential equations, boundary conditions and initial conditions appropriate to more accurate representation of the real system.

The arrangement of test apparatus used in these tests is shown in Section 5.1 and descriptions of the test specimens and relevant material properties are presented in Section 5.2. Force gage data are presented in Section 5.3. Seven film sequences have been studied quantitatively and plots of position versus time have been constructed for each specimen gage mark. A presentation and interpretation of these results is given in Section 5.6.

5.1 TEST EQUIPMENT AND PROCEDURE

The equipment used in the riser dynamic tests is shown in Figure 49.

The specimens were suspended under light tension between the loop release mechanism and the resistance element type force gage. The force gage was attached to an extremely rigid dead-man beam. Gage marks were painted on the trunk of the specimen at two-foot intervals.



NOT TO SCALE

Fig. 49. Pilot Chute Riser Dynamic Test Apparatus

The impact wheel was brought up to a rotational speed that gave a rim speed equal to approximately 300 ft/sec. The impact loop was then released and allowed to be engaged by the wheel rim hook. The resulting motion of the system was photographed against a background grid using high speed motion picture cameras. The force gage output was preserved by means of a strip chart recorder.

The (nominally) ten-inch diameter impact loop was fabricated from 6000-pound test tubular nylon cord using a "Chinese finger" joint with sufficient overlap to provide four active load carrying cords. There was no quality control on the fabrication of this part of the test structure.

The high speed films are of variable quality. Only the tests for which the high speed films are readable are considered in this report. These tests and the respective impact velocities are listed in Table 6 .

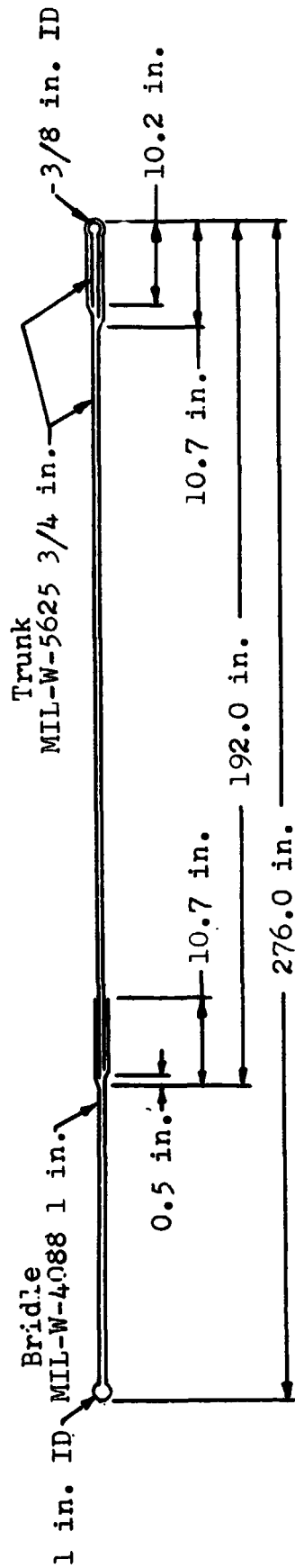
5.2 DESCRIPTION OF SPECIMENS AND MATERIAL PROPERTIES

The construction and materials of the nylon webbing specimens are shown in Figures 50 and 51. All material of a given specification was obtained from the same lot. Notice that one of the webbings in the trunk of specimen type D4 was deliberately made approximately 3 percent longer than the other. The purpose of this was to determine the effect of mismatching on riser strength.

The unstrained lineal density and the static load-strain curve for each type of webbing used in the test specimens are given in Figures 52 and 53. The straight line approximation used in the approximate linear-elastic analysis are superimposed over the nonlinear static curves.

Table 6 . Impact Velocities and Peak Deadman Force
From Pilot Chute Riser Tests

Test Number	Impact Velocity (ft/sec)	Peak Deadman Force (lb)	Specimen Description (See Section 3.0 for Details)
D3-1	284	5550	Simulates riser (double thickness trunk)
D3-2	284	5825	Simulates riser (double thickness trunk)
D3-3	300	5825	Simulates riser (double thickness trunk)
D4-5	277	5400	Same as D4 but mis- matched
D4-6	285	5000	Same as D4 but mis- matched
D5-1	275	2625	Single Thickness Trunk
D6-1	277	4980	Obtained From Riser Assembly



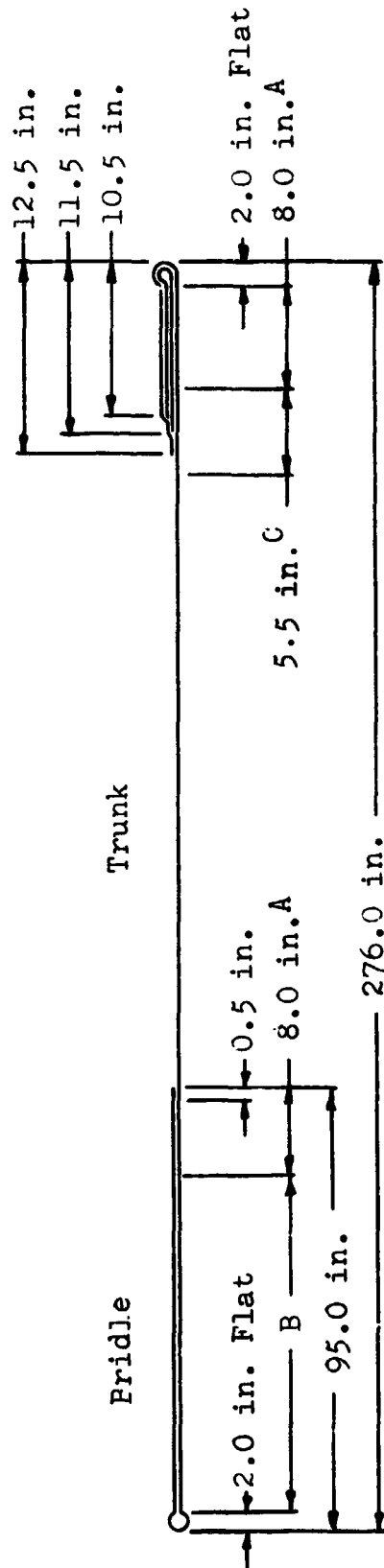
Free Lengths: Centerline Sew - One Row #3 Nylon Thd.
Overlays: 3 Pt. Stitch #3 Nylon Thd.

NOT TO SCALE

NOTES:

1. Specimen D3 as shown.
2. The MIL-W-5625 trunk section of Dr is mismatched 0.5" per 18".
3. Specimen D6 as shown except trunk and right end reinforcement are obtained from a Northrop Ventura RT516-401 Riser Assembly

Fig.50 . Pilot Chute Riser Test Specimens D3, D4 and D6



NOT TC SCALE

NOTES:

- Material MIL-W-5625 3/4 in.
- A - 3 Point Cross Stitch #3 Nylon Thd.
 - B - Centerline Stitch with #3 Nylon Thd.
 - C - Centerline Cross Stich #3 Nylon Thd.

Fig. 51 . Pilot Chute Riser Material Test Specimen

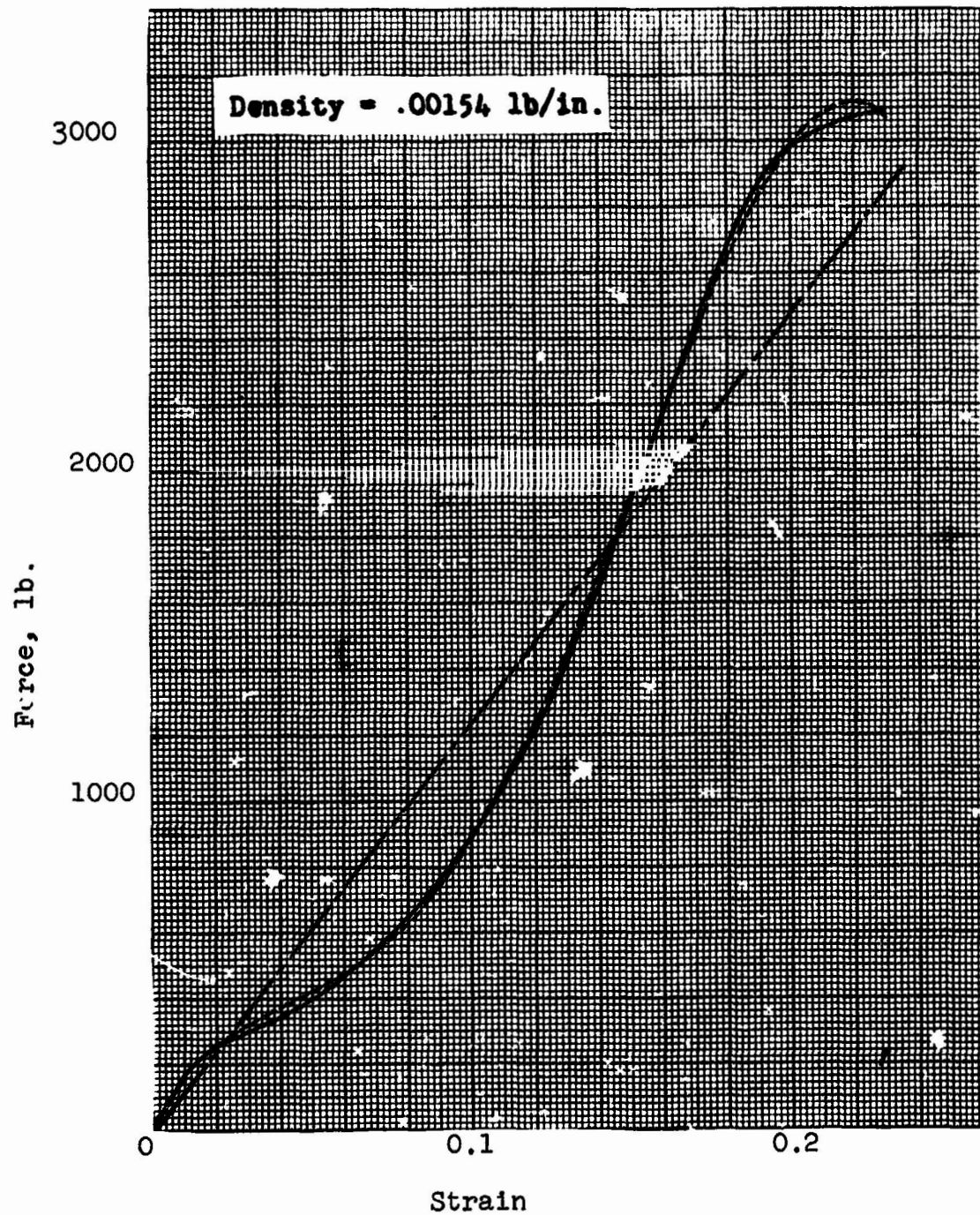


Fig. 52. Static Load - Strain Curve for a Sample of MIL-W-5625 3/4" Nylon Webbing

NORTHROP

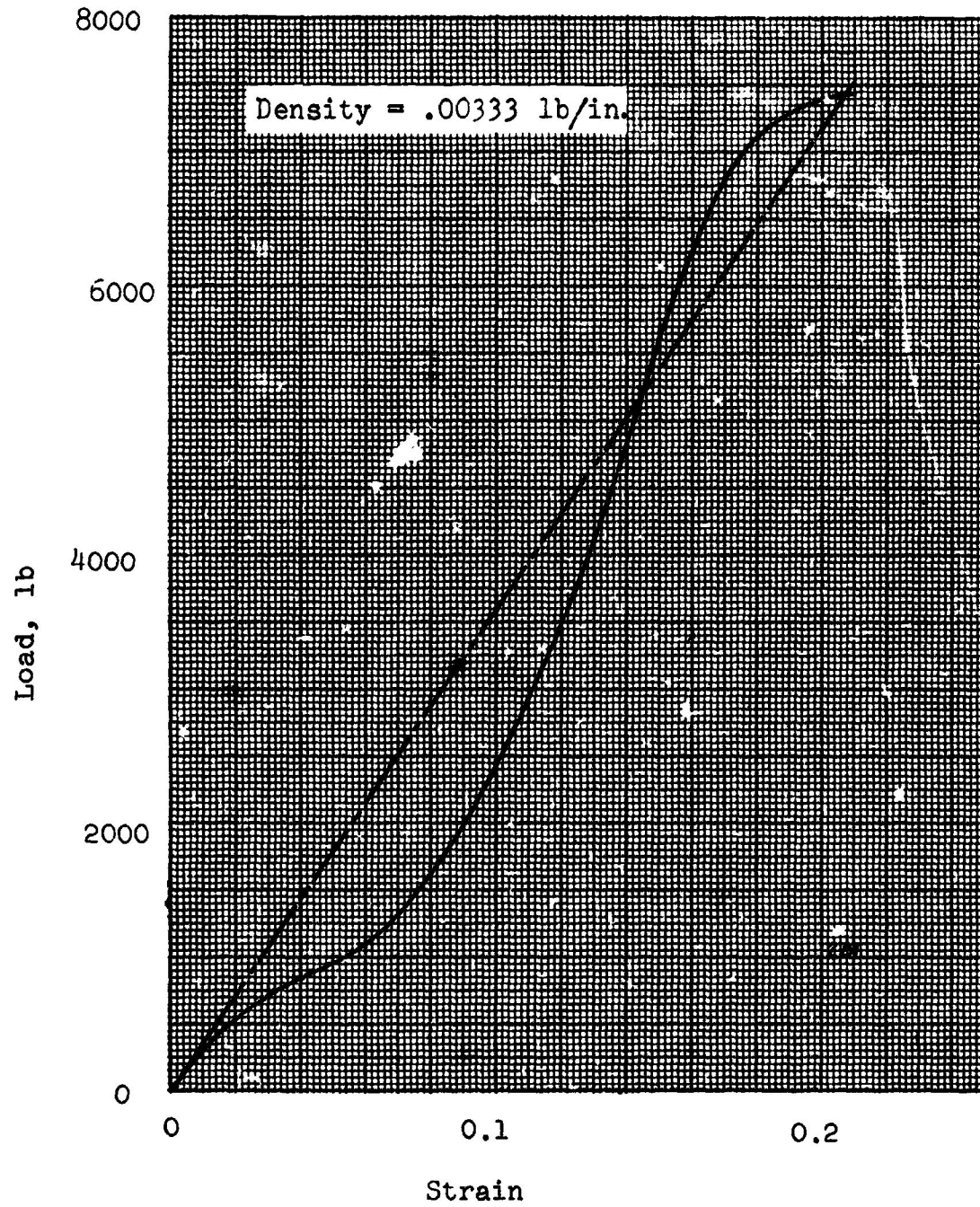


Fig.53 . Average Static Load - Strain Curve for MIL-W-4088 1" Nylon Webbing

In order to use the nonlinear curves in a computer calculation, it is necessary to either store the curve in digital form or in the form of an approximating function. An approximating function in the form of a least squares best fit fifth order polynomial has been obtained for the MIL-W-5625 3/4 inch nylon webbing used in all four types of test specimens. The expression, plotted in Figure 52 is

$$\begin{aligned} F = & (1.827041 \times 10^4) \epsilon - (3.550943 \times 10^5) \epsilon^2 \\ & + (3.680853 \times 10^6) \epsilon^3 - (1.164287 \times 10^7) \epsilon^4 \\ & + (8.459224 \times 10^6) \epsilon^5 \end{aligned}$$

Because of similarity of load-strain curves, this expression is used by scaling for the MIL-W-4088 webbing in Section 5.5.

References 23 and 25 show that for the case of constant average strain rate, the load-strain curve of nylon yarn depends upon the rate of loading. Therefore, a priori selection of the static curves for use as dynamic curves in the case of nylon in the form of webbing is not justified. However, in Section 5.5 the static curves are used as an approximation.

It is conceivable that the correct dynamic equation of state for nylon webbing is a differential equation involving stress, strain, strain rate²⁶ and perhaps even strain history²³. These tests were not comprehensive enough to derive such an equation of state but in Section 5.6 an estimate of the load-strain path actually followed by the webbing in each test is given.

5.3 FORCE GAGE DATA

Deadman force as a function of time is shown for each test in Figures 54 - 60. The experimental data did not yield a force gage time reference with respect to other events of the test. Therefore, the zero time points on the horizontal axes are at arbitrary locations. The peak deadman force for each test is given in Table 6 .

Inspection of the force gage curves shows a significant difference between the general shapes for the cases of single and double webbing trunks. For the single webbing case (Figure 59) the initial part of the curve is sloped, with small oscillations, whereas for the double webbing case (all other tests) the initial part of the curve displays large oscillations. In both cases the initial oscillations tend to decay, and a steady positive slope occurs prior to failure.

Table 6 shows that, on the average, the mismatched specimens suffered a 9 percent decrease in peak load relative to the correctly fabricated specimens. The average peak load attained by the simulated risers (D3 and D4) is 15 percent greater than the peak load attained by the riser sample (D6).

5.4 THE LINEAR-ELASTIC APPROXIMATION

5.4.1 Assumptions

As a first step in developing an understanding of the performance of the specimens in the riser dynamics tests, the linear-elastic case for longitudinal waves is considered. Eleven assumptions are involved in the construction of the mathematical model. They are as follows:

NORTHROP

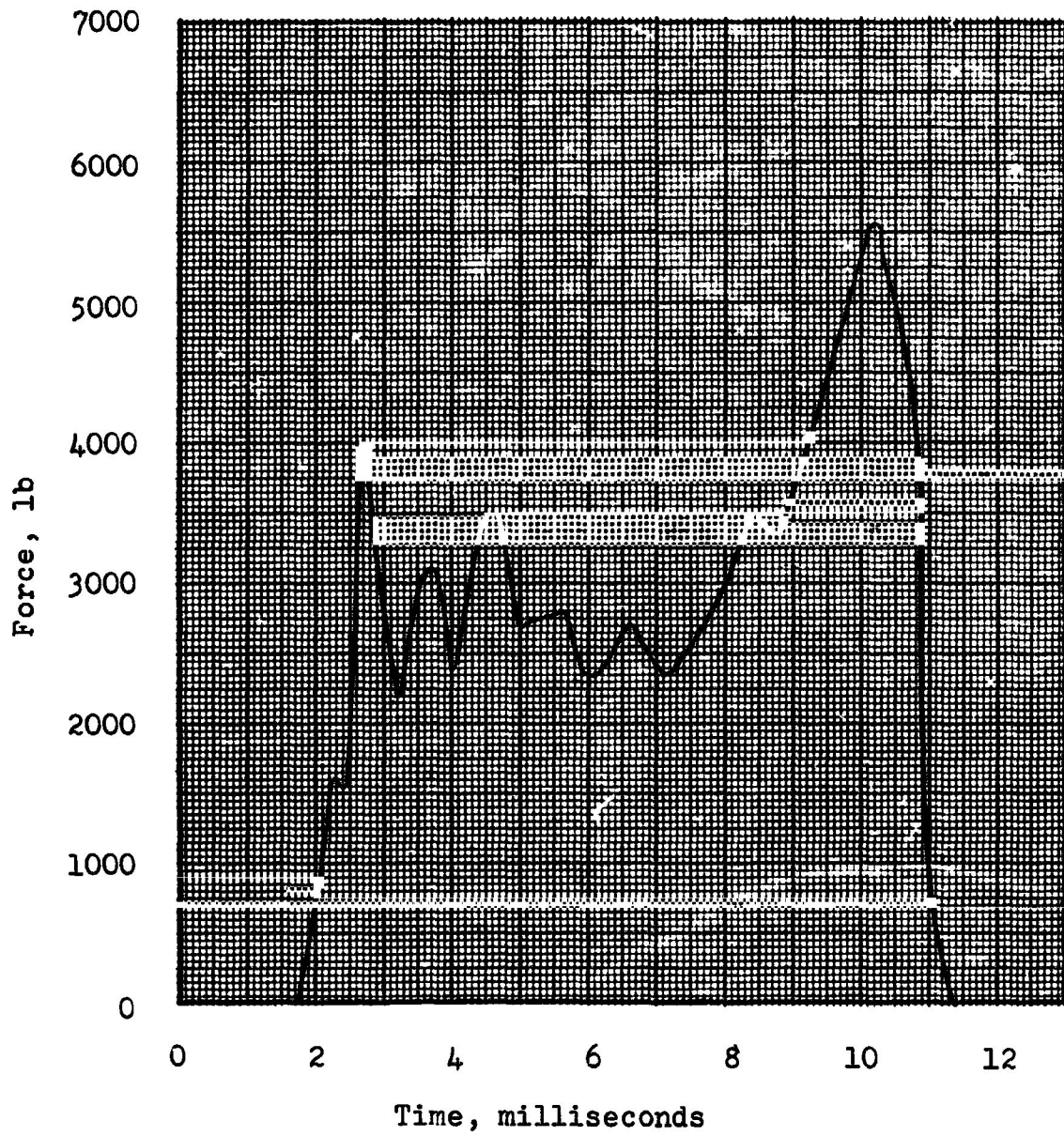


Fig. 54. Deadman Force Gage Record for
Pilot Chute Riser Test D3-1

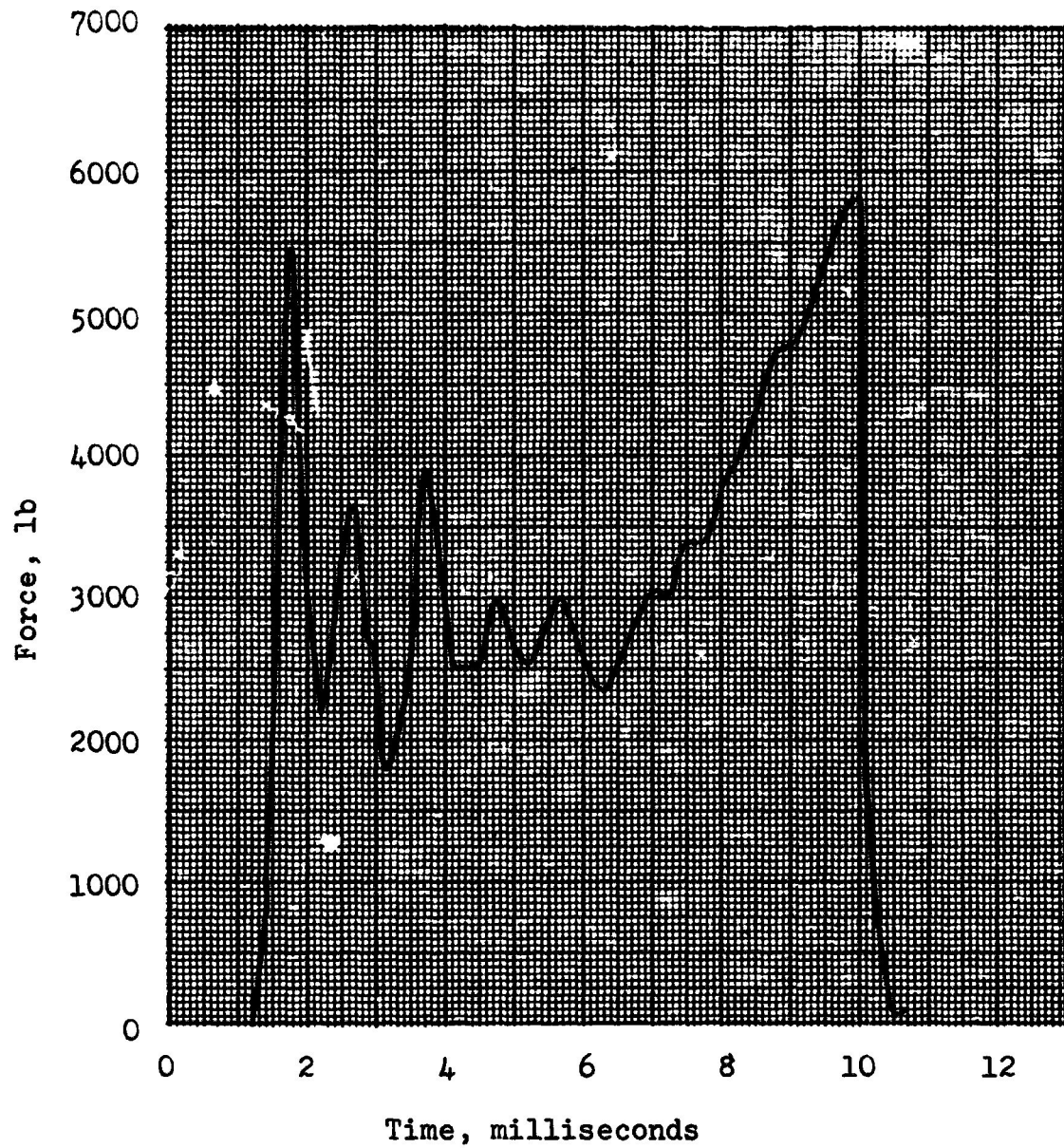


Fig. 55. Deadman Force Gage Record for
Pilot Chute Riser Test D3-2

CONTINUED

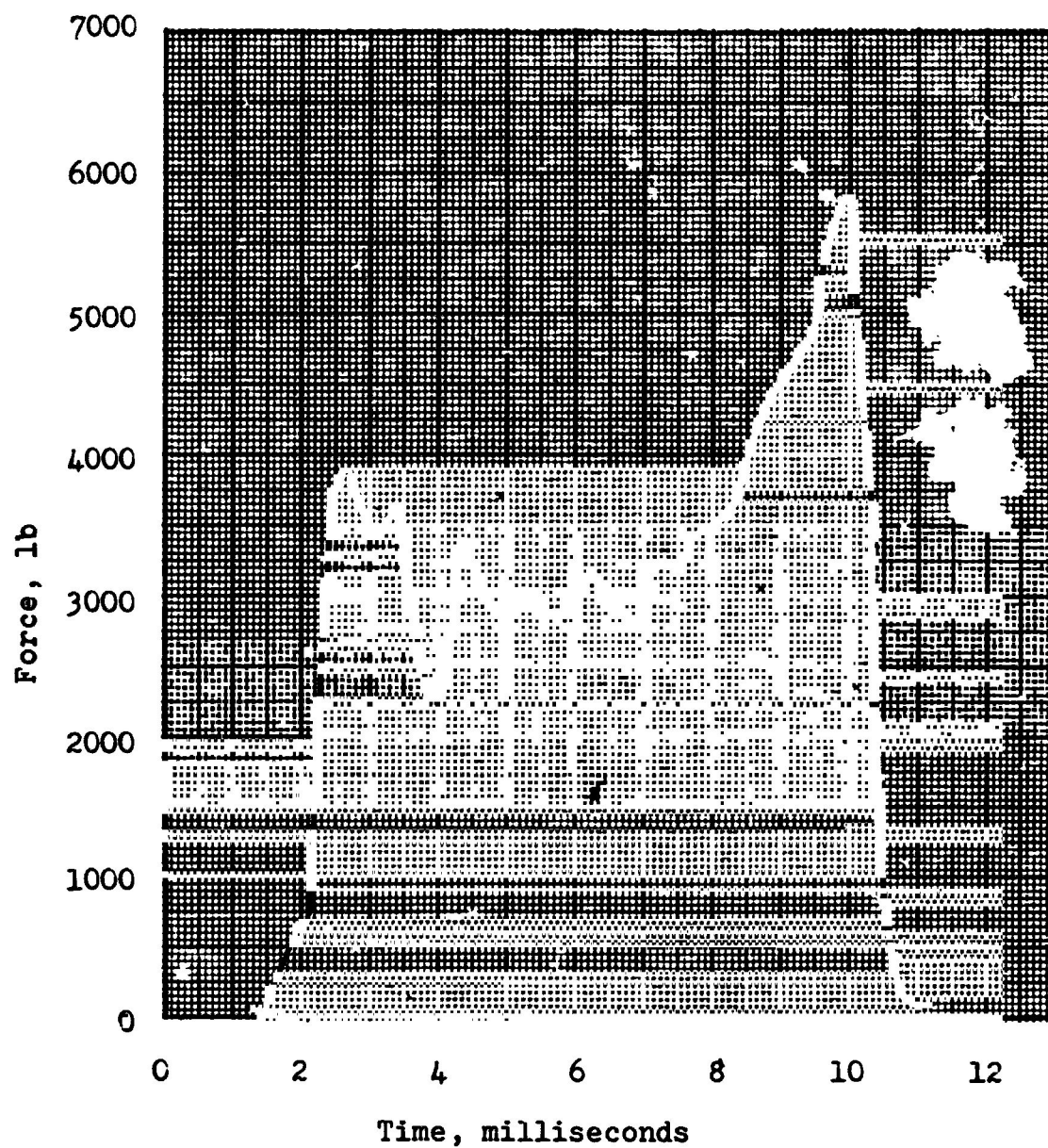


Fig. 56. Deadman Force Gage Record for
Pilot Chute Riser Test D3-3

RENTROP

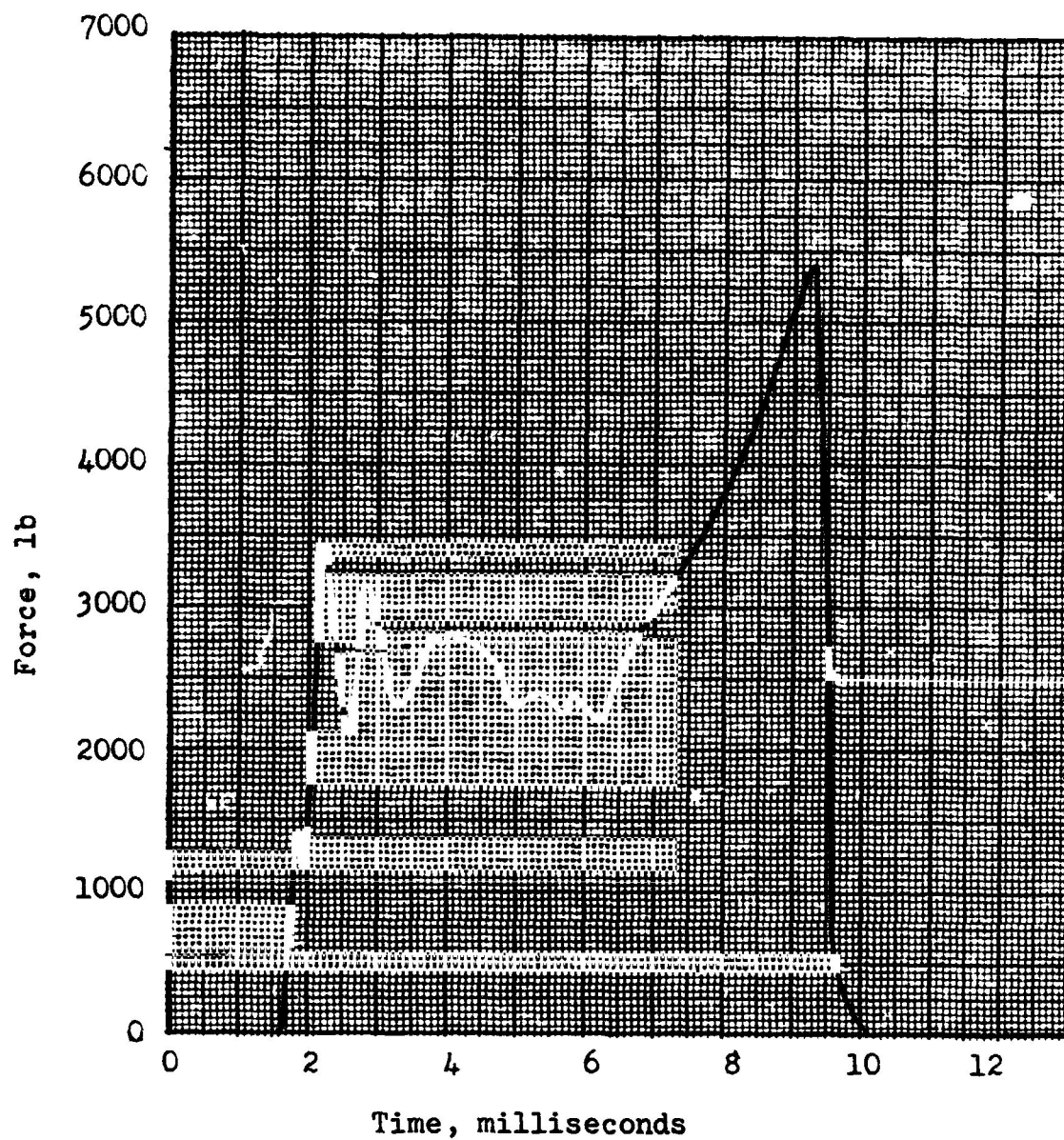


Fig. 57 . Deadman Force Gage Record for
Pilot Chute Riser Test D4-5

WORTHROP

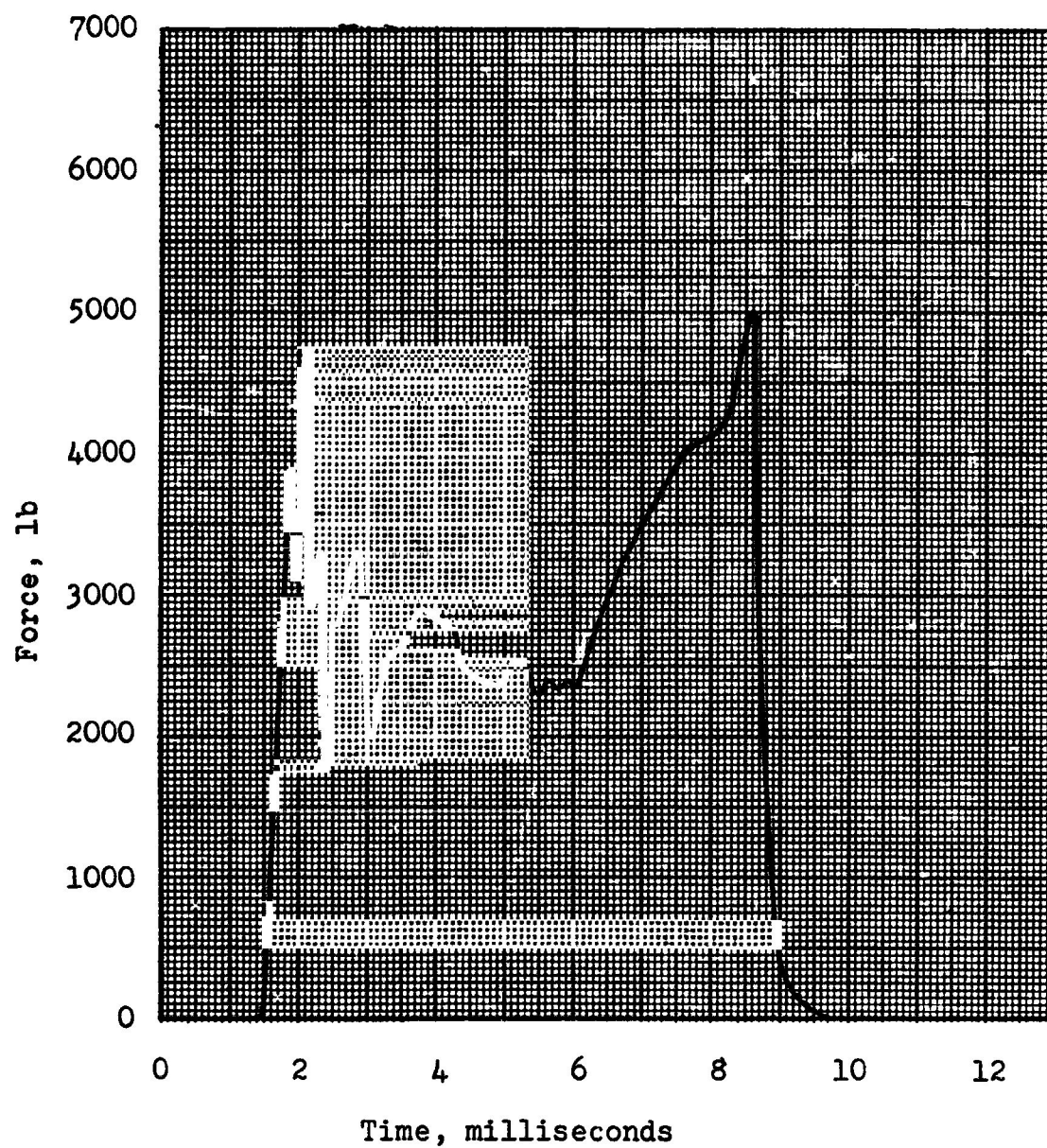


Fig.58 . Deadman Force Gage Record for
Pilot Chute Riser Test D4-6

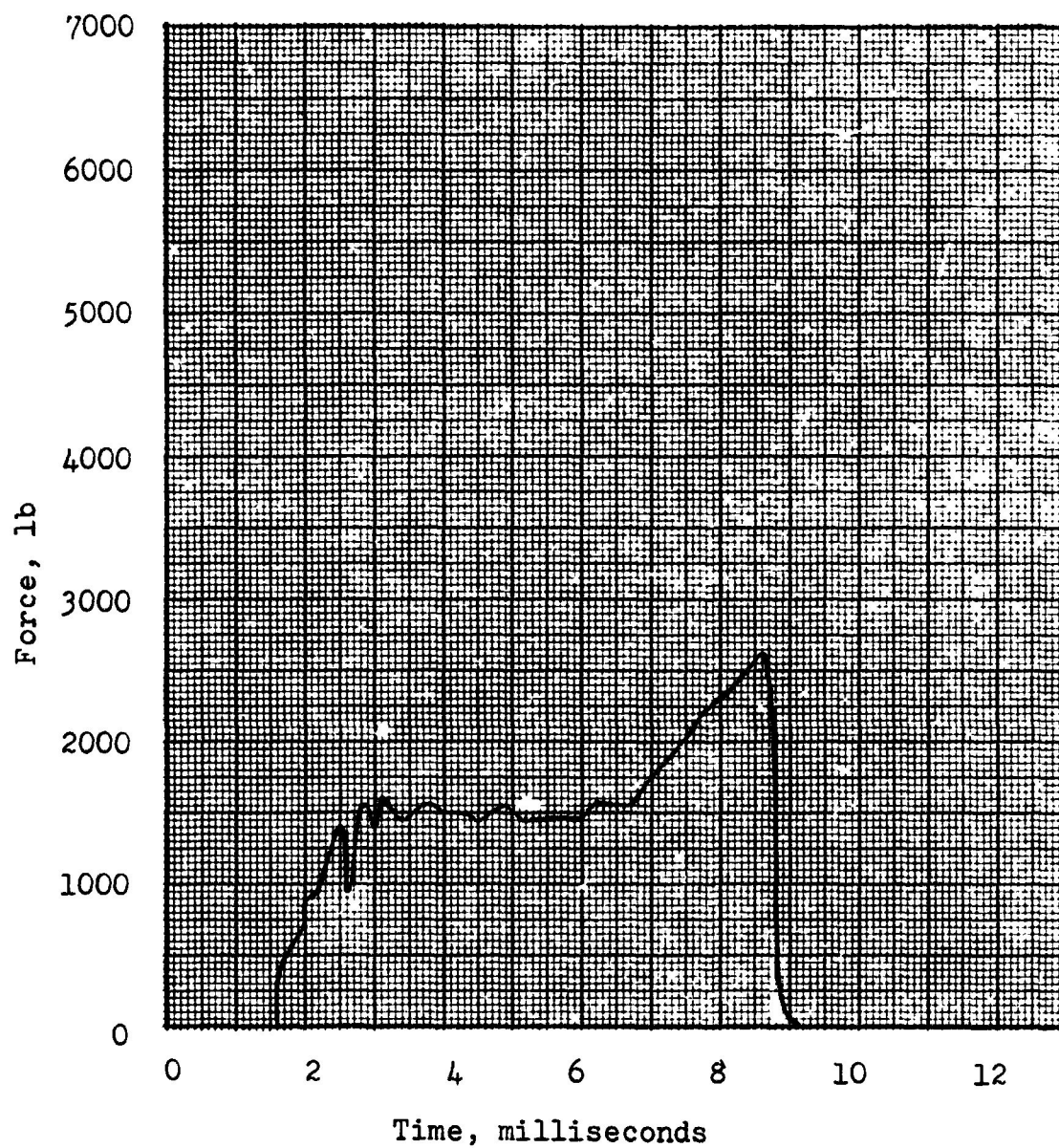


Fig. 59. Deadman Force Gage Record for
Pilot Chute Riser Test D5-1

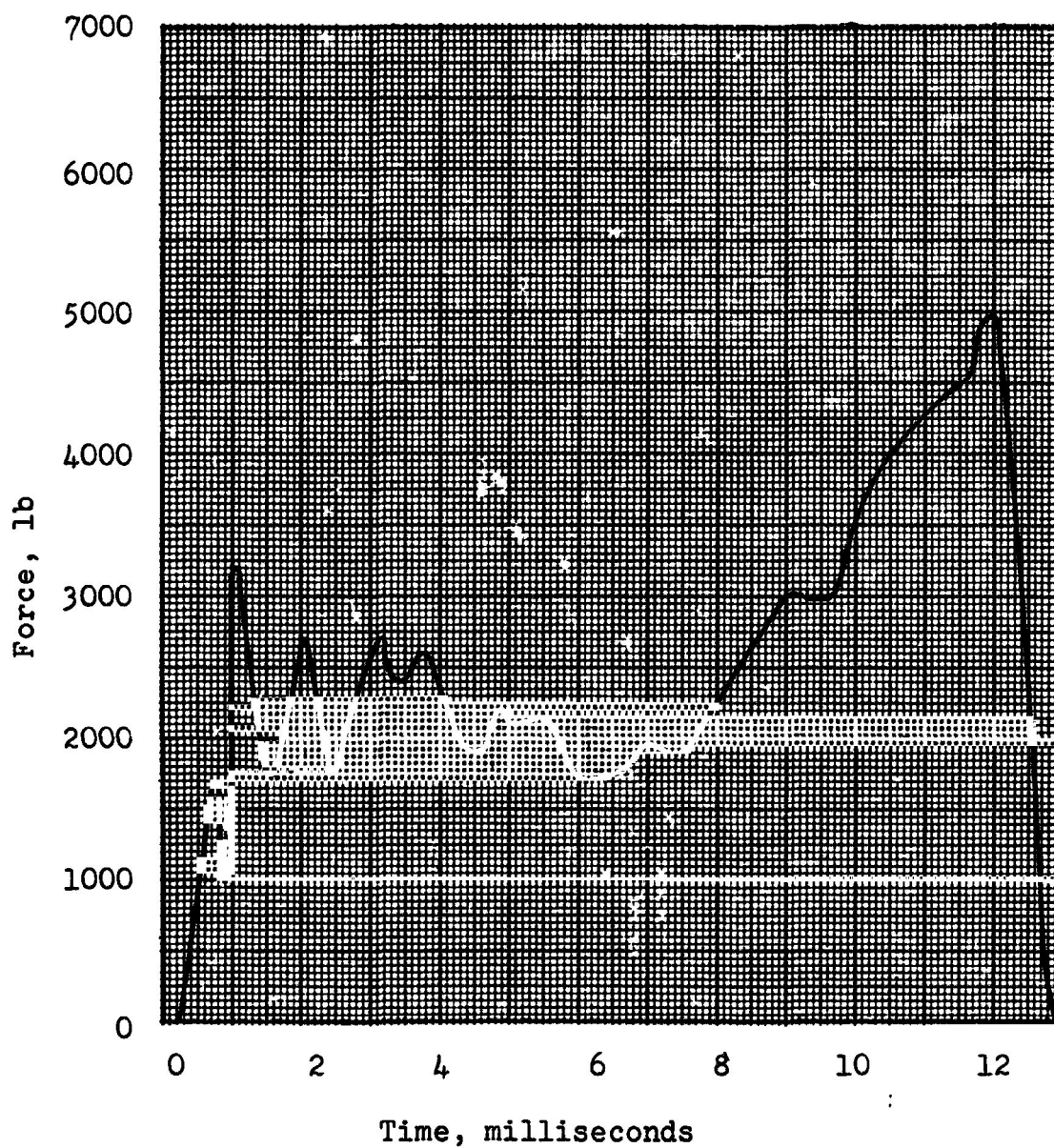


Fig. 60. Deadman Force Gage Record for
Pilot Chute Riser Test D6-1

NORTHROP

- a) The load-strain curve of the specimen materials under dynamic loading is independent of rate of loading and strain history and is related to the static load-strain curve in the secant fashion illustrated in Reference 27 and applied to the materials of the subject tests as shown in Figures 52 and 53.
- b) The end of the specimen moves at the same velocity as the rim of the impact wheel once the hook is engaged. The impact loop is assumed to possess zero stiffness until it is extended into a straight line and is assumed to be perfectly rigid thereafter.
- c) The impact wheel rim speed remains constant at its initial value V_0 . (In reality, the wheel rim speed decreases due to the reaction of the specimen.)
- d) No material is wrapped on to the impact wheel. The relaxation of this assumption makes the problem non-linear even though assumption a) is maintained.
- e) Specimen displacements are small and lineal.
- f) The wave propagation speed is very large relative to the velocity of the mass particles. Therefore, the velocity of the waves relative to the laboratory can be taken to be the same as the velocity in a reference system fixed in the specimen.
- g) Variations in lineal density and stiffness occurring over distances of four inches or less are modeled as a single step. This assumption has the effect of eliminating the details of the construction of the specimens at the ends of the overlay reinforcements.
- h) The stress, strain, displacement and velocity are uniformly distributed over the cross section of the specimen, even near discontinuities.

- i) The specimen is perfectly fixed at the deadman end.
- j) There is no interaction between transverse and longitudinal waves.
- k) The kinetic energy due to cross axis strain is negligible.

5.4.2 Method Of Analysis

The behavior of a system to which the preceding assumptions apply can be predicted by means of the application of four basic results.

- a) The longitudinal wave propagation velocity in section j of the specimen is given by:

$$c_j = \sqrt{\frac{k_j}{\rho_j}}$$

where k_j is the slope of the linear load-strain curve for the specimen material in section j and ρ_j is the respective lineal density.
(Reference 24)

- b) Immediately following the initiation of the step velocity impact at $t = 0$, a strain wave propagates away from the impact end with constant velocity

$$c_1 = \sqrt{\frac{k_1}{\rho_1}}$$

The strain in front of the wave is zero and the strain behind the wave is given by

$$\epsilon_o = \frac{V_o}{c_1}$$

(Reference 24)

- c) When a strain wave impinges on a discontinuity in the specimen, it is, in general, attenuated or amplified and a reflection wave is generated. The reflection coefficient of the discontinuity between section j and section $j + 1$ is given by:

$$R_j = \frac{\frac{k_b c_a}{k_a c_b} - 1}{\frac{k_b c_a}{k_a c_b} + 1} \quad (63)$$

and the transmission coefficient is given by

$$T_j = \frac{c_a}{c_b} (1 - R_j) \quad (64)$$

where $a = j$ and $b = j + 1$ if the wave approaches from section j and $a = j + 1$ and $b = j$ if the wave approaches from section $j + 1$. For a fixed boundary and the impacted end of the specimen, $R_j = 1$. (Reference 28)

- d) The strain at any point in the specimen at time t is equal to the algebraic sum of the amplitudes of all strain waves that have passed that point in the time interval $0, t$ (Superposition principle).

Using the above four results as rules of operation, the response of a specimen to the velocity impact can be constructed graphically. This has been done for the D5 test and the construction, which is an application of the method of characteristics, is displayed in Figure 61.

In this wave diagram, the horizontal axis is dimensionless distance from the impact end, $\frac{x}{L}$. The vertical axis is dimensionless time $\tau = t/t_p$ where t_p is the time required for a wave to propagate from one end of the specimen to the other. The slanting lines indicate the path of the wave fronts in space-time and the numbers associated with each of those lines are the amplitude of the respective wave front expressed in terms of the dimensionless strain,

$$\epsilon^* = \frac{\epsilon}{\epsilon_0}$$

where ϵ is the local strain.

The procedure used is to lay out the initial wave front locus (dimensionless slope = $c_1 t_p/L$, dimensionless amplitude = 1) extending from the origin to the first discontinuity at which point the reflected and transmitted wave amplitudes are calculated using Equations 63 and 64. The transmitted wave moves upward and to the right (in space-time) with slope corresponding to the wave propagation velocity in the second section (dimensionless slope = $c_2 t_p/L$). The reflected wave moves upward and to the left back into the region corresponding to the first section. These two new waves will then enter into further reflections at discontinuities and boundaries. As the construction proceeds, the number of waves multiplies at an increasingly rapid rate. In order to make graphical calculations feasible, waves with amplitude less than .03 are terminated and waves approaching each other within $\Delta\tau = 0.05$ are superposed. The strain level at any value of x/L and dimensionless time τ is obtained by summing the amplitudes of all waves intersecting a straight line between the points $(x/L, 0)$ and $(x/L, \tau)$.

5.4.3 Description Of The Approximate Model

The graphical wave tracing technique is applied to Test D5-1, the specimen of which is described in Figure 61. The parameters of each section of the specimen are listed in Table 7. If more than one discontinuity appears in any 4-inch length of specimen, they are lumped together into one discontinuity in this table.

5.4.4 Results

The longest uniform section of the specimen, which is referred to as the trunk of the specimen, consists of webbings with a combined rated strength equal to or less than half of the rated strength of any other section in the specimen. The strain distribution in the trunk of specimen D5 near the experimentally observed time of failure is shown in Figure 62. A significant observation is that at this instant in time, the maximum strain in the trunk occurs at a station away from either end of the trunk. This sample situation, therefore, implies the possibility of failure in such structures in free lengths of the structure if the stress concentrations at discontinuities are sufficiently mild.

In Figure 63, strain is shown as a function of time for both ends of the trunk and for the end of the webbing adjacent to the deadman. The sweep of the strain wave along the specimen is manifested in the sequence of the initial response at each station. Also shown in Figure 63 are the dimensionless ultimate strains for the material of the trunk of the specimen of Test D5-1 and one other D5 type test. There are two values because the impact velocities were not the same in the two tests performed on D5 specimens. It is interesting to note that the ultimate strain level is penetrated almost simultaneously at opposite ends of the trunk. The test films (Section 5.6) reveal simultaneous failures at the same points at approximately the same time as indicated by this approximate analysis.

Table 7 . Specimen Parameters For Approximate
Linear-Elastic Analysis

Specimen	Section No.	Left Station (in.)	Right Station (in.)	Lineal Density ρ (sl/ft)	Stiffness k (lb)	Wave Velocity c (ft/sec)
D5	1	0.00	95.00	.00115	24,800	4640
	2	95.00	264.50	.000574	12,400	4640
	3	264.50	276.00	.00230	49,600	4640

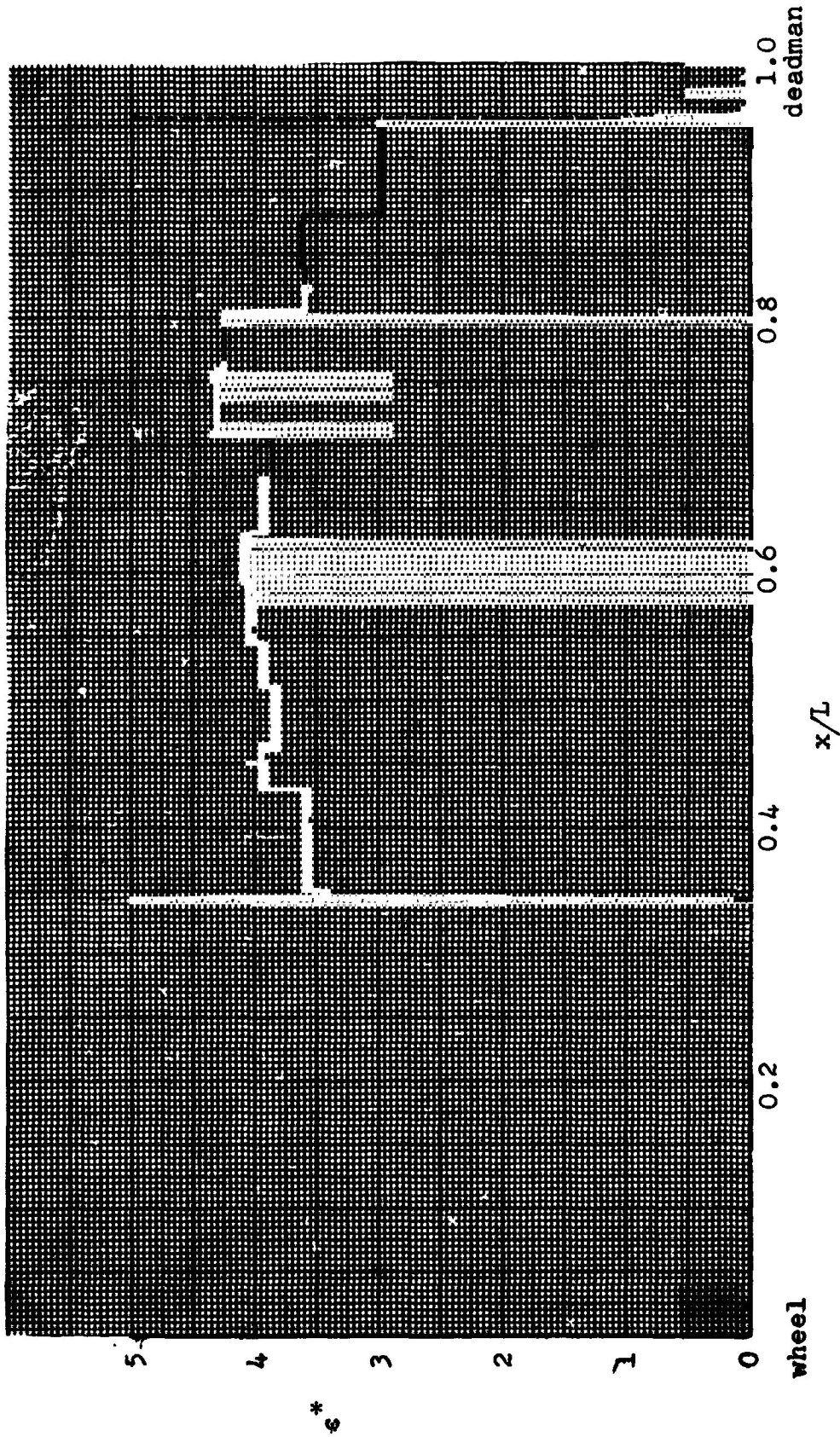


Fig. 62. Strain Distribution Along the Length of the Trunk of Specimen Type D5. Approximate Linear-Elastic Analysis, $r = 2.8$.

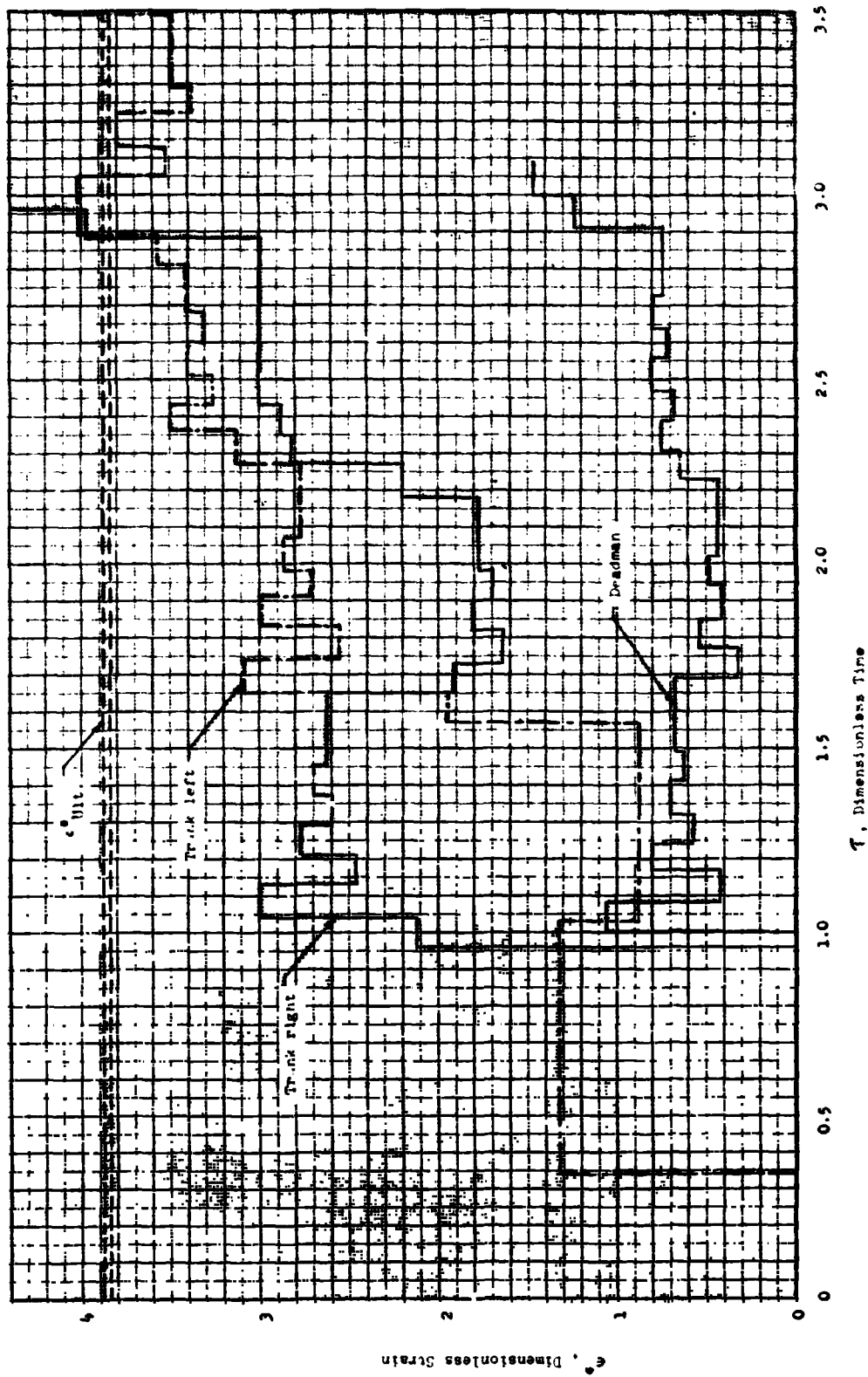


Fig. 63. Strain as a Function of Time at Three Stations, Approximate Linear-Elastic Analysis

A general observation of importance is that at all of the three stations shown, the webbing is subjected to several cycles of loading and unloading before failure occurs.

At the fixed end (deadman) of the specimen, the strain levels are generally lower than in the trunk because of the multiple layers of webbing used for reinforcement. In the tests, the load at the deadman was measured by a force gage and a comparison with the approximate analytical result is appropriate. Figure 64 gives the comparison for the case of Test D5-1. It is clear from this illustration that among the list of assumptions in Section 5.4.1 there is some combination that contributes to the introduction of significant errors.

An observation of interest is that the calculated oscillations in the strain in the specimen at the deadman end are of approximately the same period as oscillations found in the force traces. It can be seen from the wave plotting diagram that these oscillations are, at least in part, due to repeated reflections between the opposite ends of the overlay reinforcement at the deadman end of the specimen. It is also apparent that the deadman force-time history has a first order dependence on the nature of all discontinuities, even those at stations remote from the deadman end.

If wave propagation effects are neglected, that is, the tensile force in the specimen is assumed the same at all stations, then the deadman force as a function of time would be represented by the straight line in Figure 64. It can be seen that this representation is not adequate and that wave propagation effects must be included for accurate structural analyses of pilot parachute risers.

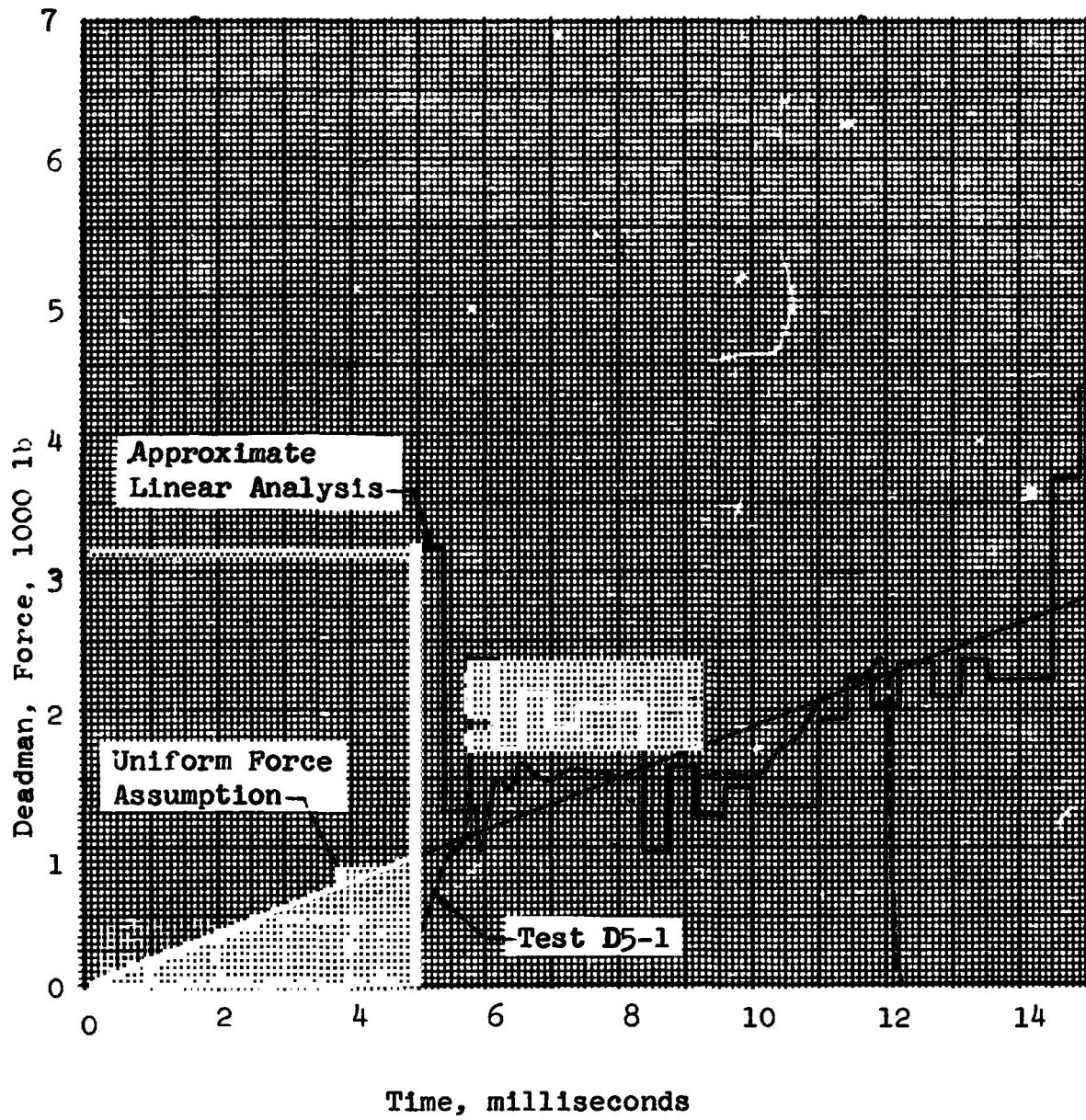


Fig.64 . Deadman Force as a Function of Time.
Specimen Type D5.

5.4.5 Effect Of Finer Resolution Of Discontinuities

In order to determine the effect of including the details of the construction of the outboard end of the deadman end reinforcement in Specimen Type D5, another wave diagram was constructed. The parameters used in this fine lumping case are listed in Table 8 . The results of this calculation are compared with the early time results ($t < 1.2$) of the previous calculation in Figure 65. Examination of this figure shows that the effect of the finer resolution is to decompose each step into a sequence of smaller steps and to increase the magnitude of the initial jump in strain. The magnitude of these effects is much less than the magnitude of discrepancies in the previous results. Therefore, the lumping of discontinuities is not considered a significant source of error.

5.4.6 Observations Regarding The Approximate Analysis

- a) The discontinuities in the specimen affect the strain history at all stations in the specimen.
- b) All stations in the specimen are subjected to cycles of loading and unloading. Therefore, hysteresis effects must be considered.
- c) The stress at some station away from the ends of a uniform section of webbing may become greater than the stress at either end.
- d) Multiple failures are to be expected in destructive tests.
- e) Wave phenomena must be considered in the analysis of the riser dynamics tests. The uniform force assumption is not suitable.
- f) This approximate model is not an adequate representation of the real system.

Table 8 . Parameters for Fine Resolution of
Discontinuities in Specimen Type D5

Section	Left Station (in.)	Right Station (in.)	Lineal Density (sl/ft)	Stiffness (lb)	Wave Velocity (ft/sec)
1	0.00	95.00	.00115	24,800	4640
2	95.00	263.50	.000574	12,400	4640
3	263.50	264.50	.00115	24,800	4640
4	264.50	265.50	.00172	37,200	4640
5	265.50	276.00	.00230	49,600	4640

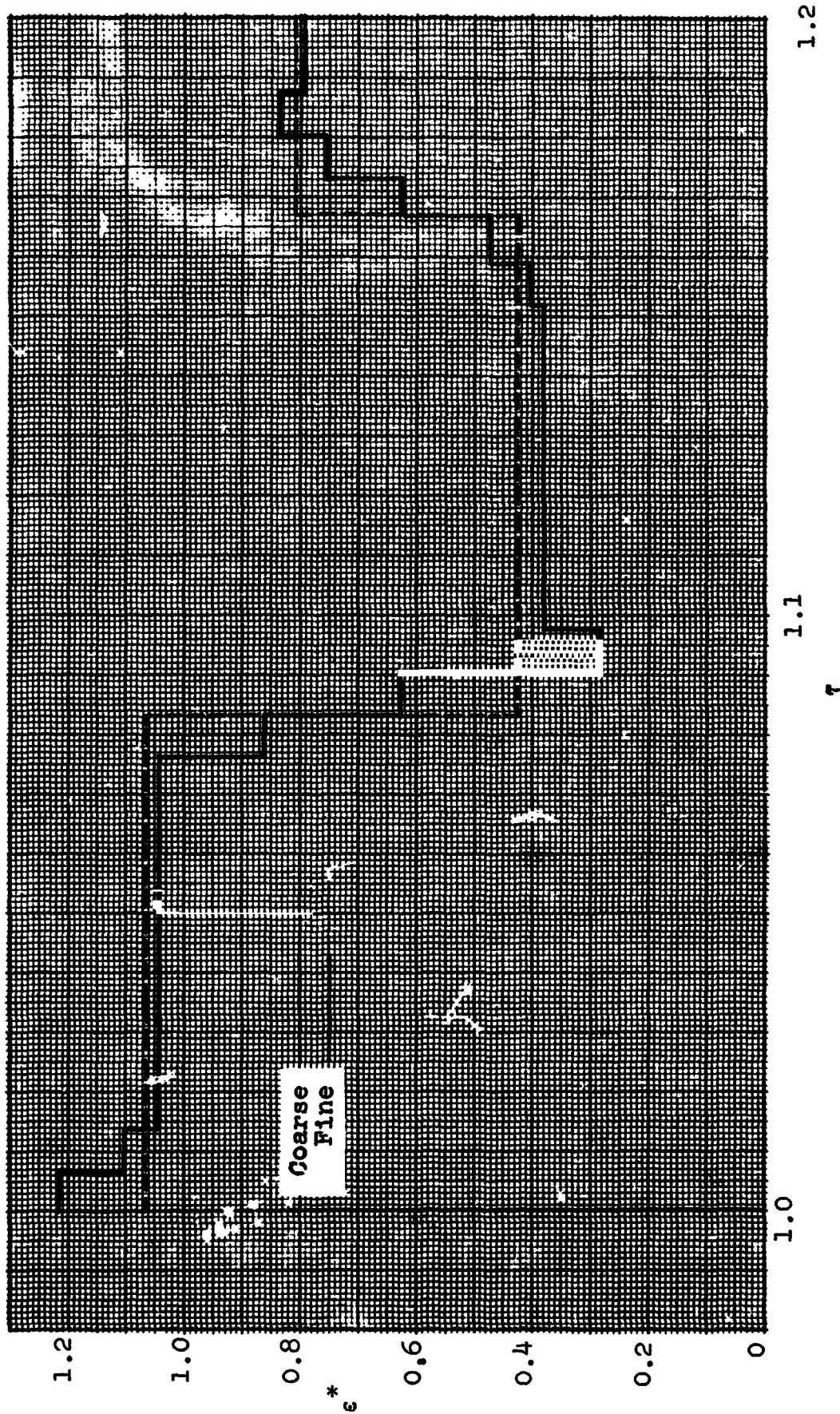


Fig. 65 . Strain at Deadman End of Specimen for the Cases of Coarse and Fine Resolution of Discontinuities

5.5 The Finite Difference Method

Section 5.4 contains a list of assumptions which, when applied to the riser dynamics test analysis, leads to unsatisfactory results. If these assumptions are revoked, the complexity of the resulting analysis increases to a level at which the use of high speed digital computers becomes a necessity.

Digital computers may be applied to this problem in three ways.

- (a) Integration of the equations of motion of an approximate system consisting of a string of mass elements connected by suitable force generating elements, which would be linear springs in the linear-elastic case.
- (b) Application of finite difference techniques to the direct integration of the system of equations of motion, continuity equations, equations of state and boundary and initial conditions.
- (c) Application of the method of characteristics.²⁹⁻³¹

Methods (a) and (b) are equivalent and possess the disadvantage that spurious oscillations are introduced into the wave profiles. Reference 33 presents a modification of method b) in which the concept of artificial viscosity is introduced to suppress these oscillations. The availability of a computer program (AFTON) which implements this modification of method b) led to the selection of this method as the analytical procedure of analysis to be used in this study.

An area of progress in this effort has been in the study and modification of the AFTON program. This program, which is described in Reference 34, computes longitudinal wave motion in one-dimensional continua by solving the finite difference

forms the appropriate hydrodynamic equations. Several required program modifications have been made.

The program was updated so that it would run on the Northrop IBM 360/65 computer. The logic was corrected so that the program would properly calculate the motions of the type observed in the laboratory tests. Also, extensive modification was completed that would allow simulation of the elimination of riser material as it passed on to the impact wheel rim. Within the duration of a typical laboratory test, a large portion of the riser sample passed onto the rim. Therefore waves must be made to reflect from the rim of the flywheel rather than from the loop end of the riser. The program logic has been changed so that it can accommodate this unusual situation.

A shortcoming of the finite difference method is that, in order to avoid the fluctuations behind a wave front as observed in the lineal spring-mass model, an "artificial viscosity" is introduced into the computation. This artificial viscosity has the (undesirable) effect of spreading an infinitesimally thin wave front (as occurs in the elastic case) into a computed wave front of finite thickness. In other words, after the continuum has been discretized into zones, the artificial viscosity causes wave fronts to be smeared over the length of several zones. This is undesirable because there were processes, sometimes important, which took place over lengths much shorter than program zone lengths. Thus, the situation is as follows. In order to reduce or eliminate the fluctuations after a wave front has passed, the artificial viscosity must be increased. But increasing the artificial viscosity smears the wave front over a greater number of zones, causing the loss of fidelity of processes over short lengths. This fidelity can be improved by increasing the number of zones in a given length, thereby reducing the actual length over which the wave front is smeared.

But such an approach has the disadvantage that the computation time increases almost proportionately with the square of the number of zones. So an attempt has been made to assess the trade-offs between residual fluctuations, wave front smearing and computation time; and to choose values of 1) the number of zones and 2) the Richtmyer-von Neumann³³ artificial viscosity constant that give reasonable results in terms of problem requirements.

An adequate number of combinations of zone length and artificial viscosity were tried to allow their respective influences to be estimated for the range studied. Stated otherwise, given limits on load overshoot and wave front smearing, satisfactory values of zone length and artificial viscosity can be chosen, and computer time can be estimated. Unfortunately, the shortest lengths (1 in.), which occur in the tapered joints, and which are believed to be important, cannot be modeled in the AFTON program because they are too short. Therefore, it will probably have to suffice to include the effects of the next shortest pieces, which are 1 ft in length.

Figure 66 is included to illustrate a typical calculation done by the AFTON program. The trace represents the force wave profile at one instant in time. This particular calculation is for the combination of 398 elements in a 23-foot uniform elastic sample and an artificial viscosity constant of 2.56. It shows both the overshoot and wave smearing described above.

The AFTON program was used to calculate the force gage response of Tests D3-2 and D5-1 for the case in which several of the linear-elastic approximate case assumptions listed in Section 5.1 are revoked. The changes with respect to the linear-elastic

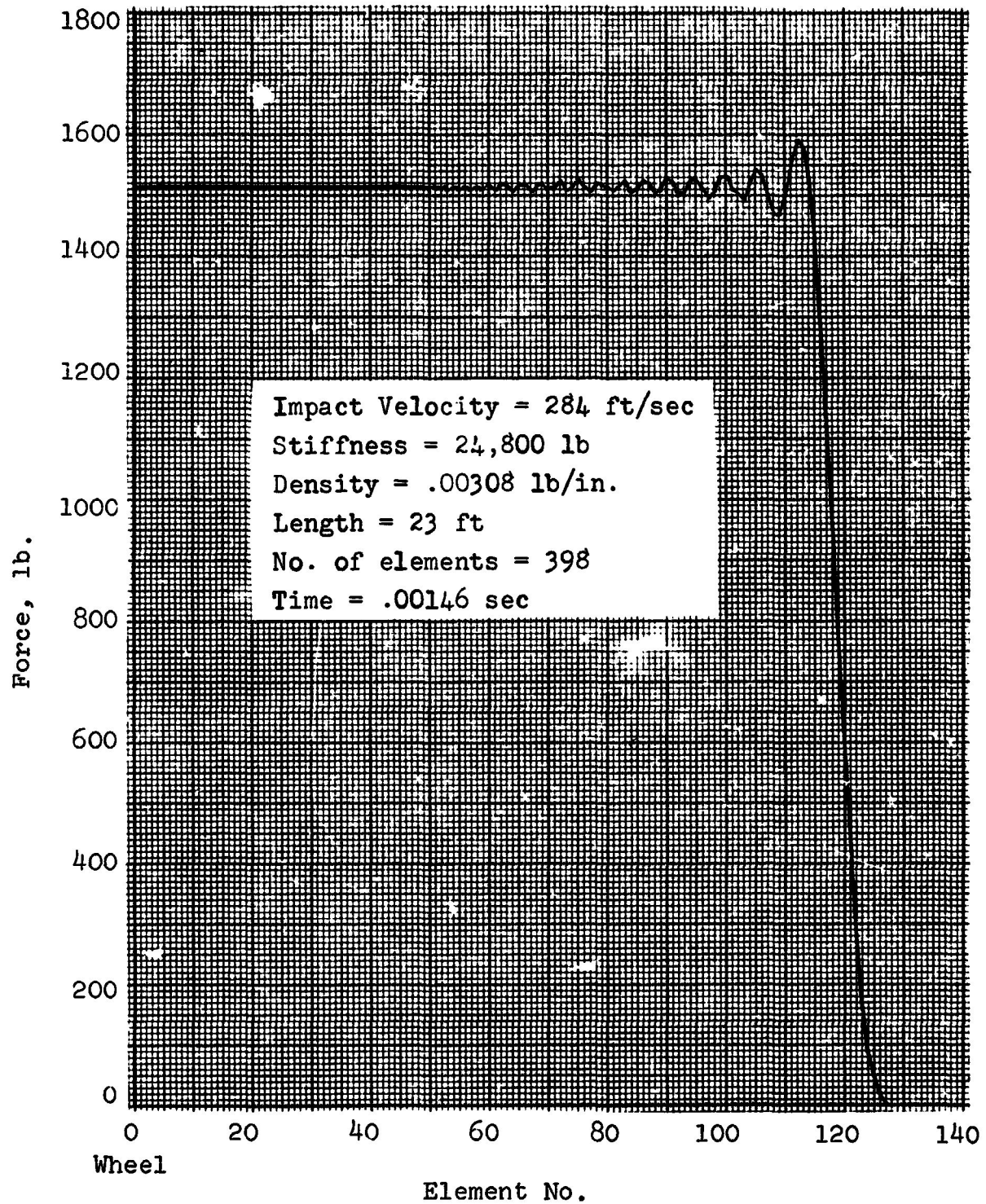


Fig. 66. Wave Profile Determined by the AFTON Program for the Case of a Uniform Specimen.

approximate case that were made are listed below using the respective Section 5.4.1 identification letters.

- a) The material is assumed to follow the non-linear static load-strain curve in an elastic manner
- b) No change
- c) The impact wheel rim speed is allowed to decay due to the reaction force of the specimen
- d) The bridle is wrapped on to the wheel rim
- e) Large displacements are allowed
- f) No restriction on magnitude of wave propagation velocity relative to particle velocity
- g) No change
- h-k) No change

Figures 67 and 68 are comparisons of the calculated force traces with the experimental curves. Since the zero time reference of the force gage data is unknown, the curves are indexed with respect to the first significant peak. Due to the presence of a short concave downwards portion near the origin of the load-strain curves, the computed force traces display a "precursor wave" effect prior to the arrival of the sharp edged wave associated with the concave upwards portion of the load-strain curves. Some of the experimental curves in Section 5.3 possess this feature but it is not as pronounced as in the calculated curve, perhaps due to viscoelastic

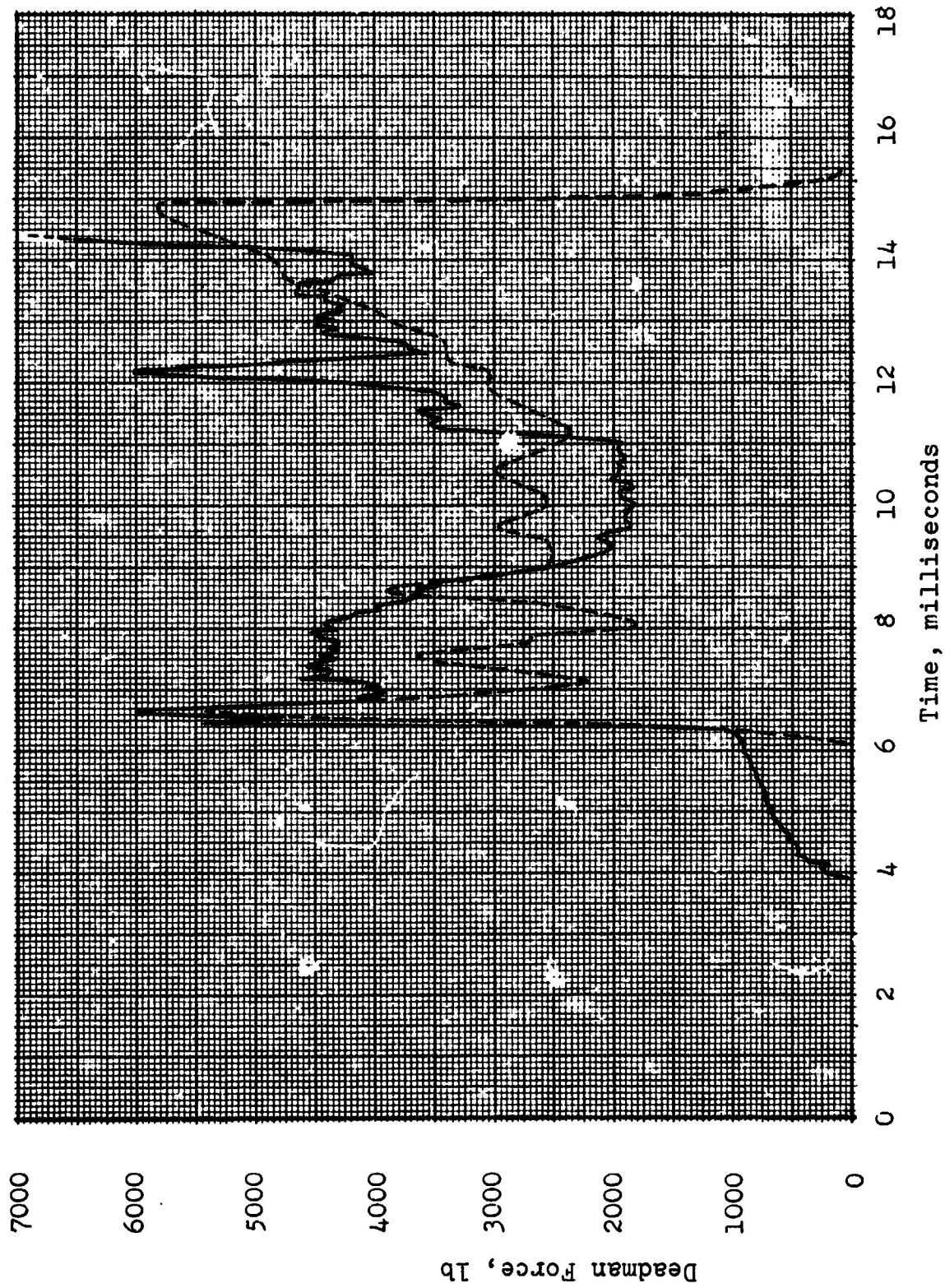


Fig. 67. Comparison of Experimental Results with Deadman Force Computed by AFTON program, Test D3-2. AFTON is Solid Line, Experimental is Dashed Line.

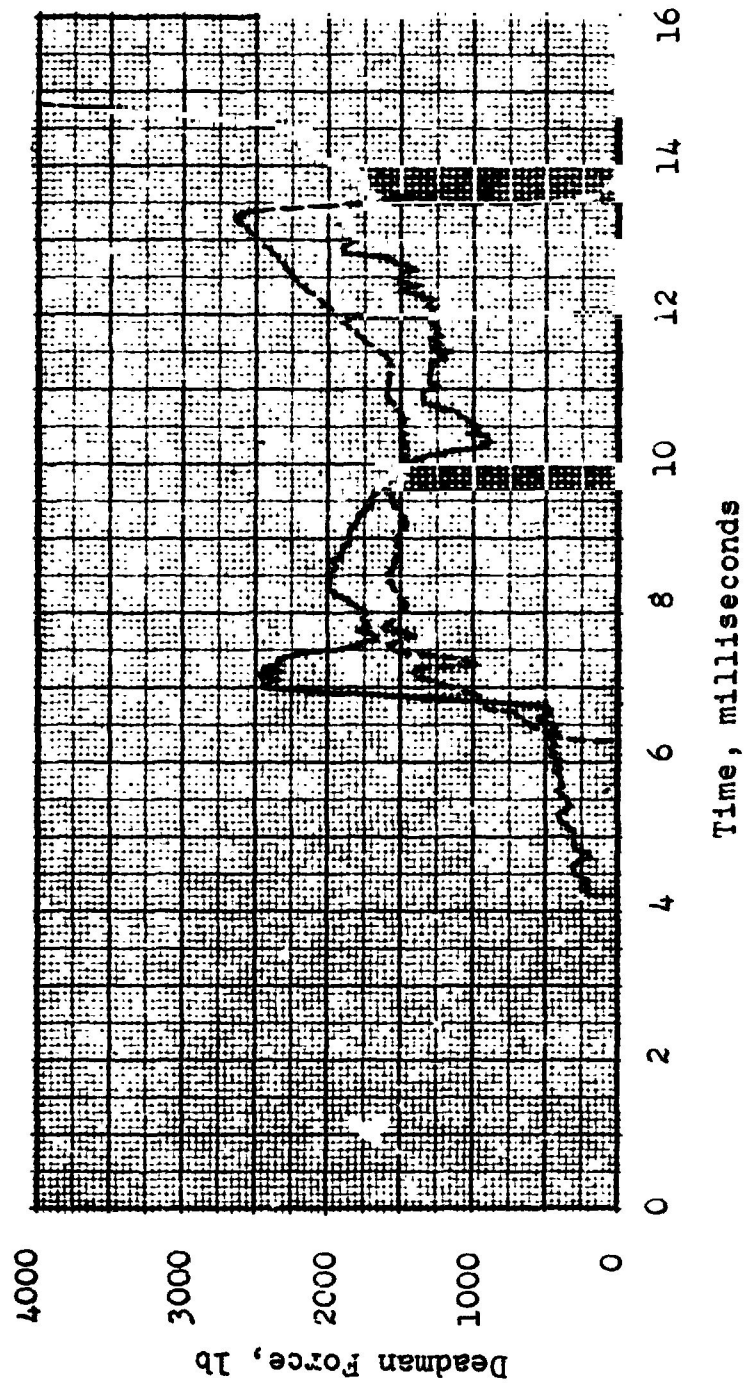


Fig. 68. Comparison of Experimental Results with Deadman Force Computed by AFTON Program, Test D5-1. AFTON is Solid Line, Experimental is Dashed Line.

NOTES

effects. In the case of test D3-2, following the precursor, the experimental and calculated curves have roughly the same general shape but it is clear that among the assumptions remaining, there exists some combination that is not justified.

In the case of Test D5-1, the initial oscillations following the precursor effect are more faithfully represented than in the case of the linear-elastic approximation (Fig. 64) and the later portion of the force trace is represented approximately as well if the time scale for the calculated curve is contracted by a factor within the range corresponding to the intertest variations in wave velocity reported in Section 5.6. However, the results for Test D5-1 confirm the need for an improved mathematical model.

5.6 ANALYSIS OF FILMS

Seven film sequences have been analyzed. Section 5.6.1 is an in depth review of one film sequence and Section 5.6.2 is a comparison of wave velocities and webbing strains as measured from all seven film sequences.

Reference 35 shows that for some materials with nonlinear load-strain diagrams the strain wave front will have a non-zero thickness and will change in shape as it progresses along the specimen, that is, each strain level may propagate with a different velocity. If this type of motion existed in the riser dynamics tests, it was not detected in the films due to the level of resolution imposed by the film framing rate. Therefore, the wave velocities obtained from reduction of the film data are referred to in the following as "apparent wave velocities" because they describe a gross effect rather than the fine details of the motion.

5.6.1 Analysis Of Test No. D5-1

Longitudinal Waves, Particle Velocities, Strain

Figure 69 is a plot in position-time space of the events occurring prior to failure in Test No. D5-1. The horizontal axis is distance from the deadman support and the vertical axis is time from the arbitrary beginning of the film sequence. The left boundary represents the point at which the bridle of the specimen is feeding on to the rim of the wheel. The right boundary represents the point at which the webbing is attached to the force gage link.

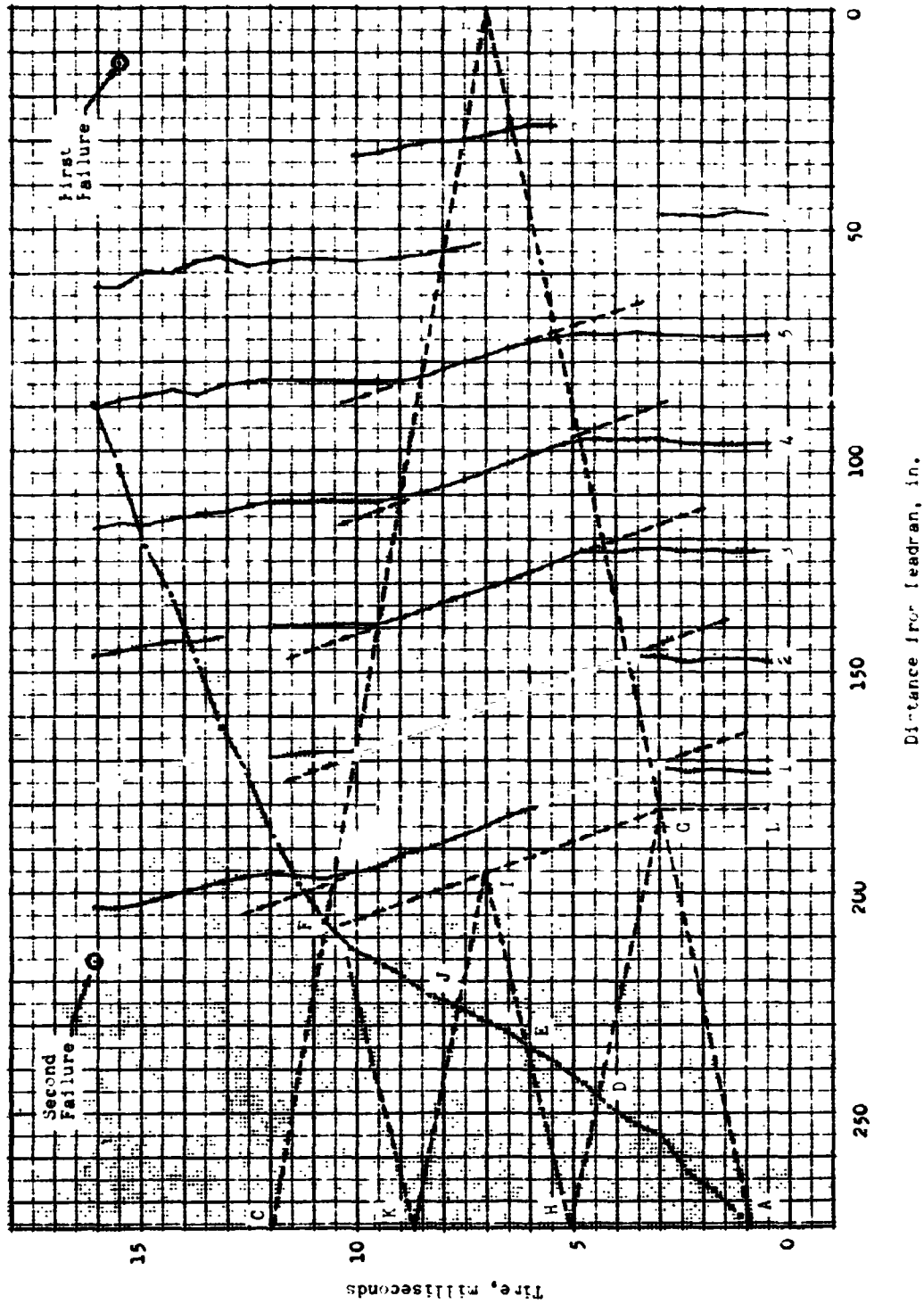


Fig. 69 . Space-Time Diagram, Test D5-1

The solid lines show the paths of the gage marks. Gaps indicate loss of data due to obscuration of gage marks by twisting of the specimen or poor contrast with the background. Discontinuities in the slope of these lines indicate the passage of a strain wave. The locus of the leading sweep of the strain wave along the length of the specimen has been drawn in as the line AB which is judged to be the straight line which passes most closely through all of the initial major discontinuities in the gage mark curves. The slope of line AB indicates an apparent wave propagation speed, $(c_l)_{AB}$, of 3790 ft/sec.

The intersection of this straight line with the left boundary of the plot gives an estimate for the time at which the wheel hook engaged the loop at the end of the specimen. In this case $t_0 = 0.9$ milliseconds. A similar straight line BC drawn through the second major slope discontinuities in the loci of the gage marks reveals a reflected wave traveling from the rigid support back towards the wheel rim. The slope of this line indicates a wave propagation speed, $(c_l)_{BC}$, of -4630 ft/sec relative to the laboratory.

Prior to the arrival of the wave AB, the gage mark loci are vertical, indicating that the webbing is stationary until the wave arrives. The action of the passage of the wave AB is to introduce a nearly constant velocity as indicated by the nearly constant slope in the gage mark loci between lines AB and BC. The velocity of the webbing relative to the laboratory indicated by the best fit slopes between lines AB and BC are given in Table 9.

The velocities of gage marks 1, 2, 3, 4, 5 differ from the wheel impact velocity of -275 ft/sec by less than 7 percent. At gage number 7, the velocity is considerably different from the impact velocity, probably due in part to the comparable

Table 9. Gage Mark Velocity After Passage of
First Wave, Test D5-1

Gage Mark Number	Velocity (ft/sec)
1	-294
2	-294
3	-294
4	-294
5	-272
6	--
7	-200
Average	-275

magnitudes of the time between the passage of the two waves and the time between exposures in the test films which gives an insufficient sampling for the accurate determination of velocity at gage number 7.

The average strains between gage marks between the passage of waves AB and BC can be computed from the distance between gage marks before and after the passage of wave AB and are tabulated in Table 10. The strain in the specimen after the passage of the second wave and the strain at the time of the first failure are also shown in Table 10.

For the webbing material on which the gage marks are placed, the ultimate static strain is given as 0.23 (Figure 52). The maximum strain discovered between the waves AB and BC is 57 percent of this value, after the wave BC it is 32 percent and at the time of failure it is 90 percent.

It is of interest to compare the velocity of the waves AB and BC relative to a coordinate system fixed to the specimen (the "Lagrangian velocity") with the velocity predicted by the linear elastic analysis. Using the results of Fenstermaker and Smith³², the Lagrangian velocity c of a longitudinal wave is given by

$$c = \frac{1}{1 + \epsilon} (c_l - V)$$

where ϵ is the strain in the material into which the wave is traveling, c_l is the wave velocity with respect to the laboratory and V is the velocity of the material into which the wave is propagating. Using as V the average gage mark velocity after the first passage of the wave and as ϵ the respective average of the strains between the gage marks, apparent Lagrangian velocities are:

$$(c)_{AB} = \frac{1}{1 + 0} (3790 + 0) = 3790 \text{ ft/sec}$$

$$(c)_{BC} = \frac{1}{1 + .0906} (-4630 + 275) = -3990 \text{ ft/sec}$$

Table 10. Webbing Strain, Test D5-1

Between Gage Marks...	Strain		
	Between First Two Waves	After Second Wave	At Time of First Failure
1 and 2	.0924	.109	.160
2 and 3	.1304	.189	.207
3 and 4	.0598	.128	.179
4 and 5	.0796	.150	.186
5 and 6	-	.064	0 \pm

The theoretical wave velocity calculated from the "secant" approximation used in the linear-elastic analysis gives a Lagrangian velocity equal to 4650 ft/sec for both waves. The first wave AB propagates with a velocity that is 82 percent of the linear-elastic case and the reflected wave BC propagates with a velocity equal to 86 percent of the linear-elastic case. However, it is shown in Section 5.6.2 that apparently equivalent test conditions produced large variations in wave velocity.

Following the passage of wave BC, the velocities of the gage marks in general reduce to values quite small relative to the impact velocity and at later times a trend toward the impact velocity is visible. As seen in the diagram resulting from the graphical wave plotting technique for the linear-elastic case (Figure 61), the wave action becomes quite complicated above the wave BC. Due to the limitations imposed on resolution of the motion by the camera framing rates, this complex wave motion cannot be traced above the line BC.

Transverse Waves

In addition to the longitudinal motion discussed above, a lateral motion of the specimen is introduced by the action of the impact wheel hook on the specimen.

The x-dash line in Figure 69 is the locus of the leading edge of the resulting lateral wave that propagates along the specimen with an initial velocity that is considerably less than the previously determined velocity of propagation of longitudinal waves. Extrapolation of this locus back to the left boundary gives $t_0 = 0.9$ milliseconds, the same value obtained by extrapolation of wave line AB.

It can be seen in Figure 69 that the locus of the transverse wave front from A to F (in the bridle portion of the specimen)

is not a straight line, indicating that the transverse wave velocity is not a constant. The reason for the variation in transverse wave velocity can be determined by inspection of the graphical wave tracing diagram for the linear-elastic case, Figure 61, where it can be seen that there exist reflected waves GH, HI, IK and KF that generate variations in the bridle webbing force which in turn produce variations in the velocity of propagation of the transverse wave.

The Lagrangian transverse wave velocity (Reference 32) is given by:

$$c_T = \sqrt{\frac{F}{\rho_0 (1 + \epsilon)}} \quad (65)$$

where F is the tensile force in the webbing, ρ_0 is the unstrained lineal mass density and ϵ is the strain in the material ahead of the leading edge of the transverse wave. The velocity relative to the laboratory is given by

$$c_{LT} = (1 + \epsilon) c_T + V \quad (66)$$

where V is the longitudinal velocity of the material in which the transverse wave is propagating.

An attempt is made here to explain the curvature in the locus of the transverse wave in the bridle by performing a computation based on best available estimates of the governing parameters.

- a) The locus of the end of the bridle is estimated by drawing a line (GF) parallel to the locus of the leftmost gage mark and passing through the intersection of the wave AB with the locus (GL) of the bridle end prior to the arrival of the wave.

- b) The actual reflected waves GH, HI, IK and KF are approximated in Figure 69 by using the slope of the initial wave AB in their construction.
- c) The longitudinal strain levels in the material into which the transverse wave is propagating are computed from the impact velocity, the observed wave velocity and the longitudinal strain wave amplitudes shown in Figure 51 for the linear-elastic case.

$$\epsilon_{AD} = \frac{V_o}{c} = \frac{275}{3790} = .0726$$

$$\epsilon_{DE} = .6667 \quad \epsilon_{AD} = .0484$$

$$\epsilon_{EJ} = .3333 \quad \epsilon_{AD} = .0242$$

$$\epsilon_{JF} = .4444 \quad \epsilon_{AD} = .0323$$

- d) The velocity of the webbing at any point in the test specimen is given by

$$V(x) = V_o + \sum_i \left[c (\epsilon_R - \epsilon_L) \right]_i \quad (67)$$

where ϵ_L and ϵ_R are the strain levels on the left and right side of the i th strain wave respectively and the summation is over all strain waves between the left (impact) end and the point in question. The webbing velocities for each segment of the AF portion of the transverse wave locus are therefore,

$$V_{AD} = V_O = -275 \text{ ft/sec}$$

$$\begin{aligned} V_{DE} &= V_O + (c)_{AB} (0.3333) (\epsilon_{AD}) \\ &= -275 + (-3790) (0.333) (0.0726) = -367 \text{ ft/sec.} \end{aligned}$$

$$V_{EJ} = V_O = -275 \text{ ft/sec}$$

$$\begin{aligned} V_{JF} &= V_O + (c)_{AB} (-.1111) (\epsilon_{AD}) \\ &= -275 + (-3790) (-.1111) (.0726) = -245 \text{ ft/sec} \end{aligned}$$

- e) The effective stiffness of the bridle is taken to be that value of bridle stiffness which gives the observed AB longitudinal wave velocity in a linear-elastic webbing

$$c = \sqrt{\frac{k}{\rho}} \quad (68)$$

Solving for k ,

$$k = \rho c^2 \quad (69)$$

For the bridle, $\rho = .00115$ slugs/ft so that

$$k = (.00115) (3790)^2 = 16,500 \text{ lb}$$

- f) With the addition of the linear expression for force

$$F = k \epsilon \quad (70)$$

all necessary information for the computation of c_{LT} , the transverse wave velocity with respect to the laboratory, is available. Substituting into Equations (65) and (66) there is obtained

$$(c_{l_T})_{AD} = 780 \text{ ft/sec}$$

$$(c_{l_T})_{DE} = 485 \text{ ft/sec}$$

$$(c_{l_T})_{EJ} = 320 \text{ ft/sec}$$

$$(c_{l_T})_{JF} = 446 \text{ ft/sec}$$

- g) Using these values of c_{l_T} , the locus of the transverse wave can be constructed in stepwise fashion. The result is shown in Figure 70 as the dash line ADEJF. The actual locus is shown as x's.

The close proximity of the two curves implies that for the type of webbing used in the bridle and for the stress levels existent in these tests, Equation (65) gives a good prediction of the transverse wave velocity and the noted curvature of the transverse wave locus in the bridle is to be expected.

At Point F (Figure 69), there occurs an increase in the transverse wave propagation velocity. It is apparent from the diagram that three contributory events occur almost simultaneously at Point F.

- a) The transverse wave passes from the bridle into the specimen trunk. The wave, therefore, moves into material with one-half of the lineal mass density of the bridle.

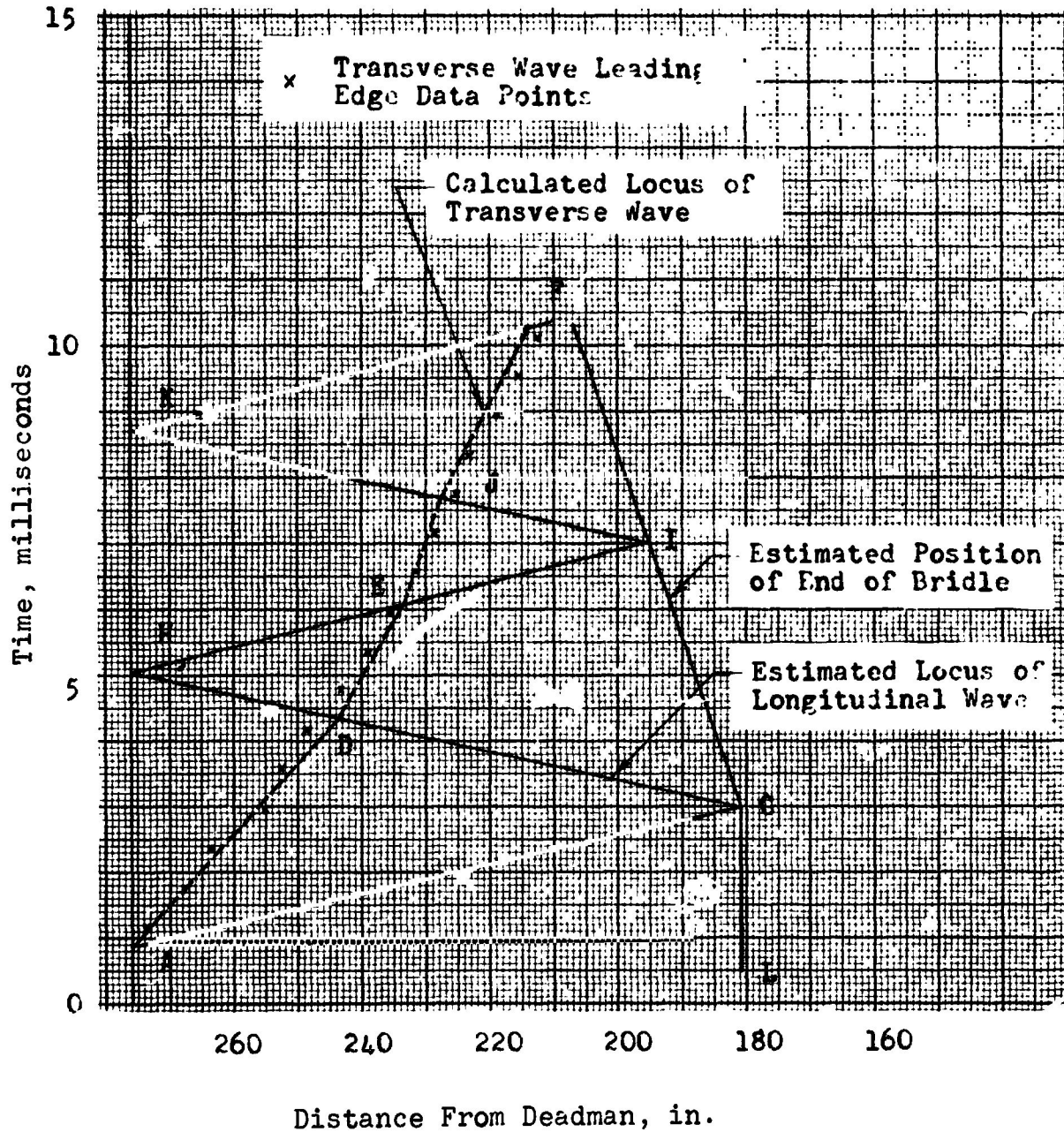


Fig. 70. Theoretical and Experimental Loci of the Transverse Wave in the Bridle, Test Type D5.

b) The positive strain wave BC arrives.

c) The positive strain wave KF arrives.

As can be seen from Equations 69 and 70, all three of these events have the effect of increasing the transverse wave propagation velocity. The multiplicity of wave fronts makes the application of the methods of calculation of the preceding section impractical in the trunk of the specimen.

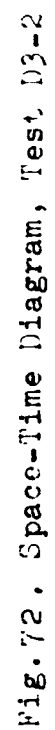
Further Observations

The two breaks are indicated by circles in Figure 69. The first failure occurs at the right end of the trunk section before the arrival of the transverse wave. The location of the second break with respect to the first implies that the second failure cannot be affected by the first without the imposition of unrealistic wave propagation velocities. The possibility of such multiple independent failures was indicated by the results of the approximate linear-elastic analysis in Section 5.4.

5.6.2 Variations In Longitudinal Wave Velocity and Strain

The films of similar tests on six additional specimens with the same trunk material as Test D5-1 were analyzed to determine the apparent propagation velocity of the first wave through the trunk and the average strain in the trunk after the passage of the first wave. The space-time diagrams obtained from the reduction of the respective film data are shown in Figures 71 to 76. The dashed lines in these diagrams are the best fit straight lines indicating the apparent wave motion and the motion of the gage marks. The apparent wave velocity, the

Fig. 71. Space-Time Diagram, Test D3-1



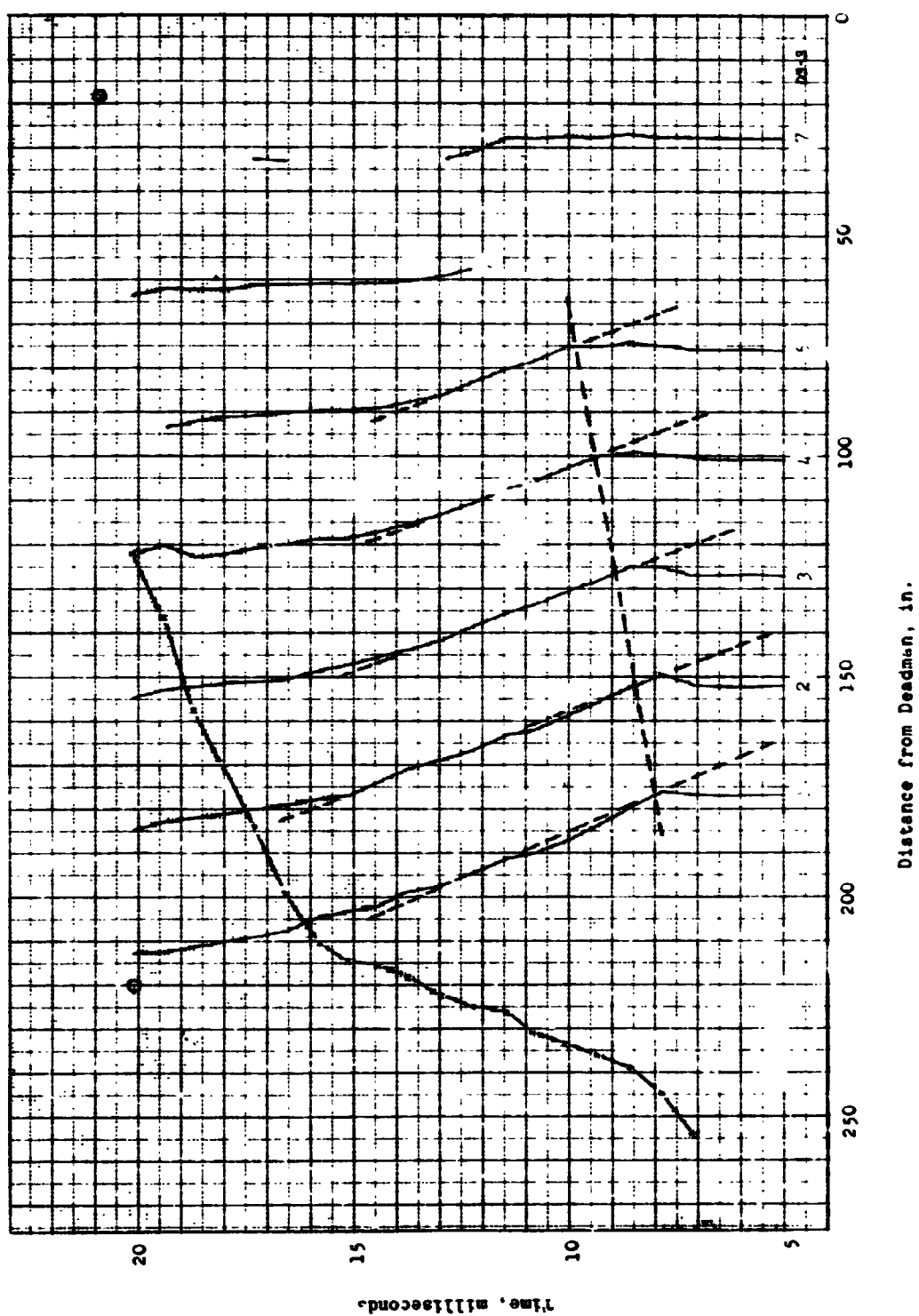


Fig. 73. Space-Time Diagram, Test D3-3

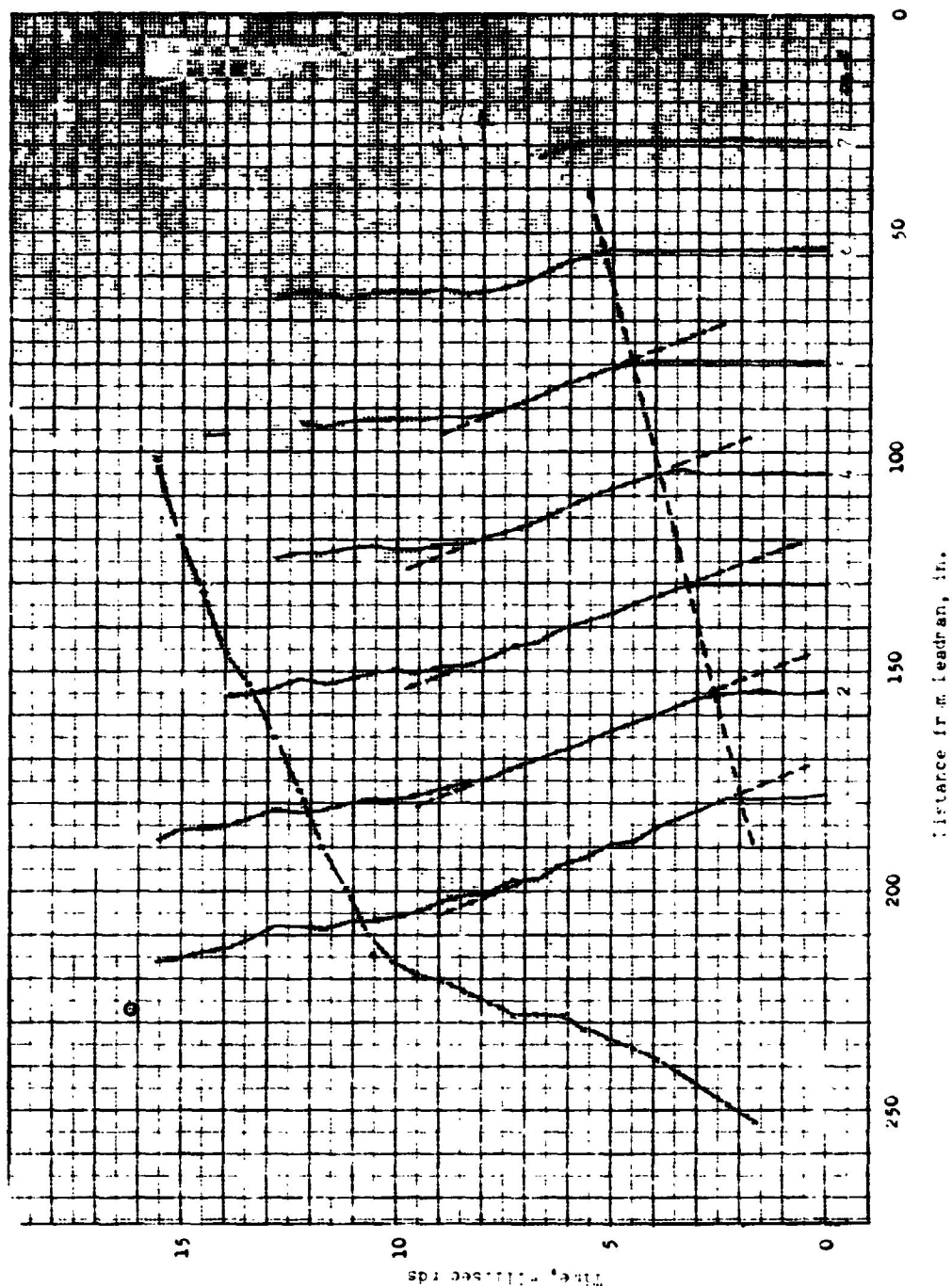


Fig. 74. Space-Time Diagram, Test D4-5

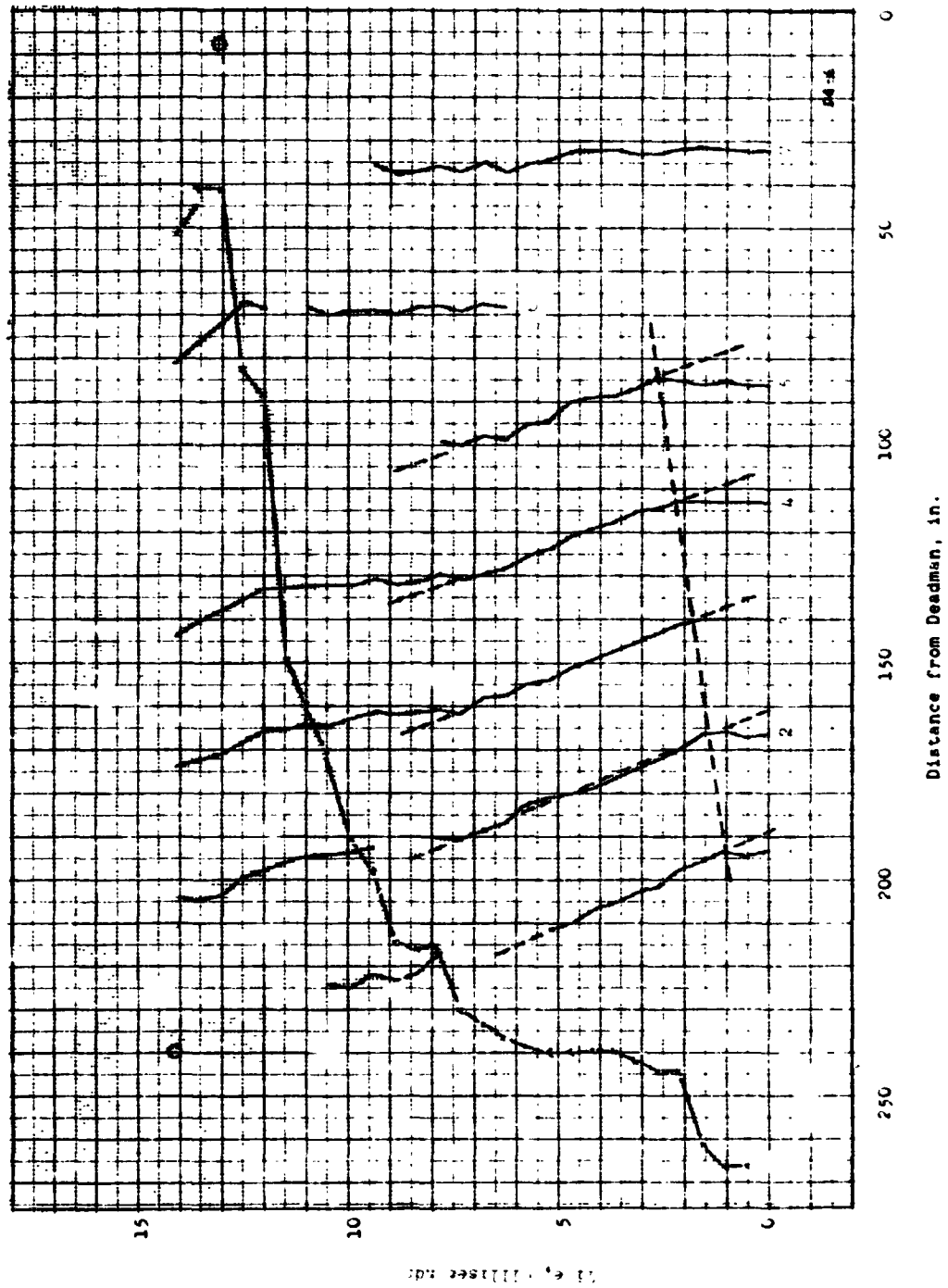


Fig. 75. Space-Time Diagram, Test D4-6

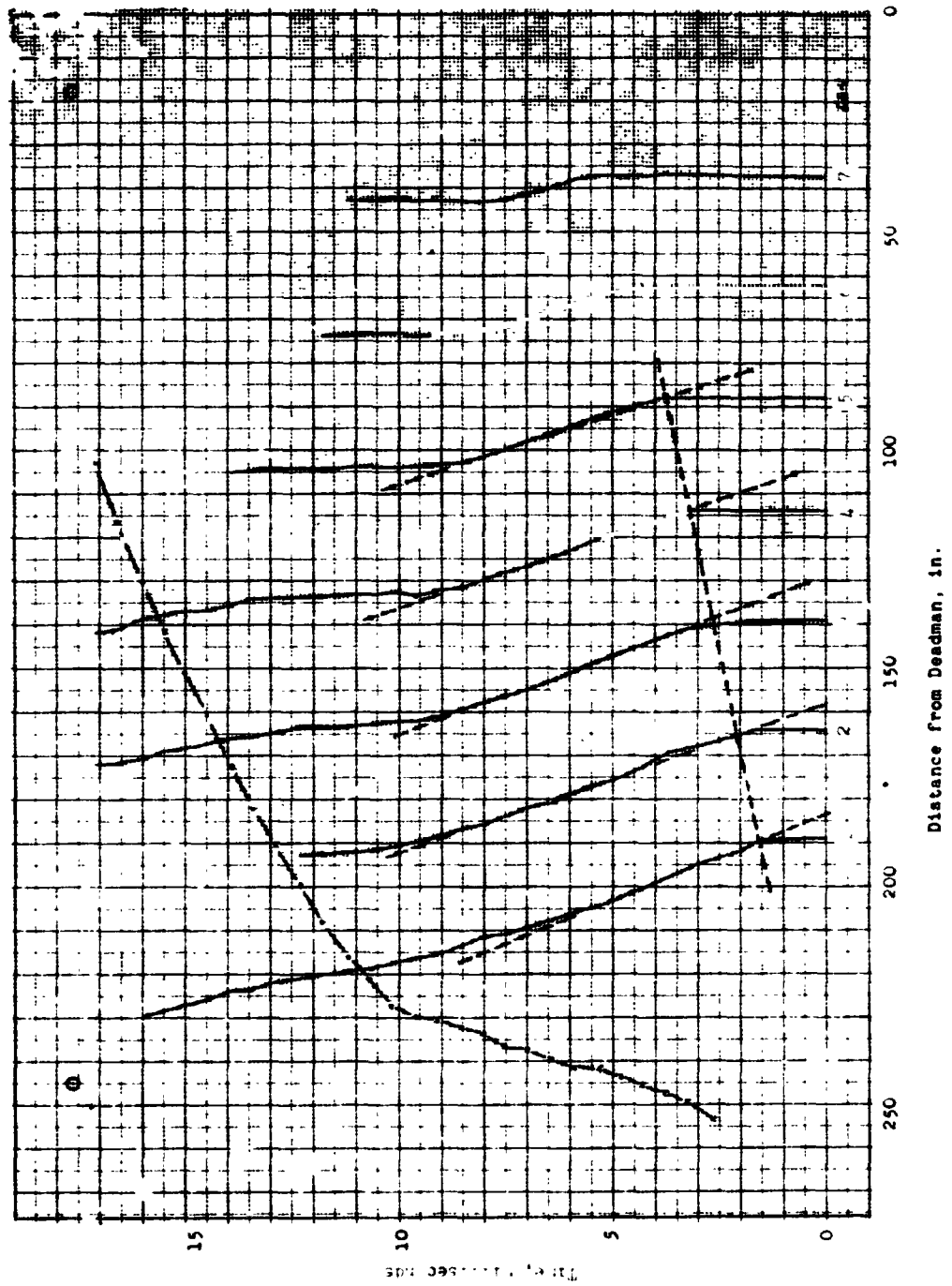


Fig. 76. Space-Time Diagram, Test Do-1

average strain after the wave, and the average particle velocity after the wave are displayed in Table 11. The entries are arranged in order of increasing average strain.

Table 11 shows large variations in apparent wave velocity and strain that do not appear to have any simple correlation with the only supposed variations between the tests, the impact velocity and the matching of the webbings in the trunk. However, there does appear to be a significant level of correlation between apparent wave velocity and strain; apparent wave velocity tends to increase as the strain decreases.

This trend is to be expected because according to References 36 and 37 the particle velocity v_i attained at station i in the specimen is given by the expression

$$v_i = \int_0^{\epsilon_i} c(\epsilon) d\epsilon \quad (71)$$

where ϵ_i is the longitudinal strain at station i and where $c(\epsilon)$ is the wave propagation velocity at the strain level ϵ .

The velocity c is given by

$$c(\epsilon) = \left(\frac{1}{\rho_0} \frac{\partial F}{\partial \epsilon} \right)^{\frac{1}{2}} \quad (72)$$

where F is the tensile force in the specimen and ρ_0 is the lineal mass density in the unstrained condition. It can be seen from Equation 71 that for approximately equal values of particle velocity v_i , large increases in wave propagation velocity must be accompanied by an appropriate decrease in the strain level attained behind the wave.

NORTHROP

Table 11. Comparison of Wave Velocities,
Particle Velocities and Strains

Test No.	Impact Velocity (ft/sec)	Wave Velocity (ft/sec)	Particle Velocity (ft/sec)	Strain	Particle Velocity, Eqn. 71, Static (ft/sec)
D3-3	-300	4700	-310	.069	-250
D4-6	-285	5550	-317	.070	-252
D3-1	-284	3040	-234	.080	-293
D6-1	-277	3850	-272	.090	-340
D5-1	-275	3790	-294	.091	-342
D4-5	-277	3230	-313	.093	-355
D3-2	-284	2550	-268	.123	-550

References 22 and 25 show that the dynamic load-strain curves, for some typical nylon yarns for the case of monotonically increasing strain at constant strain rate, approach a linear type of relationship as the rate of loading increases. Also, the slopes of the dynamic load-strain curves tend to increase with rate of loading. If the dynamic load-strain curves followed by the materials in these tests during the passage of the first wave are linear, then equation (71) becomes

$$V_1 = c\epsilon_1 \quad (73)$$

or

$$c = \frac{V_1}{\epsilon_1} \quad (74)$$

i.e., the product of the wave velocity and the final strain must be equal to the particle velocity in all tests.

Figure 77 is a plot of the left side of Equation 74 as a function of the quotient on the right side; one point is obtained for each test. If in fact the specimen trunk material did perform in a linear fashion during passage of the first wave then all of the points should fall on a line of unit slope passing through the origin. The scatter that is obtained is of the order of magnitude of the inherent errors in the determination of velocities by graphical differentiation of the data. However, there does appear to be a trend above the unit slope which could possibly be caused by a consistent small nonlinearity in the performance of the material.

It is now demonstrated that the performance of the trunk material is not governed by the static load-strain curve. This is done by using Equation 71 to compute the particle velocity using the static load-strain curve to compute $c(\epsilon)$ and the value of ϵ_1 attained behind the first wave. Since the static load-strain curve is concave upwards, shock wave effects must be taken into account as shown in References 35 and 37.

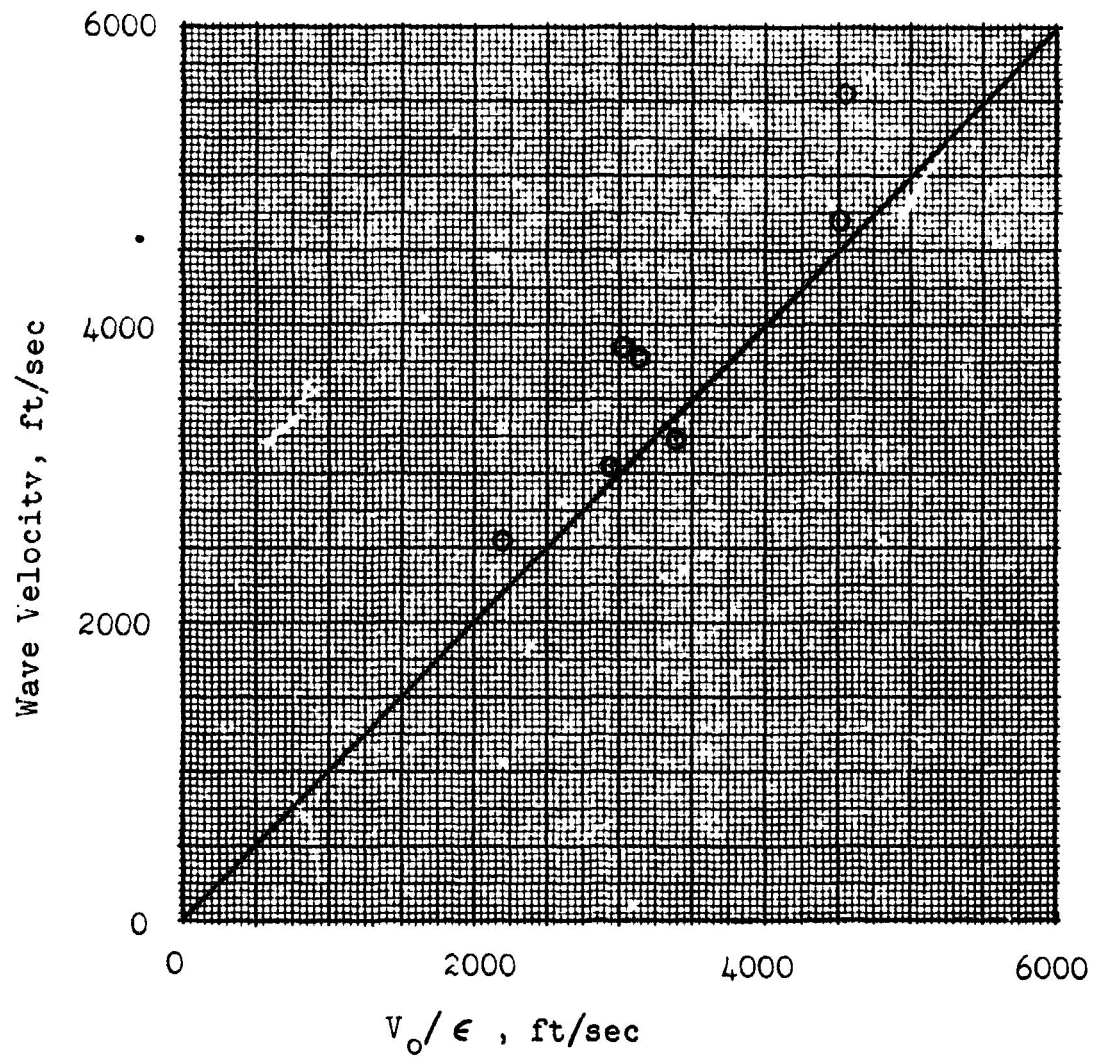


Fig. 77. Observed Longitudinal Wave Velocity vs. Wave Velocity Calculated on the Basis of a Linear Load-Strain Curve

Reference 37 gives an excellent set of examples of such calculations. The resulting values of particle velocity are given in the last column of Table 11 and there appears to be no correlation with the actual particle velocity as recorded in the fourth column of the same table. The implication is that the static load-strain curve is not in itself a valid predictor of the dynamic performance of nylon webbing.

As yet unresolved is the question of the source of the mutually consistent variations in wave velocity and strain. At the time of the writing of this report, it is believed that, even though the impact velocities were approximately equal, the rate at which the end of the specimen was accelerated to this velocity was different in each test due to variations in the construction of the impact loop, the initial shape of the loop and the manner in which it was engaged by the hook. If the dynamic load-strain curve of the specimen trunk material is a sufficiently strong function of the rate of loading, variations in apparent wave velocity and strain such as found in these tests are possible. Attempts to correlate wave velocity and strain with test environmental conditions and the amplitude of the transverse wave were fruitless.

5.6.3 Estimation Of The Dynamic Load-Strain Relationship

The velocities of the longitudinal and transverse waves and the longitudinal strain can be used to calculate the force in a specimen trunk in two regions of the space-time diagrams. When divided by the number of webbings in the trunk and plotted against the longitudinal strain in the respective region, the result is three points (one is the origin) on the dynamic load-strain curve followed by the material of each trunk in each test. Several assumptions are involved in the calculations. These assumptions are presented at the appropriate place in the following description of the procedure.

If it is assumed that the longitudinal wave shape remains constant as the first wave progresses across the specimen trunk, then, using the principle that the net force acting on the material particles containing the wave is equal to the rate of change of momentum introduced by the waves gives the following expression for the force in the specimen behind the first wave at station 1.

$$F_1 = -\rho_0 c_1 V_1 \quad (75)$$

Table 12 shows the quantities used in the calculation of force by this method and the result. The second and sixth columns give a single point on each load-strain curve.

Equations 65 and 66 can be solved for the force in the webbing to obtain

$$F = \frac{\rho_0}{1 + \epsilon} (c_1 T - V)^2 \quad (76)$$

This equation is used to compute the force in the webbing at the regions in space-time where the transverse wave locus intersects relatively smooth gage mark loci. The ingredients in the calculations and the results are displayed in Table 13.

The last two columns give an additional single point on each load-strain curve.

The resulting partial dynamic load-strain curves are shown in Figure 78. Two significant observations are that the dynamic load-strain curves in some cases lie below the static load-strain curve (shown as a dashed line) and that the material does not always follow the same curve in these tests. It is felt that the inherent scatter in the data causes the apparent variations in the sign of the curvature of the load-strain curves and does not permit the detailed inspection required to make conclusions regarding the degree of linearity of the dynamic load-strain curves.

NORTHROP

Table 12 Determination of Points on the Dynamic Load-Strain Curves
Using the First Longitudinal Wave Across the Specimen Trunks

Test No.	Average Strain	Lineal Density (sl/ft)	Wave Velocity (ft/sec)	Average Particle Velocity (ft/sec)	Force/ Webbing (lb)
D3-1	.080	.00115	3040	-234	409
D3-2	.123	.00115	2550	-268	393
D3-3	.069	.00115	4700	-310	838
D4-5	.093	.00115	3230	-313	581
D4-6	.070	.00115	5550	-317	1010
D5-1	.091	.000574	3790	-294	640
D6-1	.090	.00115	3850	-272	602

Table 13 Determination of Points on the Dynamic Load-Strain
Curves Using Transverse Wave Velocity

Test No.	Gage Marks Used	Wave Velocity With Respect to Laboratory (ft/sec)	Particle Velocity (ft/sec)	Strain	Force/ Webbing (lb)
D3-1	*				
D3-2	1,2	1486	-109	0.197	1220
D3-3	2,3	1625	-106	.186	1452
D4-5	2,3	1690	-107	0.145	1621
D4-6	2,3	2170	-117	0.160	2592
D5-1	2,3	1880	-99	0.184	1885
D6-1	3,4	1670	-155	0.218	1572

* Transverse wave locus does not intersect gage mark loci

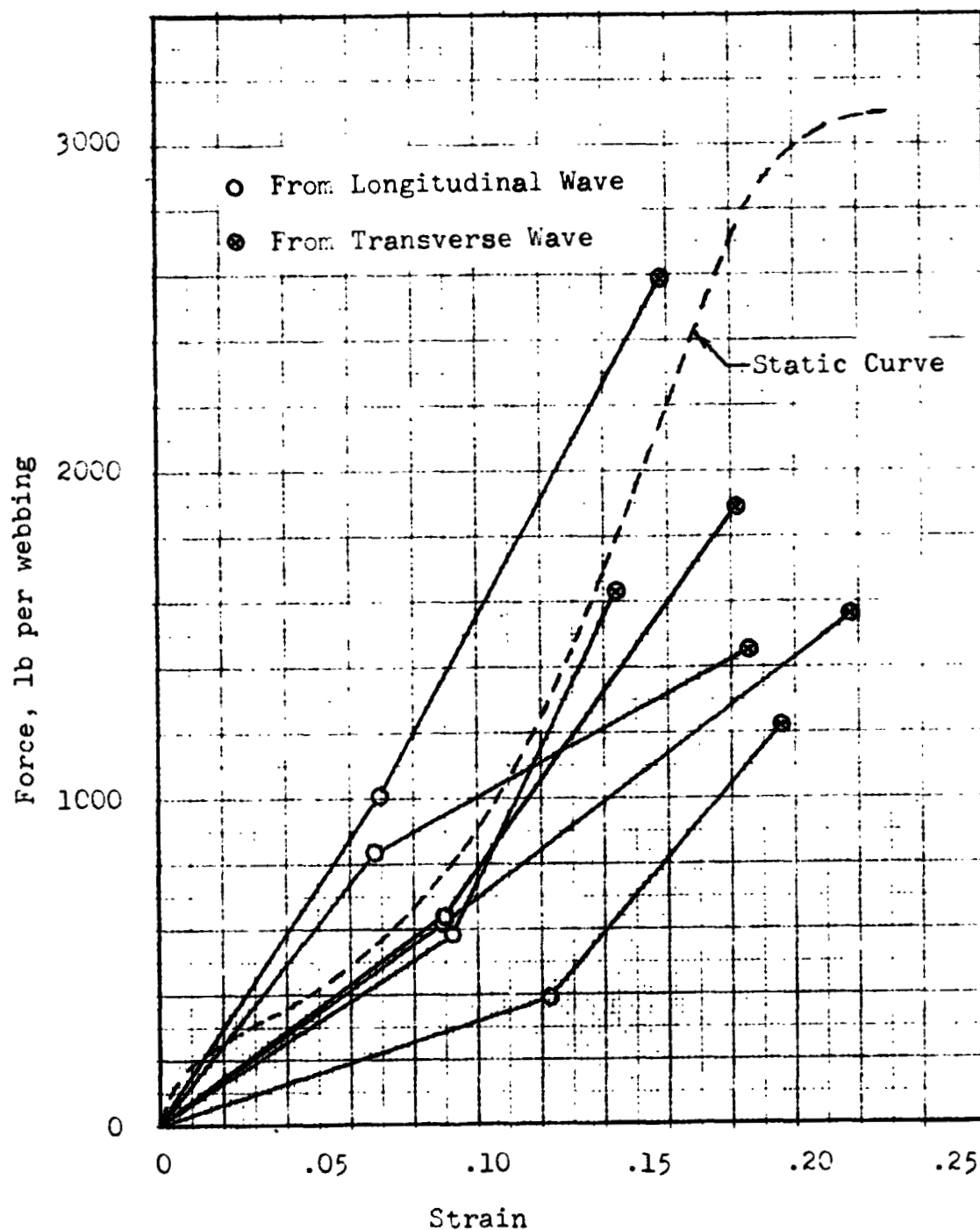


Fig. 78 Dynamic Load-Strain Curves for the Specimen Trunk Material as Determined From Wave Velocities

It should be emphasized that the load-strain curves displayed in Figure 78 are not for the usual case of monotonically increasing strain at constant strain rate. In fact, between the states indicated by the two points on each curve, the space-time diagrams indicate that for a significant interval the strain remains essentially constant.

5.7 SUMMARY OF PILOT CHUTE RISER DYNAMICS STUDY

It is shown that many aspects of the pilot chute riser test data can be explained with a linear-elastic approximate analysis. It is clear from this part of the study that wave phenomena must be considered in the structural analysis of parachute risers. That is, the mathematical model of the riser must take into account that the riser is a continuum, rather than a small number of lumped springs and masses. It is also shown that multiple failures and failures in free lengths are distinct possibilities in destructive tests and that the equation of state used in a riser dynamic analysis must take hysteresis effects into account. Comparison with experimental data shows that the linear-elastic approximation is not adequate for riser structural analysis.

A mathematical model which includes the inertia effects of the impact wheel, motion of the webbing around the impact wheel and the nonlinear static load-strain curve as the equation of state produces improved results. This mathematical model is analyzed using an existing finite-difference method computer program (AFTON) which is extensively modified to be compatible with the boundary conditions of the tests and to accept the nonlinear static load-strain curve of nylon webbing as an equation of state. Further refinement of the mathematical model is found to be necessary.

CONTINUED

A space-time diagram of one riser test is analyzed in detail with respect to the motion of the longitudinal and transverse waves and several other diagrams are analyzed in less depth. It is shown that the dynamic load-strain curves followed by the nylon webbing are approximately linear but small variations from linearity produce effects which cannot be neglected. The longitudinal wave speed appears to be sensitive to some as yet undiscovered variant in the tests, perhaps the nature of the impact loop.

REMARKS

SECTION 6.0

MEASUREMENT OF PRESSURES, LOADS, AND STRESSES

The types of measurements that are required to support the further development of the internal load prediction methods being developed for Apollo type parachutes are discussed in this section. These measurements are needed to provide input data for the internal loads analysis and to confirm the accuracy of the analysis.

During the current Apollo analysis study, the CANO stress analysis program has been refined into a powerful analytical tool. Section 6.1 discusses the CANO program input data requirements and shows how the experimental measurements to be made under the proposed test program will both provide these data and serve as a check on the validity of the method.

6.1 STRUCTURAL ANALYSIS DATA REQUIREMENTS

The analysis for determining the internal load distribution in a parachute under known external loading is given in Section 3.

Input data to CANO consists of parachute construction geometry, material load-strain curves, canopy differential pressure distribution, and applied riser load. Output includes loading and strains in radial tapes, horizontal members (sails or ribbons), suspension lines, vent lines, vent band, skirt band and reefing lines. In addition, a complete geometric definition of the parachute shape is obtained.

The CANO computer program is limited to symmetrical shapes, and it is assumed that the applied riser load is reacted by differential pressure acting normal to the local canopy surface.

For a given parachute construction there is a unique relationship between the internal stresses, the applied loading, and the geometry of the deformed canopy elements. This relationship is represented in the diagram of Figure 79a. Program CANO is arranged to proceed in the direction shown by the arrows in the diagram. The external loading, consisting of the riser load and a nondimensional pressure distribution curve, and the parachute construction details comprise the input data. The internal loading, consisting of a load for each element of the structural model, is the primary output. Definition of the canopy equilibrium shape and strains is a by-product of these computations.

The information in one block of Figure 79a is sufficient for determination of the other two. However, the accuracy of measurement that would be required to infer internal and external loading from the canopy geometry is beyond the practical limits of photographic analysis.

In the test program described in this report, it is planned that all of the parameters shown in the three blocks of Figure 79a will be measured. The redundancy thereby obtained will provide a check on the validity of the assumptions made in derivation of the analysis.

The external loading to be measured consists of the riser load and the differential pressure acting across the canopy surface. The riser force can be measured accurately by load links, but measurements of the differential pressure presents many difficulties. The practical limit for the number of pressure transducers in a test is about ten. In a ringsail parachute the pressure varies locally between the leading and trailing edge of each sail in addition to the general variation from skirt to vent. The redundant measurements of stress, strain, and shape will be valuable in deriving, from the limited pressure measurements, a pressure distribution curve which will give an accurate stress distribution for use in structural analysis.

NOTING

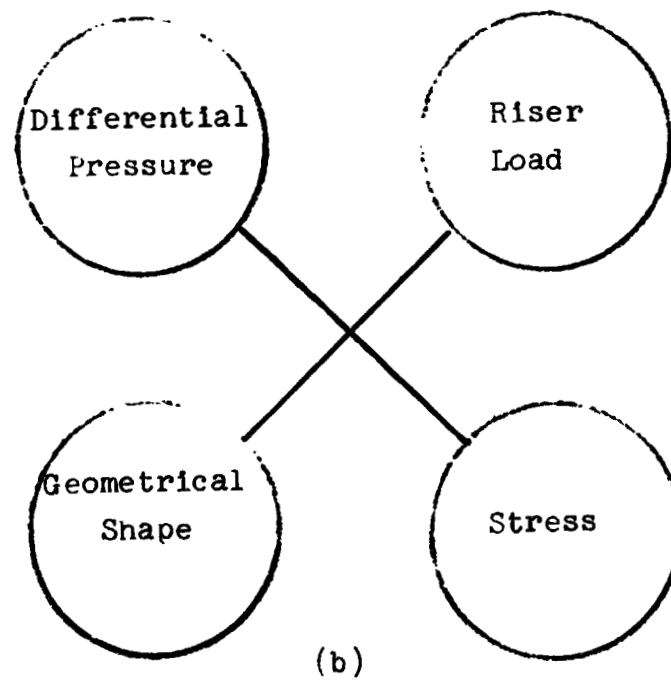
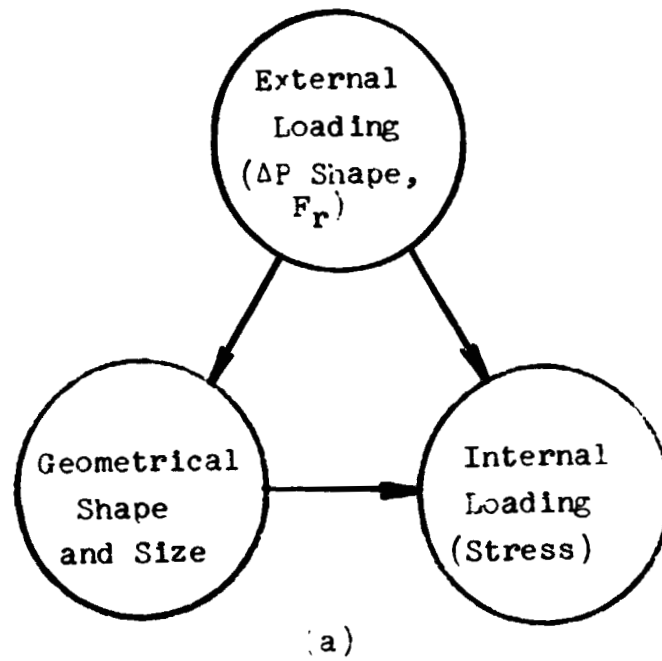


Fig. 79. CANO Program Input/Output Relationships

CONTINUED

If the external load block of Figure 79a is considered as two separate data groups, pressure distribution and riser load, the diagram shown in Figure 79b is obtained.

In Figure 79b any two blocks provide sufficient information for computation of the other two. The riser load measurement is the simplest and most reliable of the four. If it is assumed that this value is always measured accurately, the requirements for the other three measurements are less stringent. For the pressure differential and stress, only the shapes of the distribution curves are required. For the shape data, only the relative shape of the radial tape profile is necessary. This is helpful because absolute values for length measurements from photographs are the most difficult to obtain.

Since the magnitude as well as the distribution of the differential pressure will be measured, additional redundancy exists. The CANO program requires only the shape of the pressure distribution curve, the magnitude being automatically adjusted to balance the riser load. Comparison of the pressures computed in this manner with the measured values will give a check on the analysis, in particular the assumption that skin friction and drag of fluttering sails is negligible.

The simultaneous measurement of loads and strains will provide information on the dynamic and repeated loading behavior of the parachute materials. Although the CANO program is not limited to static load-strain curves, use of dynamic data is not considered worthwhile at present in view of the uncertainties in other input data.

SECRET

6.2 SUMMARY OF PRIOR WORK ON CANOPY PRESSURE MEASUREMENT

The first measurements of pressure distribution in a parachute canopy were made by Jones² in 1923 for the Advisory Committee for Aeronautics of Great Britain. A 4-foot diameter wind tunnel at the National Physical Laboratory was used for the measurements, with sting-mounted models constructed of wood, copper sheet, and silk stretched over a metal ribbed framework.

Models were approximately 8 in. in diameter and simulated a canopy shape developed by Taylor for the Advisory Committee for Aeronautics. Steady state pressures were measured by inserting two lengths of hypodermic tubing in each model surface, one flush with the interior surface and the other with the exterior surface. One end of the tube was plugged and holes were drilled at each point where pressure was to be measured. The measurements were recorded on a manometer, by uncovering one hole at a time, at velocities from 30 to 50 ft/sec and angles of attack from 0 to 10 deg.

Modern efforts at measuring pressure distribution in a steady state canopy have been carried out by Heinrich³⁸ and by Babish and Hunter³⁹. Heinrich's work also is described in the Air Force Parachute Handbook¹⁵. Stainless steel, 2.5-inch diameter models of flat circular ribbon and guide surface canopies were sting mounted and wind tunnel tested at Mach numbers between 0.6 and 1.25 over a Reynolds number range from 7×10^5 to 9.7×10^5 . Measurements of internal and external pressure distribution were made, and shadowgraph pictures were taken in an effort to aid visualization of the flow field through ribbon canopies. External pressure coefficients in the subsonic flow regime (below Mach number 0.8) were found to be relatively insensitive to Mach number. Internal pressure was found to vary little from free stream stagnation pressure at all points in the canopy.

The work carried out by Babish and Hunter was a cleverly conceived effort to arrive at three-dimensional canopy pressure distribution by pressure and flow field measurements on two-dimensional rigid models. These models represented the profile shapes of the inflated drag-producing surfaces of various types of parachutes as determined from photographic records of descending canopies. The various parachute types represented included flat circular, flat circular ribbon, ringslot and ringsail, and others. The models were tested in the Air Force Institute of Technology Smoke Tunnel and were constructed so as to completely span the test section. Test section velocity was 29 ft/sec, which provided ideal smoke streamline flow. By measuring the stream tube thickness and utilizing a theoretically developed relationship between streamtube thickness and pressure, the pressure coefficients could be obtained in regions of the flow where the streamlines were well defined. To obtain measurements in regions where the streamlines were not well defined, i.e., the stagnation and wake regions, an instrumented semicircular concave cylinder was tested. By combining the above two types of measurements, the pressure distribution over the entire surface of the two-dimensional models could be obtained. These pressure distribution data, reduced to appropriate force coefficients, were compared with previously established force coefficient data for three-dimensional models. By use of this method and appropriate assumptions, it was possible to adjust the two-dimensional data to yield the pressure distribution about an actual canopy. Difficulties were encountered, however, in that the streamlines close to the body entered the boundary layer flow, causing errors of ± 20 percent in streamtube thickness, and resulting in a corresponding lack of confidence in the pressure distribution. The primary value of this study is considered to be the excellent smoke streamline photographs and the insight which they afford into the steady state flow about the canopy.

The reports reviewed above have been concerned with the pressure distribution and flow field about a fully inflated, steady state canopy. Although these studies are important because of the insight they give into the operation of a steadily descending parachute, the object of primary interest in the current study is the pressure distribution in an inflating canopy, since it is this phase of the process which imposes maximum stresses on the canopy.

Heinrich¹⁵ obtained measurements of canopy pressure distribution on a series of fixed models representing the shape of the canopy at various stages of inflation. The results of this study were used in a subsequent paper by Heinrich and Jamison⁴⁰ on predicting canopy stresses during inflation. The tests were conducted on seven synthesized shapes at a low subsonic speed, and the pressure distributions associated with each shape were presented in the report. Although these tests may indicate the proper trends for demonstration of stress analysis techniques, it is doubtful that they satisfy the need for pressure measurements under dynamic conditions.

The only investigations made to date wherein pressure distribution was measured in an inflating canopy are those of Melzig^{20, 21, 41, 42} of the Deutsche Forschungsanstalt für Luft und Raumfahrt (DFLR), Braunschweig, Germany. Of the four published works by Melzig, three involve actual drop tests and one concerns a wind tunnel test program under infinite mass conditions. The latter will be discussed first.

The wind tunnel investigation was made in a 9 x 12 foot low speed open-jet wind tunnel at velocities between 70 and 160 ft/sec. The test models were of the following designs:

- (1) Solid cloth, circular flat - 28 gores, $D_0 = 53.5$ in.
- (2) Solid cloth, 10% flat extended - 30 gores, $D_0 = 62$ in.
- (3) Ringslot, geometric porosity 16% - 24 gores, $D_0 = 53.5$ in.

NORTHROP

The models were mounted in the tunnel in a stretched-out position with leather clamps for retention. After the tunnel was brought up to speed, the models were suddenly released. Pressure distribution (internal, external and differential) was measured in the canopy by pressure transducers attached at four specific locations. The pressure transducers were developed at DFLR, and were 1.2 in. in diameter, 0.35 in. thick, and weighed 0.2 oz each. The sensors had a capacity of ± 0.5 psi, and were compensated for temperature and for acceleration to 200 g's. The filling process was photographed from one side of the tunnel at a camera speed of 100 frames per second and individual frames were synchronized with the pressure recordings. Four identical tests of each canopy type were made at each selected test velocity. It was found that the reproducibility of the four measurements was reasonably good.

A canopy shape analysis was made based on the photographs obtained. Various phases of filling were defined by assigning an "ideal photographic shape" made up of appropriate bodies of revolution as a function of time were presented in graphical form for all four canopy types.

The remaining references on Melzig's work concern canopy pressure distributions and inflation profiles obtained during free flight drop tests. Reference 41 reports the measurements made during a series of nine drop tests of a T-10 parachute at speeds from 80 to 140 knots with a 200 lb weight attached. Differential pressure transducers identical to the type described above for the wind tunnel program were mounted at four locations in the canopy between the skirt and the vent. The pressure showed considerably more oscillation and lack of a characteristics pattern than had been the case in the wind tunnel testing presented in Reference 11. Reference 42 describes results of 18 drop tests on 28-foot diameter circular flat and hemispherical parachutes at an initial drop velocity of 118 knots. Four differential pressure transducers

NORTHROP

were again placed in the test canopies and their output recorded on an oscillograph in the drop dummy. Ground photographs of the inflating canopies were made at a speed of 100 frames per second by a 35 mm camera, and also by a camera mounted aboard the dummy. The pressure traces again showed severe oscillations in the initial (flutter) phase of the opening process. A second phase was entered in which the negative pressure peaks disappeared and the oscillation frequency decreased. Following this was a third phase in which a positive steady pressure appeared at all points in the canopy. Melzig correlated the pressure trace behavior with the canopy opening history and load traces.

The most recent work by Melzig²¹ involved drop tests of four parachute types: circular flat (C-9), 10 percent extended skirt (T-10), ringslot (two designs) and circular flat ribbon (two designs). The first ringslot had a nominal diameter of 32 feet, 32 gores, 10 cloth strips, and 15 percent geometric porosity. The second had the same dimensions but 11 instead of 10 cloth strips. The circular flat ribbon parachutes had a nominal diameter of 32 feet, 34 gores, and a geometric porosity of 15 percent. One had 83 and the other 76 concentric ribbons. Both onboard and ground cameras were used to photograph the opening process at 100 frames per second. Four DFLR differential pressure transducers were equally spaced in the canopy from skirt to vent. Riser force, vehicle dynamic pressure, and the four differential pressures were telemetered to ground receiving equipment. The vehicles were dropped from an altitude of 1000 feet at a velocity of 110 knots.

In general, the pressure histories show the same overall trends for all four types of parachutes. There are rapid fluctuations between positive and negative peaks during the flutter phase. The fluttering ends relatively soon at the vent, at which point canopy filling begins, traveling progressively toward the skirt as positive pressure is gradually established over the whole canopy.

In conclusion, Melzig states that because of the dynamics of the inflation process only qualitative information on canopy stresses can be obtained from the detailed pressure distribution measurements, and that idealization of the shape during the flutter phase can yield false results. Additionally he states that before the pressure measurements during the flutter period can be usefully applied, stress analysis techniques must be developed which account for cloth dynamics.

Despite Melzig's emphasis on cloth dynamics during the flutter phase, experience with Apollo parachutes has shown that canopy stress analysis methods which consider only filled sails have accurately predicted test failures. Therefore, special efforts to measure canopy pressure, strain, load and shape during the flutter phase are not warranted.

6.3 PRESSURE MEASUREMENT

Several types of pressure transducers have been proposed by various manufacturers for parachute application. Some manufacturers have also proposed complete pressure measurement systems including telemetry and recording instruments. However, the tests by Melzig, described in Section 6.2, are the only ones in which inflight pressure measurements were made. The Melzig type transducer is the only one which can be considered flight qualified. The following paragraphs describe the various pressure transducers and measurement systems which have been proposed.

Schjeldahl System

Schjeldahl Company, Northfield, Minnesota⁴³, has proposed a differential pressure monitoring system (Figure 80a) which does not require wires in the parachute's risers. The basic sensor is similar in operation to that developed by Melzig at DFLR except it offers improved environmental performance. However, packaged within the same unit are the sensor, electronics for a miniature FM transmitter, four small mercury batteries and signal conditioning electronics. Each unit is 2-1/2 in. in diameter, 1 in. in thickness, weighs approximately 1.75 oz and requires no external wires for operation. The miniature transmitter sends the sensor data to either a receiver-recorder or a repeater (which transmits the information to the ground) located in the payload. Lanyard switches are proposed for activating the units upon drop of the test vehicle. The system is limited to a total of seven transducers by telemetry channel availability.

RdF West System - A system using a different type of sensing element has been proposed by RdF West, Westminster, California.⁴⁴ Their system (Figure 80b) uses a variable, stretched diaphragm capacitance transducer and solid state signal conditioning electronics to provide a DC output pressure transducer system. The sensors are 1.12 in. in diameter, 1 in. in thickness, weigh 1 oz and exhibit accuracies comparable with other sensing devices. The master signal conditioner, located at the skirt of the parachute, is 1.25 x 1.25 x 2.00 inches and weighs 4 oz. The conditioner output is fed into small voltage controlled oscillators and a mixer amplifier. This unit, also located at the skirt, has an approximate volume of 4.5 in³ and weighs 4 oz. The wire carrying the mixed FM signal is run down a suspension line and connected to the tape recorder and/or transmitter. Three power supply lines are the only additional wires needed on the suspension lines.

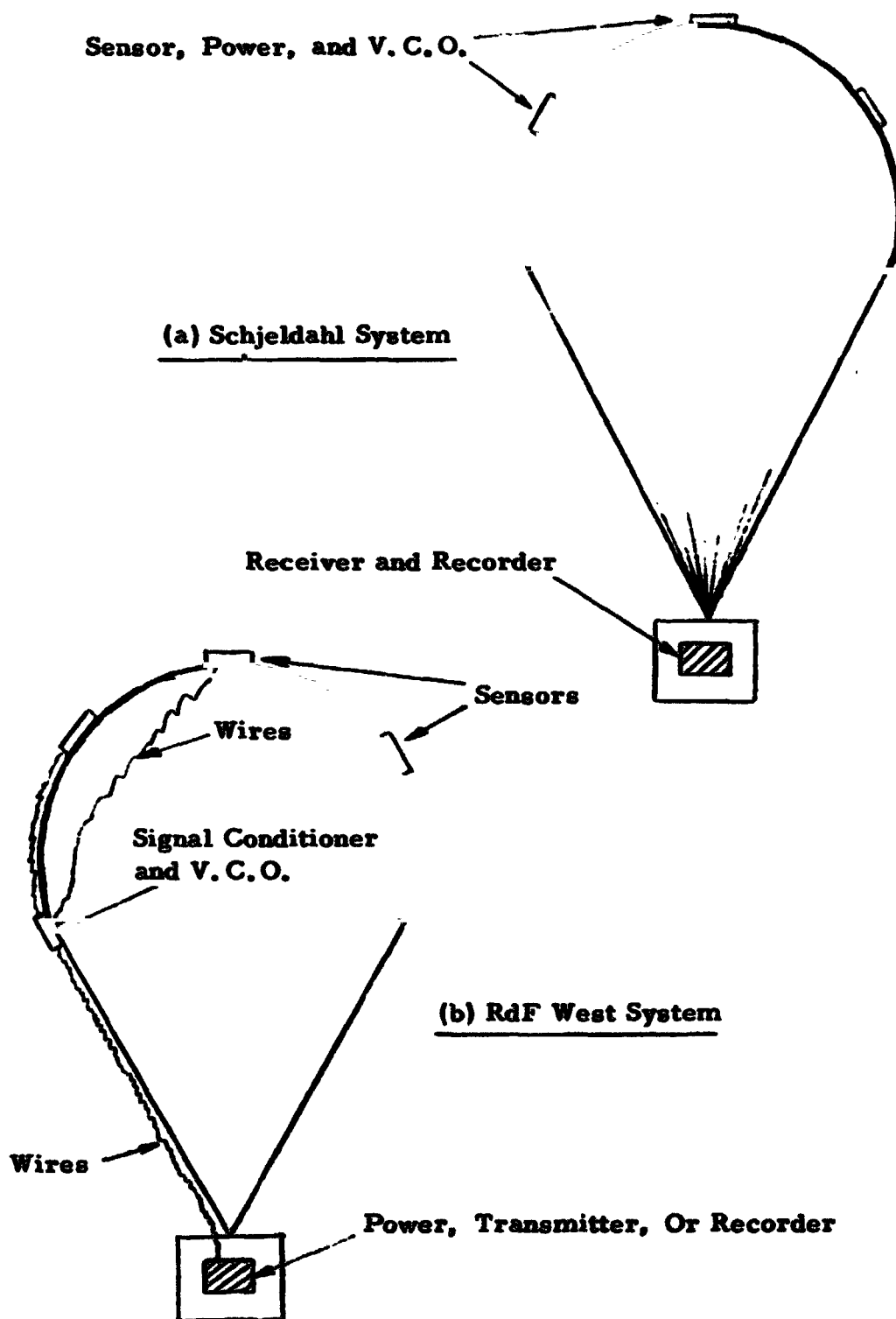
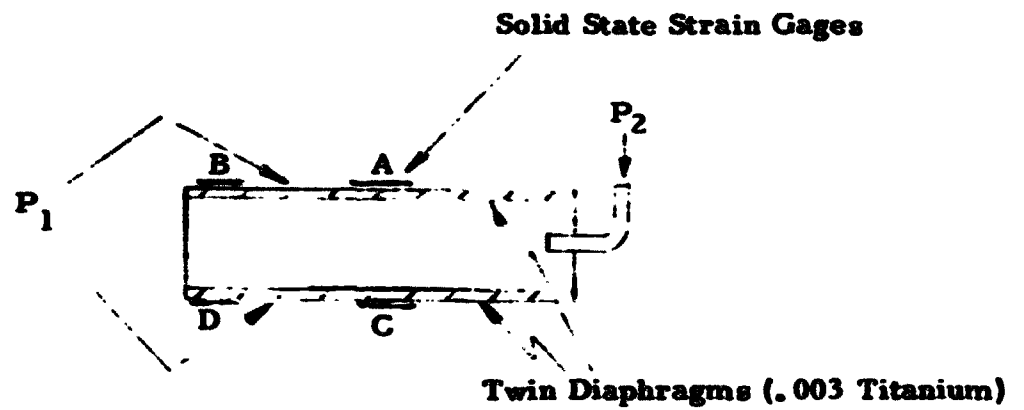


Fig. 80. Schjeldahl and RdF West Pressure Measurement Systems

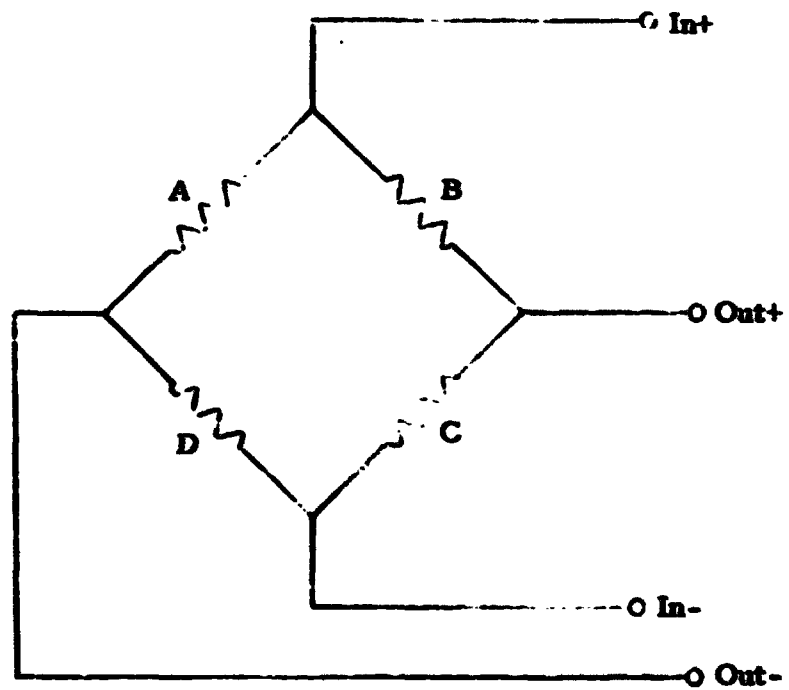
Manning Instruments Transducer - Manning Instruments Division has proposed a transducer of novel construction for measuring differential pressure in a high acceleration environment. This transducer is shown schematically in Figure 81. It consists of twin diaphragms with the external surfaces exposed to the higher pressure level. The inner surfaces are exposed to the lower pressure level. Two silicon strain gages are bonded to the external surfaces of each diaphragm. The gages on each surface are placed (Figure 81) so that gages A and C are strained in compression and gages B and D in tension when the transducer is loaded normally. The transducer is self-compensated for acceleration in that acceleration causes both diaphragms to deflect in the same direction, thereby balancing the bridge by straining gages A and B in the same direction and gages C and D in the same direction. This transducer is available in differential pressure ranges between 5 and 100 psi and weighs about 0.3 oz.

Sensotec Transducer - The Sensotec absolute pressure transducer is a miniaturized capsule (.25 in. diameter x .05 in. thick), one side of which is the active diaphragm. The diaphragm has a pressure sensitive area of .028 in² and utilizes semiconductor strain gages bonded to the inner surface. The differential pressure model has the same diameter, but is about 0.2 in. thick. The smallest differential pressure range currently available is 0-2 psi. Although no acceleration compensation is built into the transducer, Sensotec claims errors due to acceleration at 200 g would be less than 1 percent. A temperature compensation network can be built into the mounting pad.

1000000



(a) Sensor Schematic



(b) Wiring Diagram

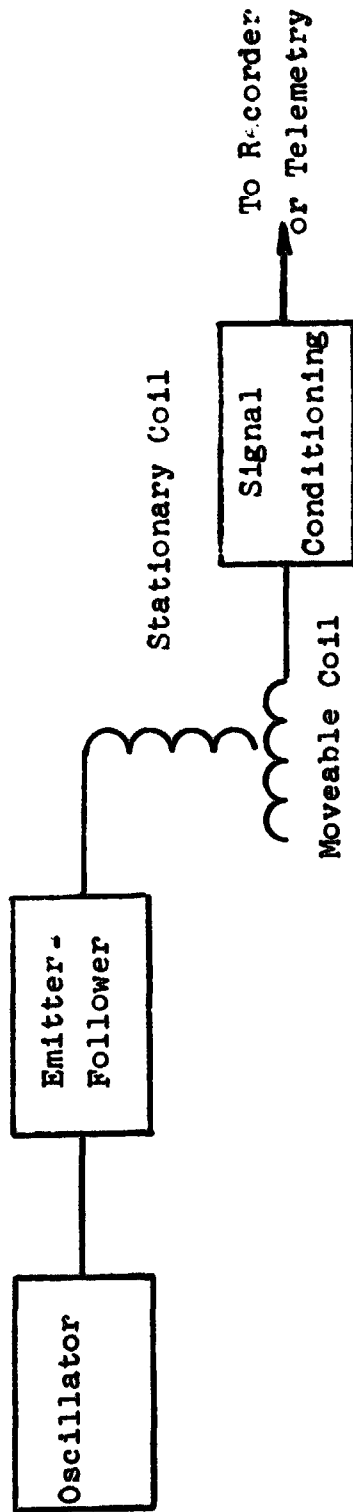
Fig. 81. Manning Instruments Pressure Transducer

6.4 STRAIN TRANSDUCERS

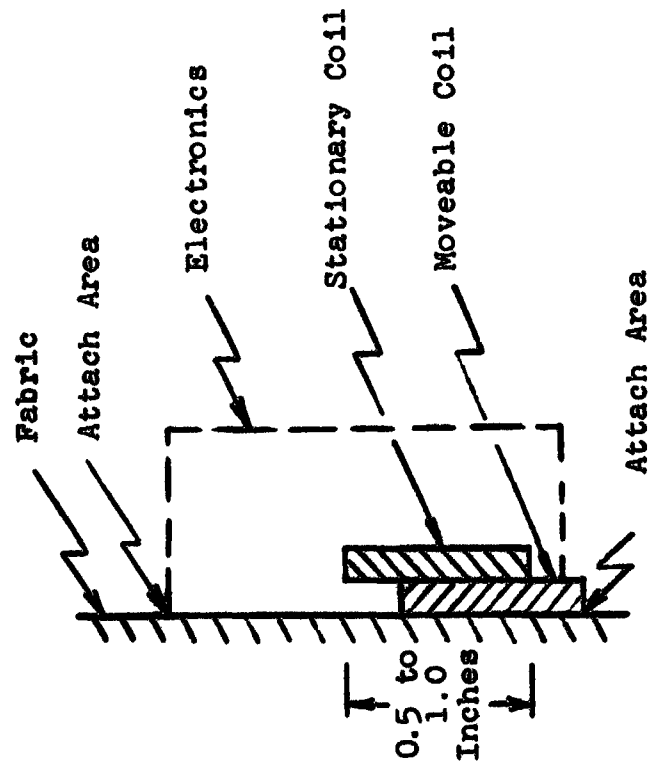
Strain Transducer Based on Inductive Circuit - During the present study, a concept was formulated for a canopy strain measurement device based on the inductive effect between two coils located near each other (Figure 82). The two coils are orthogonal, and an output null point can be realized. The coils can be mounted on the canopy cloth so that they move relative to each other as the cloth stretches. The output signal is dependent on the physical displacement of the coils, which is in turn a measure of the strain in the fabric between the attachment points of the two coils.

The electrical characteristic upon which this transducer is based is commonly used in resolvers and similar electronic equipment. However, a laboratory test program is required to develop a device of acceptable accuracy, size and weight.

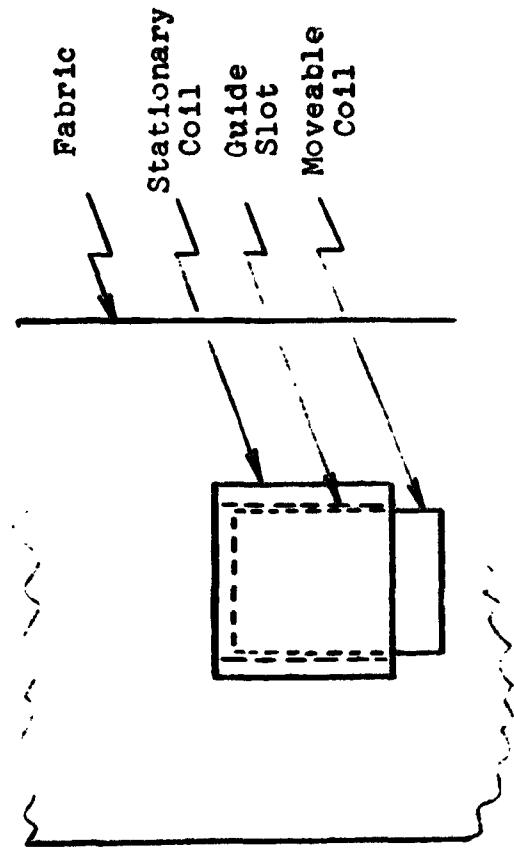
NASA Langley has performed strain measurements by bonding so-called post yield strain gages to the parachute tape members. Strain gage manufacturers claim that these gages which are made of fully annealed Constantan, can be used to measure 10-15 percent. Tests at NASA Langley have indicated good repeatability in measuring 10 percent strains during short duration dynamic load pulses. The Langley tests have shown 1 to 2 percent residual in the fabric and not due to a gage shift.



(a) Schematic of Electrical Circuit



(b) Edge View



(c) Plan View

Fig. 82 . Variable Inductance Strain Transducer

Non-electrical Strain Sensor

A non-electrical maximum strain indicator for high elongation materials has been developed by R. L. Ranes at Northrop Ventura.⁴⁵ Figure 83 shows the principle of operation of this device.

Laboratory tests conducted with these strain indicators attached to nylon parachute fabric indicate the accuracy of the instrument to be within one-percent of the gage length. This accuracy is satisfactory for the measurement of loads or strains in parachute fabrics. A number of these gages have been used in Parawing flight tests, but results have not been published. Laboratory tests under dynamic loading conditions have not been made.

6.5 LOAD TRANSDUCERS

Consideration was also given to a strain gage type transducer capable of measuring the load in the radials of ringsail type parachutes. This device is sketched in Figure 84. The transducer is intended to avoid stress concentrations in the material to which it is attached. This is accomplished by attaching identical devices to both sides of the ribbon or radial, and by incorporating stiff rubber mounts for holding the metal plates to which the strain gages are attached. The rubber stiffness is selected to be somewhat greater than that of the ribbon or radial to which it is bonded. This allows the entire load to be transferred to the strain plates without causing stress concentrations in the ribbon material.

A development program would be required to produce a transducer of this type that would be suitable for measuring parachute loads.

Considerable work has been carried out at NASA Langley on development of a miniature load transducer that is applicable to tape members of parachute canopies. This device can be sewn to the tape member at whatever location is desired. It consists of

NONHROP

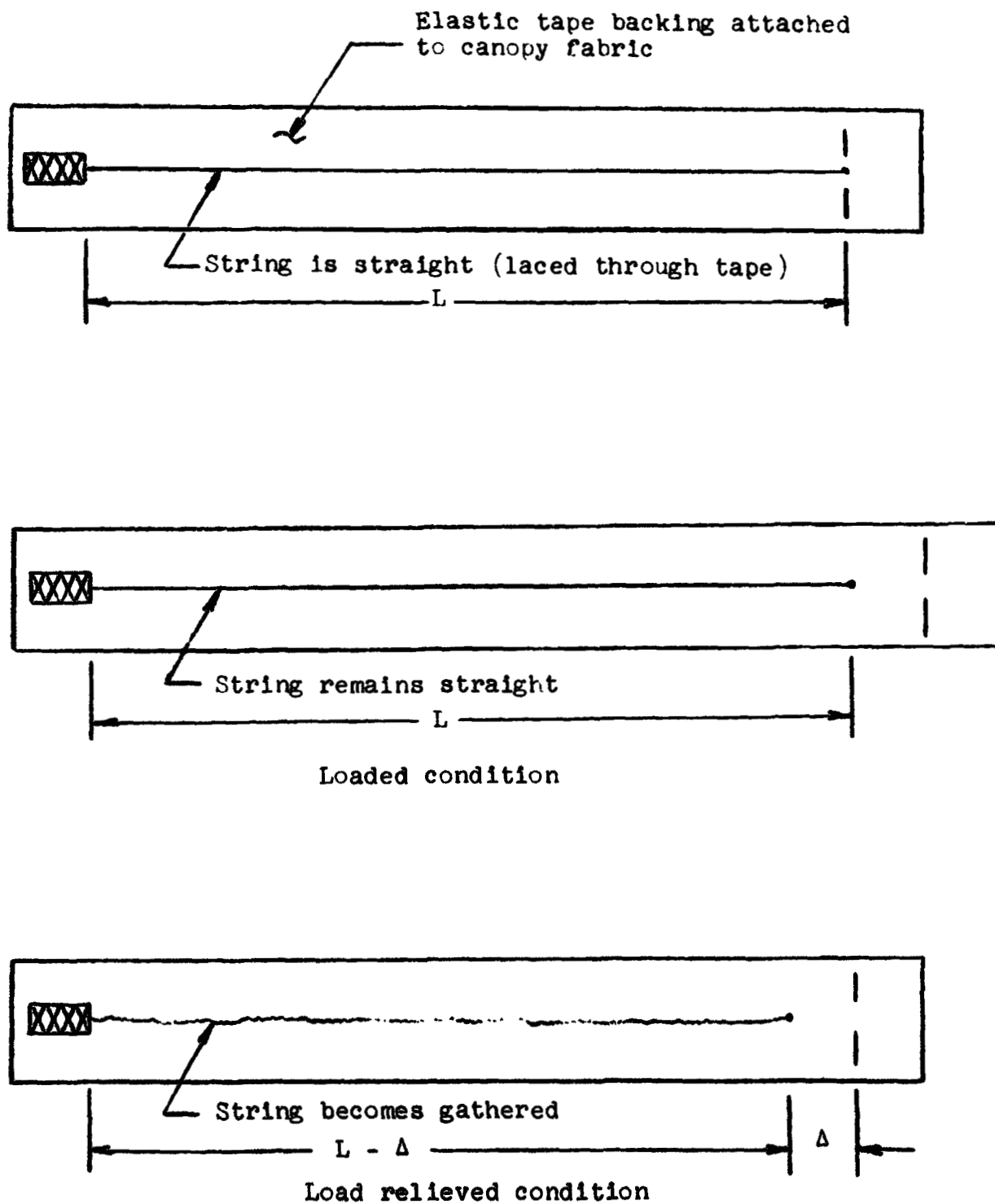


Fig . 83 . Nonelectrical Maximum Strain Sensor
(Reference 45)

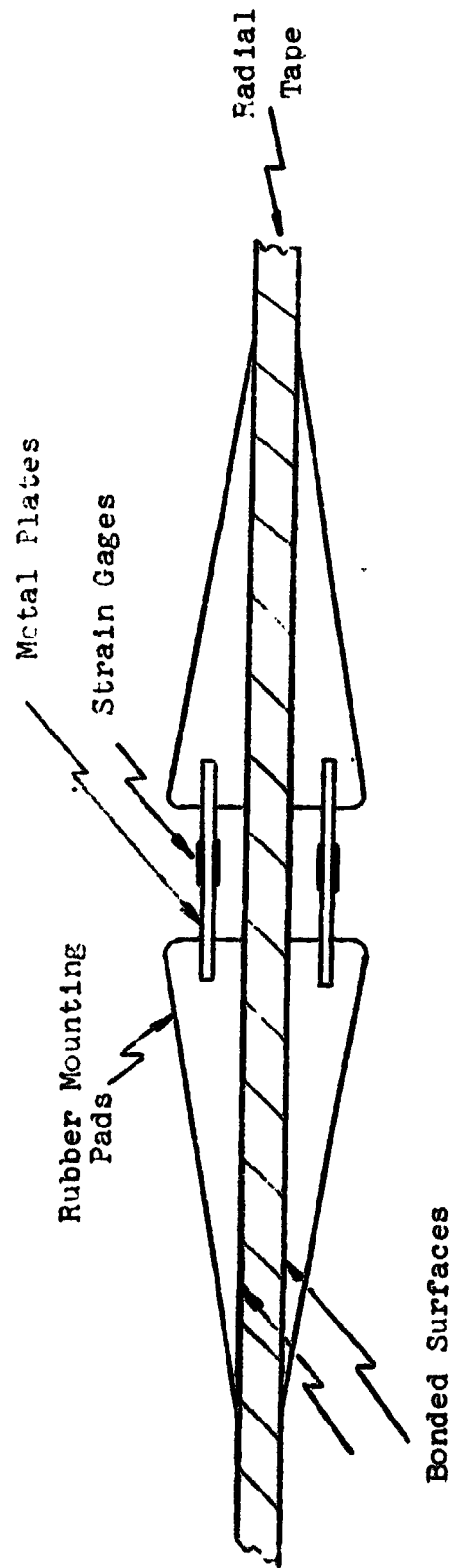


Fig. 84 . Radial Tape Load Transducer

a rectangular stainless steel plate instrumented with four small strain gages of standard design and having end tapes for attachment to the radial. Loads up to 180-lb have been measured at Langley in wind tunnel and flight tests.

6.6 PHOTOGRAPHIC INSTRUMENTATION

Inflight Testing - Accurate profile and plan view shapes of inflating parachutes are among the most valuable data to be obtained; however, these data also seem to be among the most difficult to obtain. Cameras mounted on the test vehicle obtain reasonably good plan view pictures of parachute canopies. These cameras can be calibrated by photographing a grid of known dimensions. The distance from the camera to the canopy can be fairly accurately estimated, so that determining true dimensions from such photographs is possible to perhaps 5 percent accuracy.

Good profile views seem to occur mainly by chance during flight drops, primarily because it is difficult for photo chase aircraft to maneuver so as to maintain the proper camera position. Ground photographs usually show oblique angle views, making it necessary to estimate the camera viewing angle and correct the measured profile height. Also, in the case of the drogue chute, the resolution seldom is high enough to yield a profile shape suitable for stress analysis purposes.

It is believed that the best way to overcome these problems in the proposed test series is to test at the lowest possible altitude. Ground cameras such as the El Centro "Big Eye" have focal lengths such that good resolution can be obtained from long distance, so that the drop can be made far from the camera.

NORTHROP

By making the drops at low altitude, the obliqueness of the view is reduced to a minimum. After a first order correction, the resulting profile shapes should be of sufficient accuracy to be used for comparing with shapes theoretically predicted by the CANO stress analysis program.

In summary, it is believed that presently available photographic recording means (on board cameras and long focal length ground cameras) are adequate provided the test drops are performed at low altitudes (less than 2500 ft).

Wind Tunnel Testing - Wind tunnel tests provide the best opportunities for obtaining good plan and profile views of the inflating parachute. The plan views can be photographed accurately using cameras mounted on the support pylon. Profile views, are the most difficult to obtain. One problem is that the rays of light from the image to be photographed are not parallel. If the distance from the parachute to the camera were infinite, or if an optics system capable of producing parallel rays were available (such as the Schlieren system commonly used in wind tunnels), true projections could be obtained. In the absence of such equipment, it is necessary to make corrections for the parallax error using the known distance from the camera to the parachute.

6.7 PROGRAM PLAN FOR MEASURING PARACHUTE PRESSURE DISTRIBUTION, LOAD, STRAIN AND SHAPE

This section describes a program for measurement of the parachute canopy parameters required for use in the internal loads analysis methods described in Section 3.0. It encompasses a three-part plan designed to follow a logical sequence of (1) laboratory development and testing of suitable instrumentation, (2) wind tunnel testing to obtain the required measurements and confirm the adequacy of the instrumentation, and (3) limited flight tests to obtain further measurements and to correlate wind tunnel results. The program is intended as a major step in obtaining a complete understanding of canopy stresses. The experimental program strongly interacts with and depends on the theoretical methods for predicting canopy loads and stresses, and one of its most important results would be to confirm the accuracy of the theoretical methods.

6.7.1 Laboratory Development Phase

A laboratory development phase is considered to be a vital step in any program aimed at making significant improvements in the state-of-the-art of parachute testing. Several pressure transducers are currently available for making canopy pressure measurements, and a choice as to which is the most suitable can only be made after the proper tests have been carried out. A number of new concepts for measurement of strain and load in canopy structural members need to be evaluated and improved upon. It is not recommended that laboratory evaluation of complete pressure measurement systems be carried out at this time, since it is considered that this effort would be premature prior to careful evaluation of the various available transducers.

NORTHROP

Specifically, it is recommended that the following items be included in the laboratory phase to develop and test pressure, strain and load measurement devices.

- (1) Design and test a strain transducer based on the inductive principle (Figure 82).
- (2) Design and develop a radial tape load transducer based on the principle shown in Figure 84.
- (3) Perform environmental (acceleration, vibration and thermal) tests and calibration checks on currently available pressure transducers. (This work is intended to complement calibration and environmental tests presently being performed by NASA).
- (4) Perform static and dynamic calibrations of the nonelectrical maximum strain indicator illustrated in Figure 83.

In the performance of items (1) and (2), the following general approach will be followed:

- a) Perform circuit analysis.
- b) Prepare breadboard prototype(s) - using laboratory type recording equipment.
- c) Perform laboratory tests.
- d) Make necessary design modifications.
- e) Retest.
- f) Select tentative design.
- g) Perform acceleration and temperature sensitivity tests.
- h) Select final design.

NORTHROP

- i) Select and obtain flight components.
- j) Perform room temperature checkout of flight type system.
- k) Perform acceleration and temperature sensitivity tests of flight type system.
- l) Fabricate a sufficient number of units for wind tunnel testing.

6.7.2 Wind Tunnel Phase

Preliminary Considerations A wind tunnel program will be worthwhile both for proving out the laboratory developed measurement systems as well as for obtaining useful measurements of canopy parameters during the opening process.

(Consideration was given to the El Centro Whirl Tower as an alternative to the wind tunnel for making the canopy measurements discussed above. The primary advantages of the Whirl Tower are (1) the facility of observation which it affords for tests which can be conducted under finite mass conditions and (2) the relatively low cost and simplicity of testing. However, the Whirl Tower is not appropriate for testing large parachutes having reefed stages because the time available for opening is not sufficient to allow disreefing. It would be necessary to open the parachute directly to the stage being tested. This procedure is unattractive in that it does not represent the true opening process, and no further consideration was given to the use of the Whirl Tower in the program.)

Modeling Considerations Because of the practical limitations associated with scaling the parachute opening process, it is important in wind tunnel testing to use the largest possible scale model. For the Apollo main parachute, the largest wind tunnels available should be utilized. The Ames 40 x 80-foot Tunnel and the Langley 30 x 60-foot Tunnel both can accommodate

large parachute models. The Ames Tunnel is capable of operating at dynamic pressures up to 100 psf, while the Langley Tunnel is limited to about 60 psf. Because of its larger size and dynamic pressure range, the Ames 40 x 80-foot Tunnel is the most suitable for Apollo parachute testing.

Prior experience has shown that to avoid undesirable tunnel blockage effects, the drag area of the parachute model should be limited to 15 percent of the test section area. For a test section area of 3200 ft² and a C_{D_0} of about 0.8, the maximum allowable D_0 is about 28 ft. This means that one-third scale models of the main parachute and full scale drogue chutes can be tested. Tests of a one-third scale model and a reefed full scale model of an early main parachute design were successfully carried out in the Ames Tunnel in 1963.⁴⁶

Parachute models canopies should be scaled geometrically to duplicate porosity. This means that the effective thickness, and width dimensions of the materials should be scaled.

This presents a problem in the case of the Apollo main parachute since the 1.1 ounce cloth is about the lightest nylon parachute material for which porosity can be controlled. In order to maintain the proper stiffness distribution, therefore, all of the materials should retain full scale effective thickness. For example, the radial tapes should be of the same weave with scaled width, and the strength of the suspension lines should be reduced by the first power of the scale factor rather than the square.

This will give a structure that is too stiff by the scale factor and will make it more difficult to measure strains accurately. In the wind tunnel tests, strains can be made comparable to full scale by testing at higher dynamic pressures. The tests of Reference 46 demonstrated a reasonable similarity in reefed canopy

CONTINUED

shape between a full scale and a one-third scale model constructed of the same material, as discussed above. It may be assumed that the differential pressure distribution of the two models were similar since the shapes were similar. (Figure 85)

Program Outline The objectives of the wind tunnel test program are summarized as follows:

- 1) To obtain measurements of riser force, pressure, strain and load distribution in a full scale Apollo drogue chute and a one-third scale main parachute model, and to record photographically the shape and filling characteristics.
- 2) To provide pressure distribution data for use in the CANO stress analysis program, and to provide strain, load and shape data for comparison with the program's predictions.
- 3) To verify the suitability of the selected pressure strain and load instrumentation for flight test use.

The program test schedule is presented in Table 14.

In the case of the drogue chute, the maximum available tunnel dynamic pressure of 100 psf is only half of the maximum flight dynamic pressure of 204 psf for high altitude abort. Although it would be desirable to simulate the maximum dynamic pressure, it should be possible to determine the manner in which dynamic pressure influences the measured quantities by testing in the range from 20 to 100 psf. Moreover, if the CANO stress analysis program predicts results adequately over the available range of dynamic pressure, a high degree of confidence is justified in its adequacy at design dynamic pressures since the velocity is not so high that significant compressibility effects are encountered.

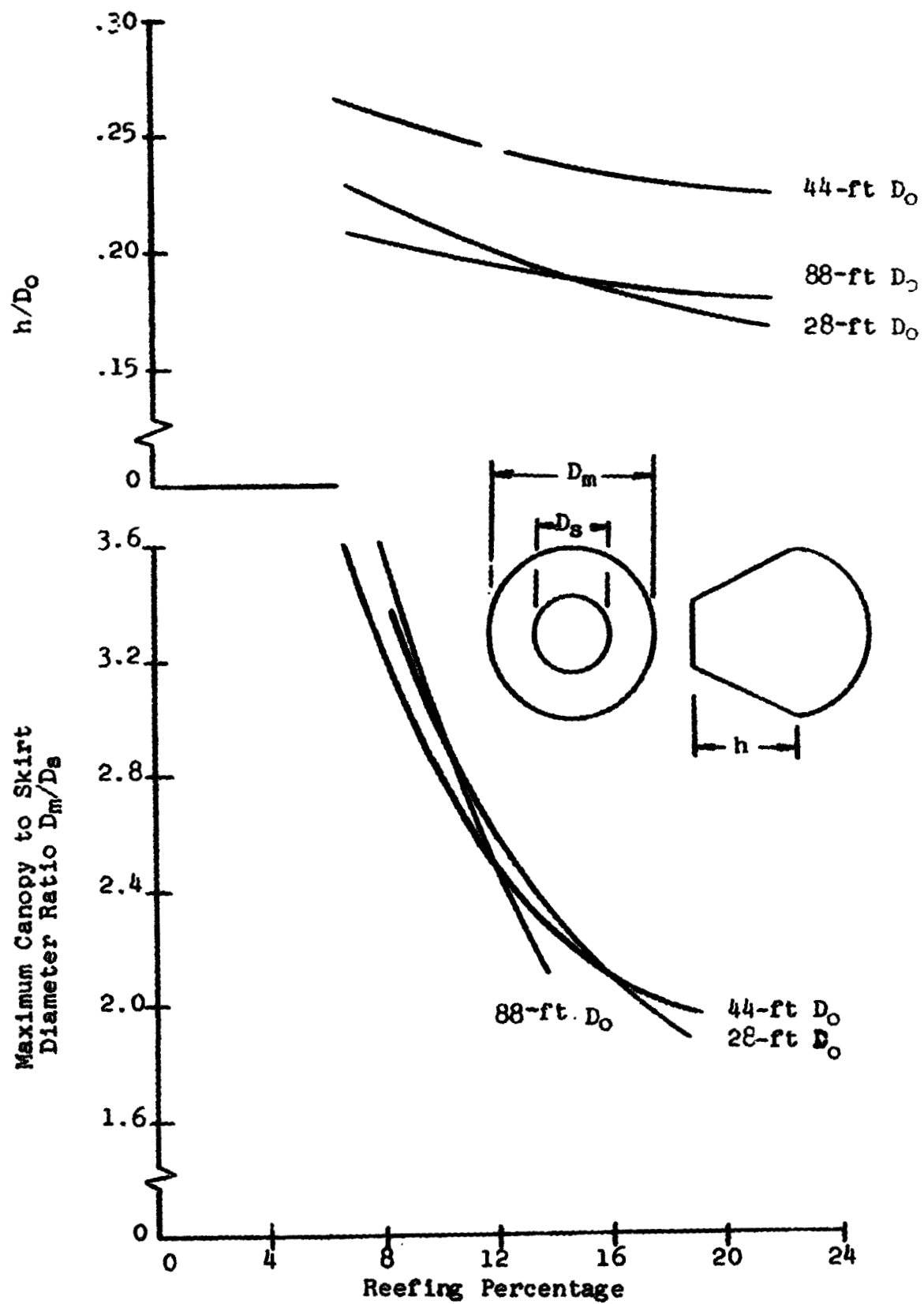


Fig.85 Canopy Growth vs. Reefing Percentage

REF ID: A66666

Table 14. Wind Tunnel Test Schedule

Run No.	Parachute	Dyn Press. (psf)	Opening Stage	Remarks
1	Drogue	20	1	Within range of Melzig pressure transducer
2			2	
3		40	1	
4			2	
5		100	1	Outside Melzig transducer range - need increased range or other type of transducer
6			2	
7-12	Drogue	Repeat of Runs 1-6		
13	28-ft D ₀ Main	90	1	
14		75	2	
15		24	3	
16		60	1	
17		50	2	
18		16	3	
19		45	1	
20		25	2	
21		8	3	
22-30	Main	Repeat of Runs 13-21		

The approach taken for the 28 foot main parachute models is to test at three dynamic pressures. (The test schedule is based on the assumption that pressure transducers suitable for testing at 90 psf dynamic pressure will be available.) The highest dynamic pressures listed for the second reefed and full open stages are approximately three times the maximum flight values for a high altitude abort.

Testing Techniques and Procedures All models will be deployed from deployment bags with the suspension lines stretched out horizontally from the pylon mount to the deployment bag position. Figure 86 shows the proposed arrangement of the model in the Ames 40 x 80 foot tunnel prior to deployment. The deployment bag is suspended from the ceiling and stabilized in the tunnel by a pilot chute.

The ceiling support lanyard, which is brought outside the tunnel through a ceiling access port, also supports the cutter line for the deployment bag tie. Figure 87 (taken from Reference 46) is a sketch of the deployment bag and lanyard arrangement. Prior to tunnel start, the pilot chute is laid on the tunnel floor. As soon as air begins to flow through the tunnel, the pilot chute inflates and assumes its intended position behind the deployment bag. The bag tie cutter is operated manually to initiate deployment. The deployment bag and pilot chute are extracted from the tunnel through the ceiling access port. Reefing lines on the model parachutes are cut by remotely initiated pyrotechnic reefing line cutters.

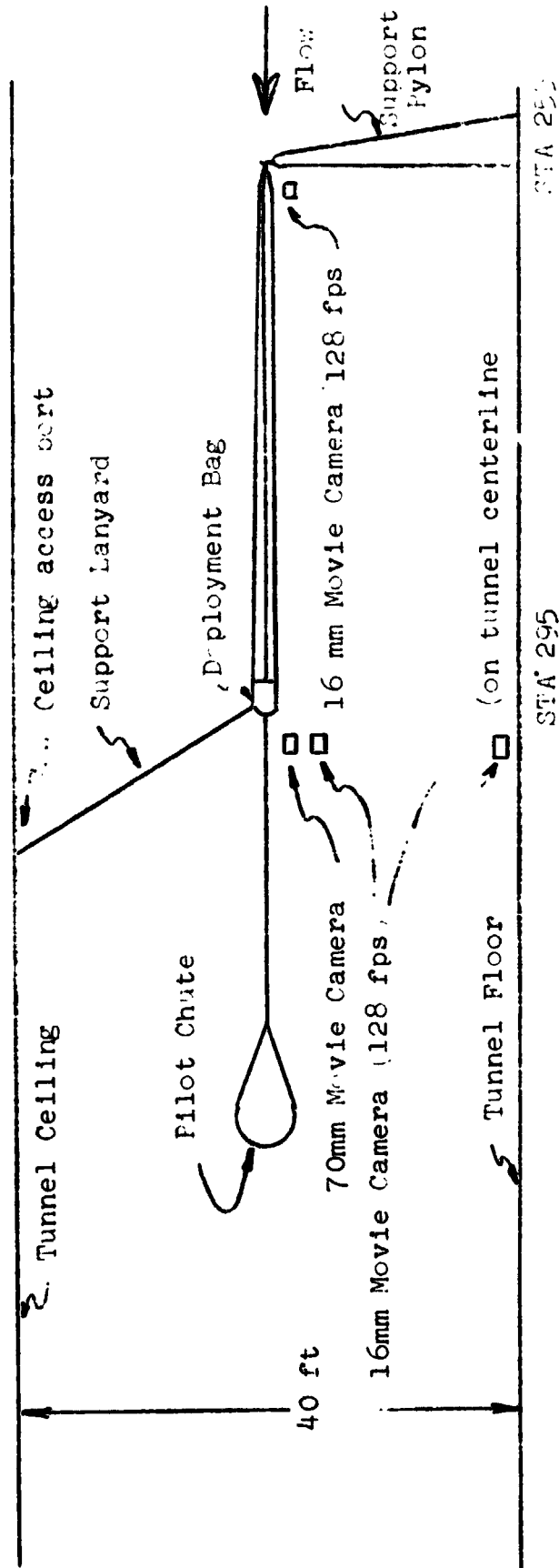


Fig. 86 . Typical Parachute Installation in 40x80-ft Tunnel

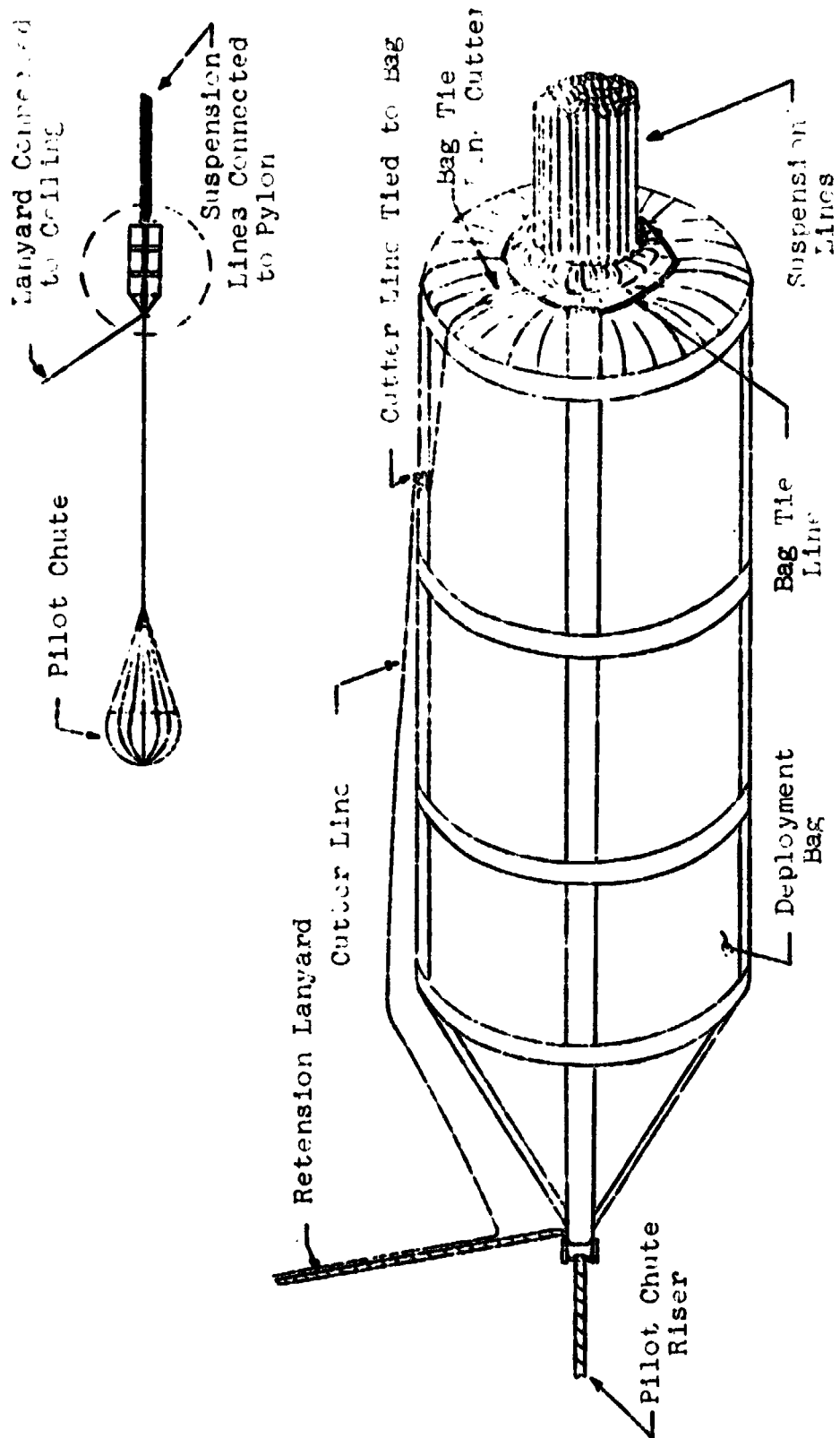


Fig. 87. Parachute Deployment Bag

Instrumentation Instrumentation for all tunnel tests to support the structural analysis methods will consist of the following:

- 1) Pressure Transducers - Ten transducers will be spaced along a radial tape and a mid-gore line.
- 2) Strain Transducers - Ten transducers will be located in positions corresponding to those of the pressure transducers, but on radials and gores adjacent to those used for the transducers, so that no sail is required to support more than one transducer.
- 3) Load Transducers - Ten transducers will be located on radial and vertical tapes.
- 4) Riser Force Load Link - An instrumented load link of standard design will be used to obtain riser force.
- 5) Reefing and Vent Line Load Links - Instrumented load links will be used to obtain reefing and vent line loads.
- 6) Photography - The suggested location of motion picture cameras is shown in Figure 86. A 16 mm camera operating at 128 frames/sec will be used to obtain axial photographs and a second camera operating at 128 frames/sec to obtain profile photographs of the inflating parachute models. A variable speed 70 mm tripod mounted camera will be used to obtain high quality profile photographs.

6) (Continued)

The cameras will be equipped with automatic timers to provide film timing marks, and will be synchronized with the oscillograph recordings by a flashing light common to all cameras and wired through the oscillograph. Camera calibration will be accomplished by photographing a grid placed at the tunnel centerline having overall dimensions equal to the parachute profile maximum dimensions. Error in measuring parachute profile diameter from the photographs will be less than 5 percent after correcting for parallax.

Output of the strain and load transducers and the riser, vent and reefing line load links will be recorded on oscillographs or Sanborn recorders.

Data Reduction - Scaled illustrations at selected times during the opening process will be prepared for each parachute tested. All pressure, strain and load data (including riser force and vent line force) will be smoothed and plotted as functions of time. From these plots, canopy pressure, strain and load profiles will be prepared at times corresponding to those selected for photographic analysis. Pressure profiles will be input into the CANO program and the program predictions will be compared with the measured strain, shape and load data.

6.7.3 Flight Test Phase

Preliminary Considerations Because of the cost and complexity of flight testing, the tests will be limited to low altitude (2500 ft) single parachute drops of one-third scale main parachute models and a small number of full scale main parachute* drops for verification purposes at high altitude (10,750 ft). This is considered reasonable in view of the fact that the test instrumentation and techniques involved are new and that interpretation of the data may be difficult, even for the simplest test conditions. Good profile shape data are considered to be of high value in correlating predictions of the CANO stress analysis program. Therefore, testing at low altitude to allow acquisition of high quality photographs is considered a worthwhile compromise.

The test objectives are summarized as follows:

- 1) To obtain inflight measurements of riser force, pressure, strain and load distribution for one-third scale and full scale Apollo main parachutes, and to record photographically their shape and filling characteristics.
- 2) To provide pressure distribution data for use in the CANO stress analysis program, and to provide strain, load and shape data for confirmation of program results.

* Full scale main parachutes suitable for testing are presently available at Northrop Ventura.

- 3) To obtain data for substantiating the scaling laws developed in Reference 1, Section 2.

Instrumentation The instrumentation will consist of:

- 1) Pressure, strain and radial tape load transducers (whatever types appear most suitable after laboratory and wind tunnel tests), located in positions within the canopy identical to those of the wind tunnel models.
- 2) Riser force, reefing and vent line load links.
- 3) Ground-based motion picture cameras of focal length such that good resolution is obtained.
- 4) Onboard cameras to record the parachute axial view during inflation.
- 5) Airborne motion picture camera coverage for the full scale drops.

All transducer outputs will be recorded by an oscillograph carried aboard the drop test vehicle, and dynamic pressure will be measured by an onboard pitot tube. All instrumentation wiring will be routed along radials and down suspension lines to the test vehicle. The data presentation format will follow that used in the wind tunnel tests.

Test Conditions The scaling laws derived in Reference 1 for velocities and masses are, respectively:

$$v_1/v_o = (r_1/r_o)^{\frac{1}{2}} \quad (\text{duplicates Froude number})$$

$$M_1/M_o = (\rho_1/\rho_o)(r_1/r_o)^3 \quad (\text{duplicates added mass ratio})$$

where the subscript 1 denotes the model and
subscript o the full scale parachute

These expressions can be used to compute test conditions which make a model parachute simulate a full scale parachute. Table 15 presents the required velocities and vehicle masses for the one-third scale parachutes for testing at 2500 ft altitude, simulating a main parachute opening at 10,750 ft after a high altitude abort.

Table 15. Test Conditions for Simulation of a Full Scale Parachute by Use of a One-Third Scale Model

<u>Parachute</u>	<u>Scale</u>	<u>Altitude (ft)</u>	<u>Velocity (ft/sec)</u>	<u>Vehicle Mass (lb)</u>
Apollo Main	Full	10,750	330	6500
Model	1/3	2,500	190	313

Modeling the structural stiffness for dynamic similtude presents a serious problem. This is readily apparent if it is recalled that the strain is proportional to load per unit area (assuming linear strain curves for simplicity), while the load is proportional to the radius cubed.

$$\frac{\epsilon_1}{\epsilon_0} \sim \frac{(F/r^2)_1}{(F/r^2)_0} \sim \frac{r_1^3 \rho_1}{r_0^3 \rho_0}$$

Thus the strains in the structural members of a geometrically scaled model (length, width, and thickness) would be only one-third that of a full scale model tested at the same air density. The model discussed in Section 6.7.2 for wind tunnel testing (full scale thickness) would experience strains of one-ninth those of the full scale model, and the actual change in length (in inches) for a given member would be only 1/27 the full scale value. It is obvious that the measurement of these small strains in fabric materials would present a problem. The strain distribution, and therefore the shape, of the model would be slightly different from the full scale parachute because of the improper stiffness modeling.

NORTHROP

If, on the other hand, the construction details of a model with proper stiffness for dynamic similtude are considered, the difficulty of this approach is apparent. A one-third scale model of the Apollo main parachute with 68 gores would have suspension lines of 24 pound cord and radials of doubled 13 pound tape. These tapes would be equivalent to a strip of 1.1 ounce cloth (42 lb/in) with a width of 0.31 inches. This problem could be alleviated somewhat by using a smaller number of gores. For the sail material, however, it would be necessary to use some material other than nylon cloth to simulate the reduced stiffness while maintaining the proper porosity.

For full scale parachute tests, it is considered that the most useful data can be obtained by testing at the actual flight altitude and velocity of 10,750 feet and 330 ft/sec., respectively. The dynamic pressure at this condition is 90 psf and will require use of a pressure transducer with twice the range of the currently available Melzig-type (Schjeldahl) transducers.

It should be noted that this limited test series is designed to determine the suitability of the canopy instrumentation as well as to obtain useful data. It is anticipated that an expanded test series including drogue chutes and clustered parachutes will be recommended as a next step.

SECTION 7.0

SUMMARY

The results of a one-year study of parachute structural analysis methods utilizing test data accumulated during the Apollo development and qualification test programs are presented.. Study results include: 1) a literature review, 2) refinement and extension of the analysis methods, 3) corroboration of the methods by comparison of analytical and test results, 4) application of the improved method to the Apollo parachutes, 5) a study of dynamic loading effects in pilot parachute risers, and 6) a study of the techniques of measuring loads, strains and differential pressures in parachutes.

A method for computing the internal load distribution for a parachute with a given applied riser load and canopy differential pressure is presented. This analysis determines the canopy shape and internal load distribution that satisfies equilibrium and boundary conditions for a given parachute. The validity of the analysis is demonstrated by comparing the analytically predicted shape with photographs of the Apollo parachutes. While many difficulties are encountered in the interpretation of film data, reasonably good correlation is obtained in comparisons of predicted and observed shapes of the drogue, pilot and main parachutes. (See Figures 21, 22, 32, 38, 39, 41 and 42).

Further verification of the method is obtained by comparing the predicted failure loads and modes for the drogue chute and three versions of the main parachutes with structural failures that occurred during the Apollo development testing. It is shown that the analysis correctly predicts the approximate failure loads and location of the failure. (See Tables 1 and 2)

The analysis is implemented in a computer program, CANO, which makes it possible to use a large digital computer (IBM 360/65) to perform the many iterative computations required for a solution. Use is made of this tool in performing several studies, as discussed in the paragraphs below.

Drogue Chute Structural Model Variation

A study of the sensitivity of the internal load distribution to variations in radial tape stiffness was made to evaluate the assumptions that must be made concerning the effect of vertical members in the modeling of ribbon parachutes. Results show variations of 8 percent in horizontal member loading for the range of radial tape stiffness investigated.

Drogue Chute Pressure Distribution

Canopy profiles and internal load distributions are computed for four different pressure distributions for the full open drogue chute. For the two extremes investigated, i.e., peak pressure at the skirt and peak pressure at the vent, maximum horizontal ribbon loading varies by 15 percent and maximum radial tape loading varies by 10 percent.

Drogue Chute Growth Study

Results of a study of the variation of the shape and internal loading in the drogue chute for different riser loading (with similar pressure distributions) show that the changes in diameter and internal loading are essentially linear.

Pilot Chute Internal Load Distribution

Internal loads are computed for the pilot chute using a structural model that simulates the slots and the seams along the edges of the horizontal panels. Results show that the midsections of the center panels are the most critically loaded areas.

Main Parachute Structural Models

Three versions of the main parachute, representing major steps in the evolution of the present design, are compared. Results show that leading edge fullness in the lower sails causes high loading in the trailing edges of these sails. Addition of reinforcing tapes to the trailing edges in critical areas lowers the load-to-strength ratio locally and also reduces the loading in the unreinforced areas. (See Figure 36)

Main Parachute Failure Analysis

Predicted failure loads and locations, based on the three structural models discussed above, are compared with structural failures that occurred during the Apollo development programs. Good agreement is shown between predicted and failure loads with a maximum spread of ± 13 percent. (See Table 2)

Main Parachute Pressure Distribution and Film Analysis

Since no information is available on the pressure distribution of reefed parachutes, the feasibility of inferring the pressure distribution from the shape of the canopy is investigated. Although the drop test films available do not give the profile views required for an accurate determination of pressure distribution, it is shown that a first approximation can be obtained from the data available. This approximation should give better accuracy in the structural analysis than the assumption of uniform pressure used in the past.

Stress-Time Study of the Main Parachute

Previous analyses considered only three instants in the opening process of the main parachute. It was assumed that maximum riser loading and maximum internal loading occurred at the time that the parachute reached its maximum inflation condition for the stage being investigated. In this study, drop test films are correlated with load traces to determine the riser load and degree of inflation at eleven instants during the opening process. Pressure distributions are also estimated at these instants by the technique discussed in the preceding paragraph. With these inputs, program CANO is used to compute the load in each parachute element. From these results, stress-time histories for each sail and for a typical radial tape are constructed. (See Figures 45 through 48 and Table 4).

Optimum Weight Calculation for the Main Parachute

The weight of an idealized main parachute in which all members are just strong enough at every point to withstand design loading is given. If realistic joint efficiencies are used in this calculation, the ratio of the Apollo main parachute weight to the optimum weight is 1.53. If 100 percent joint efficiencies are used, this ratio is 2.17. Although these optimum weights can never be achieved in practice, they can serve as a yardstick for judging the efficiency of a parachute design and, together with proper statistical data, as a sound basis for predicting the weight of a new design.

Margin of Safety Calculations for the Main Parachute

The computer program, CANO, that resulted from this study is applied in computing the margins of safety for the Apollo main parachute canopy to illustrate the refinements in structural analysis made possible by this study. The margins of safety given in Appendix B are the minimum values from 102 computer runs simulating the deployment process. The maximum applied riser loads for the one-drogue, two-main entry case are taken from Appendix C of Volume 1. Load-time histories are estimated from drogue photographs. A comprehensive set of pressure distribution curves are applied at each opening increment to cover the uncertainty in this area.

A new internal loads analysis for ribbon parachutes is also included. In this analysis, called CANO 1, the structural model includes vertical ribbons. Internal load solutions are given for the drogue chute in both the reefed and disreefed condition. The results show that a significant portion of the meridional load is carried by the vertical ribbons, thereby giving lower radial tape loading. No test data to corroborate these results are available, so the analysis must be used with caution.

A study of data obtained in dynamic loading tests of pilot chute risers is given. An approximate linear-elastic analysis produces explanations of many aspects of the test data. It is shown that longitudinal wave effects must be included in the structural analysis of pilot chute risers since multiple failures and failures in free lengths may occur at loads that would not cause failure if applied statically. It is also shown that hysteresis effects must be considered in the load-strain relationships used in the riser dynamic analysis. Improved results are obtained by

use of nonlinear static load-strain curves and a more accurate representation of the boundary conditions in a computerized finite difference method approach. Further refinement of the mathematical model is shown to be necessary. Analysis of the pilot chute riser test data shows that the dynamic load-strain curves followed by the riser nylon webbing are approximately linear, but that small variations from linearity produce effects which cannot be neglected. It is seen that the longitudinal wave speed is sensitive to some as yet undiscovered variable in the tests

With the facility provided by the CANO analysis for detailed structural modeling and for investigating many loading conditions, the accuracy of the reported structural analysis is limited mainly by the accuracy of input loading data. Although accurate methods for predicting riser loads have been developed (see Volume I), little information is available on the distribution of aerodynamic forces on the canopy. It is shown in the analysis that this distribution has a first order effect on the loading of individual parachute members. Results of a study of the techniques of measuring canopy differential pressure distribution and internal loading are given, together with a plan for a three-phase test program to acquire these data for the Apollo parachutes.

SECTION 8 CONCLUSIONS

The conclusions based on the work described in this report are as follows:

- 1) The structural analysis method implemented in computer program CANO gives a satisfactory estimate of the internal load distribution in a parachute under known riser and aerodynamic loading. This conclusion is based on comparisons of predicted shapes with drop test photographs and on comparisons of failure loads and modes with test results.
- 2) When good photographic data and riser load traces are available, it is possible to infer the canopy differential pressure distribution from the canopy shape. Typical drop test photographs do not provide the desired accuracy, however.
- 3) The analysis techniques used in the stress-time study of the main parachute can be used to predict the state of stress in a parachute throughout the opening process provided that accurate shape-time and riser force history data are available.
- 4) An analysis of the Apollo drogue chute (a conical ribbon parachute) indicates that a significant portion of the meridional load is carried by the vertical members. Corroborating test data, which could be obtained by measuring vertical ribbon and radial tape loads, are needed to verify the analysis presented.

- 5) Most of the unexpected results observed in the riser dynamics tests can be explained by a graphical linear-elastic analysis. A more accurate, nonlinear-elastic analysis can be made by using finite difference methods to solve the dynamical equations of parachute risers under impact loading.
- 6) Unusual failures such as simultaneous multiple breaks and failures in free lengths of pilot chute risers can be caused by tensile strain waves at loads that would not cause failure if applied statically. The wave speeds observed in the tests were sensitive to some as yet undetermined variables.
- 7) The most important unknown factor in parachute structural analysis is canopy differential pressure distribution. A method for predicting pressure distribution is needed for pretest structural analysis.

SECTION 9.0 RECOMMENDATIONS

Based on the results of the one-year study of structural analysis techniques for Apollo spacecraft parachutes, it is recommended that:

- 1) The stress-time analysis method presented in this report be used in future parachute design and development programs.
- 2) The internal load analysis, CANO, be used to make a systematic study of the effects of the major design parameters on parachute weights.
- 3) The concept of a theoretically optimum parachute be used for evaluating the structural efficiency of existing parachute designs, and that it be used as the basis for predicting the weight of future designs.
- 4) The study of the variation of canopy shape with pressure distribution be continued to provide a method for estimating pressure distribution from drop test photographic data.
- 5) A test program be undertaken to measure pressure, strain and load distribution in parachutes during the opening process.
- 6) Corroboration be sought, by test measurements, for the internal load analysis for ribbon parachutes developed in this report.
- 7) A method be developed for predicting differential pressure distribution on parachute canopies, preferably an analytically based method with empirical support; this is required to remove a barrier to advancement of parachute stress analysis technology.

- 8) The usefulness of photographic data be improved in future flight tests by: a) use of airborne, high resolution cameras to obtain good profile views at the critical stages of each test, b) distinctive marking of the canopy members, and c) calibration of onboard cameras before each flight.
- 9) The variable wave velocity and other phenomena be investigated by conducting tests similar to those described herein, but with greater control over the manner in which the impact load is applied to the end of the specimen. The specimens should be designed in such a way that discontinuities do not interfere with precise observation of the wave action. One series of tests should be optimized with respect to determining material properties (dynamic load-strain curve) and a second series of tests optimized with respect to determining the behavior (transmission and reflection coefficients) of joints, links and other riser components.
- 10) The AFTON computer program be applied to a complete riser model using material property and component performance data as determined in (9).
- 11) Experimental impact studies be conducted using complete riser system specimens in order that the effect of the true boundary conditions be ascertained.
- 12) That the data obtained in (9), (10) and (11) be used to develop a qualified method for dynamic analysis of pilot parachute risers.

APPENDIX A
SUMMARY OF APOLLO AERIAL DROP TESTS

The following table contains a summary of the Apollo aerial drop tests that have been conducted to date. This information can be used as a quick reference to find the test objectives, type of vehicle, parachute versions, and recorded loads for any particular drop test. The listed references indicate where this data was obtained and where additional data may be found.

Three types of reports are used to record the drop test information: Paradyamics Technical Memoranda (PTM), Flight Test Reports (FTR), and Northrop Ventura Reports (NVR).

The Paradyamics Technical Memorandums and the Northrop Ventura Reports are formalized reports which were used to compile the information resulting from the Apollo drop test program. The Paradyamics Systems Section was responsible for preparing the PTM's, and the Field Test Branch was in charge of the preparation of the NVR's. Flight Test Reports are data packages which contain test objectives, test data, and post-test evaluation of aerial drop tests. These reports were prepared by the Analytical Engineering Branch.

Reference is sometimes made to tests as being part of Block I, Block II or Block II (H). The tests associated with these blocks are as follows:

Block I	Test Series 1 thru 62 and 71
Block II	Test Series 70 and 73
Block II (H)	Test Series 80 thru 99

Table A-1 Summary of Apollo Drop Tests

Test Date	Test Number	Test Objective	Vehicle	Parachute (Dia. Ft.)	Pilot (% Do.)	Drop FR	Drop Fo	Pilot	Max Load (lbs.)	Main FR 2	Fo	Ref.	Comments
7-5-62	6-1	Single M/C Performance	ICTV	N/A	PDS 808 (9.5%)	N/A	N/A	N/R	N/R	N/A	N/R	PTM 763	Reefing Line Hang-Up
7-9-62	6-2	Same as 6-1	ICTV	N/A	PDS 808 (11%)	N/A	N/A	N/R	9600	N/A	8450	PTM 763	Pilot chute Separation
7-19-62	6-3	Same as 6-1	ICTV	N/A	PDS 808 (10%)	N/A	N/A	N/H	10100	N/A	11600	PTM 763	Split Gore During Reefed Stage
8-14-62	6-4	Single M/C Performance	ICTV	N/A	PDS 926 (10%)	N/A	N/A	N/R	N/R	N/A	N/R	PTM 763	Normal
8-22-62	6-5	Single M/C Performance	ICTV	N/A	PDS 926 (10%)	N/A	N/A	N/R	10000	N/A	19100	PTM 763	Normal
9-4-62	6-6	Single M/C Performance	ICTV	N/A	PDS 1226 (11%)	N/A	N/A	N/R	9600	N/A	16300	PTM 763	Normal
9-14-62	6-7	Single M/C Performance	ICTV	N/A	PDS 1226 (11%)	N/A	N/A	N/R	10400	N/A	15880	PTM 763	Normal
9-20-62	6-8	Single M/C Performance	ICTV	N/A	PDS 1226 (11%)	N/A	N/A	N/R	12170	N/A	15460	PTM 763	Normal
10-11-62	6-9	Single M/C Performance	ICTV	N/A	PDS 1226 (11%)	N/A	N/A	N/R	13400	N/A	15200	PTM 763	Pilot chute Separation
10-22-62	6-10	Single M/C Performance 1.5 x Design q	ICTV	N/A	PDS 927 (11%)	N/A	N/A	N/R	17400	N/A	20950	PTM 763	Reefing Line Failure Causing Split Gore
10-26-62	6-11	Single M/C Performance 1.5 x Design q	ICTV	N/A	PDS 927 (11%)	N/A	N/A	N/R	16000	N/A	10700	PTM 763	Split Gore During Reefed Stage
11-1-62	1-1	Single M/C Performance 1.6 x Design q	ICTV	N/A	PDS 1226 (11%)	N/A	N/A	N/R	16680	N/A	16270	PTM 763	Split Gore at Disreef
11-7-62	3-1	Single M/C Performance 1.6 x Design q	ICTV	N/A	PDS 1226 (11%)	N/A	N/A	N/R	15200	N/A	16540	PTM 763	Pilot chute Separation
11-14-62	3-2	Single M/C Performance 1.6 x Design q	ICTV	N/A	PDS 1226 (11%)	N/A	N/A	N/R	9570	N/A	17970	PTM 763	Pilot chute Separation Causing Canopy Failure

Table A-1 (Continued)

Test Date	Test Number	Test Objective	Vehicle	Parachute (Dia. Ft.)	Pilot	Reefing Main (1/2 D ₀)	Drumge P ₀	Max. Loads (lbs) Pilot	Max. Loads (lbs) Main P ₀	Ref.	Comments
11-20-62	3-3	Single M/C Performance	ICTV	N/A	N/A	PDS 1226	N/A	N/R	N/A	PTM 763	Normal
		1.6 x Design q				-503					
						(11%)					
11-27-62	3-4	Single M/C Performance	ICTV	N/A	N/A	PDS 1226	N/A	N/R	N/A	PTM 763	Normal
		1.6 x Design q				-505					
						(11%)					
12-3-62	25-1	Drumge Chute Performance	ICTV	PDS 1347	N/A	N/A	N/A	N/A	N/A	PTM 763	
12-4-62	25-2	Drumge Chute Performance	ICTV	PDS 1340	N/A	N/A	N/A	N/A	N/A	PTM 763	
		20 Ft. Conical Ribbon		-501							
12-4-62	7-1	Three M/C Cluster Performance	F.V.	N/A	N/A	PDS 1226	N/A	N/R	N/A	PTM 763	One chute failed to inflate
						-503					
						PDS 1226					
						-503					
						PDS 1226					
						-505					
						(All 11%)					
1-3-63	25-3	Drumge Chute Performance	ICTV	PDS 1328	N/A	N/A	N/A	N/A	N/A	PTM 763	
		15.5 ft Conical Ribbon									
1-8-63	27-1	Test of Gov't G 12D Recovery Chutes								PTM 763	Parachutes Failed
1-11-63	26-1	Two M/C Cluster Performance	ICTV	N/A	N/A	PDS 1544	N/A	N/R	N/A	PTM 763	Some Blanketing
						(13%)					
1-18-63	27-2	Test of Gov't G 12D Recovery Chutes								PTM 763	Normal
1-18-63	17-1	Drumge Performance	PTV	PDS 845	N/A	N/A	N/A	N/A	N/A	PTM 763	Normal
		Mortar Deploy		(12.4)							

Table A-1 (Continued)

Test Date	Test Number	Test Objective	Vehicle	Parachute Version & Reefing		Drogue		Max. Loads (lbs)		Ref.	Comments
				Drogue	Pilot	Main	F _z	Pilot	Main		
1-21-63	26-2	Two M/C Cluster Performance	ICTV	N/A	PDS 1543 (13%)	N/A	N/A	N/R	13370 18920	PTM 763	Normal
1-28-63	26-3	Two M/C Cluster Performance	ICTV	N/A	PDS 1550 (13%)	N/A	N/A	N/R	23230 10700	PTM 763	Aerodynamic Interference During Reefed Stare
2-4-63	26-4	Two M/C Cluster Performance	ICTV	N/A	Same Chutes used on 26-2	N/A	N/A	N/R	11360 14370	PTM 763	Normal
2-6-63	6-12	Single M/C Performance	ICTV	N/A	PDS 2021 (11%)	N/A	N/A	N/R	12150	PTM 763	Normal
2-8-63	26-5	Two M/C Cluster Performance	ICTV	N/A	PDS 1543 (13%)	N/A	N/A	N/R	15810 14450	PTM 763	Some Blanketing
2-15-63	26-6	Same as 26-5 except at 1.5 x Design Q	ICTV	N/A	PDS 1543 (13%)	N/A	N/A	N/R	18630 21680	PTM 763	Normal
2-20-63	17-2	Drogue Performance Mortar Deploy	PTV	PDS 845 (12.4)	N/A	N/A	10700	N/A	N/A	PTM 763	Normal
3-1-63	7-2	Three M/C Cluster Performance	PTV	N/A	PDS 1543 (13%)	N/A	N/A	N/R	N/R	PTM 763	Drag Chute Failure
3-8-63	26-7	Three M/C Cluster Performance	ICTV	N/A	PDS 1543 (13%)	N/A	N/A	N/R	8830	PTM 763	Partial Telemetry Failure
3-14-63	7-3	Three M/C Cluster Performance	PTV	N/A	PDS 1543 (13%)	N/A	N/A	N/R	9060 N/R 15030	PTM 763	Considerable Blanketing

Table A-1 (Continued)

Test Date	Test Number	Test Objective	Vehicle	Parachute		Version		Reefing		Drogue		Fo		Max. Loads (lbs)		Ref.	Comments
				(Dia. Ft.)	(Dia. Ft.)	Pilot	Main	(5 Fo)	(5 Fo)	FR	FR	FR	FR	FR	Pilot		
3-21-63	13-1	Three N/C Cluster Low q Attached Pilot	PTV	N/A	PDS 1543 (13')	N/A	N/A	N/A	N/A	N/A	N/A	N/A	N/A	6436	N/A	PTM 763	Normal
														10110			
														9710			
3-21-63	13-1	Drogue Chute 1.5 x Design q	PTV	PDS 845-501 (12.4)	N/A	N/A	N/A	N/A	N/A	N/A	N/A	N/A	N/A	N/A	N/A	PTM 763	Split Gire Below Rated Strength
4-2-63	24-1	Drogue Chute Low q	PTV	PDS 845 (12.4)	N/A	N/A	N/A	N/A	N/A	N/A	N/A	N/A	N/A	N/A	N/A	PTM 763	Normal
4-4-63	13-2	Three N/C Cluster Attached Pilot Chutes	PTV	N/A	PDS 1543 (13')	N/A	N/A	N/A	N/A	N/A	N/A	N/A	N/A	N/A	N/A	PTM 763	Some Blanketing
4-22-63	6-13	Single N/C Performance	ICTV	N/A	PDS 2072 (9.4')	N/A	N/A	N/A	N/A	N/A	N/A	N/A	N/A	N/A	N/A	PTM 763	Bad Telemetry
4-24-63	6-14	Single N/C Performance	ICTV	N/A	PDS 2072 (9.4')	N/A	N/A	N/A	N/A	N/A	N/A	N/A	N/A	N/A	N/A	PTM 763	Bad Telemetry
4-25-63	6-15	Single N/C Performance	ICTV	N/A	PDS 2072 (9.4')	N/A	N/A	N/A	N/A	N/A	N/A	N/A	N/A	18880	N/A	PTM 763	Normal
5-1-63	27-3	Test of 84177-503 Recovery Chutes	—	—	—	—	—	—	—	—	—	—	—	—	—	PTM 763	Parachutes Failed
5-3-63	50-1	Complete System Performance	B/P	PDS 845 (12.4)	PDS 1543 (13')	N/A	N/A	N/A	N/A	N/A	N/A	N/A	N/A	N/A	N/A	PTM 763	Heavy Damage To One Pilot. Broken W/C Suspension Lines
5-6-63	15-1	Single N/C Performance	ICTV	N/A	PDS 2072 (7.5')	N/A	N/A	N/A	N/A	N/A	N/A	N/A	N/A	9440	N/A	PTM 763	Normal
5-10-63	15-2	Drogue Chute 1.5 x Design q	PTV	PDS 2119-501 (12.4)	N/A	N/A	N/A	N/A	N/A	N/A	N/A	N/A	N/A	N/A	N/A	PTM 763	Normal
5-13-63	25-2	Two N/C Cluster Performance	ICTV	N/A	PDS 2071 (13')	N/A	N/A	N/A	N/A	N/A	N/A	N/A	N/A	13140	N/A	PTV 7-3	Split Gire after 15sec
														12450			
5-15-63	25-2	Two N/C Cluster Performance	ICTV	N/A	PDS 2072 (7.5')	N/A	N/A	N/A	N/A	N/A	N/A	N/A	N/A	13150	N/A	PTV 7-3	Link Failure
														9470			

SECRET

Table A-1 (Continued)

Test Date	Test Number	Test Objective	Vehicle	Parachute Type (Dia. Ft.)	Parachute Version	Pilot	Main (4 Do.)	Drop Altitude (ft.)	Pilot	Main (1 Do.)	Drop Altitude (ft.)	Ref	Comments
5-15-63	50-2	Complete System Performance	B/P	PDS 845-501 (12.4)	PDS 1543-501 (136)	N/A	N/A	N/A	N/R	N/A	N/A	PTM 763	Normal
5-24-63	18-3	Drogue chute 1.5 x Deflcn. a	PTV	PDS 2119-501 (12.4)	N/A	N/A	N/A	15013	N/A	N/A	N/A	PTM 763	Normal
6-12-63	50-3	Complete System Performance	B/P	PDS 845-501 (12.4)	PDS 1543-501 (136)	N/A	N/A	N/A	N/R	N/A	N/A	PTM 763	Normal
6-28-63	26-10	Two M/C Cluster Performance	ICTV	N/A	PDS 2072 (3.5%)	N/A	N/A	N/A	N/R	N/A	25340 24860	PTM 763	One chute failed to inflate
8-9-63	17-3	Dual Drogue Performance, Mortar Deploy	PTV	PDS 845 (12.4)	N/A	N/A	N/A	12000	N/A	N/A	N/A	PTM 763	Normal
8-24-63	50-4	Same as 50-3 Higher than 50-3	B/P	PDS 2119 (12.4)	PDS 1543 (136)	N/A	N/A	N/A	N/R	N/A	8116 6723 5397	PTM 763	Irregular late
8-27-63	24-2	Dual Drogue Performance, Mortar Deploy, Low g	PTV	PDS 845 (12.4)	N/A	N/A	N/A	3110 3119	N/A	N/A	N/A	PTM 763	Normal
9-6-63	50-5	Complete System Performance, Abort Cond.	B/P	PDS 845 (12.4)	PDS 1543-501 (136)	N/A	N/A	N/A	N/R	N/A	N/A	PTM 763	One M/C Failed to Inflate
10-3-63	24-3	Dual Drogue Performance	PTV	PDS 2119	N/A	N/A	N/A	10770 10220	N/A	N/A	N/A	PTM 756	Desired Test Conditions not Achieved
10-22-63	50-6	Complete System Performance, Pad Abort	B/P	PDS 2119-501 (12.4)	PDS 1543-501 (136 MO)	N/A	N/A	N/A	N/R	N/A	N/A	PTM 769	Normal

Table A-1 (Continued)

Test Date	Test Number	Test Objective	Vehicle	Parachute Drogue (Dia Ft)	Version Pilot	Reefing Main (-D ₀)	Drop Alt (ft)	Pilot	Max. Load (lbs)	Alt (ft)	Ref.	Comments
11-8-63	24-4	Dual Drogue Performance	PTV	PDS 2119	N/A	N/A	7915	N/A	N/A	N/A	PTM-777	Vehicle spinning
11-15-63	50-7	Complete System High Altitude Abort	B/P	PDS 2119-503		PDS-1543 -503	5660	N/R	N/A	N/A	PTM-793	Normal
12-5-63	50-8	Complete System High Altitude Abort	B/P	PDS 2119-503		PDS-1543 -503	7550	N/R	9982	5881	PTM-799	Normal
12-18-63	50-9	Complete System High Altitude Abort	B/P	PDS 2119-503		PDS-1543 -503	5886	N/R	11020	5870	NVR 2957	Normal
1-27-64	28-1	Performance of Permanently Attached Drogues	PTV	PDS 2119-503		PDS-1543 -507	6286	N/R	7770	3760		
2-27-64	50-10	Complete System High Altitude Abort	B/P	PDS 2119-503		PDS-1543 -507		N/R	7200	9230		
2-28-64	40-1	Two 4/C Cluster 100% Vertical Tapes	ICTV	N/A		R7118-501		N/A	11940	36000	NVR 2978	Medium Blanket
3-11-64	40-3	Two 4/C Cluster 100% Vertical Tapes	ICTV	N/A		R7118-501		N/A	17050	21400	NVR 2997	Some Blanket
3-18-64	44-1	Single 3/C Performance 35% of Ring 5 Removed	ICTV	N/A		PDS-3125 -501		N/A	16150	15010	NVR 3501	Normal
3-25-64	44-3	Single 3/C Performance 50% of Ring 5 Removed	ICTV	N/A		PDS-3125 -501		N/A	20820	14110	NVR 3507	Normal
3-30-64	40-2	Two 3/C Cluster 100% Vertical Tape	ICTV	N/A		PDS-1203 -511		N/A	9840	5710	NVR 3524	Some Blanket

Table A-1 (Continued)

Test Date	Test Number	Test Objective	Vehicle	Parachute Drogue (Dia Ft)	Pilot	Max Load (lbs)	Pilot	Dropgue P ₀	P _R	N/A	Main P _R	P ₀	Ref	Comments
4-3-64	44-4	Two M/C Cluster Performance	ICTV	N/A	PDS 1543 -525 (112 MG)	N/A	N/A	N/A	N/A	11270	N/A	11220	NVR 3523	Normal*
4-7-64	41-1	Two M/C Cluster Performance, 68 Gores	ICTV	N/A	PDS 3125-PDS 1543 501 -527 (112 MG)	N/A	N/A	N/A	N/A	20330	N/A	22580	NVR 3524	Confiscal Modif-ication of Main Parachute
4-8-64	50-11	Complete System High Altitude Abort	B/P	R 7117	R 7118	N/A	4860	N/A	N/A	7650	N/A	9750	NVR 3526	Test Objectives not Achieved
4-17-64	44-5	Two M/C Cluster Performance	ICTV	N/A	PDS 1543 -525 (112 MG)	N/A	N/A	N/A	N/A	17090	N/A	15280	NVR 3531	Normal
4-22-64	41-3	Two M/C Cluster Performance	ICTV	N/A	PDS 1543 -549 (112 MG)	N/A	N/A	N/A	N/A	17910	N/A	16350	FTR 1	Normal
4-27-64	44-8	Two M/C Cluster 5th Sail Removed	ICTV	N/A	PDS 1543 -549 (112 MG)	N/A	N/A	N/A	N/A	22400	N/A	8800	FTR 2	Some Blanketing after Disreef
4-30-64	44-6	Two M/C Cluster 1.2 x Do Suspension Line Length	ICTV	N/A	PDS 1543 -549 (112 MG)	N/A	N/A	N/A	N/A	14200	N/A	5400	FTR 3	Severe Blanketing
5-7-64	44-7	Same as 44-6 1.0 x Do Suspension Line Length	ICTV	N/A	PDS 1543 -551 (112 MG)	N/A	N/A	N/A	N/A	16200	N/A	12100	FTR 4	Normal
5-11-64	41-2	Two M/C Cluster Performance, 68 Gores	ICTV	N/A	PDS 1543 -539 (112 MG)	N/A	N/A	N/A	N/A	15300	N/A	10400	FTR 5	Split Gore after Disreef
5-14-64	44-9	Two M/C Cluster 1.4 x Do Suspension Line Length	ICTV	N/A	PDS 1543 -549 (112 MG)	N/A	N/A	N/A	N/A	17300	N/A	12300	FTR 6	Normal*

Table A-1 (Continued)

Test Date	Test Number	Test Objective	Vehicle	Parachute Version	Pilot	Main (C.D.)	Drop	FR	Drop	Pilot	Max. Loads (lbs)	Ref.	Comments
5-28-64	41-5	Two M/C Cluster Performance	ICTV	N/A	PDS 1543-555	(11.5 MG)	N/A	N/A	N/A	N/R	19800	PTR 7	Normal
6-10-64	41-6	Two M/C Cluster Performance	ICTV	N/A	PDS 1543-555	(9.7 MG)	N/A	N/A	N/A	N/R	12800	PTR 8	Normal
6-18-64	29-1	Two M/C Cluster Loads Investigation & Prediction	ICTV	N/A	PDS 1543-555	(9.7 MG)	N/A	N/A	N/A	N/R	16500	PTR 9	Broken Lines and Ripped Falls
7-1-64	48-1	Drogue Chute Reefing Characteristics	PTV	PDS 2119-515 (5.4 MG)	PDS 3125-501	(15.2 MG)	9277	7920	N/R	N/R	22350	PTR 10R	Normal
7-10-64	25-4	—	—	—	—	—	—	—	—	—	—	—	—
7-20-64	48-2	Drogue Chute Reefing Characteristics	PTV	PDS 2119-515 (5.4 MG)	PDS 3125-501	(12.1 MG)	9215	6910	N/R	N/R	11700	PTR 11	Normal
8-4-64	20-2	Three M/C Cluster Performance	ICTV	N/A	PDS 1543-557	(9.7 MG)	N/A	N/A	N/A	N/R	12640	PTR 12	Pilot Chute Separation
8-27-64	48-3	Drogue Chute Reefing Characteristics	PTV	PDS 2119-515 (5.4 MG)	PDS 3125-501	(12.1 MG)	10030	5570	N/R	N/R	14340	PTR 13	Normal
9-10-64	50-12	Complete System Dual Drogue	R/P	R 7117-503	R 7118-513	(13.4 MG)	6864	5883	N/R	N/R	N/A	PTR 16	Normal
10-2-64	50-13	Complete System Dual Drogue	R/P	R 7117-503	R 7118-513	(13.4 MG)	6827	6155	N/R	N/R	N/A	PTR 16	Normal

Table A-1 (Continued)

Test Date	Test Number	Test Objective	Vehicle	Parachute (Dia. Ft.)	Version	Pilot	Main (1 Do)	Drop	FR	Drop	Pilot	Max. Loads (lbs)	Ref.	Comments		
10-10-64	29-3	Two M/C Cluster, One Chute with 2 Stage Reefing, 75% of Sail Removed	ICTV	N/A	PDS 3125	PDS 1543	-561 (4% MQ)	N/A	N/A	N/A	N/A*	9350	22820	22350	FTB 15	Split 15% interference of Canopies, Canopy Collapse
							-567 (5% MQ)									
11-6-64	29-4	Three M/C Cluster	ICTV	N/A	PDS 1543	-561 (8% MQ)		N/A	N/A	N/A	N/A*	13250	N/A	13540	FTB 17	
												10100		5880		
												10074		7617		
11-16-64	29-3A	Two M/C Cluster, One Chute with 2 Stage Reefing, 75% of Sail Removed	ICTV	N/A	PDS 1543	-501 (8% MQ)		N/A	N/A	N/A	N/A*	9980	N/A	7580	FTB 18	Split 15%
												17120		27360		
11-24-64	46-1	Main Chute Pk Ultimate	ICTV	N/A	PDS 2119	R 7661-501 (9.5% MQ)		N/A	N/A	N/A	N/A	20800	N/A		FTB 20	Pilot separation, irregular in-clination
12-8-64	46-2	Main Chute Pk Ultimate	ICTV	N/A	PDS 3125	R 7661-501 (9.5% MQ)		N/A	N/A	N/A	N/A	17505	N/A	35055	FTB 20	Split 15% interference
12-11-64	46-1A	Main Chute Pk Ultimate	ICTV	N/A	PDS 2109	R 7661-501 (9.5% MQ)		N/A	N/A	N/A	N/A	34760	N/A	23650	FTB 25	Split 15% interference
12-18-64	46-3	Main Chute Pk Ultimate	ICTV	N/A	PDS 3125	R 7661-507 (9.5% MQ)		N/A	N/A	N/A	N/A	24380	N/A	27720	FTB 22	Split 15% interference
12-21-64	48-4	Drop Chute Reefing Characteristics	FTV	R 7579-501 (5.4)	PDS 3125	R 7661-507 (9% MQ)		9416	7940	7664	N/A	14001	N/A	27320	FTB 23	Split 15% interference
								8092	7664			14439		3321		Split 15% interference

Table A-1 (Continued)

Test Date	Test Number	Test Objective	Vehicle	Parachute Drogue (Dia. Ft.)	Parachute Pilot	Reaction Main (- Do)	Drogue No.	Pilot	Max. Loads (lbs.)	Ref.	Comments
1-8-65	48-5	Drogue Chute Reefing Characteristics	FTV	R 7579-505 (5.4)	R 7516-501	R 7527-503 (9.4)	17175 13230	N/A	15690 14740	FTF 24	Normal
1-29-65	46-4	Main Parachute F ₀ Ultimate	ICTV	N/A	R 7516-501	R 7661-509 (9.5% MO)	N/A	N/A	22900	FTF 25	Light Carafe
2-10-65	48-6	Drogue Chute Reefing Characteristics	FTV	R 7579-505 Open Only	R 7516-501	R 7561-505 (9% MO)	N/A	N/A	19560 17498	FTF 26	Normal
3-3-65	46-5	Main Parachute F ₀ Ult.	ICTV	N/A	R 7516-501	R 7661-502 (9.5% MO)	N/A	N/A	22480	FTF 27	Split Core Tear Full Open
5-6-65	60-1	Blk I Qualification	B/P	R 7620-13	R 7640-13	R 7540-535 (9.5% MO)	N/A	N/A	N/A	FTF 28	Normal
6-3-65	62-1	Blk I Qualification	B/P	R 7620-17	R 7640-13	R 7540-545 (9.5% MO)	N/A	N/A	N/A	FTF 29	Normal
8-5-65	62-3	Blk I Qualification	B/P	R 7620-1	R 7640-15	R 7540-539 (9.5% MO)	N/A	N/A	N/A	FTF 30	Interference with Pro-Parer Chute
8-3-65	62-2	Blk I Qualification	B/P	R 7620-1	R 7640-15	R 7540-539 (9.5% MO)	N/A	N/A	N/A	FTF 31	Normal
9-23-65	62-34	Blk I Qualification	B/P	R 7579-507	R 7516-501	R 7661-513 (9.5% MO)	N/A	N/A	N/A	FTF 32	One P/C did not Deploy

Table A-1 (Continued)

Test Date	Test Number	Test Objective	Vehicle	Parachute Drogue (Dia Ft.)	Pilot	Version	Reefing Main	PR	Drogue	Po	Pilot	Eq. Loads (lbs)	Ref	Comments
10-8-65	62-4	Blk I Qualification	B/P	R 7620-1	R 7640-17	R 7540-551	(9.5%W)	N/A	N/A	N/R	N/R	N/A	PTR 33	N/C Pack Hang-up
11-29-65	62-4A	Blk I Qualification	B/P	R 7620-1	R 7640-17	R 7540-551	(9.5%W)	N/A	N/A	N/R	N/R	N/A	PTR 34	Normal
12-2-65	62-7	Blk I Qualification	B/P	R 7620-1	R 7640-21	R 7540-553	(9.5%W)	N/A	N/A	N/R	N/R	N/A	PTR 35	Good N/C Deployment
1-28-66	62-8	Blk I Qualification	B/P	R 7620-1	R 7640-21	R 7540-553	(9.5%W)	N/A	N/A	N/R	N/R	N/A	PTR 36	High Rotational Rate
2-3-66	62-5	Blk I Qualification	B/P	R 7578-523	R 7515-503	R 7540-553	(9.5%W)	N/A	N/A	N/R	N/R	N/A	PTR 37	N/C Pack Hang-up
2-3-66	62-6	Blk I Qualification	B/P	R 7620-1	R 7640-21	R 7540-553	(9.5%W)	N/A	N/A	N/R	N/R	N/A	PTR 38	N/C Pack Hang-up
2-24-66	62-9	Blk I Qualification	B/P	R 7620-1	R 7640-21	R 7540-553	(9.5%W)	N/A	N/A	N/R	N/R	N/A	PTR 39	N/C Interference caused by high Rotational Rate
6-30-66	70-2		PTV	N/A	R 7516-501	R 7661-513	(9.5%W)	N/A	N/A	N/A	N/R	13930	20215	Normal
7-14-66	70-3	See next page												
8-5-66	30-1	N/C PR & Po Limit, one drogue, 2 main	PTV	N/A	R 7661-515	R 7661-515	(9.5%W)	N/A	N/A	N/A	N/R	21550	23205	Normal

Table A-1 (Continued)

Test Date	Test Number	Test Objective	Vehicle	Parachute Drogue (Dia. Ft.)	Parachute Version	Pilot Main (% Do)	Drogue Po	Pilot	Max. Loads (lbs)	Ref.	Comments
8-11-66	30-2	M/C PR Limit, Po Ult. 1 Droque, 2 Main	PTV	N/A	R 7516-501	R 7661-515 (9.5%MO)	N/A	N/R	22710	PTR 43 NVR 4081	Normal
7-14-66	70-3	M/C Steel Riser Test High Alt. Abort 2D-2M	PTV	N/A	R 7516-501	R 7661-513 (9.5%MO)	N/A	N/R	22385	PTR 41	Pilot Chute Separation, Split Gore
8-19-66	30-3	M/C PR Limit, Po Ult. 1 Droque, 2 Main	PTV	N/A	R 7516-501	R 7661-515 (9.5%MO)	N/A	N/R	23170	PTR 44 NVR 4085	Suspension Line Failure Followed by Radial Failure One Broken Suspension Line
9-1-66	70-1	M/C Steel Riser Test PR Ultimate	PTV	N/A	PDS 1203-521	DR 8058-513 (9.5%MO)	N/A	N/R	31090	PTR 45	
10-19-66	73-4	Blk II Qualification High Alt. Abort	B/P	R 7579-509	R 7516-501	R 7661-515 (9.5%MO)	N/A	N/R	N/R	PTR 46	Normal
12-7-66	73-1	Blk II Qualification Pad Abort	B/P	R 7579-509	R 7516-501	R 7661-515 (9.5%MO)	N/A	N/R	N/R	PTR 47	Moderate Blanketing
12-20-66	73-3	Blk II Qualification	B/P	R 7519-509	R 7516-501	R 7661-515 (9.5%MO)	N/A	N/R	N/R	PTR 48	Normal
1-17-67	73-5	Blk II Qualification	B/P	R 7579-509	R 7516-501	R 7661-515 (9.5%MO)	N/A	N/R	N/R	PTR 49	Interference with Forward Heat Shield
2-10-67	80-1	M/C Raising Station & Intervals	ICTV	N/A	R 7516-501	R 7661-517 (8.2/21.8)	N/A	N/A	N/A	NVR 6106	First Stage Reefing Hang-up 6 Broken Suspension Lines

Table A-1 (Continued)

Test Date	Test Number	Test Objective	Vehicle	Parachute Drogue Dia., Ft.	Parachute Pilot	Main (\$ Do)	Drop Rate	Pilot	Max. Loads (lbs)	Ref.	Comments
									FR1 Main FR2		
7-17-67	80-1R	M/C Reefing Ratios and Intervals	ICTV	N/A	R 7615-501	R 7661-517 (8.2/21.8)	N/A	N/A	13381 12749	NVR6106 13593	Normal*
7-21-67	80-2	Verify M/C Reefing Ratios	ICTV	N/A	R 7516-501	DR 7561-521 (8.2/24.0)	N/A	N/A	18700 18205	NVR6106 21790	Broken Cutter Lanyard
7-27-67	81-1	Verify M/C Reefing Ratios Two Chute Cluster	ICTV	N/A	R 7516-501	DR 7661-521 (8.2/24.0)	N/A	N/A	16107 12760	NVR6106 14131 15148	One Broken Cutter Lanyard Stage 2 Reefing Line Load = 127,196 lb
8-2-67	80-3	Verify M/C Reefing Ratios	ICTV	N/A	R 7516-501	DR 7661-521 (8.4/28.5)	N/A	N/A	15240 14760	NVR 6035A 31400	Pilot Riser Failure Stage 2 Reefing Line Load = 101 lb
8-10-67	80-3R	Verify M/C Reefing Ratios	ICTV	N/A	R 7516-501	DR 7661-523 (8.4/26.7)	N/A	N/A	15240 21236	NVR6106 23300	Pilot Riser Failure Stage 2 Reefing Line Load = 300 lb
8-25-67	80-3R1	P/C Load Data Verify M/C Reefing Ratios	ICTV	N/A	DR 7516-509	DR 7661-523 (8.4/26.7)	N/A	N/A	19768 19891	NVR 6035A 20931	Normal Stage 2 Reefing Line Load = 250 lb
8-26-67	81-3	Verify M/C Reefing Ratios P/C Performance	ICTV	N/A	DR 7516-509	DR 7661-523 (8.4/26.7)	N/A	N/A	18438 19225	NVR6106 14185	Normal Stage 2 Reefing Line Load = 234 lb
9-7-67	81-4	Verify M/C Reefing Ratios	ICTV	N/A	DR 7516-509	DR 7661-527 (8.4/26.7)	N/A	N/A	15693 15780	NVR6106 17151	Normal Stage 1 Reefing Line Load = 143 lb

Table A-1 (Continued)

Test Date	Test Number	Test Objective	Vehicle	Parachute Drogue (Dia. Ft.)	Pilot	Main (\$ Do.)	Drague \$	Pilot	Max. Loads (lbs)	Ref.	Comments
									FR1 Main FR2		
9-8-67	81-2	Verify M/C Reefing Ratios P/C Performance	ICTV	N/A	DR7516-509	DR 7661-527 (8.4/26.7)	N/A	N/A	3690 3595	NVR6106	Normal Stage 2 Reefing Line Load = 231 lb
9-19-67	80-3R2	P/C Load Data Verify M/C Reefing Ratios	ICTV	N/A	DR 7516-511	DR 7661-527 (8.4/26.7)	N/A	N/A	4650	NVR6106	Normal
10-6-67	82-2	M/C FR2 Ultimate Load	ICTV	N/A	DR 7516-501	DR 7661-525 (8.4/24.8)	N/A	N/A	N/R 20375	NVR6158	Normal
10-17-67	82-4	M/C P/O Ultimate Load	ICTV	N/A	DR 7516-501	DR 7661-525 (9.5/24.8)	N/A	N/A	N/R 22900	NVR6158	4 Broken Suspension Lines 3 Torn Sails
10-20-67	99-1	Check for Grease Contamination from Prop Plant	FTV	N/A	N/A	N/A	N/A	N/A	N/A	NVR6109	
10-30-67	84-1	D/C P/R Limit Load	FTV	R8155-501 (6.6/10.1)	R 7516-501	DR 7661-525 (8.4/24.8)	17300 15600	20800 20825	N/R	NVR6105 NVR6160	M/C Reefing at FR1 Discreet
12-8-67	99-2	D/C P/R Ultimate Load	ICTV	R8155-505 (6.6/10.1)	N/A	N/A	27100 26440	35920	N/A	NVR6064	Radial Failure During Reefed Stage, Split Gore after Discreet

Table A-1 (Continued)

Test Date	Test Number	Test Objective	Vehicle	Parachute Drogue (Dia Ft)	Pilot	Drop (% Dc)	Main (% Dc)	Drop FR	Drop PO	Pilot	Max. Loads (lbs)	Ref.	Comments
12-20-67	84-1R	D/C FR Limit Load	PTV	R 8155- 505 (6.6/10.5)	R 7516- 501 (8.4/24.8)	DR 7661- 525 (8.4/24.8)	DR 7661- 525 (8.4/24.8)	16665 17950 (8.4/24.8)	17155 16695	N/R	12000 12410 12080	NVR6160 NVR6198 10040	Normal
1-4-68	84-4	D/C FO Ultimate Load	PTV	R 8155- 507 (6.02/10.5)	R 7516- 505 (8.4/24.8)	DR 7661- 525 (8.4/24.8)	DR 7661- 525 (8.4/24.8)	12080	27250	N/R	17830	NVR6198	Normal
1-11-68	84-3	D/C FR Ultimate Load	PTV	R 8155- 507 (6.02/10.5)	R 7516- 505 (8.4/24.8)	DR 7661- 525 (8.4/24.8)	DR 7661- 525 (8.4/24.8)	3525 8920 (8.4/24.8)	Failure —		24180 28450	NVR6160	D/C Failure at Disreef
1-31-68	82-1	M/C FR Ultimate Load	ICTV	N/A	DR 7516- 505 (8.4/15.4/24.8)	DR 7661- 525 (8.4/15.4/24.8)	DR 7661- 525 (8.4/15.4/24.8)	N/A	N/A	N/R	27780	NVR6158	Test Conditions not Achieved
2-10-68	82-1R	M/C FR Ultimate Load	ICTV	N/A	DR 7516- 505 (8.4/15.4/24.8)	DR 7661- 519 (8.4/15.4/24.8)	DR 7661- 519 (8.4/15.4/24.8)	N/A	N/A	N/R	30070	NVR6158	Normal
2-14-68	99-3	D/C FR Ultimate Load	ICTV	R 8155- 509 (6.02/10.5)	N/A	N/A	N/A	21940 20325	22520 21980	N/A	N/A	N/A	Broken Oiler Lanyard
2-21-68	83-6	Verify M/C Resisting Ratio	PTV	R 8155- 509 (6.02/10.5)	R 7516- 505 (8.4)	DR 7661- 525 (8.4)	DR 7661- 525 (8.4)	11130 11440	16280 17290	N/R	12360	NVR6198	Knot in D/C Riser
3-1-68	99-4	D/C FR Ultimate Load	ICTV		N/A	N/A	N/A	19510 22140	22260 23340	N/A	N/A	NVR6080	Load Link Oscillations
3-23-68	99-5	D/C FR Ultimate Load	ICTV	R 8155- 509 (7.06/10.5)	N/A	N/A	N/A	— 24480	Failure Failure	N/A	N/A	NVR6068	D/C Riser Failure Faulty Instru- mentation

Table A-1 (Continued)

Test Date	Test Number	Test Objective	Vehicle	Parachute Version/Reefing			Max. Loads (lbs)			Ref.	Comments	
				Drogue (Dia. Ft.)	Pilot	Main (g Do)	Drogue F _o	Pilot	Main F _{R1} F _{R2} F _o			
4-4-68	85-1	Blk II H Qualification Normal Entry	B/P	R 8155- 509 (7.06/10.5)	R 7516- 505	R 7661- 519 (8.4/24.8)	7100 9550 8300	N/R	9155 6870 5045 9485 7966 6965	NVR6070	Normal	
							6200		12075 11780 10845	NVR6070	D/C Blaser Damaged	
4-24-68	85-3	Blk II H Qualification Normal Entry, 1 Drogue	B/P	R 8155- 509 (7.06/10.5)	R 7516- 505	R 7661- 519 (8.4/24.8)	8750 14500	N/R	10725 —	—	Instrumentation Damaged	
5-1-68	85-2	Blk II Qualification Pad Abort	B/P	R 8155- 509 (7.06/10.5)	R 7516- 505	R 7661- 519 (8.4/24.8)	5330 4780 5710	N/R	13600 13200	10355 10650	NVR6070 Normal	
5-14-68	85-6	Blk II H Qualification Pad Abort, No Drogue	B/P	N/A 509 (8.4/24.8)	R 7516- 509	R 7661- 519 (8.4/24.8)	N/A N/A	N/P	12850 13475 9500	9950 6720	NVR6070 Normal	
6-6-68	85-5	Blk II H Qualification High Alt. Abort, 1 Drogue	B/P	R 8155- 509 (7.06/10.5)	R 7516- 509	R 7661- 519 (8.4/24.8)	11555 10970	N/R	12748 9618 10653	8267 5040 7610	NVR6070 Normal	
6-7-68	85-4	Blk II H Qualification Normal Entry, One Drogue	B/P	R 8155- 509 (7.06/10.5)	R 7516- 509	R 7661- 519 (8.4/24.8)	9610 14630	N/R	11670 11085 10570	9000 9225 9020	6370 7535 7560	Twisting of M/C Risers
7-3-68	85-7	Blk II H Qualification High Alt. Abort, 1 Drogue 2 Main	B/P	R 8155- 509 (7.06/10.5)	R 7516- 509	R 7661- 519 (8.4/24.8)	N/R N/R	N/R	13597 9962	16429 9529	13900 10366	Twisting of M/C Risers
7-16-68	99-5R	D/C FR Ultimate Load	PTV	R 8155- 509 (7.06/10.5)	R 7516- 509	R 7661- 519 (8.4/24.8)	28340 25930	Failed Failed	Failed	—	—	Programmer Failure

Table A-1 (Concluded)

Test Date	Test Number	Test Objective	Vehicle	Parachute (Dia. Ft.)	Dropgue (g. Do.)	Reefing	Dropgue (FR)	Dropgue (FO)	Pilot	Max. Loads (lbs)	Main (FR2)	Ref.	Comments
9-12-68	86-1	High Alt. Commanded Abort	B/P	N/A	R 7516-509	R 7661-519 (8.4/24.8)	N/A	N/A	N/R	9910	11595	NVR6347	Normal, Two H/C Canopies used Previously
		Low g. No Dropgues								8425	8420		
										8205	7850	6775	
11-6-68	87-1	Verify Strength of Blk I M/C Pack Stores 18 Months	ICTV	N/A	R 7516-509	R 7661-515 (9.5)	N/A	N/A	N/R	26950	N/A	NVR6330	Split Core During Reefed State. Bridle Failure
11-11-68	86-2	System Performance Normal Entry	B/P	R 8155-509 (7.66/10.5)	R 7516-509	R 7661-519 (8.4/24.8)	10000	14650	N/R	N/R	N/R	NVR6377	High Roll Rates. Main Chute Lines Twisted
1-7-69	86-3	High Altitude Abort at Max. g	B/P	R 8155-509 (7.66/10.5)	R 7516-509	R 7661-519 (8.4/24.8)	15360	11045	N/R	10250	10455	NVR6388	Severe blanketing of one main parachute
							15495	10855		6405	3760	435	
										8425	missed stage	13990	
1-22-69	86-4	Pad Abort	B/P	R 8155-509 (7.66/10.5)	R 7516-509	R 7661-519 (8.4/24.8)	14650	7745	N/R	12540		NVR6399	Some blanketing
							14225	7005		9175	7500	4540	
										10010	8485	5800	

APPENDIX B
EXAMPLE MARGIN OF SAFETY CALCULATIONS FOR THE APOLLO
MAIN PARACHUTE

Margin of safety calculations for one design condition for the Apollo main parachute, and a comparison with the values given in the Block II (H) stress analysis¹⁹ are presented in this appendix to illustrate the refinements in parachute structural analysis made possible by this study.

Design loads are based on the maximum loads for the one-drogue, two-main (1D/2M) entry condition computed in Appendix C of Volume I.¹ A load-time history corresponding to these maximum stage loads is constructed analytically with the aid of drop test films and load traces from representative flight conditions and configuration. Canopy differential pressure distributions are estimated from shape data observed in drop test films and from the wind tunnel data of Reference 20. The uncertainty in this parameter is satisfactorily resolved by applying a set of pressure distribution curves that covers the range that can be reasonably expected to occur. Loadings for all elements of the canopy structural model (see Section 4.3.1) are computed by means of program CANO. Safety factors, temperature degradation factors, and joint efficiencies are taken from the Block II (H) stress analysis, Reference 19, pp 281-292.

RISER LOADING

The design ultimate loads for the one-drogue, two-main entry case are obtained by multiplying the limit loads computed in this study (Appendix C of Volume I) by a safety factor of 1.35. The table below gives the new loads used in this analysis, and also the corresponding values, for comparison, from Reference 19.

GROUP

Design Ultimate Loads - 1D/2M Entry Condition

	<u>New Load</u> (1.35 x Limit Load from Volume I)	<u>Old Load</u> (From Reference 19)
First stage	25,200 lb	27,350 lb
Second Stage	24,800 lb	31,600 lb
Open	25,200 lb	29,700 lb

For this analysis, internal loads are computed at critical time instants throughout the opening process. These events, called inflation states in this analysis, correspond to the inflation of the individual sails. For example, Inflation State 1 occurs just as Sail 1 inflates and ceases to flutter randomly. By identifying this event in drop test films and correlating the timing with load traces, the fraction of the maximum stage load present at each inflation state can be established. Design loads are obtained by multiplying the stage design load by this factor.

Table B-1 summarizes the design loads used in this analysis.

Table B-1		
Inflation State	Fraction of Max. Stage Load	Design Ultimate Load, lb
1	.741	18,670
2	.806	20,310
3	.882	22,200
4	1.00	25,200
5	.819	20,310
6	1.00	24,800
7	.819	24,800*
8	.591	24,800*
9	.645	16,250
10	.795	20,030
11	1.000	25,200
12	.952	23,990

-
- * Maximum load is applied throughout latter portion of this stage to cover uncertainty in inflation-time history.

PRESSURE DISTRIBUTION

Program CANO proportions local pressure acting on each element in accordance with any specified distribution curve and adjusts overall magnitude to balance the applied riser load. Variations in the shape of the pressure curve have a first order effect on the stresses in individual elements. Because of the many practical problems involved in direct measurement of differential pressures in inflating parachutes, no measurements were made during the Apollo test programs. Some knowledge of this parameter has been gained indirectly from drop test photographic coverage by comparing observed canopy shapes with shapes computed by the CANO computer program, using assumed distribution curves (see Section 4.3.3). Pressure measurements made by Melzig^{20,21} in wind tunnel and flight tests, while not directly applicable to the Apollo parachutes, provide general knowledge of the variations in pressure distribution during inflation. However, the available data is not considered accurate enough for prediction of precise pressure distributions for use in the stress analysis. To provide a conservative analysis, a comprehensive set of distribution curves that covers the worst cases that can be reasonably expected to occur is applied for each inflation state. The family of curves shown in Figure B-1 resulted from shape analysis of Apollo drop test films, from Melzig's test results^{20,21}, and from a computer study of the effect of pressure distribution curve shapes on internal loading. As shown in Figure B1, a pressure peak is applied at various locations in the inflated portion of the canopy from the vent to the leading edge. For each inflation state, load calculations for the entire canopy are made for a number of pressure curves, selected to give peak pressures on each sail in turn. Table B-2 gives a summary of the results of these calculations in the form of load-strength ratios (applied load ÷ rated strength) for the critical element of each sail for the loading conditions considered.

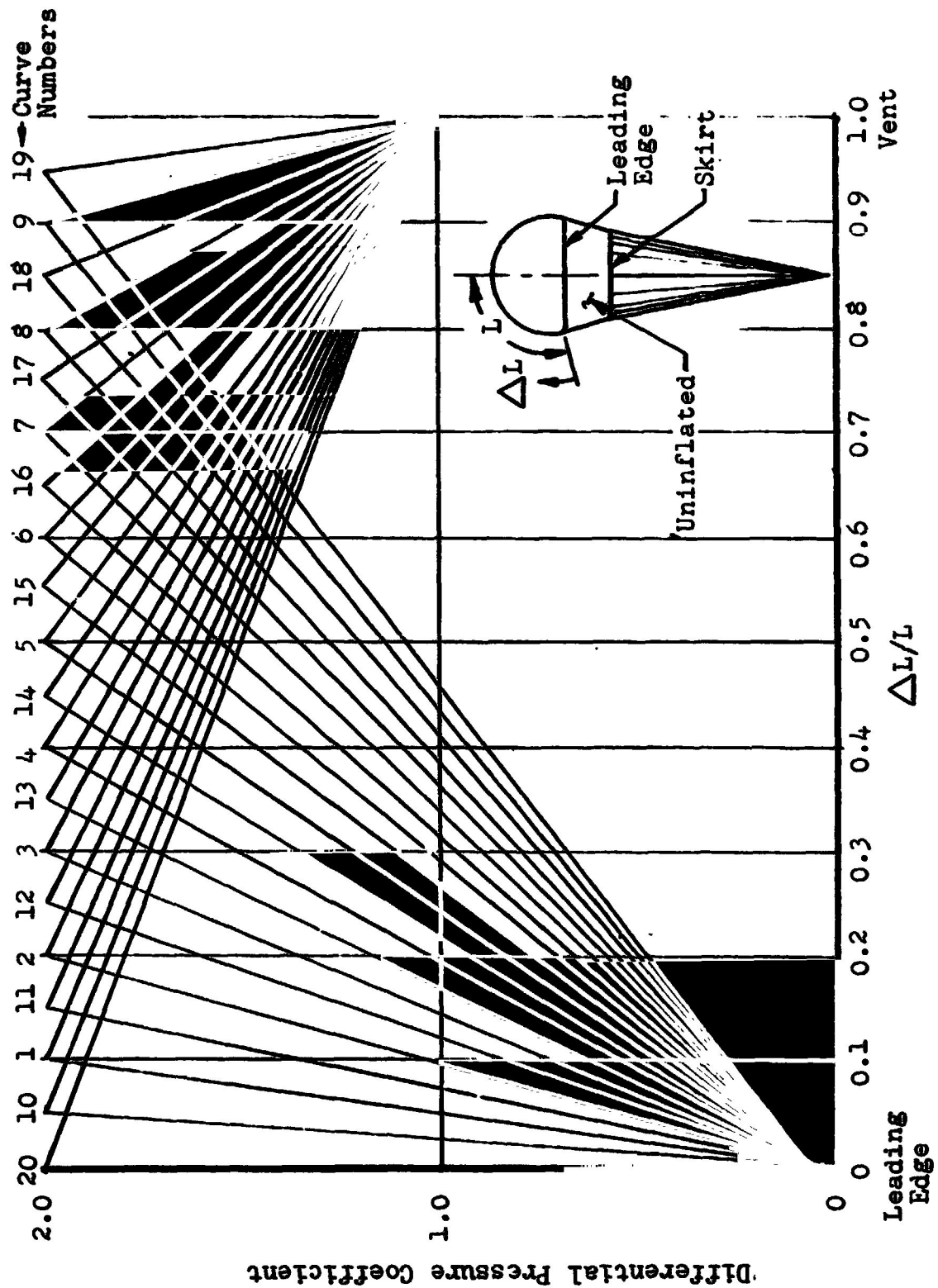


Fig. B1. Pressure Distribution Curves

NORTHROP

Table B-2 Sail Load-Strength Ratios

Load lb	Pressure Curve No.	Sail Number											
		1	2	3	4	5	6	7	8	9	10	11	12
First Stage													
18,670	9	.36											
20,310	9	.37	.07										
20,310	5	.34	.18										
22,220	9	.36	.25	.03									
22,220	16	.38	.33	.04									
22,220	3	.35	.34	.10									
25,200	9	.40	.35	.06	.02								
	17	.39	.38	.08	.02								
	5	.37	.37	.19	.03								
	12	.35	.35	.26	.06								
25,200	20	.32	.33	.28	.10								
Second Stage													
20,310	9	.31	.30	.10	.02	0							
	8	.31	.31	.13	.02	0							
	6	.29	.30	.20	.03	0							
	4	.27	.28	.23	.07	0							
20,310	13	.25	.26	.23	.09	.04							
24,800	9	.35	.34	.20	.04	.02	.02						
	18	.34	.34	.22	.04	.02	.02						
	7	.33	.34	.26	.06	.02	.02						
	5	.29	.31	.28	.12	.03	.02						
	6	.27	.29	.28	.19	.09	.02						
	11	.27	.28	.28	.20	.11	.09						
	9	.33	.33	.24	.07	.03	.03	.01					
	18	.32	.33	.25	.07	.03	.03	.01					
	7	.30	.32	.28	.12	.04	.03	.01					
	15	.28	.30	.29	.18	.05	.04	.02					
	3	.25	.28	.28	.23	.12	.10	.03					
	11	.23	.26	.27	.24	.16	.15	.08					
	9	.31	.32	.26	.12	.04	.03	.02	.01				
	17	.29	.31	.28	.16	.05	.04	.03	.01				
24,800	6	.27	.29	.29	.22	.07	.06	.03	.01				

CONTINUED

Table B-2 (Concluded)

Load lb	Pressure Curve No.	Sail Number											
		1	2	3	4	5	6	7	8	9	10	11	12
24,800 ↑ ↓ 24,800	4	.24	.27	.28	.25	.14	.13	.05	.02				
	13	.23	.25	.27	.25	.17	.16	.06	.02				
	12	.23	.25	.26	.25	.19	.12	.10	.03				
	1	.22	.24	.26	.25	.24	.26	.15	.09				
	20	.21	.24	.26	.25	.27	.16	.19	.10				
Third Stage													
16,250 ↑ ↓ 16,250	9	.19	.20	.18	.11	.04	.03	.02	.01	.01			
	8	.18	.19	.19	.12	.04	.04	.01	0	.01			
	16	.17	.18	.19	.16	.06	.05	.03	.02	.01			
	14	.14	.16	.17	.16	.13	.13	.05	.02	.01			
	3	.13	.14	.16	.16	.16	.08	.12	.04	.01			
	2	.12	.14	.15	.15	.18	.21	.16	.07	.02			
20,030	1	.12	.13	.14	.15	.19	.22	.19	.10	.04			
20,030 ↑ ↓ 20,030	5	.16	.18	.19	.19	.19	.21	.12	.04	.02	.01		
	4	.14	.16	.18	.18	.22	.25	.19	.06	.03	.01		
	3	.14	.15	.19	.18	.23	.27	.24	.12	.04	.01		
	2	.13	.14	.16	.17	.24	.28	.27	.18	.07	.02		
25,200	1	.06	.12	.15	.17	.23	.28	.29	.22	.10	.05		
25,200 ↑ ↓ 25,200	9	.23	.25	.25	.22	.14	.15	.08	.04	.02	.01	.01	
	7	.20	.23	.25	.24	.20	.22	.13	.05	.03	.02	.01	
	15	.17	.20	.23	.23	.27	.30	.22	.09	.04	.02	.01	
	14	.16	.19	.22	.23	.29	.33	.29	.15	.05	.02	.01	
	13	.15	.17	.20	.23	.29	.34	.33	.23	.08	.03	.01	
	12	.13	.16	.19	.22	.29	.34	.26	.29	.15	.05	.02	
	2	.13	.15	.18	.22	.29	.33	.35	.30	.18	.07	.03	
23,990	1	.12	.14	.17	.21	.28	.33	.35	.30	.23	.13	.06	
23,990 ↑ ↓ 23,990	18	.20	.23	.24	.22	.19	.21	.14	.06	.03	.02	0	0
	6	.12	.19	.22	.23	.27	.31	.26	.15	.05	.03	.02	.01
	5	.15	.17	.21	.23	.29	.34	.32	.21	.08	.03	.02	.01
	3	.12	.14	.18	.21	.28	.33	.35	.32	.21	.09	.04	.01
	20	.04	.10	.13	.16	.23	.29	.33	.35	.31	.28	.24	.10

NOTES

MARGINS OF SAFETY WITH NEW LOADS

The critical load-strength ratios from the CANO solutions are used, together with joint efficiencies and design factors from the Block II(H) stress analysis¹⁹, to compute the margins of safety for the major canopy components.

$$MS = \frac{J_{\text{oint Eff}} \times \text{Thermal Factor} \times \text{Abrasion Factor}}{\text{Load-Strength Ratio} \times \text{Unsym. Load Factor}} - 1$$

Corresponding margins from Reference 19 are also shown for comparison. The difference in the compared margins is due to the revised load input values and the refined stress analysis.

Sails

The critical load-strength ratios shown in Table B-2 are used, together with the design factors listed below, to calculate the margins shown in Table B-3.

Design factors:

Joint Efficiency	0.55	Thermal Factors	
Abrasion Factor	1.00	First Stage	0.87
Unsym. Loading	1.05	Second Stage	0.92
		Open	0.94

Table B-3. Sail Margins of Safety with New Loads

Sail Number	Margin of Safety		
	1st Stage	2nd Stage	Open
1	.15	.48	1.5
2	.22 (.05)*	.40	1.2
3	.63	.67 (.17)*	1.0
4	high	.90	1.05
5		.82	.69
6		.89	.46
7		1.6	.40
8		high	.43
9			.58
10			.72 (.10)*
11			1.2
12			high

* Values shown in parenthesis () are margins given in Reference 19 for the 1D/2M entry condition.

Suspension Lines

Maximum suspension line loads from the calculations discussed above are:

First stage	371 lb
Second stage	367 lb
Third stage	379 lb

Rated strength and design factors from Reference 19 are:

Rated strength	650 lb
Joint efficiency	0.86
Thermal factors	
First stage	0.87
Second stage	0.92
Open	0.94
Abrasion factor	0.96
Unsymmetrical loading	1.05

Margins of Safety with New Loads

	<u>Present Analysis</u>	<u>From Reference 19</u>
First stage	0.20	
Second stage	0.28	0.0
Open	0.27	

Skirt and Vent Bands

Maximum loads computed for the skirt and vent bands for the full open, split gore condition are:

Skirt band	1240 lb
Vent band	3590 lb

Rated strength and design factors from Reference 19 are:

Rated strength	Skirt band	2400 l.
	Vent band	5200 .

NOTHING

Joint efficiency	0.95
Abrasion	0.96
Thermal	0.96

Margins of Safety with New Loads

Skirt band	=	0.69
Vent band	=	0.27

Corresponding values are not shown in Reference 19 since the entry condition was not critical for these members.

Radial Tapes

Maximum radial tape loads from the previous calculations are:

First stage	381 lb
Second stage	415 lb
Open	379 lb

Rated strength and design factors from Reference 19 are:

Rated strength	$2 \times 350 = 700$ lb
Joint efficiency	0.89
Abrasion factor	0.96
Unsymmetrical load	1.05

Thermal

First stage	0.87
Second stage	0.92
Open	0.96

Margins of Safety with New Loads

	<u>Present Analysis</u>	<u>From Reference 19</u>
First stage	MS = .30	
Second stage	MS = .26	.09
Open	MS = .44	

CONTINUED

CONCLUDING REMARKS

This analysis could be extended to other design cases where applicable empirical data (load-inflation history) is available. It is of interest to note here that the calculations for each of the 68 solutions reported in Table B-2 would have required approximately one man-week of effort with the analysis tools available at the beginning of this study. With program CANO, additional solutions (once the structural model is set up) are obtained by a single punched card input. Execution time on a large digital computer (IBM 360/65) averages less than two minutes per solution.

The example case (one-drogue, two-main, entry) is presented to illustrate the improved stress analysis made possible by this study. The foregoing MS calculations are therefore intended to provide an illustration of the techniques and not to establish official changes in the Apollo ELS margins of safety of record.

REFERENCES

1. Mickey, F. E., McEwan, A. J., Ewing, E. G., Huyler, W.C., Jr., and Khajeh-Nouri, B., "Investigation of Prediction Methods for the Loads and Stresses of Apollo Type Spacecraft Parachutes, Volume I - Loads", NVR-6431, June 1970, Northrop Ventura, Newbury Park, Calif.
2. Jones, R. A., "On the Aerodynamic Characteristics of Parachutes," R&M No. 862, June 1923, Aeronautical Research Council, Great Britain.
3. Stevens, G. W. H., and Johns, T. F., "The Theory of Parachutes with Cords over the Canopy," R&M No. 2320, July 1942, Aeronautical Research Council, Great Britain.
4. Beck, E., "The Parachute Considered as a Flexible Shell of Rotation," ATI-32297, November 1942, USAF Translation of German Report No. BR-281.
5. Jaeger, J. A., Culver, I. H. and Della-Vedova, R. P., "A Study of the Load Distribution in a Conical Ribbon Type Parachute," Report No. 8641, August 1952, Lockheed Aircraft Corp., Burbank, Calif.
6. Culver, I. H., "Load Distribution in a Conical Ribbon Parachute," Report No. 8541, October 1951, Lockheed Aircraft Corp., Burbank, Calif.
7. Culver, I. H., Kinghorn, G. and Della-Vedova, R. P., "A Note on the Aeroelastic Stability of Reefed Ribbon Parachutes," Report No. 8544, August 1952, Lockheed Aircraft Corp., Burbank, Calif.
8. Della-Vedova, R., "Determination of Forces at the Skirt of a Reefed Parachute," Report No. 8543, October 1952, Lockheed Aircraft Corp., Burbank, Calif.
9. Topping, A. D., Marketos, J. D. and Costakos, N. C., "A Study of Canopy Shapes and Stresses for Parachutes in Steady Descent," TR-55-294, October 1955, Wright Air Development Center, Ohio (AD 103 963).
10. Lester, W. G. S., "A Note on the Generalization of Elastic Curves Representing Parachute Shapes," TN-ME-357, July 1962, Royal Aircraft Establishment, England (AD 290 294).
11. Heinrich, H. G. and Jamison, L. R., Jr., "Stress Analysis of a Parachute during Inflation and at Steady State," FDL-TDR-64-125, February 1965, Wright-Patterson Air Force Base, Ohio (AD 461 387).
12. Heinrich, H. G. and Jamison, L. R., "Parachute Stress Analysis," Paper presented to Final Phase Aerodynamic Deceleration Course, July 1965, University of Minnesota, Minnesota.

REFERENCES

13. Heinrich, H. G., and Monson, D. J., "Stress Analysis of Parachutes," Paper presented to Course on Aerodynamic Deceleration, July 1961, University of Minnesota, Minnesota.
14. Heinrich, H. G. and Jamison, L. R., "Parachute Stress Analysis during Inflation and at Steady State," Paper presented to AIAA Entry Technology Conference, October 1964, Williamsburg, Virginia.
15. Chernowitz, C., ed., "Performance of and Design Criteria for Deployable Aerodynamic Decelerators," ASD-TR-61-579, December 1963, AFFDL, Wright-Patterson Air Force Base, Ohio.
16. Asfour, K. J., "Analysis of Dynamic Stress in an Inflating Parachute," Journal of Aircraft, Vol. 4, No. 5, September - October 1967, pp. 429-434.
17. Speakman, L. and Topp, G., "Strength Analysis - Apollo Earth Landing System," May 1966, NVR 3735A, Northrop Ventura, Newbury Park, Calif.
18. Ranes, R., Topp, G., and Utzman, C., "Strength Analysis - Apollo Earth Landing System, Block II," NVR-4055, March 1967, Northrop Ventura, Newbury Park, Calif.
19. Utzman, C., Mullins, W., Reynolds, D., Farnsworth, R. and Labbe, J., "Strength Analysis - Apollo Block II Earth Landing System, Weight Accommodation Program," NVR-6112A, Sept. 1968, Northrop Ventura, Newbury Park, Calif.
20. Melzig, H. D., and Schmidt, P. K., "Pressure Distribution during Parachute Inflation--Phase I, Infinite Mass Opening Case," AFFDL-TR-66-10 (AD 482 534), March 1966.
21. Melzig, H. D., and Saliaris, C., "Pressure Distribution during Parachute Opening," AFFDL-TR-68-135, February 1969, Wright-Patterson Air Force Base, Ohio.
22. McEwan, A. J., Huyler, W. C. Jr., Mullins, W. M. and Reynolds, D. T., "Description of Computer Programs for the Analysis of Apollo Parachutes," NVR-6428, June 1969, Northrop Ventura, Newbury Park, Calif.
23. Lyons, W. James, Impact Phenomena in Textiles, M.I.T. Press, Cambridge, Mass., 1963, p. 142, Figure 6.19, 20.
24. Op. cit. pp 72-78.
25. Hall, I. H., "The Tensile Properties of Textile Yarns at Very High Strain Rates," High Speed Testing, Vol. 4, Interscience Publishers, New York 1964, pp 237-256.

NORTHROP

26. Malvern, L. E., "The Propagation of Logitudinal Waves of Plastic Deformation in a Bar of Material Exhibiting a Strain Rate Effect," Journal of Applied Mechanics, Vol. 18, June 1951, pp 203-208.
27. Coskern, R. J., Morgan, H. M., and Chu, C. C., "Behavior of High Strength Parachute Components at Impact Velocities up to 700 Feet Per Second," High Speed Testing, Vol. 3, Interscience Publishing, New York, 1962, p. 103, Fig. 15.
28. Ringleb, Friedrich O., "Cable Dynamics," NAEF Report ENG-6169, December 1956, U. S. Naval Air Material Center, Philadelphia, Pennsylvania, pp 65-67.
29. Malvern, L. E., "Plastic Wave Propagation in a Bar of Material Exhibiting a Strain-Rate Effect," Quarterly of Applied Mathematics, Vol. 8, No. 4, January 1951, pp 405-411.
30. Mortimer, R. and Hoburg, J. F., "MODIT 21 A Computer Code for One-Dimensional Elastic Wave Problems," NASA CR-1306, April 1969.
31. Chou, P. C., Mortimer, R. W., "Solution of One-Dimensional Elastic Wave Problems by the Method of Characteristics," Journal of Applied Mechanics, Vol. 34, No. 3, September 1967, pp 745-750.
32. Fenstermaker, C. A., and Smith, J. C., "Stress-Strain Properties of Textile Yarns Subjected to Rifle Bullet Impact," High Speed Testing, Vol. V, Interscience Publishing, New York, 1965, pp 125-146.
33. von Neumann, J., and Richtmyer, R. D., "A Method for the Numerical Calculation of Hydrodynamic Shocks," Journal of Applied Physics, Vol. 21, March 1950, pp 232-237.
34. Trulio, J. G., "Studies of Finite Difference Techniques for Continuum Mechanics," NVR-3582, December 1964, Northrop Ventura, Newbury Park, Calif. (AD 613 351).
35. Coskren, R. J., Chu, C., "Investigation of the High Speed Impact Behavior of Fibrous Materials - Part III, Impact Characteristics of Parachute Materials", WADD-TR-60-511, Part III, May 1963.
36. von Karman, Theodore and Duwez, Pol, "The Propagation of Plastic Deformation in Solids", Journal of Applied Physics, Vol. 21, October 1950, pp 987-994.
37. Hausknecht, D. F., Kessler, R. and Darienzo, M. F., "An Investigation of the Materials and Constructions of Tension Members for Use in Aircraft Arrestment Equipment," ASD TN-61-66, June 1961, Wright-Patterson Air Force Base, Ohio (AD 268 209), pp 49-56.

REFERENCES

38. Heinrich, H. G., et al, "Pressure Distribution in Transonic Flow of Ribbon and Guide Surface Parachute Models," WADC 59-32, February 1959, Wright-Patterson Air Force Base, Ohio.
39. Babish, C. A. and Hunter, W. C., "Visualization of the Flow Field about Parachute Canopy Models and Approximation of Canopy Pressure Distributions," FDL-TDR-64-136, January 1965, Wright-Patterson Air Force Base, Ohio.
40. Heinrich, H. G. and Jamison, L. R., Jr., "Parachute Stress Analysis during Inflation and at Steady State," Journal of Aircraft, Vol. 3, No. 1, 52-58 (1966).
41. Melzig, H. D., "The Change in Pressure Distribution on Parachute Canopies during Inflation," paper presented at the Aerodynamic Deceleration Course, July 1965, University of Minnesota.
42. Melzig, H. D., "The Dynamic Pressure Loading on Parachute Canopies," paper presented to AIAA Aerodynamic Deceleration Systems Conference, September 1966, Houston, Texas.
43. Anon, "Proposal for a Differential Pressure Monitoring System", G. T. Schjeldahl Company, May 1967, Northfield, Minnesota.
44. Anon, "Technical Proposal for Differential Pressure Transducer System, RdF West, February 1968, Westminster, California.
45. Ranes, R. J., "Nonelectrical Maximum Strain Gage," Patent Disclosure No. NV/68-6, July 1968, Northrop Ventura, Newbury Park, California.
46. Groat, J. F. Jr. and Nash-Boulden, S. S., "Analysis of Apollo Main Parachute Wind Tunnel Test Using Full, Half and Third Scale Models," NVR-2928, January 1964, Northrop Ventura, Newbury Park, California.